Solid Lipid Matrices for Delivery of Laundry Actives and Lipid Membrane Transport

CHIFUNDO NYASHA MICHELLE NTOLA

How to cite:

NTOLA, CHIFUNDO NYASHA MICHELLE (2017) Solid Lipid Matrices for Delivery of Laundry Actives and Lipid Membrane Transport. Doctoral thesis, Durham University.

Solid Lipid Matrices for Delivery of Laundry Actives and Lipid Membrane Transport

Chifundo Nyasha Michelle Ntola

A thesis submitted in partial-fulfillment of the
requirements for the degree of Doctor of Philosophy

Department of Chemistry

Durham University

July 2016

Thesis accepted by:

Dr Ritu Kataky (supervisor)

Dr Sharon Cooper (internal examiner)

Dr Aoife Morrin (external examiner)

Department of Chemistry

Durham University

July 2016

Abstract

The work presented in this thesis reports the preparation and characterisation of novel solid lipid microparticle (SLM) and solid lipid nanoparticle (SLN) systems for applications in delivery of laundry actives and transport of electroactive substances into lipid membranes. The SLM and SLN systems studied are: silicone-loaded SLM, dye-loaded SLM, dual-active SLM (both silicone and dye) and ferrocene-loaded SLN (Fc-SLN).

Silicones are used as fabric softeners in laundry applications and dyes are used to enhance the hue of fabrics. The incorporation of two actives into one, *dual-active SLM*, is a concept that could enable compact formulation and optimized formulation manufacture. The ferrocene-loaded SLN system represent the group of electroactive nanoparticles that could potentially find applications in biosensors, targeted delivery and other biomedical applications.

The SLM and SLN systems were prepared using lauric acid as the lipid matrix. Silicone-loaded SLM systems were prepared using solvent-assisted methods with either ethanol or n-hexane as the solvent. They were stabilized with a combination of a primary alcohol ethoxylate (C14-15) (neodol 45-7) and polysorbate 80 (tween 80) as surfactant/co-surfactant). The silicones used were: polydimethylsiloxane (PDMS)(10,000 cST and 100,000 cSt), terminal amino-functionalised silicone (TAS) and a tertiary amino-functionalised silicone (PK10).

The dye-loaded SLM systems, incorporating Coomassie Brilliant Blue R (CBB or BB) and ethyl violet (EV, Basic Violet 4) as hueing dyes were prepared using the double emulsion method, also descriptively known as the water-in-oil-in-water (w/o/w) emulsion method. The inner emulsion, w/o was stabilized using a low HLB surfactant, Brij 80 and the outer emulsion

o/w was stabilized using a high HLB surfactant, tween 80. For the dual-active SLM system, PK10 silicone was added to the lipid phase before emulsification.

The Fc-SLN system was prepared using the solvent emulsification/evaporation method. The surfactants used were poloxamer 188 and tween 80. The lipid membrane systems used were: solid-supported self-assembled monolayer (SAM) and tethered bilayer lipid membrane. The SAM was prepared by chemisorption of a thiolipid, 1,2-dipalmitoyl-sn-glycero-phosphothioethanol (DPPTE) onto a gold surface. Self-assembled monolayers were used as a lower leaflet or tether for the BLM system; an upper leaflet of 1-palmitoyl-2-oloeyl-sn-glycero-3-phosphocholine (POPC) was added by vesicle fusion. The characterisation and penetration of Fc-SLN into lipid membranes was studied using electrochemical methods such as cyclic voltammetry (CV), differential pulse voltammetry (DPV), electrochemical impedance spectroscopy (EIS) and Resonance Enhanced Surface Impedance (RESI).

The SLM and SLN systems where characterised using laser diffraction and dynamic light scattering (DLS) for particle size analysis, optical microscopy and electron microscopy for morphology and particle size, small angle X-Ray Scattering (SAXS) and differential scanning calorimetry (DSC) for crystallinity and structural arrangement and chemical analysis using FTIR, solid state NMR and TGA.

Ad Majorem Dei Gloriam

(All for the greater glory of God)

- *St Ignatius of Loyola (1491-1556)*

Declaration

The work described in this thesis was carried out in the Department of Chemistry at Durham University from April 2012 to July 2016. All the work is my own, unless stated otherwise. No part of this work has been previously submitted for a degree at this or any other university.

Statement of Copyright

Acknowledgements

I am delighted to take this opportunity to acknowledge and extend my gratitude to those that have made this thesis a possibility and all those that have added value to my PhD journey.

First and foremost, I would like to thank my supervisor, Dr Ritu Kataky. I am forever indebted to you for allowing me the opportunity to embark on this journey, for always seeing the best in me even when I myself failed to believe and sharing creative and intelligent insights into this project.

I am grateful to all the members of the Kataky Lab, both past and present who have gone out of their way to share their time and expertise and have contributed to my experience in the last 4 years: Dr Paula Lopes, Dr Alice Delcourt-Lancone, Dr Rui Campos, Dr Mehrin Chowdhury and, soon to be doctor, Yousillya Bunga.

I am grateful to Dr Sharon Cooper and members of her group for making our shared office and lab facilities a pleasant place to work, for access to the SAXS equipment and occasionally offering technical assistance, especially Dr Helen Ramsey and Ms. Helen Riggs.

I would like to acknowledge the experimental facilities at Durham University: EPSRC Solid State NMR facility with many thanks to Dr David Apperley, Thermal Analysis facility, with many thanks to Mr Doug Carswell, The GJ Russel Group Microscopy Facility with many thanks to Dr Buddhika Mendis and Mr Leon Bowen.

I would also like to thank Durham University and Procter and Gamble (P&G, UK) for financial support through the CEMENT (SMC^3) partnership and for providing an environment where I could share my research ideas and findings and receive constructive feedback and ideas, especially Dr Anju Brooker and Dr Mauro Vaccaro (P&G) for allowing me to get a taste of industrial scientific processes and for all the help and support.

Many thanks to my mother, who has always been there throughout the whole journey providing encouragement, motivation and a listening ear. You have been my rock and my strength, I would not have completed this without you. Many thanks to my father, who was always there to remind me to never lose sight of the goal.

I would also like to extend my gratitude to: my uncle Mr Christopher Kateera, who inspired in me a passion and love for science, my brother Joseph, the rest of my family, old friends and those that I have picked up along the course of the PhD.

Lastly, to my fiancé, Buyinza Kabakubya, you have been an invaluable help, support and motivation. My gratitude to you is beyond words. *Webale nyo, mwagalwa*.

THANK YOU ALL

Nyasha

Table of Contents

List of Symbols

Symbols	Meaning	Units/Value
B	Magnetic field	T
C	Capacitance	F
cSt	Kinematic viscosity	$m^2 s^{-1}$
d	Hydrodynamic diameter	nm
D	Translational diffusion coefficient	$cm^2 s^{-1}$
E	Potential	V
e^-	Electron	-
F	Faraday constant	96485.4 C mol^{-1}
h	Planck's constant	$6.626176x10^{-34}$ J s
i	Current	A
k_B	Boltzman constant	1.38099×10^{-23} J K^{-1}
R	Resistance	Ω
T	Thermodynamic temperature	℃
η	dynamic viscosity	mPa
λ	Wave length	Å

List of Abbreviations

Abbreviations	**Meaning**
AE1S	Alcohol Ethoxylate (non-ionic surfactant)
ALM	Aqueous Liquid Module
ATR-FTIR	Attenuated Total Reflection- *Fourier Transforms Infrared*
BB	Brilliant Blue dye
BLM	Bilayer Lipid Membrane
CPE	Constant Phase Element
CV	Cyclic Voltammetry
DPV	Differential Pulse Voltammetry
DLS	Dynamic Light Scattering
DPPTE	1,2-Dipalmitoyl-*sn*-Glycero-3-Phosphothioethanol (sodium salt)
DSC	Differential Scanning Calorimetry
EIS	Electrochemical Impedance Spectroscopy
EV	Ethyl Violet (dye)
Fc/Fc+	Ferrocene/Ferrocenium ion
FTIR	Fourier Transform Infrared Spectroscopy
HEPES	4-(2- Hydroxyethyl)piperazine-1- ethanesulfonic acid
HPLC	High-Performance Liquid Chromatography
PDMS	Polydimethylsiloxane
POPC	1-Palmitoyl- 2-Oleoyl-sn-glycero- 3-PhosphoCholine
NMR	Nuclear Magnetic Resonance Spectroscopy

SAM	Self-Assembly Monolayer
SAXS	Small Angle X-ray Diffraction
SEM	Scanning Electron Microscope
SLM	Supported Lipid Membrane
SLN	Solid Lipid Nanoparticle
SLP	Solid Lipid Particle
TEM	Transmission Electron Microscopy
RESI	Resonance Enhanced Surface Impedance
UV/VIS	Ultraviolet–Visible Spectroscopy
WAXS	Wide Angle X-ray Diffraction

List of Figures

List of Tables

1. Introduction

Solid lipid carrier matrices are a fairly recent discovery that has proven invaluable in the pharmaceutical and cosmetic industries.[1,2] They combine the advantages of traditional delivery vehicles, e.g. emulsions and liposomes with the advantages of newer delivery matrices such as gel networks and polymeric nanoparticles.[3] In addition to the active compound, solid lipid particles are comprised of three basic ingredients: lipid(s), surfactant(s) and water. The purpose of this thesis is to highlight the applicability of SLM and SLN systems outside of the currently accepted fields of application. To this amount, methods of preparation, characterisation and in-situ studies are reported in this thesis.

Chapter 2 provides detailed background information of delivery matrices, solid lipid nanoparticles, aspects of laundry formulations and fabric maintenance and introduction to lipid membranes. This is just to provide a basic understanding of the problems to address and to provide a framework to build up on in the proceeding chapters.

Chapter 3 reports the experimental methods used in all the investigations reported in this thesis, including background information on the science behind the techniques and methods applied in characterisation and analysis.

Amongst their many desirable properties, solid lipid particles enable controlled or triggered release of actives, which is important in numerous applications.[4] In chapter 4, the pH-triggered release of fabric softener (silicone), under laundry conditions is reported. High molecular weight silicones used in fabric softeners are both hydrophobic and lipophobic. Encapsulating the silicone in a solid matrix enables dispersion of silicones in aqueous solutions and enhances stability of the silicones in formulation; this prevents agglomeration, which would result in undesirable oil droplets on fabrics. In addition, encapsulating the silicones in a solid matrix prevents interaction of the silicones (especially aminofunctionalized silicones) with anionic surfactants in formulation.[5] The pH-triggered release of silicones and deposition onto fabrics is verified using laser diffraction, optical microscopy and scanning electron microscopy.

The compatibility of SLM and SLN systems with both hydrophobic and hydrophilic actives in addition to high loading capacities contribute to their outstanding applicability.[6,7] In chapter 5, the co-encapsulation of hueing dyes and silicone oil using the double-emulsion method is reported. This concept promises a lot of applications, not only in the formulation of compact laundry products but also in other applications where co-encapsulation of moieties is essential.

Chapter 6 introduces a novel concept of electroactive SLN systems, where a method of encapsulating redox active species into a lauric acid matrix is highlighted. Similar systems of ‘soft’ electroactive nanoparticles have been reported using polymeric nanoparticles, hydrogel nanoparticles and dendrimers.[8–10] The Fc-SLN system combines the advantages of soft electroactive nanoparticles with the numerous advantages of SLN systems. This system promises applications in biosensor systems, targeted delivery and other biomedical applications. Electrochemical characterisation of the Fc-SLN using DPV and EIS was carried out to investigate the electrochemical response of the ferrocene entrapped on the lipid matrix and the electrochemically induced release from the matrix. The real time penetration of Fc-SLN into SAM and BLM systems was studied using resonance enhanced surface impedance (RESI). The objective of the study of penetration of the Fc-SLN into lipid membranes was to investigate the viability of SLN systems as a method of transporting electrochemical tags across lipid membranes. This study also serves the purpose of immobilizing electrochemically active species into supported lipid membranes for mediated electron transfer applications. The understanding of interactions of solid lipid matrices with lipid membranes is also of significant importance in both the laundry and skincare industries. In the laundry industry, it is important to know the effect of the matrix on skin upon contact with product, as in the case of handwashing, and also upon contact with materials treated with the matrix. In skincare applications, it is important to know whether the lipid matrix penetrates the skin or adsorbs to the surface; penetration into the skin is essential for hydration and delivery of dermal delivery of actives whereas adsorption onto the skin is essential for locking in the moisture (moisturisation). Bilayer lipid membranes are acceptable models for cell membranes and could help understand the interaction of the solid lipid matrices with skin. Indeed, the potential applications of this system are both exciting and well varied.

1.1 References

1 M. Uner and G. Yener, *Int. J. Nanomedicine*, 2007, 2, 289–300.

2 S. A. Wissing and R. H. Müller, *Int. J. Pharm.*, 2003, 254, 65–68.

3 G. Yoon, J. W. Park and I.-S. Yoon, *J. Pharm. Investig.*, 2013, 43, 353–362.

4 R. H. Müller, K. Mäder and S. Gohla, *Eur. J. Pharm. Biopharm.*, 2000, 50, 161–177.

5 US5034218 A, 1991.

6 M. Shah, Y. K. Agrawal, K. Garala and A. Ramkishan, *Indian J. Pharm. Sci.*, 2012, 74, 434–42.

7 L. Becker Peres, L. Becker Peres, P. H. H. de Araújo and C. Sayer, *Colloids Surf. B. Biointerfaces*, 2016, 140, 317–23.

8 H. Cho, J. Bae, V. K. Garripelli, J. M. Anderson, H.-W. Jun and S. Jo, *Chem. Commun.*, 2012, 48, 6043–6045.

9 S. Ishii, J. Kaneko and Y. Nagasaki, *Macromolecules*, 2015, 48, 3088–3094.

10 K. Takada, D. J. Díaz, H. D. Abruña, I. Cuadrado, C. Casado, B. Alonso, M. Morán and J. Losada, *J. Am. Chem. Soc.*, 1997, 119, 10763–10773.

2. Background information

Colloidal systems such as emulsions, micelles, liposomes, polymeric particles and solid lipid nanoparticles have been instrumental in drug and cosmetic delivery applications in the last few decades.[1] The versatility of colloidal particles across a wide range of applications is responsible for the increasingly growing interest of this field of research. Emulsions and microemulsions are ubiquitous entities in our daily lives, ranging from naturally existing emulsions such as milk to manufactured emulsions such as fabric softeners. Lipid emulsions have been used since the early 1960s as a vehicle to administer parenteral nutrition and medication to critically ill patients.[2–4] The instability of emulsions limit their applications as delivery vehicles. The term microemulsion was conceived by Bowcott and Schulman in 1955 to describe the thermodynamically stable and optically clear emulsions, stabilized with an alcohol as a co-surfactant.[5,6] Microemulsions are currently used in a wide range of applications such as crude oil recovery, detergency, cosmetics, skin and hair care and drug delivery.[6,7] Liposomes saw huge strides in development and research interest since Bangham et al., reported their discovery.[8] Liposomes are phospholipid vesicles that comprise of at least one concentric bilayer (Figure 2.1).[9] The possibility of controlled/triggered release fueled the interest in liposomes as delivery vehicles.[8,10] Liposomal research spans across various areas such as imaging, vaccines, cosmetics, biosensing and targeted drug delivery as well as the food and farming industries.[8,11,12] The downside of liposomes is the lack of reliable, cost effective and reproducible methods of large scale production.[11,13] Polymeric particles have been investigated

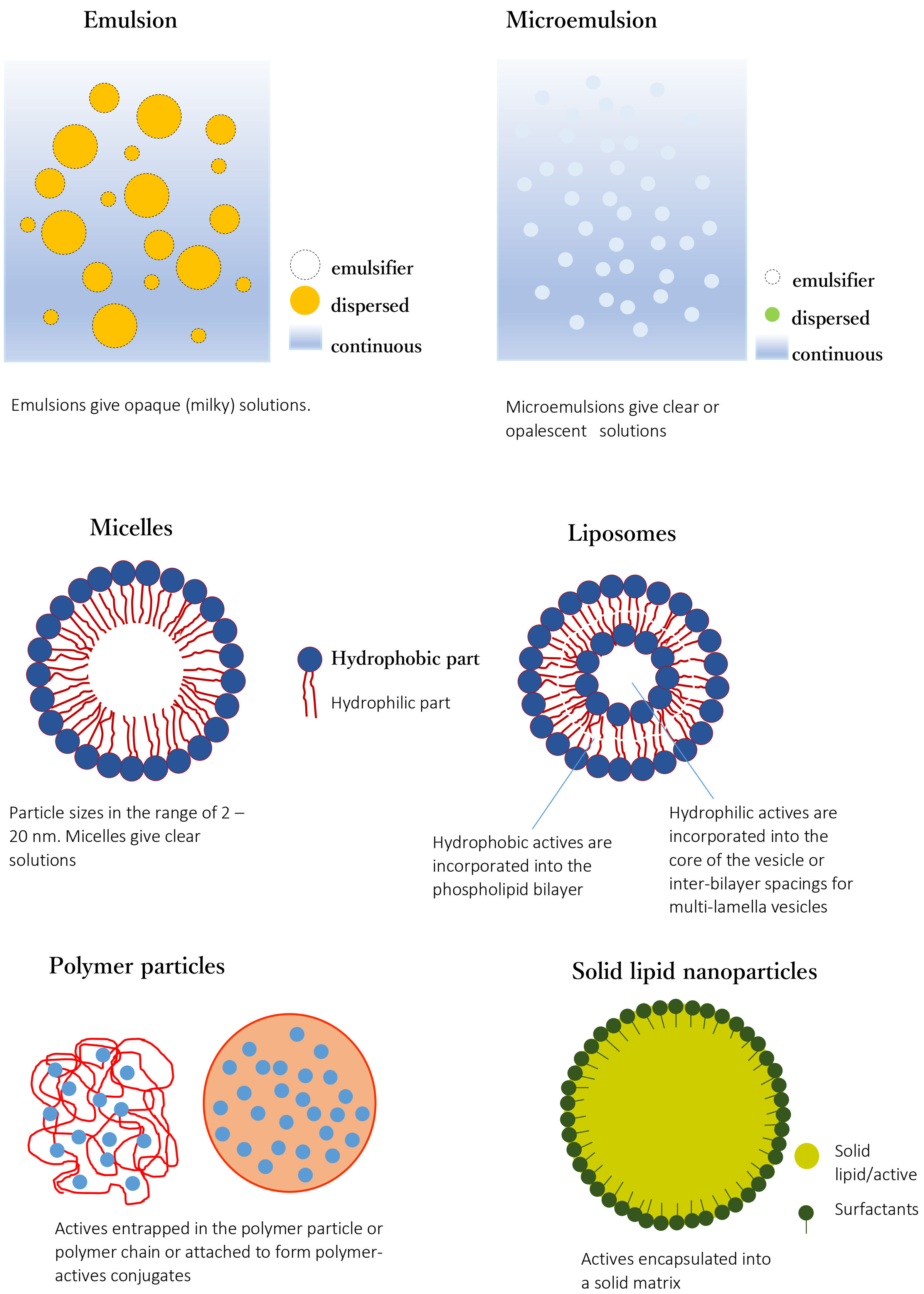
Emulsion

Emulsions give opaque (milky) solutions.

Microemulsion

Microemulsions give clear or opalescent solutions

Micelles

Particle sizes in the range of 2 – 20 nm. Micelles give clear solutions

Liposomes

Hydrophobic actives are incorporated into the phospholipid bilayer

Hydrophilic actives are incorporated into the core of the vesicle or inter-bilayer spacings for multi-lamella vesicles

Polymer particles

Actives entrapped in the polymer particle or polymer chain or attached to form polymer-actives conjugates

Solid lipid nanoparticles

Actives encapsulated into a solid matrix

Figure 2.1. Schematic presentation of traditional delivery matrices, polymeric nanoparticles and solid lipid nanoparticles

as an alternative to traditional delivery methods. Polymer based particles offer versatility in terms of applications and the possibility of tunable release characteristics and targeted delivery.[14] However, the long standing issue with polymeric particles is biological compatibility and higher toxicity risks, especially for particles in the nanosize and microsize ranges.[14] A schematic representation of the delivery vehicles is shown in Figure 2.1. A great deal of attention has been focused on an alternative carrier matrix that embodies the desirable characteristics of the earlier generation of delivery matrices whilst minimising problems with large scale production and toxicity.[15] Solid lipid matrices are similar to oil emulsions except the liquid lipid component is replaced with a solid lipid.

2.1. Solid Lipid Carrier Matrices

Solid lipid carrier matrix is a broad term that encompasses microspheres,[16–18] micropellets,[19] nanopellets,[20] nanospheres,[21] hollow spheres[22] , lipid drug conjugates (LDC)[23,24] and nanostructured lipid carries (NLC).[25–28] The work of Speiser et al., reporting the production of solid lipid micropellets by spray drying[19] and the production of solid lipid nanopellets for peroral administration,[20] marshalled the extensive research in solid lipid matrices. Solid lipid carrier matrices can be classified according to application, size range, preparation method and structural arrangement. The desired particle size affects the applicability and choice of preparation method, so for simplicity the following sections address solid lipid carrier matrices according to size range.

2.1.1. Solid Lipid Microparticles (SLM)

Solid lipid microparticles (SLM) are a class of solid lipid carrier matrices with particle sizes in the range of 1 – 1000 μm. They have been investigated as potential delivery vehicles in food engineering, pharmaceutical, cosmetics and hair care applications.[29–32] A recent report outlines the potential application of SLM in the development of functional foods that are loaded with bioactive compounds.[33] Albertini et al., reported the successful incorporation of a sunscreen agent avobenzone into solid lipid microparticles.[34] Solid lipid microparticles have received attention in oral drug delivery applications due to their ability to mask the taste of some drugs and have been shown to prevent the gastric irritation associated with non-steroidal anti-inflammatory drugs (NSAIDS) such as ibuprofen.[30,35] This can be attributed to the shielding effect and slow release properties of SLM. The main distinguishing factor between SLM and other solid lipid matrices is the size range. Different applications require specific size ranges of carriers for effective delivery.[36] In drug delivery applications, particle sizes around 10 µm and below are optimal for ocular delivery,[37] 150 µm and below for subcutaneous injection and nanometer size range for transfollicular delivery for deep penetration into the hair root.[38]

2.1.2. Solid Lipid Nanoparticles and Nanostructured Lipid Carriers

Solid lipid nanoparticles (SLN) came into the picture in 1991 as an alternative to liposomal and polymeric particles.[39] The submicron solid lipid carriers, SLN share much of the same advantages, but are preferred over SLM in other applications due to the smaller particle size and higher surface area. Solid lipid nanoparticles are favored in cosmetics and dermal applications due to the higher occlusion and adhesive effect when in contact with surfaces.[40]

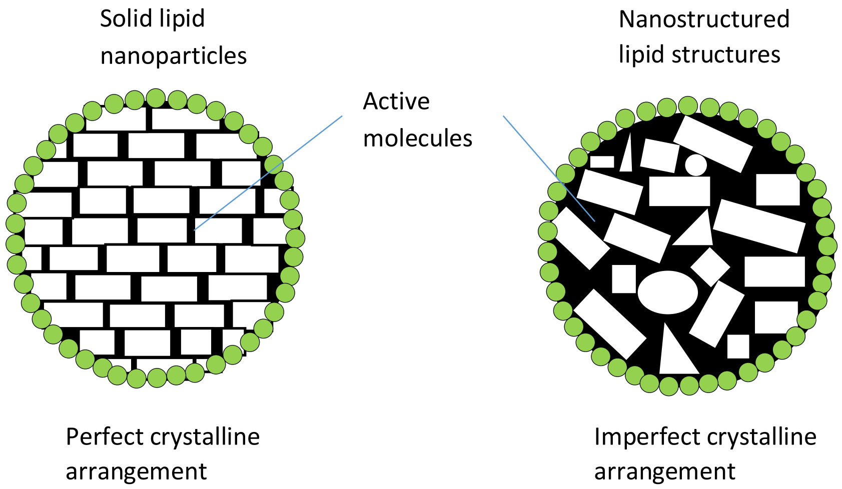

Figure 2.2. An illustration of the ordered arrangement in solid lipid nanoparticles and nanostructured lipid carrier systems

Another solid lipid carrier matrix has received a lot of attention recently is nanostructured lipid carriers (NLC). Nanostructured lipid carriers were first reported in 1999 in a patent assigned to Pharmasol GmbH, Berlin and have become the new generation of solid lipid carrier matrices. [41,42] NLC matrices are made of a mixture of lipids, unlike SLN and SLM systems that comprise of one lipid. The differences in the size of the lipids hinders the crystalline arrangement of the lipids and the disordered arrangement creates more gaps which can accommodate more of the actives (Figure 2.2). SLN and NLC systems have been used in cosmetic products since the beginning of the second millennium and have been investigated as a suitable carrier in drug delivery applications.[43,44] NLC systems are favored over SLN systems in cosmetic applications; however SLN are more preferred in applications where the perfect crystalline arrangement is important (such as UV absorption in sunscreens).

Lipid drug conjugates can fall in either the nanoparticle or microparticle size range. LDC systems were developed to aid the delivery of hydrophilic molecules using lipid matrices.[45] The hydrophilic actives are synthetically attached to the lipid molecule by salt formation (e.g. with a fatty acid) or by covalent linking (e.g. to ethers and esters).[46] Solid lipid nanoparticles or microparticles are subsequently prepared, using the lipid-drug conjugate as the lipid component to give an LDC system.

2.1.3. SLM and SLN Production: Ingredients

The ingredients used in the preparation of solid lipid carriers comprise of lipid(s), emulsifier(s) and water.[47] Lipids from various groups and different kinds of surfactants have been successfully used in the preparation of SLN and SLM systems.[48]

2.1.3.1. Lipids

Lipids are a family of naturally occurring amphipathic molecules which include: monoglycerides, diglycerides, triglycerides, phospholipids, fatty acids, waxes and steroids.[49] Lipids comprise of a hydrocarbon component and a functional group which determines the type of lipid (Figure 2.3). Generally, the lipids used in the preparation of solid lipid matrices are those that are usually solid at room temperature. However, it has been shown that solid lipid microparticles can be prepared from fully hydrogenated canola oil using supercritical carbon dioxide.[33]

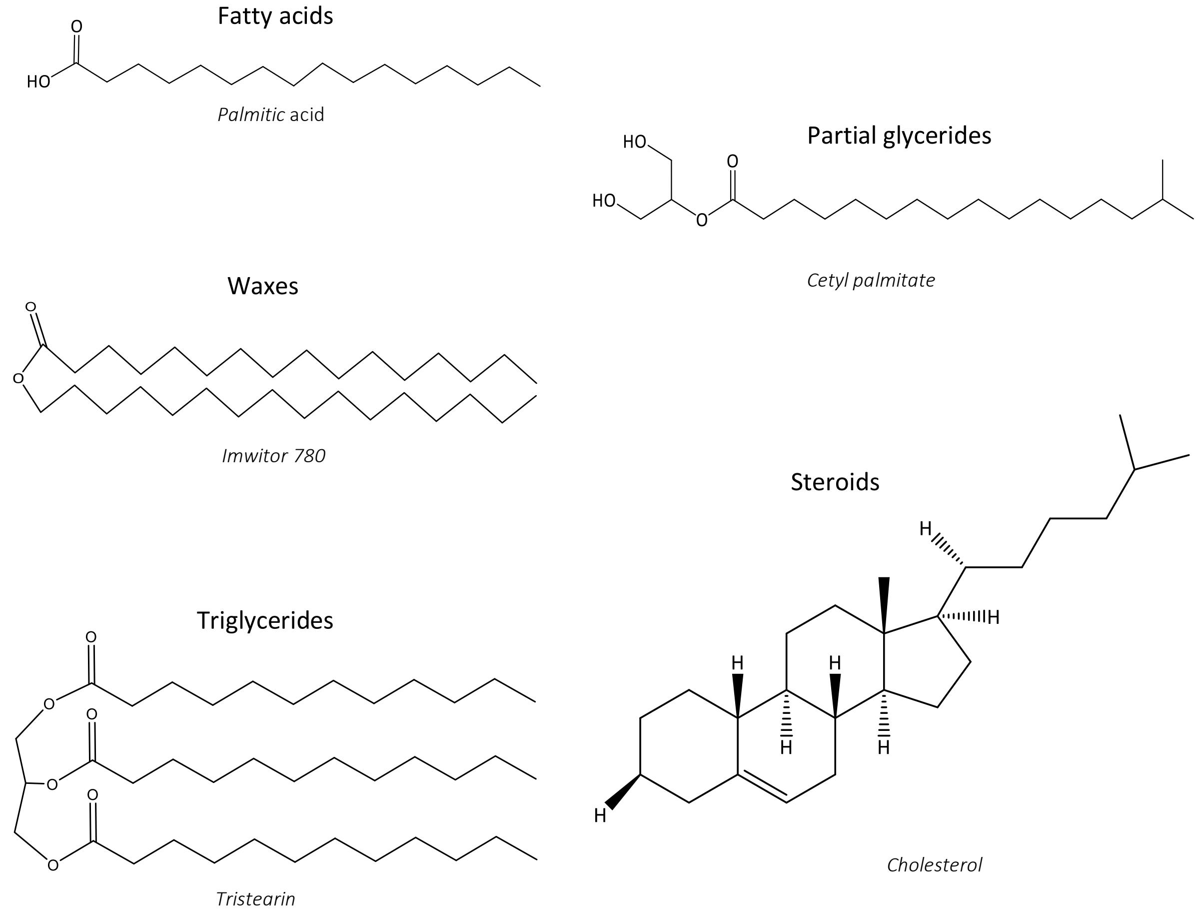

Figure 2.3. Chemical structures of lipids from different classes used in the preparation of solid lipid matrices

2.1.3.2. Emulsifiers

All classes of emulsifiers regardless of molecular weight, charge or chemical composition can be efficiently used to produce solid lipid particles. The choice of emulsifier is limited by the intended application, for instance, cationic surfactants are more suited for intracellular gene delivery.[42] Phospholipids (e.g. lecithin and phosphatidylcholine),[50–53] non-ionic wetting agents (e.g. poloxamer 188 and polysorbate 80),[54–59] cholates (e.g. sodium glycocholate and sodium taurodeoxycholate),[60–62] polar polymers (e.g. PVA and PVP)[63–65] and short chain alcohols (e.g. n-butanol)[66,67] have been used as emulsifiers or co-emulsifiers in SLN and SLM systems. A co-emulsifier is not always necessary but can be useful in preventing agglomeration. The amount of emulsifier used depends on the concentration and chemical properties of the lipid and on the method of preparation used. Some lipids have self-emulsifying tendencies, which reduces the amount of emulsifier required.

2.1.4. SLM and SLN Production: Methods

Various methods of solid lipid nanoparticle preparation have been reported. The preparation can be broken down into three main stages: (i) the emulsification of the lipid component with or without the active component in an aqueous solution with stabilisers, (ii) particle size and morphological optimisation and (iii) dilution in cold water to precipitate the particles (Figure 2.4). The different methods of optimising particle size and morphology are: high-pressure homogenization, ultra-sonication, high-shear homogenization, microemulsion, solvent evaporation, and solvent diffusion. The same processes can be applied to the preparation of microparticles when used with relevant parameters.

2.1.4.1. High Pressure Homogenisation

High-pressure homogenization (HPH) produces nanoemulsions by forcing liquid under high pressure through a microsized gap. The excipient solution is accelerated over a very short

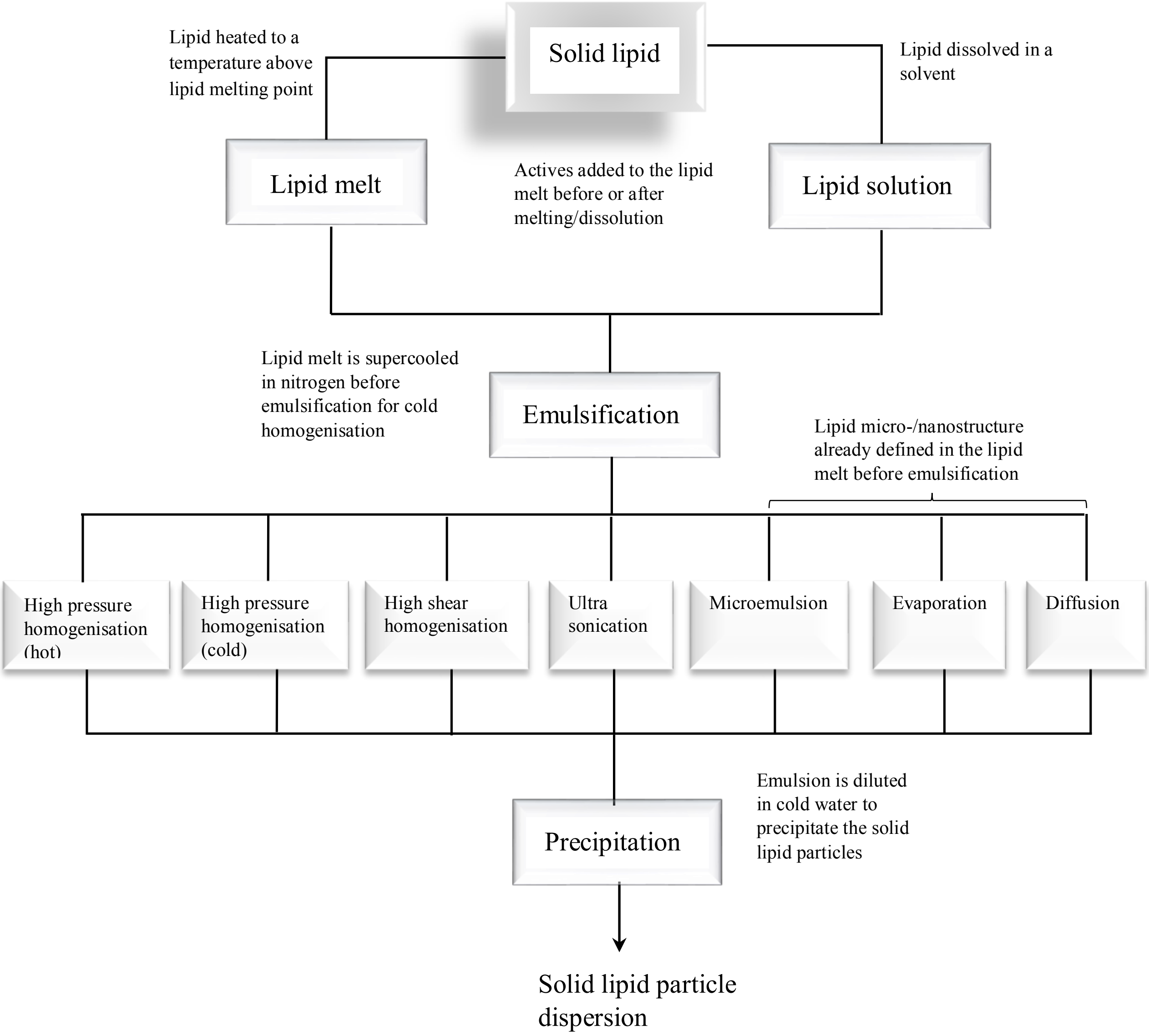

Figure 2.4. Schematic diagram showing the processes involved in the preparation of solid lipid particle dispersions

distance to high velocities above 1000km/h, subjecting the particles to very high shear stress and cavitation force. [48] This breaks down the particles to sub-micron range. HPH is said to be a more reliable technique, producing more uniform particles compared to other methods.[46,47] However, a report by Silva et al., disagrees and proves that ultra-sonication is equally effective.[68] There are two HPH methods used in the preparation of SLN systems: hot homogenization and cold homogenization. Hot homogenization refers to the method where the active-loaded pre-emulsion is at temperatures above the lipid melting point. The pre-emulsion is usually produced by means of high shear homogenisation. It is not ideal for volatile and heat sensitive actives.[15] The alternative method, cold homogenization involves rapid cooling of the lipid melt using dry ice or liquid nitrogen.[48] A pre-emulsion is obtained by milling the dry, active-loaded lipid to obtain microparticles, which are subsequently dispersed in an aqueous solution. The pre-emulsion is introduced to the high-pressure homogeniser while temperature is controlled to ensure that there is no increase in temperature due to the high pressures inside the homogeniser.[48] Cold homogenisation prevents drug loss to the aqueous phase through partitioning during homogenisation.[15] HPH is convenient method for both small scale lab production as well as large scale industrial production. However, the relatively high cost of the equipment serves as a deterrence from this technique.

2.1.4.2. High Shear Homogenisation and Ultra-Sonication

High shear homogenisation and ultra-sonication were the earliest methods used in the preparation of solid lipid nanoparticles.[20,69] A rough emulsion is prepared by adding the lipid melt with the active to the aqueous phase. Nanoparticles/microparticles are formed by subjecting the solution to high shear forces using a homogenizer (e.g Ultra Turrax®) and ultra-sonication probes. The relatively low cost of equipment and ease of preparation make these methods more desirable for small scale production. However, ultra-sonication is often associated with metal contamination and both methods are known to give non-uniform particle sizes.[48]

2.1.4.3. Microemulsion

The microemulsion method, first reported by Gasco, is a non-mechanical method that involves the preparation of an optically transparent mixture of the drug and the lipid melt.[16] The aqueous phase (with emulsifiers) is preheated to the same temperature as the lipid melt and subsequently added to the lipid whilst stirring and maintaining the temperature. The mixture is diluted with cold water and cooled to solidify the particles. The micro- or nanostructure is already defined in the emulsion and so no extra energy is required to optimize the particle size.[70] The typical volume ratio between the hot emulsion and the cold water is high (between 1:25 to 1:50), which gives a comparatively low lipid content.[48] This is the main disadvantage of this method, as the excess water needs to be removed by lyophilisation or ultra-filtration to give a concentrated dispersion.[71] The other disadvantage of this method is the high concentration of surfactants needed to stabilise the particles.[71]

2.1.4.4. Solvent Emulsification/Evaporation

The solvent emulsification/evaporation, developed by Sjostrom and Bengestal, is similar to the microemulsion method except an organic solvent is used to dissolve the lipid and the actives to create an optically transparent solution.[72] Water-immiscible solvents, such as cyclohexane, chloroform and dichloromethane are used with this technique.[70] The lipid-solvent mixture is emulsified in the aqueous phase and stirred until the solvent is evaporated. The hot emulsion is diluted and cooled to precipitate the particles. A clear disadvantage of this method is the use of organic solvents and the possibility of solvent residues, which maybe toxic. However, this method avoids the use of heat in the production making it ideal for thermally unstable actives. This method can be used to produce reproducible SLN systems with sizes as small as 25 nm, reproducibly.[48,72,73]

2.1.4.5. Solvent Emulsification/Diffusion

The solvent emulsification/diffusion technique is similar to the solvent emulsification/evaporation method but uses a water-miscible solvent. Trotta et al., reported the preparation of solid lipid nanoparticles of glyceryl monostearate (GMS) by dissolving the lipid in a water saturated solvent (benzyl alcohol or butyl lactate), followed by emulsification in a solvent saturated aqueous solution with emulsifiers.[74] Upon dilution of the solvent saturated emulsion with cold water the lipid phase solidifies instantly due to diffusion of the water-miscible solvent to the continuous phase. Drug loaded nanoparticles of sizes below 100 nm with very low polydispersity can be achieved using this method.[75] Some of the solvents that have been used with this technique include ethyl formate,[76] methanol[77] and isobutyric acid.[78] Similar to the solvent emulsification/evaporation method, the main disadvantage of this technique is the use of solvents and the possibility of toxic solvent residues.

2.1.4.6. Other Reported Methods

Battaglia et al., outlines the preparation of stearic acid SLN systems using the coacervation method.[79] This method was achieved by dispersion of sodium stearate in a PVA 9000 aqueous solution while heating at 48 °C (just above the Krafft Point for sodium stearate) and stirring at ~300 rpm continuously to give a clear micellar solution. A model drug, amphotericin B (AmB) was then added whilst stirring until the drug completely solubilized. The coacervating solution (lactic acid) was added dropwise, until the mixture reached pH 4.0 and the resulting suspension was subsequently cooled in a water bath. The successful preparation of SLN systems using this method has been proven in other reports.[80–83] A recent article reported the successful preparation of an SLN system of octadecane using the phase inversion temperature (PIT) method, where a mixture of the oil, water and surfactants was heated to a temperature above the phase inversion temperature and held at that temperature for 10 min while stirring, followed by rapid cooling in a water bath at 5 °C.[84] This method relies on the temperature related changes in the properties of non-ionic surfactants such as molecular geometry, packing and oil-water partitioning.[85–87] The phase inversion temperature is the temperature at which an emulsion inverts (e.g from o/w to w/o) due to the temperature dependence of HLB values for non-ionic surfactants.[88] At T << PIT, the head groups are highly hydrated, which favours the o/w conformation; at T >> PIT the head groups are dehydrated, which favours the w/o conformation.[84] Other methods which have been used in SLM and SLN preparation include the supercritical carbon dioxide method and the electrohydrodynamic method. The former method was applied using fully hydrogenated soybean oil as the lipid phase to give hollow SLN and SLM with diameters up to 298 nm and 40 μm respectively.[22] The latter was used to produce a maltol-loaded SLN system using stearic acid as the lipid phase.[89]

2.1.5. SLN and SLM Characteristics and Characterisation

2.1.4.1. Particle Size and Polydispersity

Particle size and polydispersity are important parameters in the assessment of quality of carrier matrices. The particle size and morphology of SLN and SLM systems is greatly influenced by the method of preparation and the choice of ingredients. This can be exploited to achieve a desired size range suitable for the intended application. One of the factors affecting the particle size is the viscosity of the lipid phase. The viscosity of the dispersed phase is determined by the temperature of the emulsion, melting point and molecular weight of the lipid.[90] SLN systems prepared using hot HPH have shown correlation between particle size and lipid melting point.[91] The viscosity of the lipid phase is also affected by the concentration of the lipid in the lipid/solvent mix for the solvent emulsification/evaporation method. In hot HPH, heating the pre-emulsion at higher temperatures results in relatively smaller nanoparticles due to the reduced viscosity of the lipid.[92] The homogenisation step can be repeated several times to ensure a uniform distribution of sizes. However, increasing the number or cycles and the homogenisation pressure increased the kinetic energy of the particles which can encourage coalescence and result in increased particle sizes.[93] The solvent emulsification/evaporation method gives very small nanoparticles (< 30 nm), which has not been achieved by any other method even with identical compositions.[47] For high shear homogenisation, increasing the stirring rate has been shown to have an insignificant effect on the particle size but improves the polydispersity index.[48] The concentration of emulsifier also plays an important part in the particle size outcome. High concentrations of the emulsifier reduce the surface tension and encourages partitioning of the dispersed phase. Addition of a co-emusifier has also been shown to reduce the particle size.[93]

2.1.4.2. Loading Capacity and Entrapment Efficiency

The suitability of a carrier matrix for a particular application hinges on its ability to encapsulate the intended active compound. The loading capacity is a measure of concentration of active compounds encapsulated in the matrix. The entrapment efficiency gives a measure of how much of the active ingredient added during preparation has been successfully incorporated. The entrapment efficiency depends on the amount of actives added during preparation and the loading capacity of the matrix. The loading capacity is strongly influenced by the lipid component, the physical and chemical structure of the lipid and the interactions between the lipid and active compound. Successful encapsulation prerequisites solubility or miscibility of the actives in the lipid matrix.[39] The physicochemical structure of the lipid also determines the capacity of the lipid to hold actives; highly crystalline lipid arrangements hinder encapsulation and complex lipid mixtures give higher loading capacities by preventing the formation of a ‘perfect’ lattice.[71] Another factor that affects the loading capacity is the chemical nature of the active compound. Hydrophilic actives give much lower loading capacities compared to hydrophobic drugs. Loading capacities exceeding 50% for hydrophobic compounds have been reported while this value is yet to be met with hydrophilic compounds.[94] The high solubility of hydrophilic actives in the aqueous phase facilitates partitioning of the actives from the lipid melt into the continuous phase, hence minimising effective encapsulation. The double emulsion method (i.e. the hydrophilic actives are emulsified in the lipid phase and then the lipid phase is emulsified in an aqueous phase before cooling) has been shown to enhance the incorporation of hydrophilic actives into solid lipid matrices. Peres et al., recently reported the encapsulation of hydrophilic dyes in a stearic acid matrix using the double emulsion method.[95]

Solvent-assisted double emulsion method has been shown to enhance the encapsulation of a hydrophobic and lipid-insoluble drug, Raloxifen HCl.[96] The cold homogenisation method can also enhance the incorporation of hydrophilic active due to the immobilisation of the lipid/active component by freezing in liquid nitrogen. This prevents the partitioning of the hydrophilic molecules into the aqueous phase.

2.1.4.3. Model of Incorporation

There are three different models of incorporation suggested for solid lipid matrices, namely: solid solution, enriched core model and enriched shell model (Figure 2.5).[39] The model of incorporation alludes to the localisation of the drug in the matrix. The model of incorporation is influenced by the chemical properties of the lipid and the active components and the interactions between them. The solid solution method of incorporation is where the active molecules are homogenously dispersed throughout the matrix. This method of incorporation is facilitated by strong interactions between the lipid and the active compound. Solid solution lipid matrices can be achieved using the cold homogenisation method; the active compound is dissolved in the lipid component and frozen in liquid nitrogen to give a solid solution before homogenisation.[97] The enriched shell model pertains to the localisation of the active molecules in the shell of the particles. SLN and SLM systems assume the enriched shell model of

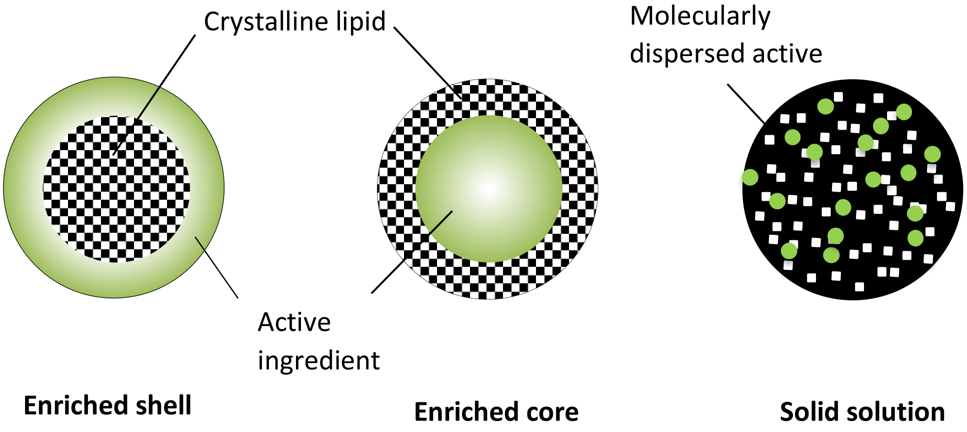

Figure 2.5. Schematic presentation of suggested models of incorporation for solid lipid carrier matrices

incorporation during cooling when the lipid recrystallises and repartitions into the core of the particles, leaving a high concentration of the active molecules in the shell of the particles.[98] The enriched core method is achieved when the active molecule crystallises or precipitates before the lipid recrystallises. The active repartitions into the core of the dispersed phase and the lipid recrystallises around the active-enriched core upon further cooling.[98] This usually occurs where the concentration of the actives in the lipid melt is close to the saturation solubility.[39] DSC, X-ray diffraction and AFM have been used to determine the model of incorporation of enriched shell and solid solution SLN systems of Compritol 888 ATO and Dynasan 112.[97]

2.1.4.4. Crystallinity and Polymorphic Modifications

Crystallinity and polymorphic modifications are important aspects in the characterisation of SLN and SLM systems as they strongly influence the incorporation, retention and release of actives. Amphipathic lipid molecules are capable of assuming highly stable 3D crystalline arrangements. A lipid can exist in different crystalline forms called polymorphs. There seven known crystal systems that crystalline materials can adopt (Figure 2.6).[99] Out of the seven possible crystal systems, the three main forms found in lipids are: hexagonal, triclinic and orthorhombic.[100] Hexagonal subcell packing, also known as the α-polymorph is the least thermodynamically stable of the three. [101,102] The triclinic subcell packing, β-polymorph is the most thermodynamically stable form, while the orthorhombic subcell packing, β' form is a metastable form that is intermediate between the α- and β-polymorph.[101,102] During production, the lipid solidifies in the α-form and transitions to the β'-polymorph and then β-polymorph upon cooling.[103] While the thermodynamic stability of the lipid improves with these transformations, the loading capacity of the lipid is diminished.[39,103] This results in premature release of the actives from the matrix; hence the lipid crystallinity and polymorphic transformations of the lipid affect the stability of SLN and SLM systems. DSC and X-Ray

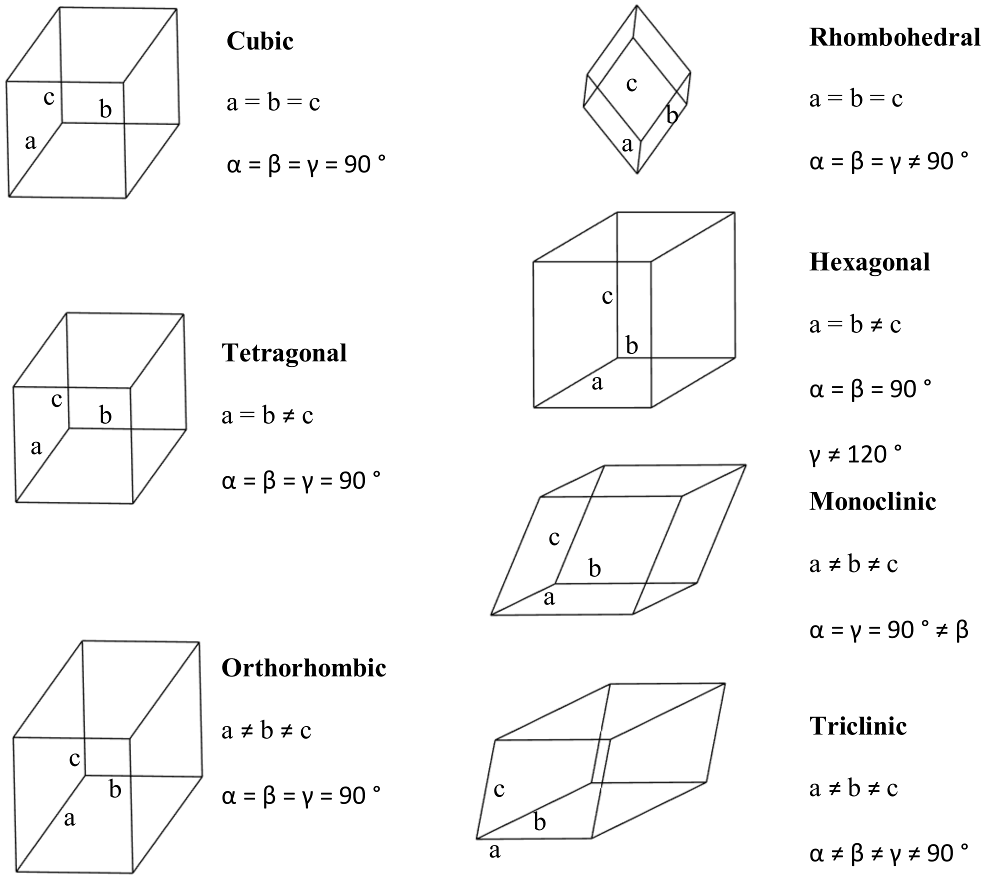

Figure 2.6. Seven types of crystal systems found in crystalline materials where a, b and c are vectors in three different planes and α is the angle between b and c, β is the angle between a and c and γ is the angle between a and b

scattering methods are used in the investigation of lipid crystalline forms in solid lipid matrices.[104,105] Different polymorphic forms exhibit different melting temperatures and enthalpy of fusion due to the differences in the thermodynamic stability; hence DSC can be used to distinguish between the different polymorphic forms. X-Ray diffraction methods can be used to determine the polymorphic form due to the fact that each subcell packing has a unique diffraction pattern. Using WAXS, the α-polymorph is characterised by one strong diffraction line at 4.15 Å, the β'-polymorph gives two strong diffraction lines at 3.8 Å and 4.2 Å, whereas the β-polymorph produces a whole series of diffraction lines with one prominent line at 4.6 Å.[102,106] Other analytical methods such as FTIR and Raman spectroscopy can also provide structural information in solid lipid matrix systems.[39]

2.1.4.5. Release Profile

The release mechanism and release profile from SLN and SLM systems is influenced by many factors such as: the model of incorporation, media, particle size, type and concentration of stabilisers. Systems with an enriched shell model of incorporation express burst release behaviour, which can be as fast as 100 % release within 5 min from SLN systems.[97,107] The solid solution model of incorporation has been shown to prolong release over several weeks.[97,107] Release from a solid solution matrix occurs by diffusion of the actives through the lipid or by degradation of the lipid matrix. Diffusion from SLN and SLM systems is retarded due to the low mobility of actives in the solid matrix, hence the prolonged release. The crystallisation behaviour of the lipid also affects the mobility of actives in the matrix; a high degree of crystallinity lowers mobility and consequently, the release rate. Release from an enriched core model is membrane controlled and governed by Fick's law of diffusion.[98] This is because the lipid shell encapsulates the active enriched core like a surrounding membrane. The particle size affects the rate of release from the matrix; smaller particles have high surface areas and short diffusion distances hence faster release. Higher loading capacities increase the rate of initial release from the particles due to the higher concentration gradient between the lipid matrix and the surrounding environment. The type and concentration of emulsifier, which affect the surface properties of the carrier particles also influence the rate of release. Low surfactant concentrations have been shown to prolong release from SLN systems.[27] Physicochemical properties of the active molecules such as: molecular weight, viscosity, diffusion coefficient and partition coefficient also play an important role in the release kinetics.[39]

Release from SLN and SLM systems can be triggered by degradation of the matrix. Increasing the temperature to the melting point of the lipid results in burst release. Higher temperatures also increase the mobility of the active molecules in the matrix which results in faster release rates. The photothermal release of Nile Red from a lauric acid SLN system co-loaded with gold has been reported.[108] The pH of the surrounding media can trigger the degradation of the lipid matrix resulting in a burst release.[109,110] High pH values (> pKA value of the lipid) result in deprotonation of the lipid matrix followed by dissolution of the matrix. Highly acidic pH conditions also result in corrosion of the matrix by protonation of the lipid head group. Enzymes can also be used to trigger the degradation of the matrix.[111] Olbrich et al., reported the lipase triggered degradation of Dynasan 114 and 116 solid lipid nanoparticles. On the other hand, surface modification of SLN and SLM systems has been used to prevent environmental triggered burst release and enable targeted delivery. Coated SLN systems have been reported to improve stability, prolong blood circulation times in drug delivery applications and enable targeted delivery.[54,112–114]

2.1.5. New Applications of Solid Lipid Matrices

This thesis reports the preparation and characterisation of SLM systems in laundry applications (Chapter 4 & 5) and an electroactive SLN system for penetration into lipid membranes. This is the first report of sold lipid matrix systems in such applications.

2.1.5.1. Solid Lipid Microparticles for Delivery of Laundry Actives

Delivery vehicles in laundry are useful in the delivery of detergents, softeners, dyes, enzymes by enhancing their stability in formulation. Strampach et al., reported the application of oxidation resistant tissue matrix for laundry actives.[115] Anderson and Schindler reported the controlled release of poly-n-isopropylacrymide for the delivery of laundry actives.[116] Other laundry delivery matrices such as grafted silicone polymers have been investigated.[117] Solid lipid microparticles are a cheaper alternative to polymeric laundry delivery vehicles due to the low cost of the ingredients and the comparatively simple methods of production. Moreover, methods of SLM preparation by HPH are already widely available on an industrial scale as the same methods are used in preparation of oil emulsions. The biodegradability and low toxicity is essential for laundry formulations due to the high possibility of skin contact and the possibility of exposure to aquatic life through the municipal disposal system. The lipids used in SLM preparation are mainly physiologically compatible lipids and environmentally friendly surfactants can be chosen as stabilisers. In addition to isolation of the laundry actives, SLM systems enables controlled release, which enhances stability in formulation and improves the efficiency of delivery. SLM systems could potentially be the next generation of laundry delivery vehicles.

2.2. Introduction to Textile Fibres

The term *textile* is a comprehensive term that covers clothing, carpets, upholstery, tapes, etc. Textile fibres are defined as natural or synthetic fibres which can be spun into a yarn or made into a fabric by interlacing or interlooping using suitable methods such as weaving, knitting, braiding, felting and bonding.[118] Textile fibres are classified into three main groups: natural, regenerated and synthetic fibres. Regenerated fibres, for instance, viscose and acetate fibres, are manufactured from natural polymers which are developed in the form of continuous filament fibres.[119] Synthetic fibres are manufactured industrially from petroleum or coal-tar sources .[120] Synthetic fibres include polyesters, nylons, and acrylics.[121] Regenerated and synthetic fibres can both the classified as man-made fibres. Natural fibres are the most commonly used textile fibres, and these include cotton, flax and rami. They are produced from plants, animals or minerals and are composed mainly of cellulose.[122] Polyester and cotton fabrics have been selected to represent synthetic and natural fibres respectively, in the work covered in Chapter 4 and 5.

2.2.1. Cotton Fibres

Cotton fibres are staple fibres made almost entirely of cellulose and are in fact a source of the purest cellulose.[123] Cotton is the oldest fibre and is quite popular because of its versatility. It is a seed hair fibre, where each cotton fibre is a single elongated cell emerging from the epidermis to the surface of the cottonseed.[123] Cotton fibres are classified according to their source and staple length.[120] The staple length is also dependant on source, and can have values in the range of 12-60 mm and widths of 15-24 µm.[124] During growth, the cotton fibre is cylindrical, with a well-defined lumen, but as the fibres dry, they shrink and twist resulting in convolutions (Figure 2.7).[120,125] These convolutions differentiate cotton fibres from other fibres. The morphological structure of the cotton fibre comprises four different layers; a cuticle, a primary wall, a secondary wall and a lumen (Figure 2.8). The cuticle (cotton wax) is made up of saturated fatty acids, waxes and pectin compounds.[126] It is a thin outer layer enclosing the cotton fibre, which serves the purpose of protecting the fibres from mechanical and chemical damage and is partially removed during processing to improve wettability of the fibres.[127] The primary wall is about 0.5 µm thick and is composed mainly of cellulose fibrils and pectin.[128] The cellulose fibrils are arranged in the form of concentric spirals at 70 degrees about the fibre axis.[120,126] The secondary cell is about 5 – 10 µm thick and makes up the bulk of the weight of the cotton fibre.[129] It is made up almost entirely of pure cellulose and is further classified into three layers; the layers comprise of cellulose fibrils that differ in fineness and spiral angle about

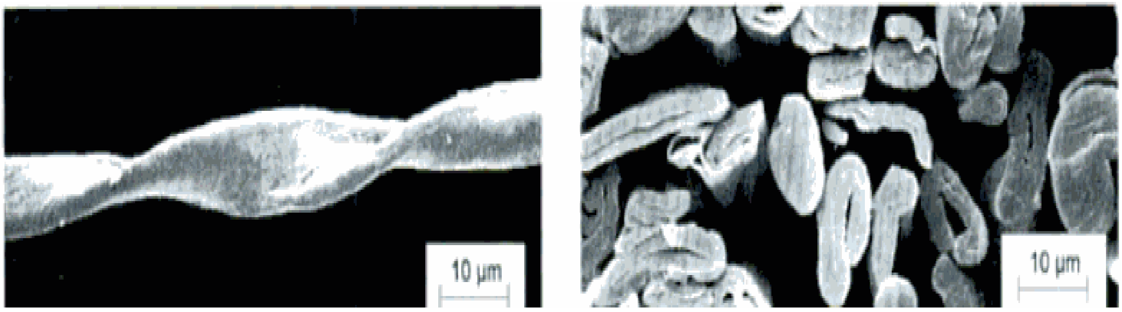

Figure 2.7. SEM images showing the appearance of cotton fibres (a) showing the convolutions and (b) the cross section showing the shrunken and twisted fibres and the lumen. Reprinted from Ref 125 with permission from Hanser Publications

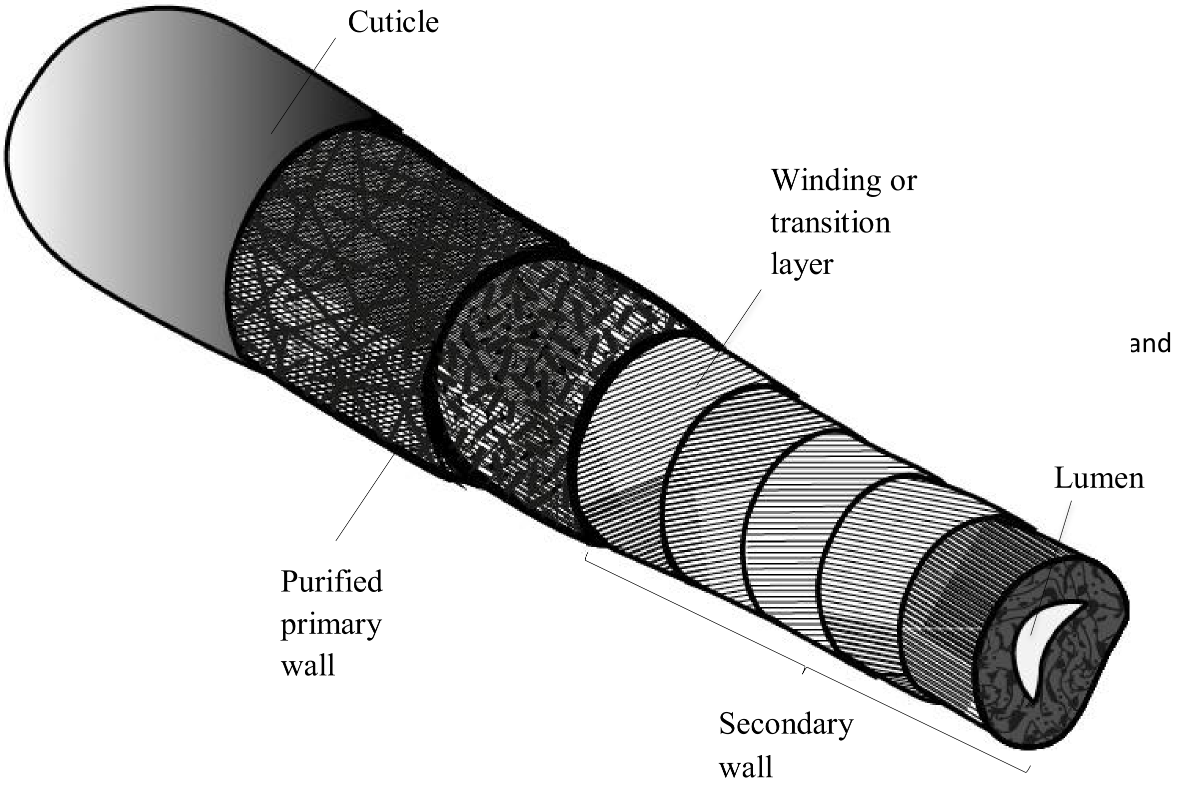

Figure 2.8. A computer generated image showing the morphological structure of cotton fibre and the different layers of organisation

the matrix.[123] The lumen or the cavity is the cylindrical void at the centre of the fibre making up 30- 35% of the total cross sectional area of the cotton fibre during growth, but this is reduced to 5% after drying.[120] Native cotton fibres (bolls) are harvested from cotton plants, deseeded and cleaned before production of yarns. The cleaned staple fibres are oriented by stretching in a process called carding before spinning into continuous filaments (Figure 2.9).[130]

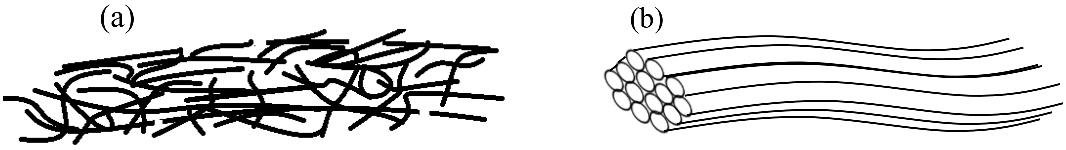

Figure 2.9. Schematic illustrating the difference between (a) staple fibres before orientation and spinning into (b) continuous filaments

2.2.2 Polyester Fibres

Polyester is the most popular and dominant fibre in the synthetic fibre industry in terms of production volume.[119,131] Polyesters are preferred over other synthetic fibres due to their inexpensive production and sourcing and their exceptional physical properties.[131] Polyester fibres are defined as fibres containing at least 85 % of a polymeric ester of a substituted aromatic carboxylic acid, such as p-hydroxybenzoic acid, polybutylene terephthalate, polytrimethylene terephthalate and polyethylene terephthalate (PET).[119,131] The most commonly used polymer in polyester fibre production is PET (Figure 2.10). PET was invented in 1941 by the British chemists John R. Whinfield and James T. Dickson while working for Calico Printer's Association, Manchester.[132] Their invention was built upon the earlier discoveries of Wallace H. Carothers, which led to the invention of nylon.[133] PET is synthesised by the two step growth polymerisation of terephtalic acid and ethylene glycol. It can also be produced by the ester exchange reaction between dimethyl terephthalate and ethylene glycol at 250 -300 °C in the presence of a catalyst.[119] The resulting polymer can be dried to give a solid polymer or directly taken through the melt spinning process to produce continuous filament fibres and instantaneously solidifies. The filaments are drawn by stretching at elevated temperatures to about 4 – 5 times their original length.

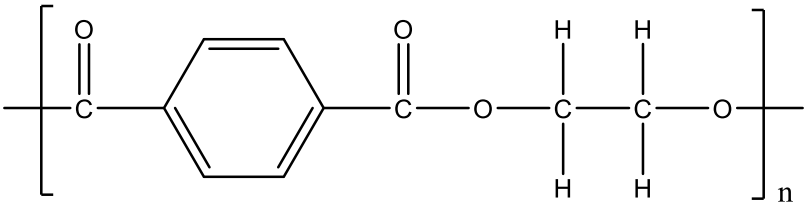

Figure 2.10. Chemical Structure of 1,4 polyethylene terephthalate (PET) which is most commonly used in the production of polyester fibres

2.2.3 Fabric Finishing

Fibre yarns are assembled from filament or stable fibres or a combination of the two; the filaments can be synthetic, natural or hybrid. Yarns are woven into continuous fabric which can be used in home furnishings, clothing and other applications.[134] Fabrics go through finishing processes to enhance attractiveness and usability. Textile finishing in the wider sense covers all the processes that the fibres go through; from yarning, weaving to the consumer. The finishing processes can be divided into four main groups: mechanical processing, heat setting, chemical processing and surface coating.[119] Mechanical finishing of fabrics involve the use of mechanical action to impart desired effects onto fabrics, these include: *calendaring* to flatten and smoothen the fabric surface, *singeing* to burn off protruding fibre ends and *compressive shrinkage* to minimise shrinkage during washing.[135] Heat setting applies mainly to synthetic fabrics to stabilise the fibres and the surface coating finish imparts functional properties depending on intended application e.g. anti-bacterial finish and water repellent finish. Chemical finishing involves all the chemical aided processes applied before or after the other finishing processes. The chemical processes in the preliminary stages of the textile finishing include: desizing, scouring and bleaching. Desizing is the first stage of cleaning that removes starch and other sizing compounds applied to the yarn before the weaving process.[136] Dilute acids, enzymes and oxidative compounds such as chlorine are used to achieve this. Scouring is critical step in the pretreatment of fibres especially for natural fibres.[137,138] Scouring is a cleaning process that removes impurities and additives such as oils, fats, pectins and waxes which are naturally abundant in the cuticle of the cotton fibre.[136] Scouring imparts hydrophilicity and permeability to textile fibres, which is essential for the subsequent finishing processes. The bleaching process is applied to impart whiteness to natural fibres, which by nature are not white. Bleaching is not entirely necessary for synthetic fibres as optical brighteners can be incorporated into the polymers during fibre production.[139] After the preliminary processes, fabrics go through the dyeing or printing process to impart color; white fabrics bypass this step after bleaching. The final chemical finishing processes are aimed at providing properties that are desirable to the consumer such as a soft handle, crease resistance, water repellency and many more. A soft handle is critical for fabrics used in clothing due to the sensitive nature of skin to touch and is one of the dominant factors influencing the consumer's choice.[140] The pretreatment and coloration processes with harsh chemicals leave the textile fibres brittle and undesirable aesthetically and in terms of comfort. Treatment with textile softeners can overcome these effects in natural fibres and also impart a 'natural feel' to synthetic fibres.[141] The perceived softness of textile materials is a combination of quantifiable mechanical properties that can accurately predict the human response and perception of softness. According to the Kawabata Evaluation System (KES) softness can be quantified by a combination of bending, compression, surface friction and roughness, tension and shear tests.[142,143] The fabric handle is the perceived sensation to touch of the textile material felt by the skin and is enhanced by application of fabric softeners during the finishing process.[144] Cationic surfactants have been used in the textile industry since the late 1930s to impart softness and additionally improve colour fastness of dyed fabrics.[145] Silicones are a newer generation of fabric softeners that have become widely recognised for their exceptional ability to enhance the softness, aesthetic appeal and impart and excellent hand during finishing. Amino functionalised silicones are the most efficient group of silicone softener when applied under acidic conditions.[145] The protonation of the amine groups by the acid, imparts a positive charge to the polymer, which enables strong electrostatic bonds with the slightly negatively charged fabric surfaces.

2.2.4. Laundry Formulations

Fabric care is an essential part of household textile maintenance for the sustained usability and appeal to the consumer. A wide variety of fabric care products currently adorn shelves of aisles upon aisles of superstores in developed countries. According to the 2015 annual report for the fast moving consumer goods giant, P&G, fabric care and homecare products are leading the market with \$22.3 billion in net sales.[146] The main objectives in fabric maintenance can be classified into three segments: cleaning (lifting soils), restoring the finishing properties (e.g. softness and whiteness) and imparting additional desirable properties (e.g. fragrance). The home based cleaning process of fabrics is aided by chemical agents, mechanical agitation and suitable quality water. Soap is one of the oldest known agents for textile cleaning. However, the last century has seen a rise in synthetic detergents and an increase in complexity of fabric care formulations due to growing consumer demand and market share competition.[147] The detergency mechanism suggested by Venegas illustrates the complex nature of the laundry detergency process (Figure 2.11).[148] Hydration of the soil (i.e. grease, dust, food stains, etc) is facilitated by the presence of water; the presence of surfactants enhances hydration by lowering the surface tension of the water. Surfactants play an important role in the lifting of soils and

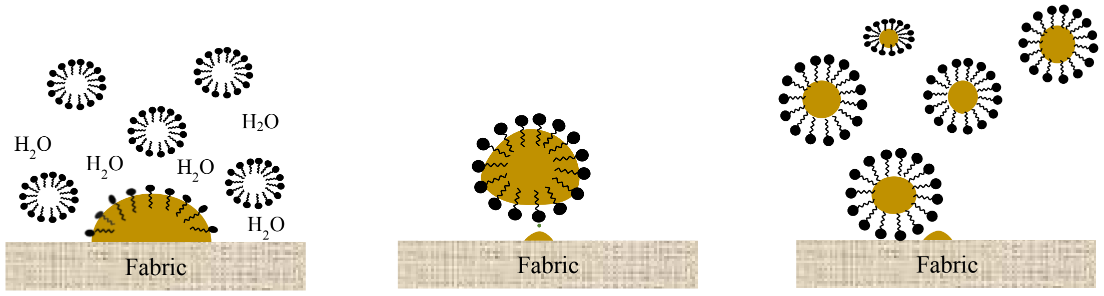

1. Hydration of the soil/stain

2. Lifting the soil from the fabric surface

3. Fragmentation of the soil to aid suspension

4. Prevent redeposition of soil

5. Bleach

6. Deposit actives

Figure 2.11. Schematic depicting the mechanism of detergency in laundry as suggested by Vegenas (ref 148)

breaking them down into small pieces. Enzymes also play a part in soil lifting by breaking them down chemically and also prevent redeposition. Other formulations contain anti-redeposition substances to minimise the high likelihood of reabsorption of soils.[148] Bleaching agents help minimise the appearance of stains remaining on the fabric surface and restore whiteness. Active ingredients such as soil release polymers, optical brighteners, fabric softeners, hueing dyes and perfumes are deposited onto the fibre surface to impart desired properties. Other ingredients in laundry detergent formulations include builders, defoamers, buffers and suds suppressors.

2.2.4.1 Surfactants

The major component of any detergent formulation is the surfactant system. A variety of surfactants (both ionic and non-ionic) are combined to create an effective surfactant system. Anionic surfactants make up the bulk of surfactant systems in most detergent formulations.[149] They are derived from petrochemical sources, vegetable oil and animal fats.[150,151] Anionic surfactants used in laundry detergents include linear alkylbenzoate sulfonate (LAS), alcohol

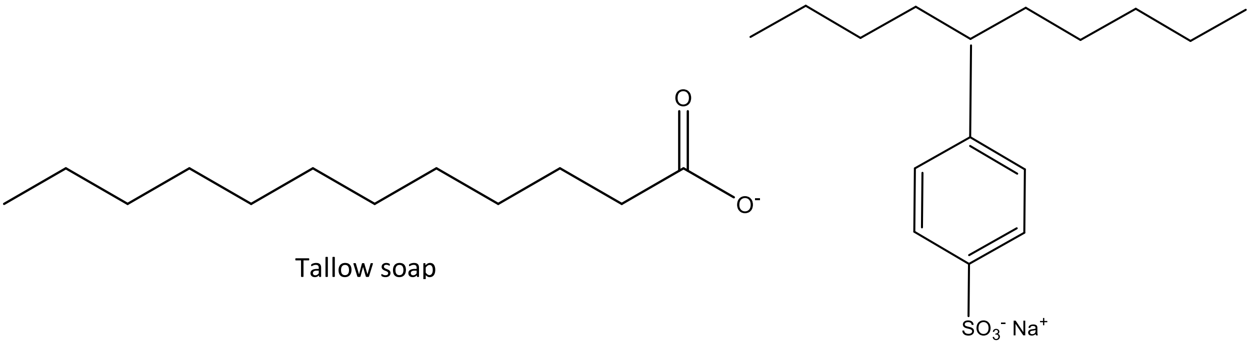

Tallow soap

Linear alkylbenzene

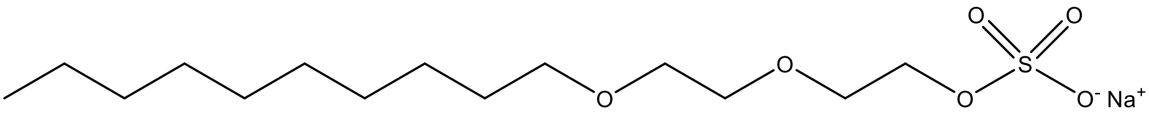

Alcohol ether sulfate (AEOS)

Figure 2.12. Chemical Structures of some anionic surfactants used in laundry detergent formulations (a) tallow soap (b) LAS (c) AEOS

ether sulfate (AEOS) and soap (Figure 2.12). The ionic hydrophiles (e.g –COO^- and –SO_3^-) are responsible for the high HLB values associated with anionic surfactants.[151] The second major class of surfactants in laundry surfactant systems is nonionic surfactants such as alcohol ethoxylates.[149] The combination of anionic and nonionic surfactants provides a synergistic cleaning effect, especially for oily soils.[149] The addition of small amounts of cationic surfactants to anionic surfactant systems to give a pseudo-nonionic surfactant has been reported to exhibit improved oily soil removal.[152]

2.2.4.2 Enzymes

The concept of detergent enzymes is attributed to Otto Röhn according to his 1913 patent on the use of pancreatic enzymes in detergent formulations.[153] Enzymes are protein molecules that can catalyse the breaking down of specific soils. Proteases were the first enzymes introduced to laundry formulations due to their ability to remove stubborn protein based stains such as blood, milk and grass.[154] Lipases enhance the removal fatty soils and α-amylases aid the removal of starch-based soils.[155] Cellulases are relatively new in detergent formulations and are said to be effective at removing particulate soils, maintain and restore colour and impart a soft and polished finish to fabric surfaces.[154] Enzyme containing detergents, termed biological detergents, contain enzyme stabilisers and buffers to ensure optimum pH levels for high performance. Most detergent enzymes operate at optimum pH ranges from 9 – 11.[155]

2.2.4.3 Builders

Builders are organic or inorganic substances added to detergent formulations in order to increase the efficiency of the surfactants. Surfactants, especially anionic surfactants, are sensitive water hardness (i.e Ca^{2+}, Mg^{2+} and HCO^{3-} mineral content).[149] Builders maintain the efficiency of surfactants by reducing the mineral content water through chelation, precipitation or ion exchange, thereby optimising the cleaning efficiency of surfactants. Builders can also aid the fabric cleaning process by lifting oily soils and preventing redeposition. They can also be used to impart an alkaline pH to the wash water. The types of builders used is dependent on the local regulations, water quality and consumer preferences/circumstances, for instance, detergent formulations are tailored for different countries. Some examples of builders used in laundry detergents include: sodium tripolyphosphate (STPP), carbonates (sodium or calcium), sodium silicates and zeolites.

2.2.4.4 Bleach

Bleaches in laundry detergent formulations act by destroying the chromophoric groups responsible for colour in soils.[156] This is achieved via oxidative attack facilitated by: chlorine-based bleaches (e.g. sodium hypochlorite), peroxide-based bleaches (e.g. perborate monohydrate), activated peroxide systems (e.g. N'N'' –tetraacetyl ethylene diamine, TAED) and metal catalysts (e.g. phthalocyanine metal complexes).[155–157] The bleaching system chosen is based on compatibility with the surfactant and enzyme system.

2.2.4.5 Optical Brighteners

Optical brighteners, also known as fluorescent brightening or whitening agents (FBA or FWA) are used in laundry detergents to overcome the visible effects of stains and the natural yellowing of fabrics due to aging.[158,159] They are employed to complement the effect of the bleaching system and are known for imparting a *'whiter than white'* appearance to fabrics. Optical brighteners adsorb to the fabric surface and absorb ambient light to emit a blue color which reduces the appearance of yellowing due to stains and aging.[159]

2.2.4.6 Colourants and Colour Protection

Dyes and pigments are used in laundry formulations for numerous reasons. Colour is added for aesthetic purposes to make the products more desirable to the consumer. However, colourants are most importantly applied to enhance the visual appearance of both coloured and noncoloured fabrics.[160] The addition of substantive blue or violet dyes in laundry detergent formulations has been in practice since the 1800s.[160] Bluing agents counteract the yellowing effect of fabric due to aging and are used in combination with optical brighteners to achieve this effect. Colour protection polymers are added to detergent formulations to prevent transfer of dyes during washing. Coloured fabrics tend to lose colour with repeated washes due to the harshness of detergents and bleach on the adsorbed dyes. Color protection agents prevent the deposition of the fugitive dyes onto other fabrics by directly protecting the dyes on the fabric surface (e.g. with functionalised silicone polymers) or inhibiting transfer using polymeric inhibitors such as polyvinyl pyrrolidone.[161]

2.2.4.7 Perfumes

Fragrances are added to laundry formulations in order to mask the strong odours from the detergent ingredients (e.g. bleach) and to impart a fresh and clean scent to washed fabrics. Perfumes are made up of a combination of fragrances comprising with different volatilities to provide both immediate and long lasting impact scents. Due to the volatility and instability of perfumes, they are usually encapsulated in polymeric matrices such as polyurethane, to provide stability and controlled release.[162] Perfumes in fabric care can be incorporated in detergent formulations, fabric conditioners or spray on fabric refreshers such as *febreze* (P&G).

2.2.4.8 Fabric Softener

The softening finish applied to textiles during preparation has the propensity to fade with repeated wash cycles resulting in loss of the initial softness of the fabrics. In addition, the mechanical agitation applied during washing and the static forces introduced during tumble drying or air drying can give fabrics a harsh feel.[163] Application of fabric softeners restores the softness and handle of fabrics and also imparts additional desirable characteristics e.g. ease of ironing.[155,164] Fabric softeners in laundry are usually applied during the rinse cycle (as in rinse added softeners) or more recently during the wash cycle (as in 2-in-1 detergent/softener formulations). Fabric softener impregnated sheets can also be used to apply softener to fabrics during tumble drying or by spraying during ironing.[163] Cationic surfactants such as: dihydrogenated tallow dimethyl ammonium chloride (DHTDMAC), amido-imidazoline quats, amino silicones and ester quats are the most commonly used fabric softeners in fabric care formulations. Cationic surfactants are incompatible with the anionic surfactants used for cleaning which compromises the efficiency of 2-in-1 detergent formulations.[163]

2.3 Introduction to Lipid Membranes

Biological cell membranes are phenomenal structures found in all living cells and in some organelles. The membrane is a naturally 'smart' structure that serves as a barrier between the intra-cellular and extra-cellular environment while facilitating cell signalling processes and selectively regulating the transport essential molecules, ions and nutrients into the cell and waste products out of the cell.[165,166] The fluid mosaic model suggested by Singer and Nicholson in 1972 illustrates the complex nature of a biological cell membrane.[167] The cell membrane is about 4 – 8 nm in thickness and is predominantly composed of lipids, majorly phospholipids

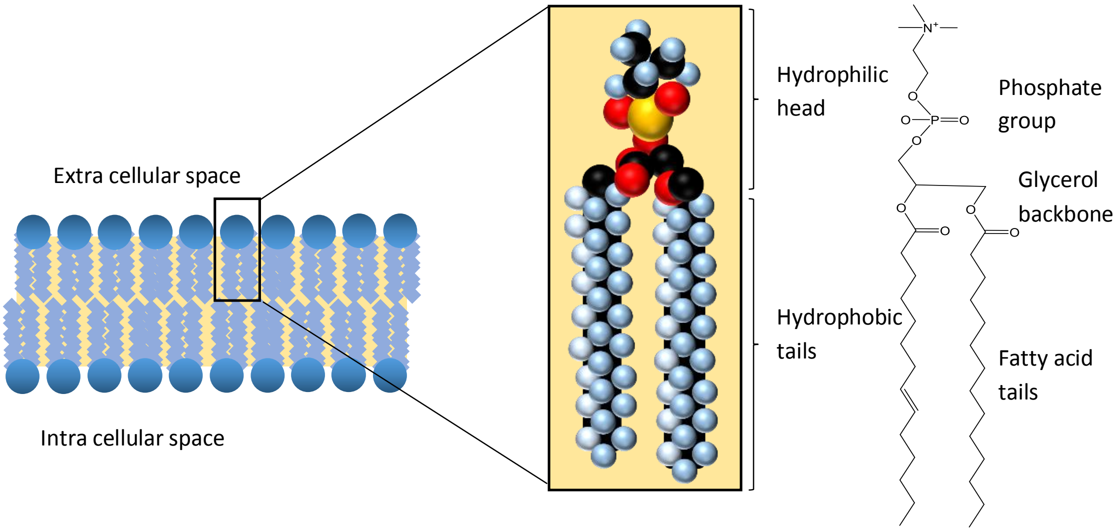

Figure 2.13. Schematic presentation the structure of a phospholipid molecule. Phospholipids aggregate to form bilayer lipid structures and constitute at least 50 % of animal cell membranes

as well as glycolipids and cholesterol.[168] Phospholipids are amphipathic molecules that generally comprise of two hydrophobic fatty acid chains and a hydrophilic phosphate group joined together by a glycerol or other polyol molecule (Figure 2.13).[169] The phospholipid bilayers assume the basic function of restricting exchange between the intracellular and the extracellular environment. Small molecules like O_2 and CO_2 can passively travel through the membrane by diffusion, while water soluble ions and most biological molecules cannot pass through the hydrophobic lipid chains.[165] Active transport or uphill transport is the assisted movement of ions and molecules across the membrane facilitated by protein channels. Most animal cell membranes consist of approximately 50% lipid by weight and the rest is made up of protein.[168] The carbohydrate portions of glycolipids and glycoproteins constitute 5 to 10% of the membrane mass. The percentage by weight of proteins is increased by the fact that proteins are much larger than lipids, thus one protein molecule corresponds to about 50 – 100 lipid molecules.[168] The model cell membrane can be simplified to a bilayer lipid membrane (BLM) in investigations in order to circumnavigate the complexity of the cell membrane.

2.3.1 Bilayer Lipid Membranes

The concept of BLM systems is said to have originated from the observations made by the 17th century scientist, Robert Hooke.[170] Robert Hooke's observations of 'black holes' in ultrathin films of soap bubbles were later supported by Isaac Newton's findings three decades later and have been a profound backbone onto which the lipid bilayer phenomena was built.[170] The first reports of the successful creation of self-assembled BLM was reported in the 1960s in the work done by Mueller et al., who reproduced a bilayer lipid membrane between two aqueous solutions.[171] This type of membrane is also referred to as free standing membranes or as 'black lipid membrane'. Further advances have led to more stable and long lasting lipid membranes, solid supported bilayer lipid membranes (sBLM) and tethered bilayer lipid membranes (tBLM), which are anchored to the solid substrate by chemical interactions.[172–174] tBLM systems can be created by the fusion of vesicles on a self-assembled monolayer (SAM) driven by hydrophobic interactions. SAM and BLM systems are of interest in biological research as cell membrane models and in electrochemical applications as barriers for electron and ion transport as well as other applications.

2.3.2 Self Assembled Monolayers

Self-assembled monolayers are formed by the spontaneous arrangement of amphifunctional molecules on a substrate, resulting in thermodynamically stable structures. In 1946, Zisman et al., reported the assembly of 1-Eicosanol ($C_{20}H_{42}0$) on metal substrates, this was the genesis of self-assembled monolayers.[175] SAM have since received tremendous interest due to their large range of applications. They provide a stable base for the formation of bilayer lipid membranes and they can operate as integrated molecular systems when added functionality is introduced to the SAM.[176] SAM systems find various applications in electrochemistry, including electrode selectivity to molecules, organisation and structural arrangement of recognition species on the electrode surface, prevention of corrosion and charge exclusion.[176,177] Alkanethiols and dialkanethiols are among the extensively researched SAM on gold surfaces due to their simple and convenient assembly (Figure 2.14). They interact with the gold surface by chemisorption, which is driven by the high affinity of sulphur to gold resulting in a covalent bond with a bond energy of 45 – 50 kcal/mol.[178] This process takes place within one minute of submersion of the substrate in a thiolate solution. However, the orientation of molecules on the surface to form a densely packed monolayer is a slow process, requiring several hours to form a uniform film.[179] The re-organisation process is driven by the Van der Waals forces between the alkyl chains, therefore, longer alkyl chain thiols result in more ordered monolayer with less defects.[180,181]

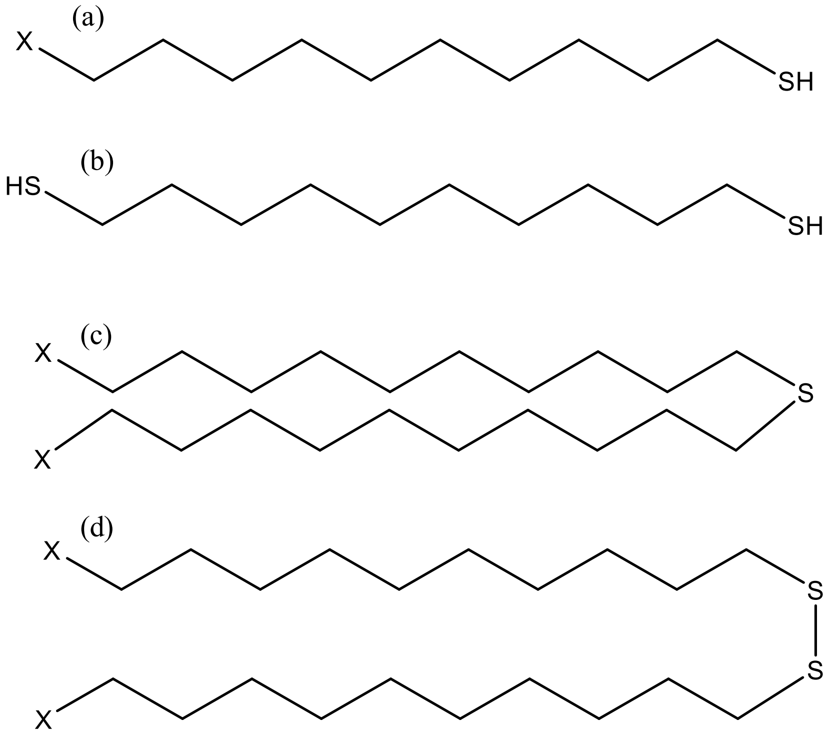

Figure 2.14. Examples of thiolated molecules used in SAM formation on gold surfaces (a) alkanethiol (b) alkanedithiol (c) dialkylsulfide (d) diakyldisulfide

2.4. References

1 G. Tiwari, R. Tiwari, B. Sriwastawa, L. Bhati, S. Pandey, P. Pandey and S. K. Bannerjee, *Int. J. Pharm. Investig.*, 2012, **2**, 2–11.

2 P. C. Calder, G. L. Jensen, B. V Koletzko, P. Singer and G. J. A. Wanten, *Intensive Care Med.*, 2010, **36**, 735–49.

3 M. Adolph, *Ann. Nutr. Metab.*, 1999, **43**, 1–13.

4 K. Hippalgaonkar, S. Majumdar and V. Kansara, *AAPS PharmSciTech*, 2010, **11**, 1526–40.

5 J. E. Bowcott and J. H. Schulman, *Zeitschrift für Elektrochemie, Berichte der Bunsengesellschaft für Phys. Chemie*, 1955, **59**, 283–290.

6 M. Giustini, S. Murgia and G. Palazzo, *Langmuir*, 2004, **20**, 7381–4.

7 L. M. Prince, in *Microemulsions Theory and Practice*, Elsevier Science, 2012, pp. 1–19.

8 T. M. Allen and P. R. Cullis, *Adv. Drug Deliv. Rev.*, 2013, **65**, 36–48.

9 J. Pietkiewicz, M. Sznitowska and M. Placzek, *Int. J. Pharm.*, 2006, **310**, 64–71.

10 B. S. Pattni, V. V Chupin and V. P. Torchilin, *Chem. Rev.*, 2015, **115**, 10938–10966.

11 D. Lasic, *Trends Biotechnol.*, 1998, **16**, 307–321.

12 A. Akbarzade, R. Rezaei-Sadabady, S. Davaran, S. W. Joo, N. Zarghami, Y. Hanifehpour, M. Samiei, M. Kouhi and K. Nejati-Koshki, *Nanoscale Res. Lett.*, 2013, **8**, 1–9.

13 A. Wagner and K. Vorauer-Uhl, *J. Drug Deliv.*, 2011, **591325**, 1–9.

14 W. B. Liechty, D. R. Kryscio, B. V. Slaughter and N. A. Peppas, *Annu. Rev. Chem. Biomol. Eng.*, 2010, **1**, 149–173.

15 S. Mukherjee, S. Ray and R. S. Thakur, *Indian J. Pharm. Sci.*, 2009, **71**, 349–358.

16 US, US 5250236 A, 1993.

17 S. Sugiura, M. Nakajima, J. Tong, H. Nabetani and M. Seki, *J. Colloid Interface Sci.*, 2000, **227**, 95–103.

18 G. Yener, *Int. J. Pharm.*, 2003, **258**, 203–207.

19 T. Eldem, P. Speiser and A. Hincal, *Pharm. Res.*, **8**, 47–54.

20 EP0167825, 1986.

21 R. Cavalli, O. Caputo and M. R. Gasco, *Eur. J. Pharm. Sci.*, 2000, **10**, 305–9.

22 J. Yang and O. N. Ciftci, *Food Bioprod. Process.*, 2016, **98**, 151–160.

23 M. Muchow, P. Maincent and R. H. Muller, *Drug Dev. Ind. Pharm.*, 2008, **34**, 1394–405.

24 C. Olbrich, A. Gessner, O. Kayser and R. H. Müller, *J. Drug Target.*, 2002, **10**, 387–96.

25 A. Beloqui, M. Á. Solinís, A. Rodríguez-Gascón, A. J. Almeida and V. Préat, *Nanomedicine*, 2016, **12**, 143–61.

26 L. Montenegro, F. Lai, A. Offerta, M. G. Sarpietro, L. Micicchè, A. M. Maccioni, D. Valenti and A. M. Fadda, *J. Drug Deliv. Sci. Technol.*, 2015, **32**, 100–112.

27 R. H. Müller, M. Radtke and S. A. Wissing, *Adv. Drug Deliv. Rev.*, 2002, **54**, S131–S155.

28 R. H. Müller, R. D. Petersen, A. Hommoss and J. Pardeike, *Adv. Drug Deliv. Rev.*, 2007, **59**, 522–30.

29 J. D. Lopes, C. R. F. Grosso, G. de Andrade Calligaris, L. P. Cardoso, R. C. Basso, A. P. B. Ribeiro and P. Efraim, *Eur. J. Lipid Sci. Technol.*, 2015, **117**, 1681–1902.

30 T. H. Gugu, S. A. Chime and A. A. Attama, *Asian J. Pharm. Sci.*, 2015, **10**, 425–432.

31 C. Gu, C. Hu, C. Ma, Q. Fang, T. Xing and Q. Xia, *Eur. J. Lipid Sci. Technol.*, 2016, **118**, 1093–1103.

32 F. Li, L. Yang, C. Zhao and Z. Du, *Anal. Methods*, 2011, **3**, 1601–1606.

33 O. N. Ciftci and F. Temelli, *J. Food Eng.*, 2016, **178**, 137–144.

34 B. Albertini, M. Mezzena, N. Passerini, L. Rodriguez and S. Scalia, *J. Pharm. Sci.*, 2009, **98**, 2759–69.

35 S. Milak, N. Medlicott and I. G. Tucker, *J. Microencapsul.*, 2006, **23**, 823–31.

36 A. Lauterbach and C. C. Müller-Goymann, *Int. J. Pharm.*, 2015, **494**, 445–52.

37 M. Ali and M. E. Byrne, *Expert Rev. Clin. Pharmacol.*, 2008, **1**, 145–61.

38 A. Lauterbach and C. C. Mueller-Goymann, *Int. J. Pharm.*, 2014, **466**, 122–32.

39 R. H. Müller, K. Mäder and S. Gohla, *Eur. J. Pharm. Biopharm.*, 2000, **50**, 161–177.

40 E. B. Souto and R. H. Müller, *Int. J. Cosmet. Sci.*, 2008, **30**, 157–65.

41 PCT/EP00/06535, 2001.

42 R. H. Muller, R. Shegokar and C. M. Keck, *Curr. Drug Discov. Technol.*, 2011, **8**, 207–227.

43 A. Hommoss, Freie Universität Berlin, 2008.

44 C.-L. Fang, S. A. Al-Suwayeh and J.-Y. Fang, *Recent Pat. Nanotechnol.*, 2013, **7**, 41–55.

45 M. D. Joshi and R. H. Müller, *Eur. J. Pharm. Biopharm. Off. J. Arbeitsgemeinschaft für Pharm. Verfahrenstechnik e.V*, 2009, **71**, 161–172.

46 S. A. Wissing, O. Kayser and R. H. Müller, *Adv. Drug Deliv. Rev.*, 2004, **56**, 1257–72.

47 W. Mehnert and K. Mäder, *Adv. Drug Deliv. Rev.*, 2001, **47**, 165–196.

48 W. Mehnert and K. Mäder, *Adv. Drug Deliv. Rev.*, 2012, **64**, 83–101.

49 J. McMurry, *Organic Chemistry*, Cengage Learning, 2011.

50 M. A. Schubert and C. C. Müller-Goymann, *Eur. J. Pharm. Biopharm.*, 2005, **61**, 77–86.

51 F. Shi, J.-H. Zhao, Y. Liu, Z. Wang, Y.-T. Zhang and N.-P. Feng, *Int. J. Nanomedicine*, 2012, **7**, 2033–43.

52 C. Qi, Y. Chen, Q.-Z. Jing and X.-G. Wang, *Int. J. Mol. Sci.*, 2011, **12**, 4282–93.

53 J. Liu, T. Gong, C. Wang, Z. Zhong and Z. Zhang, *Int. J. Pharm.*, 2007, **340**, 153–162.

54 T. M. Göppert and R. H. Müller, *Eur. J. Pharm. Biopharm. Off. J. Arbeitsgemeinschaft für Pharm. Verfahrenstechnik e.V*, 2005, **60**, 361–72.

55 T. M. Göppert and R. H. Müller, *J. Drug Target.*, 2003, **11**, 225–31.

56 S. Zhang, J. Yun, S. Shen, Z. Chen, K. Yao, J. Chen and B. Chen, *Chem. Eng. Sci.*, 2008, **63**, 5600–5605.

57 P. Ekambaram and H. S. A. Abdul, *J. Young Pharm.*, 2011, **3**, 216–20.

58 J. Mazuryk, T. Deptuła, A. Polchi, J. Gapiński, S. Giovagnoli, A. Magini, C. Emiliani, J. Kohlbrecher and A. Patkowski, *Colloids Surfaces A Physicochem. Eng. Asp.*, 2016.

59 M. S. Oliveira, S. V Mussi, D. A. Gomes, M. I. Yoshida, F. Frezard, V. M. Carregal and L. A. M. Ferreira, *Colloids Surf. B. Biointerfaces*, 2016, **140**, 246–53.

60 H. Bunjes, M. H. J. Koch and K. Westesen, *J. Pharm. Sci.*, 2003, **92**, 1509–20.

61 H. Salminen, T. Helgason, S. Aulbach, B. Kristinsson, K. Kristbergsson and J. Weiss, *J. Colloid Interface Sci.*, 2014, **426**, 256–63.

62 L. Arana, C. Salado, S. Vega, O. Aizpurua-Olaizola, I. de la Arada, T. Suarez, A. Usobiaga, J. L. R. Arrondo, A. Alonso, F. M. Goñi and I. Alkorta, *Colloids Surf. B. Biointerfaces*, 2015, **135**, 18–26.

63 D. Pooja, L. Tunki, H. Kulhari, B. B. Reddy and R. Sistla, *Data Br.*, 2016, **6**, 15–9.

64 X. F. Wang, S. L. Zhang, L. Y. Zhu, S. Y. Xie, Z. Dong, Y. Wang and W. Z. Zhou, *Vet. J.*, 2012, **191**, 115–20.

65 H. A. Ebrahimi, Y. Javadzadeh, M. Hamidi and M. B. Jalali, *Daru*, 2015, **23**, 46.

66 M. M. Mojahedian, S. Daneshamouz, S. M. Samani and A. Zargaran, *Chem. Phys. Lipids*, 2013, **174**, 32–8.

67 Y.-C. Kuo and L.-J. Wang, *J. Taiwan Inst. Chem. Eng.*, 2014, **45**, 755–763.

68 A. C. Silva, E. González-Mira, M. L. García, M. A. Egea, J. Fonseca, R. Silva, D. Santos, E. B. Souto and D. Ferreira, *Colloids Surf. B. Biointerfaces*, 2011, **86**, 158–65.

69 USS 188837, 1993.

70 J. HUO and S. Zhou, *J. Med. Coll. PLA*, 2007, **22**, 385–390.

71 S. Das and A. Chaudhury, *AAPS PharmSciTech*, 2011, **12**, 62–76.

72 B. Sjöström and B. Bergenståhl, *Int. J. Pharm.*, 1992, **88**, 53–62.

73 B. Siekmann and K. Westesen, *Eur. J. Pharm. Biopharm.*, 1996, **43**, 104–109.

74 M. Trotta, F. Debernardi and O. Caputo, *Int. J. Pharm.*, 2003, **257**, 153–160.

75 M. Trotta, M. Gallarate, F. Pattarino and S. Morel, *J. Control. Release*, 2001, **76**, 119–28.

76 F. Q. Hu, H. Yuan, H. H. Zhang and M. Fang, *Int. J. Pharm.*, 2002, **239**, 121–128.

77 Y. Luo, D. Chen, L. Ren, X. Zhao and J. Qin, *J. Control. Release*, 2006, **114**, 53–59.

78 M. Trotta, R. Cavalli, M. E. Carlotti, L. Battaglia and F. Debernardi, *Int. J. Pharm.*, 2005, **288**, 281–288.

79 M. A. Bianco, M. Gallarate, M. Trotta and L. Battaglia, *J. Drug Deliv. Sci. Technol.*, 2010, **20**, 187–191.

80 L. Battaglia, M. Gallarate, R. Cavalli and M. Trotta, *J. Microencaps.*, 2010, **27**, 78–85.

81 J. Hao, F. Wang, X. Wang, D. Zhang, Y. Bi, Y. Gao, X. Zhao and Q. Zhang, *Eur. J. Pharm. Sci.*, 2012, **47**, 497–505.

82 M. Gallarate, M. Trotta, L. Battaglia and D. Chirio, *J. Drug Deliv. Sci. Technol.*, 2010, **20**, 343–347.

83 L. Battaglia, I. D'Addino, E. Peira, M. Trotta and M. Gallarate, *J. Drug Deliv. Sci. Technol.*, 2012, **22**, 125–130.

84 S. Gao and D. J. McClements, *Colloids Surfaces A Physicochem. Eng. Asp.*, 2016, **499**, 79–87.

85 K. Shinoda and H. Saito, *J. Colloid Interface Sci.*, 1968, **26**, 70–74.

86 K. Shinoda and H. Arai, *J. Phys. Chem.*, 1964, **68**, 3485–3490.

87 N. Anton and T. F. Vandamme, *Int. J. Pharm.*, 2009, **377**, 142–7.

88 G. Broze, *Handbook of Detergents: Properties*, Taylor & Francis, 1999.

89 M. Eltayeb, P. K. Bakhshi, E. Stride and M. Edirisinghe, *Food Res. Int.*, 2013, **53**, 88–95.

90 P. C. H. Wong, P. W. S. Heng and L. W. Chan, *Eur. J. Lipid Sci. Technol.*, 2015, n/a-n/a.

91 B. Siekmann and K. Westesen, *Pharm. Pharmacol. Lett.,* 1992, **1**, 123–126.

92 R. Lander, W. Manger, M. Scouloudis, A. Ku, C. Davis and A. Lee, *Biotechnol. Prog.*, **16**, 80–5.

93 B. Siekmann and K. Westesen, *Pharm. Pharmacol. Lett*, 1994, **3**, 194–197.

94 H. Bunjes, M. Drechsler, M. H. Koch and K. Westesen, *Pharm. Res.*, 2001, **18**, 287–93.

95 L. Becker Peres, L. Becker Peres, P. H. H. de Araújo and C. Sayer, *Colloids Surf. B. Biointerfaces*, 2016, **140**, 317–23.

96 M. Nabi-Meibodi, A. Vatanara, A. R. Najafabadi, M. R. Rouini, V. Ramezani, K. Gilani, S. M. H. Etemadzadeh and K. Azadmanesh, *Colloids Surfaces B Biointerfaces*, 2013, **112**, 408–414.

97 A. zur Mühlen, C. Schwarz and W. Mehnert, *Eur. J. Pharm. Biopharm.*, 1998, **45**, 149–155.

98 M. Uner and G. Yener, *Int. J. Nanomedicine*, 2007, **2**, 289–300.

99 D. E. Sands, *Introduction to Crystallography*, Courier Corporation, reprint., 2012.

100 C. Freitas and R. H. Müller, *Eur. J. Pharm. Biopharm.*, 1999, **47**, 125–32.

101 F. J. Hildago and R. Zamora, in *Handbook of Food Science, Technology, and Engineering - 4 Volume Set*, eds. Y. H. Hui and F. Sherkat, CRC Press, 2005, pp. 1–21.

102 F. D. Gunstone, J. L. Harwood and A. J. Dijkstra, *The Lipid Handbook with CD-ROM, Third Edition*, CRC Press, 2007.

103 K. Mäder, in *Nanoparticulates as Drug Carriers*, ed. V. P. Torchilin, Imperial College Press, 2006, pp. 187–212.

104 K. Westesen, B. Siekmann and M. H. J. Koch, *Int. J. Pharm.*, 1993, **93**, 189–199.

105 V. Jenning, A. F. Thünemann and S. H. Gohla, *Int. J. Pharm.*, 2000, **199**, 167–177.

106 A. G. Marangoni and S. S. Narine, *Physical Properties of Lipids*, CRC Press, 2002.

107 R. H. Müller, C. Schwarz, A. Zur Mühlen and W. Mehnert, *Proc Int Symp Control Rel Bioact Mater.*, 1994, **21**, 146–147.

108 J. Lee and J.-C. Kim, *Colloids Surfaces A Physicochem. Eng. Asp.*, 2015, **484**, 441–448.

109 H.-H. Chen, W.-C. Huang, W.-H. Chiang, T.-I. Liu, M.-Y. Shen, Y.-H. Hsu, S.-C. Lin and H.-C. Chiu, *Int. J. Nanomedicine*, 2015, **10**, 5035–48.

110 S. Kim, M.-J. Stébé, J.-L. Blin and A. Pasc, *J. Mater. Chem. B*, 2014, **2**, 7910–7917.

111 C. Olbrich, O. Kayser and R. H. Müller, *J. Nanoparticle Res.*, **4**, 121–129.

112 J.-H. Kim, Y. Kim, K. H. Bae, T. G. Park, J. H. Lee and K. Park, *Mol. Pharm.*, 2015, **12**, 1230–41.

113 M. Garcia-Fuentes, C. Prego, D. Torres and M. J. Alonso, *Eur. J. Pharm. Sci.*, 2005, **25**, 133–43.

114 Y.-C. Kuo and S.-J. Cheng, *Int. J. Pharm.*, 2016, **499**, 10–9.

115 1987.

116 US 20140271863, 2014.

117 R. J. Perry, *Delivery System Handbook for Personal Care and Cosmetic Products*, Elsevier, 2005.

118 H. V. S. Murthy, *Introduction to Textile Fibres*, CRC Press, 2016.

119 A. K. R. Choudhury, *Textile Preparation And Dyeing*, Science Publishers, 2006.

120 S. P. Mishra, *A Textbook Of Fibre Science And Technology*, New Age International, 2000.

121 C. M. Carr, *Chemistry of the Textiles Industry*, Blackie Academic & Professional, 1995.

122 S. Sekhri, *Textbook of Fabric Science: Fundamentals to Finishing*, PHI Learning, 2012.

123 C. H. Haigler, L. Betancur, M. R. Stiff and J. R. Tuttle, *Front. Plant Sci.*, 2012, **3**, 104.

124 R. A. Festucci-Buselli, W. C. Otoni and C. P. Joshi, *Brazilian J. Plant Physiol.*, 2007, **19**, 1–13.

125 B. Wulfhorst, T. Gries and D. Veit, *Textile Technology*, Hanser Publishers, 2006.

126 E. A. Flint, *Biol. Rev.*, 1950, **25**, 414–434.

127 Y. Zhang, S. Chen, M. Xu, A. Cavaco-Paulo, J. Wu and C. Jian, *Appl Env. Microbiol*, 2010, **76**, 6870–6876.

128 A. T. Moore, *Stain Technol.*, 1953, **28**, 149–54.

129 H. Haigler, Candace, B. Singh, G. Wang and D. Zhang, in *Plant Genetics and Genomics: Crops and Models*, ed. A. H. Paterson, Springer US, New York, NY, Vol 3., 2009, pp. 385–417.

130 S. Sekhri, *Textbook of Fabric Science: Fundamentals to Finishing*, PHI Learning Pvt. Ltd., 2012.

131 A. J. East, in *Synthetic Fibres: Nylon, Polyester, Acrylic, Polyolefin*, ed. J. E. McIntyre, Elsevier, 2004, p. 308.

132 UK, 578,079, 1941.

133 US, US2130523 A, 1938.

134 S. Adanur, *Handbook of Weaving*, CRC Press, 2000.

135 S. Adanur, *Wellington Sears Handbook of Industrial Textiles*, CRC Press, 1995.

136 Q. Wei, *Surface Modification of Textiles*, Elsevier Science, 2009.

137 M. İ. Bahtiyari and K. Duran, *J. Clean. Prod.*, 2013, **41**, 283–290.

138 J. Ellis, in *Chemistry of the Textiles Industry*, Springer Science & Business Media, 1995, pp. 249–275.

139 J. M. Cardamone and W. M. Marmer, in *Chemistry of the Textile Industry*, ed. C. Carr, Springer Science & Business Media, 2012, pp. 45–98.

140 M. D. Teli, in *Functional Finishes for Textiles: Improving Comfort, Performance and Protection*, ed. R. Paul, Elsevier, 2014, pp. 123–147.

141 B. Wahle and J. Falkowski, *Rev. Prog. Color. Relat. Top.*, 2002, **32**, 118–124.

142 A. Causa and A. Netravali, in *Structure and Mechanica of Textile Fibre Assemblies*, ed. P. Schwartz, Elservier, 2008, pp. 4–45.

143 C. K. Chan, X. Y. Jiang, K. L. Liew, L. K. Chan, W. K. Wong and M. P. Lau, *J. Mater. Process. Technol.*, 2006, **174**, 183–189.

144 W. D. Schindler and P. J. Hauser, *Chemical Finishing of Textiles: Woodhead Publishing Series in Textiles*, Elservier, 2004.

145 J. Wang and Y. Zhu, in *Handbook of Detergents, Part D: Formulation Volume 128 of Surfactant Science*, ed. M. S. Showell, CRC Press, 2016, pp. 279–304.

146 P&G, *http://www.pginvestor.com/Cache/1001201800.PDF?O=PDF&T=&Y=&D=&FID=1001201800&iid=4004124*, 2015, 88.

147 R. A. Watson, in *ion Volume 128 of Surfactant Science*, ed. M. Showell, CRC Press., 2016, pp. 51–104.

148 M. G. Venegas, in *Powdered Detergents*, ed. M. S. Showell, CRC Press, 1997, pp. 285–312.

149 M. Zappone, A. Kaziska and G. Bogush, in *Handbook of Detergents, Part E: Applications*, ed. U. Zoller, CRC Press, 2008, pp. 69–82.

150 B. Fell, in *Anionic Surfactants: Organic Chemistry*, ed. H. W. Stache, CRC Press, 1995, pp. 1–38.

151 J. Cross, in *Anionic Surfactants: Analytical Chemistry*, ed. J. Cross, CRC Press, 2nd edn., 1998, pp. 1–34.

152 US, US5441541 A, 1995.

153 DE283923 C, 1913.

154 E. K. Baas, M. M. P. Bollier, P. F. Plank and D. S. Winetzky, in *Enzymes in Detergency. Volume 69 of Surfactant Science*, eds. J. H. van Ee and M. Onno, CRC Press, 1997, pp. 24–57.

155 F. U. Ahmed, in *Handbook of Detergents, Part E: Applications Volume 141 of Surfactant Science*, ed. U. Zoller, CRC Press, 2008, pp. 201–286.

156 M. S. Showell, in *Handbook of Detergents, Part D: Formulation Volume 128 of Surfactant Science*, ed. M. Showell, CRC Press, 2016, pp. 1–26.

157 A. B. Sorokin and E. V. Kudrik, *Catal. Today*, 2011, **159**, 37–46.

158 R. Adams, *Focus Pigment.*, 2009, **2009**, 1–3.

159 K. Hunger, *Industrial Dyes: Chemistry, Properties, Applications*, John Wiley & Sons,

2007.

160 R. L. Mahaffey Jr, in *Handbook of Detergents: Properties*, ed. G. Broze, CRC Press, 1999, pp. 721–742.

161 J. Gauthier-Lafaye, R. Gresser, G. Guerin, D. Joubert and C. Vergelati, in *Proceedings of the 4th World Conference on Detergents: Strategies for the 21st Century*, ed. A. Cahn, 1999, pp. 190–194.

162 S. N. Rodrigues, I. M. Martins, I. P. Fernandes, P. B. Gomes, V. G. Mata, M. F. Barreiro and A. E. Rodrigues, *Chem. Eng. J.*, 2009, **149**, 463–472.

163 A. Farooq, A. Mehreteab and J. J. Mastrull, in *Detergency of Specialty Surfactants*, ed. F. E. Friedli, CRC Press, 2001, pp. 255–280.

164 A. Sachdev, S. Krishnan and J. Shulman, in *Liquid Detergents, CRC Press, 1996, vol. 19.*, ed. K.-Y. Lai, CRC Press, 2nd edn., 2005, pp. 239–318.

165 W. Stillwell, *An Introduction to Biological Membranes: From Bilayers to Rafts*, Newnes, 2013.

166 J. Lombard, *Biol. Direct*, 2014, **9**, 32.

167 S. J. Singer and G. L. Nicolson, *Science (80-.).*, 1972, **175**, 720–731.

168 Cooper. Geoffrey M, *The Cell*, ASM Press, Sunderland (MA), 2nd edn., 2000.

169 J. R. Silvius, in *Phospholipids Handbook*, ed. G. Cevc, CRC Press, 1993, pp. 1–22.

170 H. T. Tien and A. L. Ottova, *J. Memb. Sci.*, 2001, **189**, 83–117.

171 P. Mueller, D. O. Rudin, H. T. Tien And W. C. Wescott, *Nature*, 1962, **194**, 979–80.

172 B. Raguse, V. Braach-Maksvytis, B. A. Cornell, L. G. King, P. D. J. Osman, R. J. Pace and L. Wieczorek, *Langmuir*, 1998, **14**, 648–659.

173 E. T. Castellana and P. S. Cremer, *Surf. Sci. Rep.*, 2006, **61**, 429–444.

174 R. P. Richter, R. Bérat and A. R. Brisson, *Langmuir*, 2006, **22**, 3497–505.

175 W. C. Bigelow, D. L. Pickett and W. A. Zisman, *J. Colloid Sci.*, 1946, **1**, 513–538.

176 S. Dong and J. Li, *Bioelectrochemistry Bioenerg.*, 1997, **1**, 7–13.

177 S. Hosseinpour, M. Forslund, C. M. Johnson, J. Pan and C. Leygraf, *Surf. Sci.*, 2016, **648**, 170–176.

178 L. Strong and G. M. Whitesides, *Langmuir*, 1988, **4**, 546–558.

179 C. D. Bain, E. B. Troughton, Y. T. Tao, J. Evall, G. M. Whitesides and R. G. Nuzzo, *J. Am. Chem. Soc.*, 1989, **111**, 321–335.

180 T. Wink, S. J. van Zuilen, A. Bult and W. P. van Bennekom, *Analyst*, 1997, **122**, 43R 50R

181 P. J. Wakelyn, N. R. Bertoniere, D. P. Thibodeaux and A. D. French, *Cotton Fiber Chemistry and Technology*, CRC Press, 2006.

182 P. J. Wakelyn, N. R. Bertoniere, D. P. Thibodeaux and A. D. French, *Cotton Fiber Chemistry and Technology*, CRC Press, 2006.

3. Experimental Methods and Techniques

This chapter reports all the methods and materials used in this thesis and briefly gives background information of the theory behind the techniques used. The preparation of SLM and SLN systems used in different chapters and the characterisation methods are described here. The preparation of lipid membranes for the work covered in chapter 6, the methods used in characterisation of the lipid membranes and those used in the investigation of penetration of an electroactive SLN system into lipid membranes are also described here.

3.1. Preparation of SLM and SLN matrices

Solvent based methods of preparation: solvent emulsification/evaporation and solvent emulsification/diffusion methods were employed in the preparation of SLM and SLN systems investigated in this thesis. Silicone-loaded SLM systems were investigated in Chapter 4, dye-loaded SLM systems were reported in chapter 5 and a ferrocene-loaded system is reported in chapter 6. All the SLM and SLN systems were based on a lauric acid matrix.

3.1.1 Reagents and Chemicals

The surfactant Neodol 45-7 (AE1S) and silicones: polydimethysiloxane with viscosities 10,000 cSt and 100,000 cSt (PDMS10 and PDMS100 respectively), terminal aminosilicone (TAS) and multi-amino functionalised silicone (PK10) were all supplied by Procter and Gamble, UK. Lauric acid ($C_{12}H_{24}O_2$), brilliant blue R ($C_{45}H_{44}N_3NaO_7S_2$), ethyl violet ($C_{31}H_{42}N_3Cl$), Ferrocene ($Fe(C_2H_5)_2$), tween 80 ($C_{64}H_{124}O_{26}$), Span 80 ($C_{24}H_{44}O_6$), sodium carbonate (Na_2CO_3) and sodium bicarbonate ($NaHCO_3$) were all purchased from Sigma Aldrich, UK.

Poloxamer 188 ($C_5H_{10}O_2$) and HPLC grade n-hexane were purchased from Fisher Scientific, UK. Absolute ethanol and deionised water (˜18 MΩ) were used in all preparations.

3.1.2. Silicone-Loaded SLM Preparation

Lauric acid (3g) was heated to 55 °C together with the silicone oil (0.3 g) to give the lipid/silicone melt. The solvent (2 ml of n-Hexane or 5ml of ethanol) was added to the melt to enhance miscibility. An aqueous solution was prepared by dissolving 1.5 g of AE1S and 0.75 g of tween 80 in 125 ml of deionised water at 55 °C. The lipid/melt and solvent mixture was added dropwise to the aqueous solution while stirring continuously; the emulsion was stirred for an additional 60 minutes while maintaining the temperature at 55 °C to evaporate the solvent. The emulsion was diluted with cold water at 4 °C and simultaneously cooled in an ice bath at for 10 minutes to solidify the particles and give an SLN dispersion. The resulting dispersions were dried by centrifuging for 10 mins at 10,000 rpm to remove excess water and filtered using a grade 1 qualitative filter paper with a 11 µm pore size (Whatman®). The particles were further dried in a CaCl dessicator for at least 48 hrs.

3.1.3. Dye-Loaded SLM Preparation

Two dye-loaded systems were prepared for both BB and EV dye: single-active system (dye only) and the dual-active system (dye and silicone). The systems were both prepared using the double emulsion method. For the dual-active SLM system, lauric acid (4.5 g), span 80 (2.5 g) and PK10 silicone (0.5 g) were mixed at 55 °C to give a molten lipid phase; for the single-active dye SLM system, 5 g of lauric acid was used. The solvent, n-hexane (5 ml) was added to the lipid phase and mixed thoroughly. A dye solution was prepared by dissolving 50 mg of the dye in 2 ml of water. The dye solution was added to the lipid mixture dropwise while stirring and the resulting emulsion was optimised by high shear homogenisation for 15 minutes at 3,000 rpm using a T18 digital Ultra Turrax®, IKA®. The w/o emulsion was added to a 100 ml aqueous solution of tween 80 (5% w/v) while stirring continuously at 300 rpm; the w/o/w emulsion was placed in an ice bath immediately to solidify the particles. This process should be completed in less than 60 sec to ensure efficient entrapment. The particles were dried using the same method reported in section 3.1.2.

3.1.4. Ferrocene-Loaded SLN Preparation

Ferrocene-loaded particles were prepared using the solvent emulsification evaporation method. The lipid mixture, lauric acid (3 g) and ferrocene (0.3 g), was heated to 55 °C while stirring and n-hexane (2 ml) was added. The lipid mixture was added dropwise to a 100 ml aqueous solution (1.5% w/v poloxamer 188 and 0.75% w/v tween 80) at 50 °C, while stirring continuously and stirred for a further 60 minutes to allow evaporation of the solvent. The emulsion was mixed by high shear homogenisation for 20 minutes at 10,000 rpm and subsequently diluted in 150 ml deionised water at 4 °C.

3.2. Preparation of Lipid Membranes

3.2.1. Reagents and Chemicals

Potassium ferrocyanide ($K_4Fe(CN)_6$), potassium ferricyanide ($K_3Fe(CN)_6$), potassium nitrate (KNO_3), hydrogen peroxide (50% wt in water), 4-(2-Hydroxyethyl)piperazine-1-ethanesulfonic acid (HEPES), 1-palmitoyl-2-oleoyl-*sn*-glycero-3-phosphocholine (POPC) were purchased from Sigma-Aldrich, UK. The lipid, 1,2-dipalmitoyl-sn-glycero-phosphothioethanol (DPPTE) (sodium salt) was purchased from Avanti Polar Lipids, USA (Figure 3.1). Laboratory grade chloroform and sulphuric acid were obtained from Fisher Scientific. Solvents were used without further purification. All buffers and solutions were prepared using deionised water from a Sartorius Arium® Comfort ultrapure water system (resistivity ≥ 18 MΩ cm).

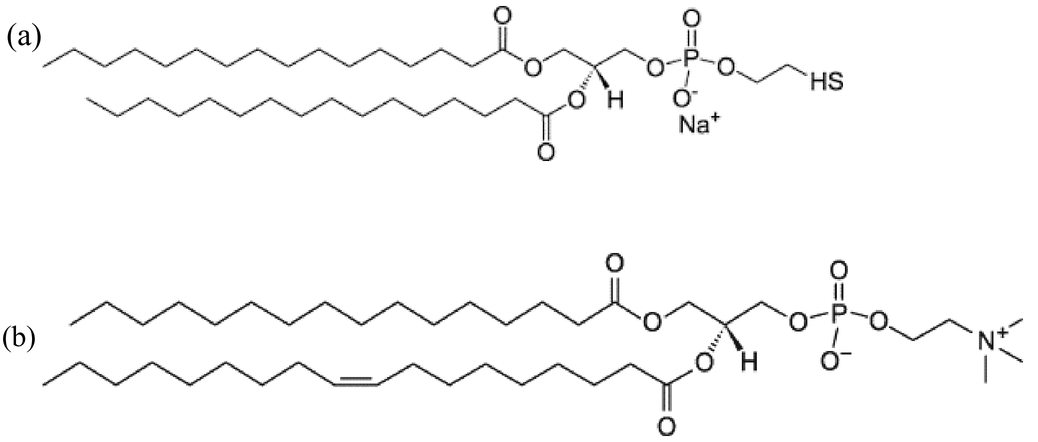

Figure 3.1. Chemical structures of the lipids used in electrode modification (a) DPPTE (b) POPC

3.2.2 Immobilization of Lipid Membranes

A thin film integrated electrode system, combining a gold working electrode (150 nm thickness and 0.8 mm^2 area) and platinum reference and auxiliary electrodes, was purchased from MicruX Technologies. Electrodes were cleaned electrochemically before use by repeatedly cycling 0.1 M H_2SO_4 between -1.0 and +1.0 V for 20 cycles at a scanning rate of 0.1 V/s. (adopted from manufacturer's recommendation). The electrodes were subsequently rinsed with a jet stream of water for one minute and subsequently dried under a stream of nitrogen gas. A stock solution of DPPTE in chloroform (25 mg/mL) was prepared and stored at -20 °C to prevent oxidation.[1] The lipid solution was prepared from the stock solution by evaporating the chloroform under a slow stream of argon and dissolving the resulting lipid film in ethanol to give a solution of 1 mM.[2] The SAM layers were immobilized by exposing the gold working electrodes to the lipid solution for 24 hrs at 4 °C. To form a BLM, an upper leaflet of POPC was added to the immobilized SAM surface. A stock solution of POPC was evaporated under a slow stream of argon; the resulting lipid film was rehydrated in 0.1 M HEPES buffer to give a solution a solution of 1 mg/mL POPC.[3] To give unilamellar vesicles, the rehydrated lipids were stirred using a vortex stirrer for 5 minutes and subsequently sonicated for 40 minutes while maintaining the temperature at 20 °C to avoid heating the lipid. The electrodes were rinsed with ethanol to rid the surface of unbound lipids and dried under a stream of argon. The same method was applied for the modification of gold sensor chips for RESI studies.

3.3. Characterisation of SLN and SLM Systems

3.3.1. Particle Size

Light scattering techniques such as laser diffraction, dynamic light scattering and photon correlation spectroscopy are useful techniques in the characterisation of particle size in SLM and SLN systems. The choice of method chosen is largely dependent on the size range of the particles, sample volume and availability of equipment. Laser diffraction is more effective for particles in the microparticles and hundreds of nanoparticle range and so was used for analysis of SLM systems in chapter 4 & 5.[4,5] Dynamic light scattering is more effective for particles in the submicron and to a few micrometers and was used in the analysis of the SLN system in chapter 6.[6]

3.3.1.1. Laser Diffraction

Laser diffraction is a technique that computes particle size distributions from angular variations in intensity of scattered light; a laser beam passes through the sample and is scattered by the dispersed particles at scattering angle that is dependent on the particle size (Figure 3.2).[7] An array of detectors at different scattering angles collects scattering intensity data, which is analyzed using the Mie and Fraunhofer theories to report the particle size as the diameter of an equivalent sphere.[8] The Mie theory, also known as the Lorenz-Mie theory, relates the interaction between an electromagnetic wave plane and a particle (assuming a spherical shape), to the particle's diameter and complex refractive index (eqn 3.1. where χ is a dimensionless size parameter, m is the refractive index of the particle, d is the particle diameter and λ is the wavelength of the laser).[8,9]

$$\chi = \frac{\pi m d}{\lambda} \qquad \text{Eqn. 3.1}$$

Particles with a size larger than the incident wavelength and a refractive index that is significantly different from that of the medium will scatter most of the light in the forward direction. Smaller particles scatter the light at large angles relative to the laser beam, whereas large particles have small angular scattering intensity.[7] The Lorenz-Mie theory does not apply to large particles where the particle size is larger than 10 % of the beam wave at the beam waist. The Fraunhofer theory is a simplified version of the Mie theory and addresses the diffraction resulting from large particles.[8–10] Particles in the submicron range have a lower particle size to wavelength ratio, which reduces the scattering effects and the dependency of particle size to angular scattering intensity. This makes laser diffraction less ideal for nanoparticle analysis. Mie and Fraunhofer theories both assume a spherical particle shape which is not always the case in SLM systems. However, the finite nature of the detector system and particle rotation during measurement can smooth the intensity fluctuations caused by the surface roughness;

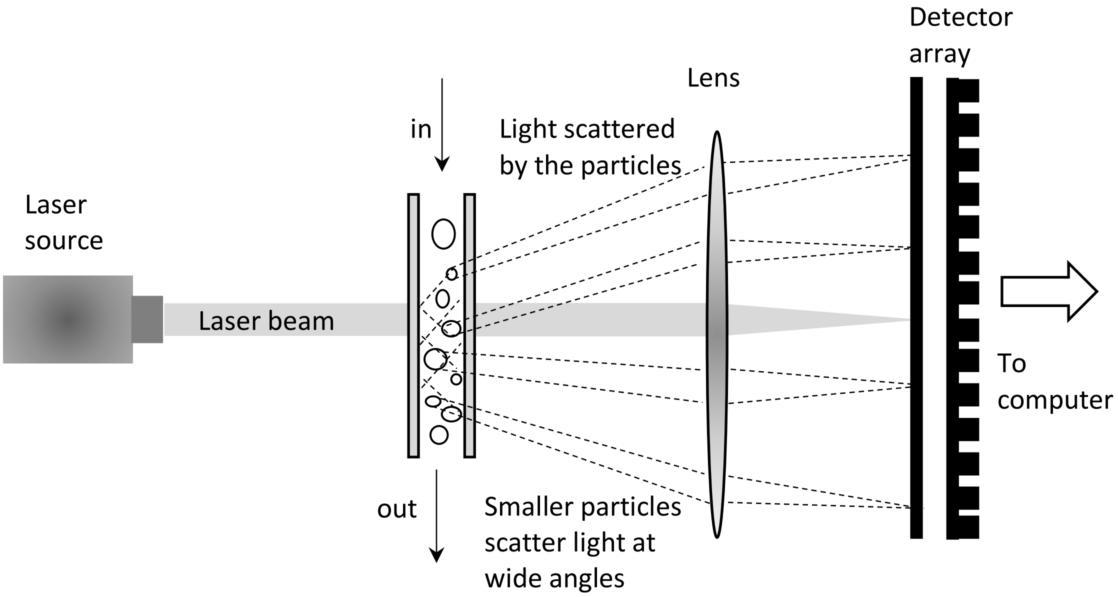

Figure 3.2. An illustration of the basic set up of a laser diffractometer. The laser beam is scattered by the sample to an extent that corresponds to the size of the particles and the scattered light is detected by an array of detectors

thus, the spherical assumption can still be applied to non-spherical system to give an estimate of particle size diameter.

3.2.1.1.1 Equipment and Methodology

Particle size analysis for the SLM systems in chapter 4 and 5 was carried out using a LS 13 320 Laser Diffraction Particle Analyser, Beckman Coulter. The SLM dispersions were added to the aqueous liquid module (ALM) filled with distilled water; enough sample was added to ensure an acceptable obscuration rate as indicated by the measuring software. The measurements were taken at room temperature. For the pH dependent particle size change studies, a Na_2CO_3/ $NHCO_3$ buffer (0.1 M and 0.3 M respectively) was also added to the liquid module to give a pH of 10.5. The pH was continuously monitored during the measurement. An ultrasonicator probe was used throughout the whole course of the experiment to prevent gas bubbles.

3.2.1.2. Dynamic Light Scattering

Dynamic light scattering, also known as quasi-elastic light scattering measures the changes in light scattering intensity as a result of the Brownian motion of particles (or molecules); the intensity fluctuations are used to calculate the velocity of the particles which can be translated to particle size using the Stokes-Einstein theory.[11–13] Brownian motion is the random movement of particles resulting from the bombardment of the particles by the molecules (or atoms) from the surrounding media. The velocity of the particles in the media is dependent on the particle size; larger particles move slower than smaller particles.[14] The Stokes-Einstein relationship (Eqn 3.2) defines the relationship between the hydrodynamic diameter (d) and the translational diffusion coefficient (D), where k is the Boltzman constant, T is the thermodynamic temperature and η is the dynamic viscosity; the velocity due to Brownian motion is defined by the translational diffusion coefficient.[12]

$$d = \frac{kT}{3\pi \eta D} \qquad \text{Eqn 3.2}$$

The light from the light source is scattered by the particle motion and is collected by either the right angle detector (90 °) or the back angle (173 °).[15] The scattering data is digitally processed in real time using a correlator, which calculates the correlation function and analyses the decay of this function to give the diffusion coefficient.[11] DLS also assumes the particles are spherical and reports the diameter of a sphere with the same translational diffusion coefficient as that of the particles.[15]

3.2.1.2.1 Equipment and Methodology

Particle size analysis for the SLN system in chapter 6 was measured by DLS using a Zetasizer μV, Malvern Instruments. The measurements were taken at a 90 ° angle and the temperature was set to 25 °C. The nanoparticle dispersions were diluted by a factor of 10 in deionised water for DLS measurements. The refractive index of the particles was set to 1.430 (the refractive index of lauric acid) and the absorption value was set to 1.00. The software inbuilt parameter value for water (the dispersant) were chosen (viscosity = 0.8872 cP and refractive index = 1.333). The sample holder was a DTS0012 disposable cuvette.

3.3.2. Morphology

Imaging techniques are important in the morphological characterisation of nanoparticle and microparticle systems and they often complement light scattering techniques in particle size analysis. Microscopy methods such as optical microscopy and electron microscopy are instrumental in the characterisation of SLN and SLM morphology. Optical microscopy was employed in the characterisation of particle size and morphology for the silicone-loaded SLM systems in chapter 4 and the dye-loaded systems in chapter 5. It was also used in the study of real time dissolution of the lipid matrix. TEM was used in the analysis of the Fc-SLN systems particle size and morphology. SEM was used in the characterisation of the dye-loaded SLM system morphology as well as the silicone-loaded SLM systems on polyester and cotton fabric surfaces.

3.2.2.1. Light Microscopy

Light microscopy utilizes the ancient discovery of bending light using a lens to give a magnified image. The general components of an optical microscope comprise of an illuminator, a set of lens, a camera (usually CCD) and an eyepiece. The sample is illuminated by a light source; the light path can be modified to improve the contrast of the resulting image. Some of the light path modification techniques used in modern microscopes include: bright field, dark field, cross polarized and phase contrast modifications.[16,17] Bright field microscopy applies no optical contrast to the light source and is effective in analysis of stained specimen or substrates that have an inherent contrast in optical properties.[18] Dark field microscopy uses a dark field condenser or a patch stop to prevent unscattered light from reaching the objective lens resulting in a dark appearance of the background with a bright appearance of the scattering sample; it is useful in the study of unstained samples.[19] Polarized light microscopy enables visualization of molecularly ordered substances; when polarized light is passed through molecularly ordered structures, changes to the refractive index (birefringence) and absorption (dichroism) properties are induced.[20] The difference between the light transmitted or reflected from the different planes of organization within the specimen is referred to as retardance, and is utilized to investigate the anisotropic properties of molecularly ordered structures.[21,22] Phase contrast illumination converts alterations in the incident light wave front induced by inhomogeneity in optical properties within the specimen into brightness contrast, thus enabling high contrast visualization of non-stained samples.[23] Generally, microscopes will have a set of interchangeable objective lenses with different magnification powers. The condenser lens focuses the light onto the sample, which then passes through the objective lens onto the eyepiece lens or camera.

3.2.2.1.1 Equipment and Methodology

The morphology of silicone-loaded SLM and dye-loaded SLM was studied using a GT Vision GXCAM microscope coupled with GX Capture software. Phase contrast and bright field microscopy together with a X40 magnification objective lens was used. The SLM dispersions were diluted in deionised water by a factor or 10 and placed in a petri dish for imaging. For the study of pH and dependent morphological changes, a Na_2CO_3/$NHCO_3$ buffer was added to the petri dish to give a pH of 10.5 and the real time morphological changes were recorded.

3.2.2.2. Scanning Electron Microscopy

Scanning Electron Microscopy (SEM) produces high magnification images by scanning a focused beam of electrons over the specimen surface. The microscope is composed of various components as shown in Figure 3.3. The electron beam is generated by the electron gun which is either thermionic or a field emission gun and is accelerated to energies of 1 KV – 30 KV by the anode.[24] Condenser lenses are put in place to de-magnify the beam such that the beam has a diameter of a few nanometres at the specimen surface.[25] The scanning coils enable the beam to be scanned across the surface of the specimen and control the position of the beam on the sample. The incident electron beam interacts with the specimen and is scattered in both an elastic and inelastic manner to give off secondary electrons, backscattered electrons, auger electrons and X-rays. The scattered light is collected by the respective detectors and reconstructed to produce an image.[24] The type of radiation emitted is dependent on the depth of penetration of the beam into the sample. Specimens for SEM must be dry and electrically conductive; non-conducting specimens result in charging of the specimen, which not only affect the image quality, but can also damage the specimen. Specimens can be made conductive by coating with a thin layer (5 – 50 nm) of carbon, gold, or gold-palladium in a process called utter coating.

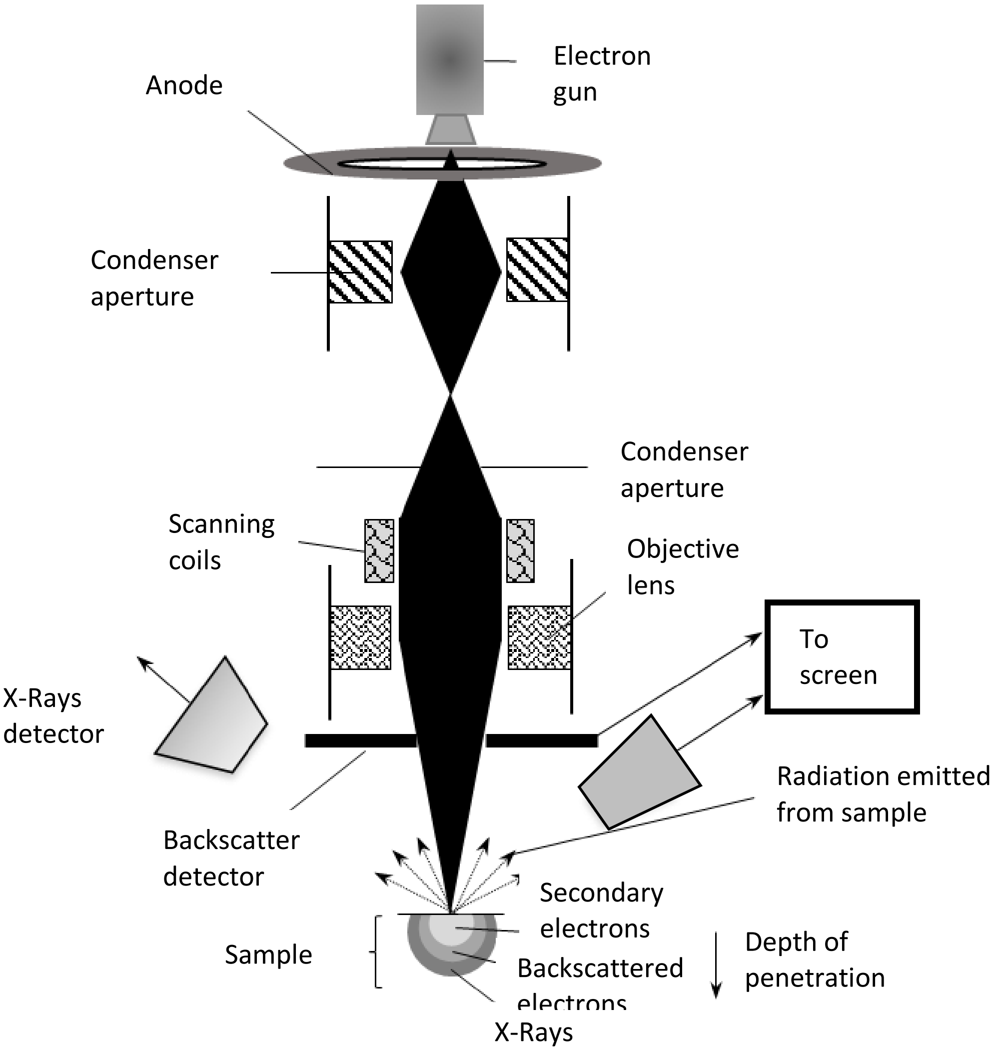

Figure 3.3. Illustrating the setup of a scanning electron microscope

3.2.2.2.1 Equipment and Methodology

SEM analysis was carried out using an SU-70 FEG SEM, Hitachi. The samples where mounted onto 12.5 mm stubs, Agar Scientific. For the silicone SLM systems, pre-washed cotton and polyester swatches (2 x 2 cm) were treated in a dilute SLM dispersion (300 ppm silicone); the dispersions were diluted with either water or Na_2CO_3/$NaHCO_3$ buffer (pH 10.5). The swatches were immersed in the dispersions at 30 °C for 30 minutes while stirring and subsequently dried on a rack at room temperature overnight. The dried samples where cut into smaller pieces and mounted onto aluminium stubs. For the analysis of dye-loaded SLM systems, the dispersion was directly deposited onto the aluminium stub and left to dry overnight. The mounted samples were coated with a 50 nm layer of gold-palladium using a Cressington sputter coater. The accelerating voltage was set to 10 kV, which is high enough to obtain good resolution images without charging the specimen.

3.2.2.4. Transmission Electron Microscopy

TEM is a technique that utilizes transmission of the electron beam through the specimen to project an image onto a screen. TEM uses the same principle as light microscopy but unlike light microscopy, TEM has a much higher depth of field and resolution and is capable of reaching magnifications of magnitude 1 x 10^6.[26] Similar to SEM, TEM equipment comprises an electron gun that emits electrons from a cathode (Figure 3.4). The electron beam is accelerated by an anode into the vacuum chamber, where electromagnetic coils (condenser lenses) concentrate the electrons into a more powerful beam and enable the control of beam position.[27] The electron beam, passing through the sample, interacts with the sample and are either absorbed, transmitted or back-scattered. Transmission occurs when the electron beam passes through the sample and retains all of their energy (elastic scattering) or some of it (inelastic scattering) as the electrons continue down the column. The regions of the specimen that are not electron transparent will absorb all the energy from the electron beam and terminate their path; the absorbing regions will appear as dark spots in conventional TEM images.[28] The transmitted beam is passed through the objective lens, which forms an inverted initial image which is magnified by the intermediate lens and further magnified by the projector lenses before projection onto a screen.[29] The intermediate lens and projector lens system both enable control of the magnification of the image by controlling the power of the lens.[28]

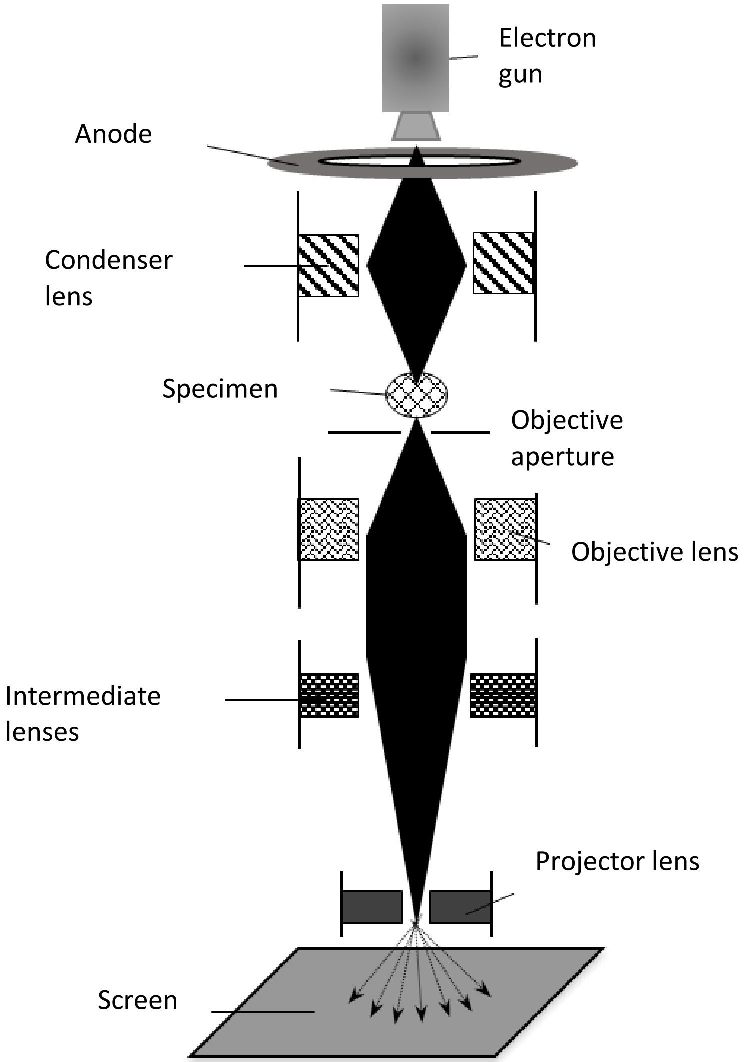

Figure 3.4. Illustrating the basic setup of a transmission electron microscope

3.2.2.4.1 Equipment and Methodology

Due to the low melting temperature of the lauric acid matrix, TEM analysis of the Fc-SLN was carried out at -50 °C (cryo-TEM) using a 2100F FEG TEM, JEOL. The SLN dispersion was diluted by a factor of 10 in deionised water. The dilute dispersion was deposited onto a holey carbon grid (Agar Scientific) using a dropper pipette and allowed to dry in air before insertion into the imaging column. An accelerating voltage of 200 kV was used.

3.3.3. Chemical Analysis

Chemical analysis of the SLN and SLM systems was used to investigate the composition and the chemical interactions between the lauric acid matrix and the actives. Chemical analysis of solid lipid matrix systems is an important characterisation as it can determine the model of incorporation and consequently, the mechanism of release. Additionally, it can be important in the investigation of concentration of actives incorporated into the matrix.

3.2.3.1. Fourier Transform Infra-Red

Infrared spectroscopy (IR) is a vibrational spectroscopy technique that utilizes the unique electromagnetic absorption and emission properties of interatomic bonds to produce a spectrum (fingerprint) which can be correlated to the compound in question. At temperatures above the absolute zero, all bonded atoms have molecular vibrations.[30] Covalent bonds can vibrate and rotate in several modes depending on the degree of freedom and number of atoms in the molecule. Molecular vibrations are characterised by a change in bond length (stretching) and bond angle (bending) and can be in-phase (symmetrical) or out of phase (asymmetric) (Figure 3.5). The frequency of vibration is dependent on the mass of the atoms and force constant, which is dependent on the strength of the bond.[31,32] For a diatomic molecules, the vibrational frequency is defined by Hooke's law as shown in Eqn 3.3 where k is the force constant and μ is the reduced mass.[31,32]

$$f = \frac{1}{2\pi}\sqrt{\frac{k}{\mu}} \qquad \text{Eqn 3.3}$$

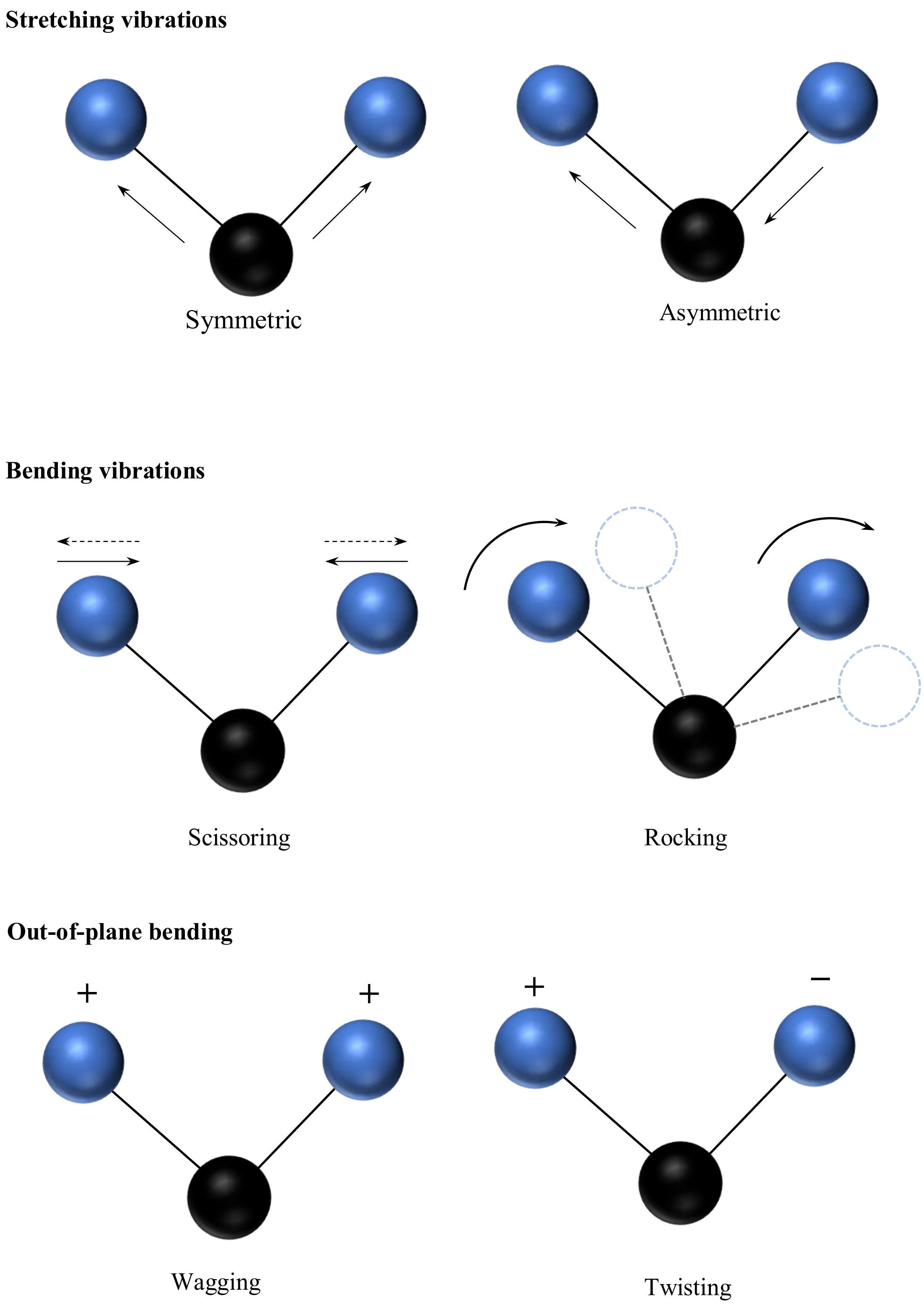

Figure 3.5. Schematic illustration of the different types of molecular vibrations

The components of an FTIR equipment comprise of a source, interferometer, sample holder and a digital processing system (Figure 3.6). The source is an element that emits electromagnetic radiation in the infra-red region when electricity is passed through it; the resistance of the element to electricity causes it to heat up and release infrared radiation.[33] Silicon carbide is commonly used as an element in IR sources; other suitable elements include ceramic, tungsten and carbon rods.[34,35] The interferometer also known as the Michelson interferometer consists of a beam splitter and two mirrors; one is a fixed mirror and the other is a movable mirror.[36] The beam splitter splits the radiation beam into two equal parts and one is directed to the stationary mirror and the other to a moving mirror; the two beams are recombined, passed through the sample and refocused onto the detector. The detector measures the intensity as a function of optical path difference (retardation).[33,37,38] An interferogram is formed by recording the intensity response at different values of retardation; the intensity of the detected signal is dependent on the optical path length and wavenumber.[37,39] Molecular

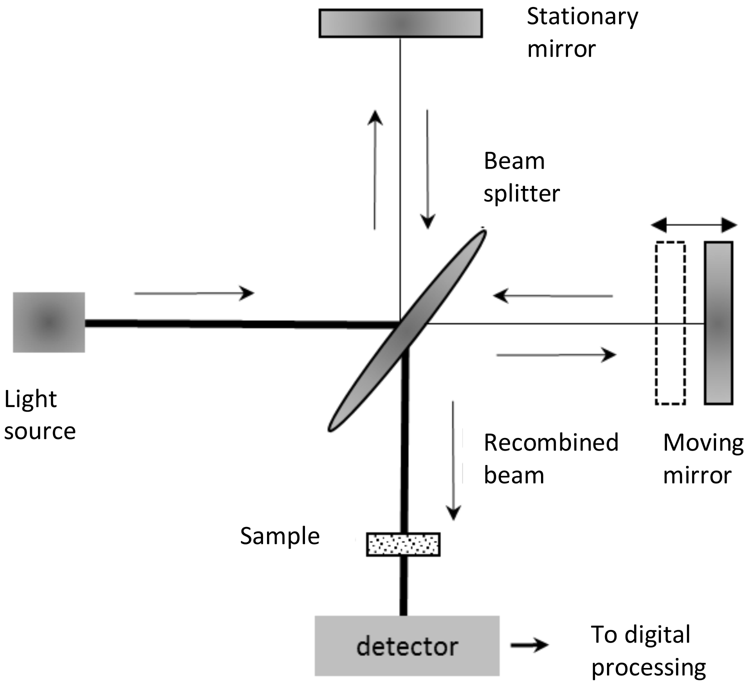

Figure 3.6. Schematic representation of the basic the setup of a Michelson interferometer set up for infrared spectroscopy

vibrations that induce a change in the net dipole moment can absorb infrared radiation and are referred to as *IR active* vibrations. A sample will absorb all the radiation with frequencies that resonate with the molecular vibration frequencies within the sample.[39,40] FTIR is mostly carried out in the mid-infrared region with wavenumbers from 4000 – 400 cm^{-1}. The interferogram generated from a beam that passes through the sample contains all the information about the energy absorbed at different frequencies. The interferogram is digitised using an analogue-to-digital converter and subsequently transformed from a time-domain signal to a frequency domain spectrum by applying a Fourier transform.[33] Combining FTIR with Attenuated Total Reflection (ATR) enables analysis of particles in the solid and liquid phase with only minimal or no prior sample preparation. In ATR, the infrared beam is passed through a crystal (reflecting surface) at an angle greater than critical angle for internal reflection so that it is reflected at least once resulting in an evanescent wave.[41] The reflecting surface (crystal) is made up of infra-red transparent materials such as thallium bromoiodide and has direct contact with the sample.[42] The evanescent wave penetrates the sample to a depth of 0.5 to 2 μm; the changes to the evanescent wave as a result of interaction with the sample is measured by the detector and processed to give a spectrum by applying the Fourier transform.[41,43]

3.2.3.1.1 Equipment and Methodology

A Spectrum 100 (PerkinElmer) ATR-FTIR was used in all investigations. The crystal surface was cleaned thoroughly with acetone and a background scan was taken; this process was applied at the start and repeated after every sample. The sample (dried SLM and SLN systems) was placed on the ATR crystal and secured using a force gauge at 140 Nm. The scan was applied at a resolution of 16 cm^{-1} and measurements were taken in transmission mode.

3.2.3.2. Solid State NMR

Nuclear Magnetic Resonance (NMR) spectroscopy is a powerful and non-destructive method for discerning the physicochemical structure of compounds by analyzing the behavior of the nuclear spin (I) of naturally abundant nuclei in the presence of an external magnetic field (B_o).[44] Some examples of naturally abundant nuclei used in NMR include: ^{1}H, ^{13}C, ^{15}N, ^{19}F and ^{29}Si. Nuclear spin is a fundamental property of atomic nuclei pertaining to angular momentum and is determined by the composition of subatomic particles composing the nuclei;[45] protons and neutrons both have a spin (I=1/2) and net charge of +1e and 0 respectively. Nuclei with an even mass number and even charge number will have no nuclear spin, nuclei with an odd mass number have half integer spin values (I = n/2 where n=1,3,5,7…) and nuclei with an even mass number but an odd charge number will have an integer spin (I = n where n =1,2,3,4…).[46] Nuclei with non-zero spin have a magnetic moment (μ) which is proportional to the spin; the magnetic moment is generated by the rotation of the charged nuclei along the axis of the spin.[46] A magnetic moment in an external magnetic field experiences a torque, which induces a perpendicular change in angular momentum and results in a phenomenon called the Larmor precession, where the magnetic moment 'precesses' around the axis of the magnetic field.[47] According to quantum theory, a non-zero spin nuclei can adopt one of 2I + 1 energy levels when placed in a uniform magnetic field, B_o; for instance, 1H has a spin I=1/2 hence can adopt 2 orientations (Figure 3.7).[44] If a radiofrequency (rf) wave with sufficient energy is applied to non-zero spin nuclei in a constant B_o magnetic field, a transition to a higher or lower energy level is induced resulting in the absorption or emission of energy.[46] The energy of the wave should match the energy difference between the transition levels according to the relationship

$$\underbrace{hv_o}_{\text{energy of an}} = \underbrace{\frac{\mu B_o}{I}}_{\substack{\text{energy difference between}\\ \text{transition levels}}} \qquad \text{Eqn 3.4}$$

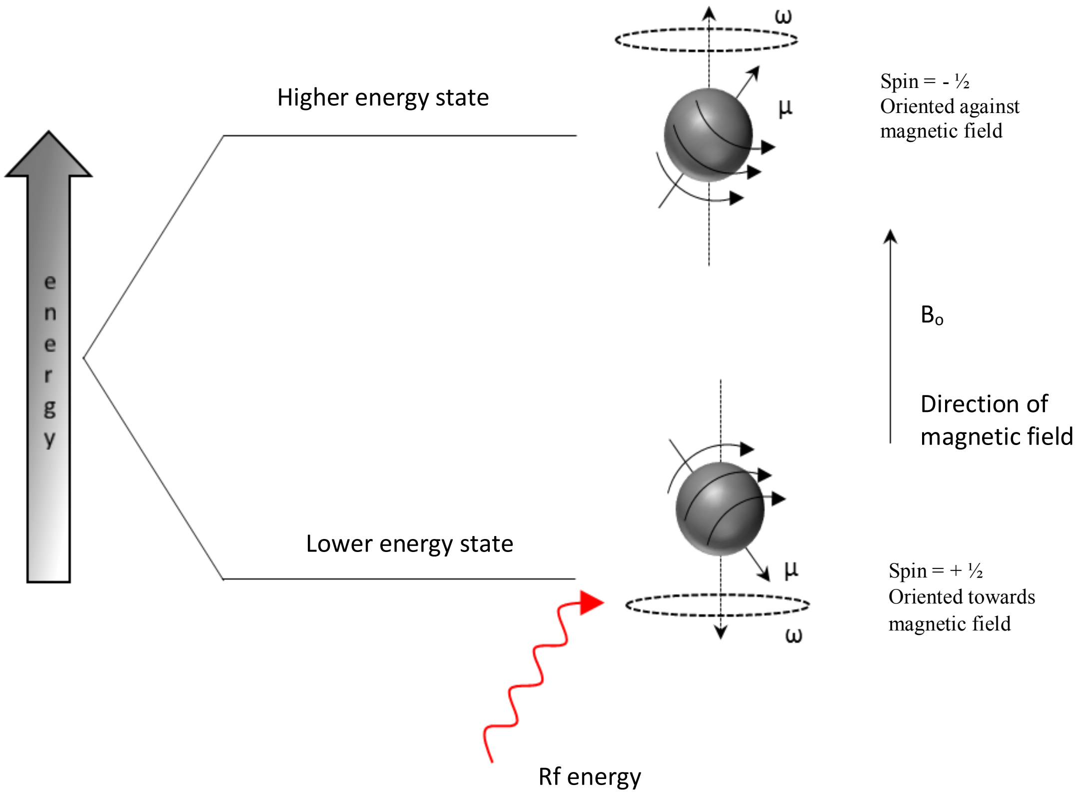

Figure 3.7. An Illustration of the spin states of a nucleus spin (I=1/2)

where v_o is the frequency of the rf wave and h is Plank's constant.[47] The population of nuclei adopting the high energy and low energy states is distributed according to Boltzmann distribution such that there is more nuclei on the lower energy level than that on the higher energy level.[46] This results in a net absorption of energy from which an NMR absorption spectra can be obtained. Isolated nuclei in a magnetic field, B_o will *feel* all the force of the magnetic field. However, the total magnetic field experienced by the nuclei is also dependent on the local electronic environment as well as the presence of other nuclei, which is the case in molecules and compounds.[48] Consequently, the magnetic field experienced by the nuclei is always less than that exacted by the external field; this is known as the shielding effect. Shielding causes differences in the Larmor precession frequency (ω_{larmor}) of identical nuclei in different molecular environments and the variations are reflected in NMR spectra as a chemical shift.[48] The chemical shift is measured against a known standard trimethylsilane (TMS) is an accepted standard for ^{1}H, ^{13}C and ^{29}Si.[49] Solid state NMR is an indispensable tool in the investigation of chemical structures, interactions as well as macromolecular properties such as polymorphism.

3.2.3.2.1 Equipment and Methodology

All NMR measurements were carried out on dried solid lipid matrix systems using the EPSRC National Solid-State NMR service at Durham University. A Varian VNMRS spectrometer with a 9.4 T magnet operating at 79.44 MHz for ^{29}Si and 100.56 MHz for ^{13}C was used in all investigations. For silicone-loaded SLM systems, a direct-excitation ^{29}Si spectrum was recorded at ambient temperature using with an rf pulse duration of 6.4 μs and the measurement duration was set to 101 μs with at least 20 repeats for each measurement. Neat tetramethylsilane was used as a standard in both ^{29}Si and ^{13}C.

3.2.3.4. Thermogravimetric Analysis

Thermogravimetric Analysis (TGA), is a destructive analytic technique that utilises the temperature dependent weight changes in materials to give information on the composition and chemical interactions in substrates. The specimen is heated at a constant, user-defined rate or maintained at the same temperature and the weight change is monitored continuously using a microbalance. Weight loss in chemical substrates can result from thermal decomposition, evaporation of volatile constituents or water when carried out in an inert environment. In the presence of oxygen, oxidation of metallic substrates and oxidative decomposition of organic substrates can occur.[50] Weight gain can result from the uptake or chemical reactions with substances from the atmosphere. TGA reports the percentage weight change as a function of temperature or time to give a TGA curve. TGA data can be presented as a first derivative of the TGA curve to give a differential thermogravimetric (DTG) curve, which gives the rate of weight change with time or temperature and also enhances the visual appearance of the temperatures at which the chemical events occur.

3.2.3.4.1. Equipment and Methodology

The TGA measurements were carried out using a Perkin Elmer Pyris I under nitrogen gas at a rate of 0.5 ml/s. The weight loss was recorded for samples (approx. 5 mg) heated in an aluminium oxide crucible at a rate of 10˚C/min. Quantitative information on the loading capacity was obtained by exploiting the differences in the onset temperatures for chemical events between excipients of the SLM. The silicones used in this investigation have a higher thermal stability compared to the lipid matrix and exhibit negligible mass loss at temperatures up to 250˚C.

3.3.4. Crystallinity and Melting Behavior

The crystalline arrangement within solid lipid matrices is of interest due to the impact it has on the stability of the particles, retention of actives, encapsulation efficiency and the model of incorporation and release. The combination of X-Ray diffraction techniques and differential scanning calorimetry has proven useful in the characterisation of structural arrangement of solid lipid matrix systems.

3.2.4.1. Differential Scanning Calorimetry

Differential Scanning Calorimetry (DSC) is an analytical method that measures the heat exchange between the substrate and the surrounding environment to obtain information on the temperature dependent reactions and transitions. Physical events in chemical substrates (e.g. phase transitions and polymorphic transitions) are associated with a flow of energy into the sample (endothermic) or out of the sample (exothermic).[51] The heat flux to the sample is measured relative to an inert reference either by the power compensated or heat-flux mechanism.[52] In power compensated DSC, the temperature of the sample is adjusted to compensate for the temperature differences between the sample and the reference.[53] Heat-flux DSC uses the temperature difference between the sample and the reference (ΔT) to calculate the heat flow to the sample (q) using the following relationship

$$q = \frac{\Delta T}{R} \qquad \text{Eqn 3.5}$$

where R is the resistance of the thermoelectric disc.[54] Parameters such as melting temperature (T_m), glass transition temperature (T_g) and recrystallisation can be obtained from the DSC curve.[51] Enthalpy of fusion (ΔH) can be calculated as the integral area under the melting peak and is used to calculate the crystallinity of solid lipid matrices as a percentage of the bulk lipid.[55] DSC thermograms can also be used to investigate the interactions between the lipid and other excipients in solid matrix systems.[56]

3.2.4.1.1. Equipment and Methodology

A Q1000 DSC (TA) was used for the DSC measurements. The dried samples (~5 mg) were heated at a rate of 10°C/min from room temperature to 100°C followed by a cooling cycle and a subsequent heating cycle. TA Universal Analysis software was used in the analysis of DSC data.

3.2.4.2. X-Ray Scattering

X-Ray scattering methods are indispensable in the investigation of structural information of crystalline compounds. X-Rays behave in a similar way to visible light but have shorter wavelengths in the order of 1 Å, hence can be used to probe structural information at an atomic and interatomic level.[57] Crystalline materials are characterised by a highly ordered lattice or repeating patterns, which can be described as planes with fixed interplanar distances (Figure 3.8). Similar to visible light, X-Rays experience a form of scattering (diffraction) when they

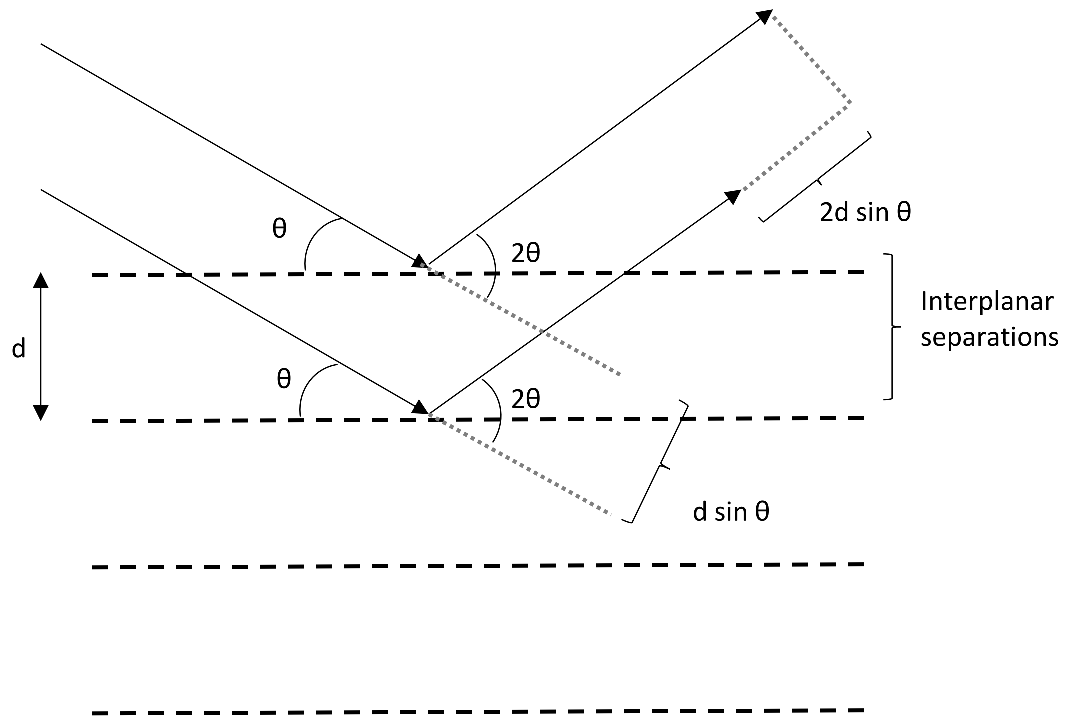

Figure 3.8. An illustration of the diffraction of X-rays in by different planes in ordered structures

encounter an obstacle or an aperture of a similar order of magnitude to their wavelength. X-rays in crystallography equipment are generated by a cathode ray tube; they are polarized and passed through a collimator to focus the beam before they are directed towards the specimen at a specified angle.[58] In Wide Angle X-Ray Diffraction (WAXS) the beam coincides with the sample at a wide angle. WAXS can be used to determine the crystal cell block parameters and hence the polymorphic form.[59] In small angle x-ray scattering (SAXS), the angle of incidence is in the range 0.1 – 10 °, which enables the characterisation of macromolecular structures with scattering vectors (q) in the range of 0.1 – 10 nm^{-1}.[60] Electron clouds surrounding atoms in the specimen serve as 'obstacles' resulting in the diffraction of the x-ray beam at an angle, Θ, where each repeating plane is a diffracting interface. The beams diffracted by different planes have different path lengths and can coincide to give an interference pattern. When waves coincide out of phase (destructive interference) no signal is produced and when they coincide in phase (constructive interference) they produce a signal that can be recorded by the detector.

SAXS measurements report variations in peak intensity, which is the wave amplitude of the interfered waves as a function of the scattering vector (q) where q is defined as

$$q = \frac{4\pi}{\lambda}\sin\frac{\theta}{2} \qquad \text{Eqn 3.6}$$

and λ is the wavelength of the beam and Θ is the angle of incidence (Figure 3.8).[61] The peak positions can be related to interplanar separation distances (d) using Bragg's Law,

$$n\lambda = 2d\sin\frac{\theta}{2} \qquad \text{Eqn 3.7}$$

where Θ is the angle of incidence, n is an integer and λ is the wavelength of the beam[61] such that

$$d = \frac{2\pi n}{q} \qquad \text{Eqn 3.8}$$

3.2.4.2.1. Equipment and Methodology

The SAXS measurements were carried out on SLM and SLN dispersions using a Bruker Nanostar with an X-ray source operating at 40 kV and 35 mA at 3600 frames per acquisition. X-ray diffraction was measured using a Hi-star 2D detector held at either 66 cm or 1 m from the sample. Both the sample and detector were placed under vacuum. The detector measures the radiation at each angle and produces the final SAXS diffraction spectrum.

3.3.5. Loading Capacity and Entrapment Efficiency

The loading capacity (LC) is a quantified measure of the capacity of the lipid matrix to hold actives. It is defined as the percentage ratio of the incorporated drug to the lipid; it is essentially the percentage concentration of the actives in the matrix. The entrapment efficiency (EE) is the percentage ratio of the amount of the active incorporated to the amount of active added during preparation.

$$\mathrm{LC} = \frac{\text{amount of encapsulated active}}{\text{amount of active + lipid}} \times 100\% \qquad \text{Eqn 3.9}$$

$$\mathrm{EE} = \frac{\text{amount of encapsulated active}}{\text{amount of active added}} \times 100\% \qquad \text{Eqn 3.10}$$

In order to calculate EE and LC values, it is essential to measure the concentration of the actives loaded into the matrix. Quantification of high molecular weight silicones is not straight forward as most analytical methods are not sensitive enough or applicable to silicones. Quantification of silicones was carried out using ^{29}Si NMR and TGA as detailed in chapter 4. Ferrocene and dye concentration measurements were carried out using UV/VIS spectroscopy.

3.2.5.2. UV/VIS Spectroscopy

UV/VIS spectroscopy is a useful technique in the qualitative and quantitative determination of analytes that absorb radiation in the ultraviolet and visible region (190 – 780 nm).[62] Absorption of light in the UV/VIS region results from electronic transitions within the analyte molecules; electrons in the ground state are promoted to higher energy levels by absorbing radiation possessing energy that is equivalent to the energy difference between the two levels. The amount of light absorbed is related to the concentration of the analyte by the Bouguer-Lambert-Beer law

$$A = log_{10}\left(\frac{I_o}{I}\right) = \mathcal{E}\, l\, c \qquad \text{Eqn 3.11}$$

where A is the absorbed light, I_o is the intensity of incident light, I is the intensity of transmitted light, $\mathcal{E}$ is the absorption coefficient, l is the path length of the sample and c is the concentration of the analyte.[63]

3.2.5.2.1. Equipment and Methodology

Measurements were taken using a HR2000 CG UV-NIR, Ocean Optics coupled with a DH2000 UV-VIS-NIR, Mikropack light source. UV grade disposable PMMA cuvettes (Kartel) were used in the investigation. Calibration curves were constructed for the dye and ferrocene systems in water and ethanol, respectively. For the dye-loaded SLM dispersions, the concentration of unloaded dye was measured by dilution the supernatant; 100 μL of the supernatant was added to deionised water to make a 2 ml solution. For the ferrocene-loaded systems, the concentration of ferrocene in the matrix was measured by dissolving 0.05 g of Fc-SLN in 2 ml of ethanol. The measurements were taken as an average of 10 scans at an integration time of 3 ms and averaged over 6 repeat measurements.

3.4 Electrochemical Characterisation of Lipid Membranes

Electrochemical methods were employed to ensure the successful immobilization and integrity of the lipid membranes and to study the effect of the Fc-SLN on the electrochemical properties of supported SAM and BLM systems. Differential pulse voltammetry (DPV), cyclic voltammetry (CV) and electrochemical impedance spectroscopy were employed for this study.

3.4.1. Electroanalytical Methods

Electroanalysis pertains to the employment of electrochemistry as an analytical tool. Electrochemistry is a field dating back to the early 19th century, pioneered by Michael Faraday; it is the study of chemical processes associated with charge transfer.[64,65] Charge transfer is the exchange of charge (e.g. electrons or ions) at an interface (e.g. liquid-liquid interface or solid-liquid interface) in a process called reduction-oxidation reaction or *redox* reaction in short. When two surfaces are brought in contact, a potential is established due to excess free charges and charge transfer can occur between the interfaces either spontaneously (as in galvanic cells) or as a result of an external electrical force (as in electrolytic cells).[66] Electrochemical techniques can be classified into two main groups: potentiometry and voltammetry. In potentiometry, the potential of the electrochemical cell is measured at a fixed current (usually 0 A); the potential is correlated to the concentration of the analyte in the cell.[67] Voltammetry techniques report the concentration dependant current response of electrochemical cells as a response to the application of an external potential. The dependence of the peak current (I_p) on the concentration of the electroactive species is governed by the Randles-Sevcik equation

$$I_p = 0.4463\, nFCA\left(\frac{nFvD}{RT}\right)^{1/2} \qquad \text{Eqn 3.12}$$

where n is the number of electrons involved in the redox reaction, F is the Faraday's constant

(9.6485 x 10^4 C mol^{-1}), C is the bulk concentration (mol/dm^3), A is the electrode surface area (cm^{-2}), v is the scan rate (V/s), D is the diffusion coefficient (cm^2/s), R is the universal gas constant (8.314 J/mol K), T is the temperature (K).[68] This expression can be simplified if the solution is at 298 K to

$$I_p = 2.69\ x\ 10^5(n^{3/2}v^{1/2}D^{1/2}AC \qquad \text{Eqn 3.13}$$

The standard electrochemical cell for voltammetry comprises a three electrode system: a working electrode, a reference electrode and a counter electrode. The working electrode, usually made of carbon, mercury and inert metals such as gold and platinum, is where the electrode reactions take place. The reference electrode is a stable electrode with a defined electrode potential such as the standard hydrogen electrode (SHE = 0.0V) and saturated calomel electrode (SCE = 0.242 V).[67] Metal wires such Ag, Pt and Ag/AgCl can also be used as reference electrodes; this class of reference electrodes is known as pseudo-reference electrodes.[69] In a three electrode system, the external potential is applied between the working electrode and the reference electrode. A counter electrode, usually a metal foil or coil, has a comparatively large surface area so as to provide a low resistance path for current flow; this prevents current flow between the reference and the working electrode to maintain a stable system.[70] Two electrode systems (working + reference) and four electrode systems (2 working + reference + counter) can also be used in voltammetry studies. Voltammetry methods can be further classified into potential sweep and pulse methods. Potential sweep methods refers to techniques where a linear potential waveform is applied, e.g. linear sweep voltammetry and cyclic voltammetry. In pulse voltammetry, a pulse or staircase waveform is applied in order to minimise the non-faradic current contribution and so enhance the charge-transfer current response.[71] Non-faradic processes such as adsorption and desorption processes can alter potential and solution composition at the solid-liquid interface. When a potential is applied to the electrode, the surface can become polarised leading to the migration of ions by attractive or repulsive forces, changing the potential and the composition of the interface; this phenomena is referred to as the *electrical double layer*.[66] The electrical double layer can be described using the Gouy-Chapman model or more comprehensively using the Helmholtz model. The suggested structure of the solid-liquid interface comprises an inner Helmholtz plane or Stern layer (solvent layer and specifically adsorbed ions), an outer Helmholtz plane (non-specifically

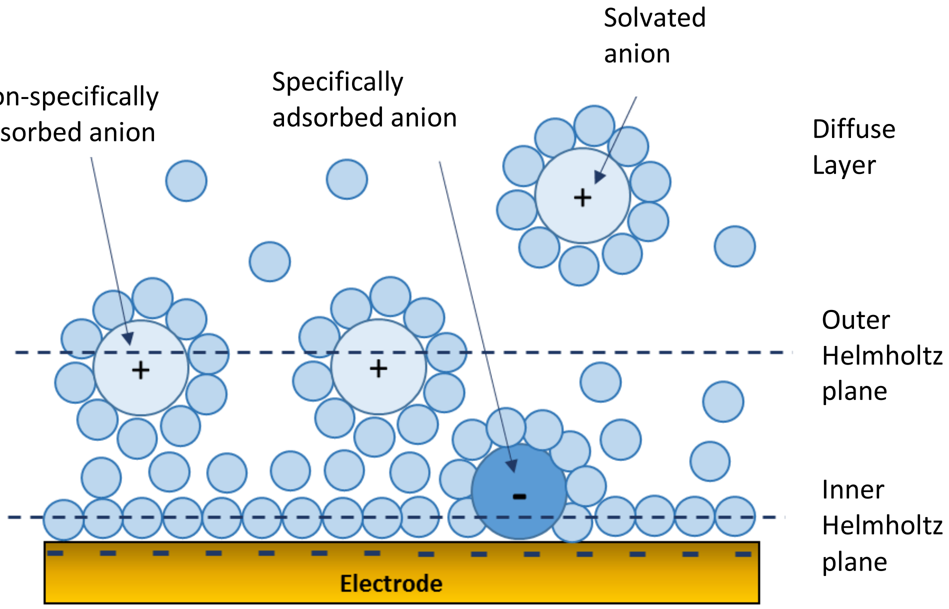

Figure 3.9. An Illustration of the proposed structure of the electrode-electrolyte surface (not to scale)

adsorbed ions and solvated ions), a diffuse layer which is a boundary to the bulk electrolyte solution (Figure 3.9).[66,71]

The separation of charges at the electrode-electrolyte interface imparts capacitive behaviour to the double layer and results in the flow of a non-faradic current called a charging current or capacitive current.[70] The capacitance of the electrical double layer (C) is related to the charge stored up by the interface (q) and the potential across the interface (E) according to the following relationship

$$C = \frac{q}{E} \qquad \text{Eqn 3.14}$$

Cyclic voltammetry, in combination with electrochemical impedance spectroscopy, is powerful for the study of solid-liquid interfacial properties, both faradic and non-faradic. Pulse voltammetry methods such as DPV enable the study of interfacial faradic processes with high sensitivities by minimising the non-faradic current response.

3.4.1.1. Differential Pulse Voltammetry

DPV is a potential step method where the potential waveform applied is in the form of pulses superimposed on a staircase (Figure 3.10); typically the pulse height is ~50 mV and the step height of the stair case is ~10 mV.[71] The change in current ΔI is reported as a function of the magnitude of the potential applied; $\Delta I = I_2 - I_1$ where I_1 and I_2 is the current response before and after the pulse is applied. This minimises the current response resulting from non-faradic electrode process (mostly capacitive) due to the short duration of the pulse and thus enhances sensitivity to electroactive species at low concentrations to the order of 10^{-7} M.[71,72]

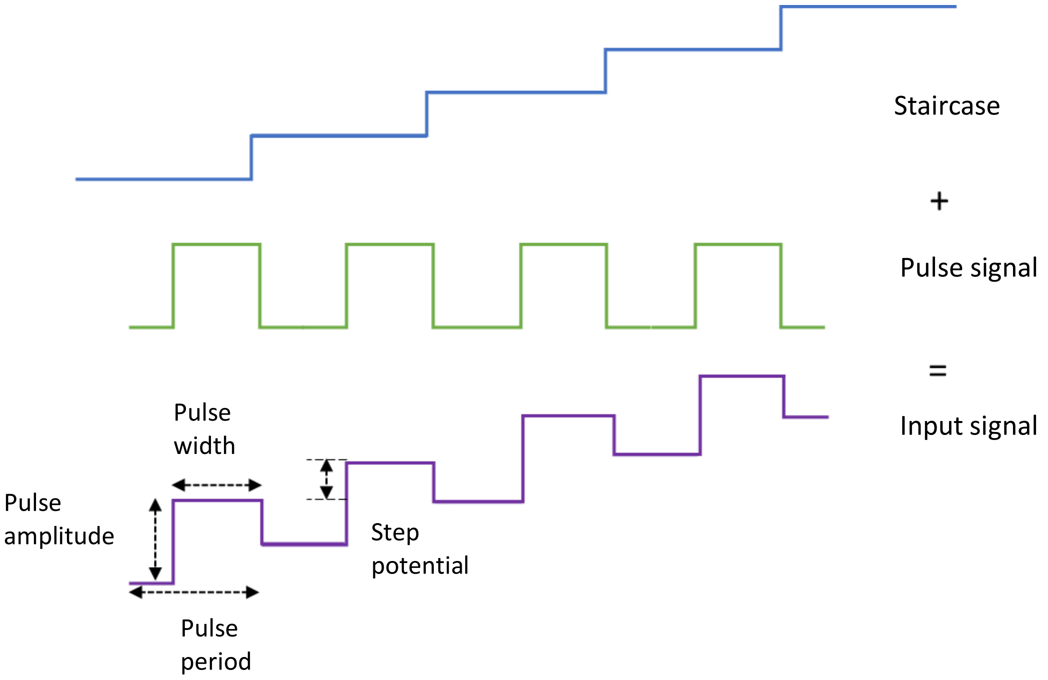

Figure 3.10. The potential signal waveform for DPV obtained by the superimposition of a pulse signal onto a staircase

3.4.1.2. Cyclic Voltammetry

Cyclic voltammetry is a fast and simple amperometric technique that measures the faradic current as a function of working electrode potential to give both qualitative and quantitative information about the electrochemical processes in the system.[73] It is almost always the first port of call for investigations of electrode processes in electrochemical cells. Potential is applied to the form of a triangular waveform; the potential applied to the working electrode is linearly increased from the lower vertex (E_1) to the upper vertex (E_2) or vice versa and is linearly scanned back to the initial value (Figure 3.11). The rate of potential sweeping, scan rate, is a defined parameter in voltammetry measurements. The current response to the potential sweep due to faradic and charge transfer processes is recorded and presented as a function of potential. A current peak is observed for the forward scan and reverse scan as the potential reaches the redox potential for the species involved for a reversible system. The shape of the

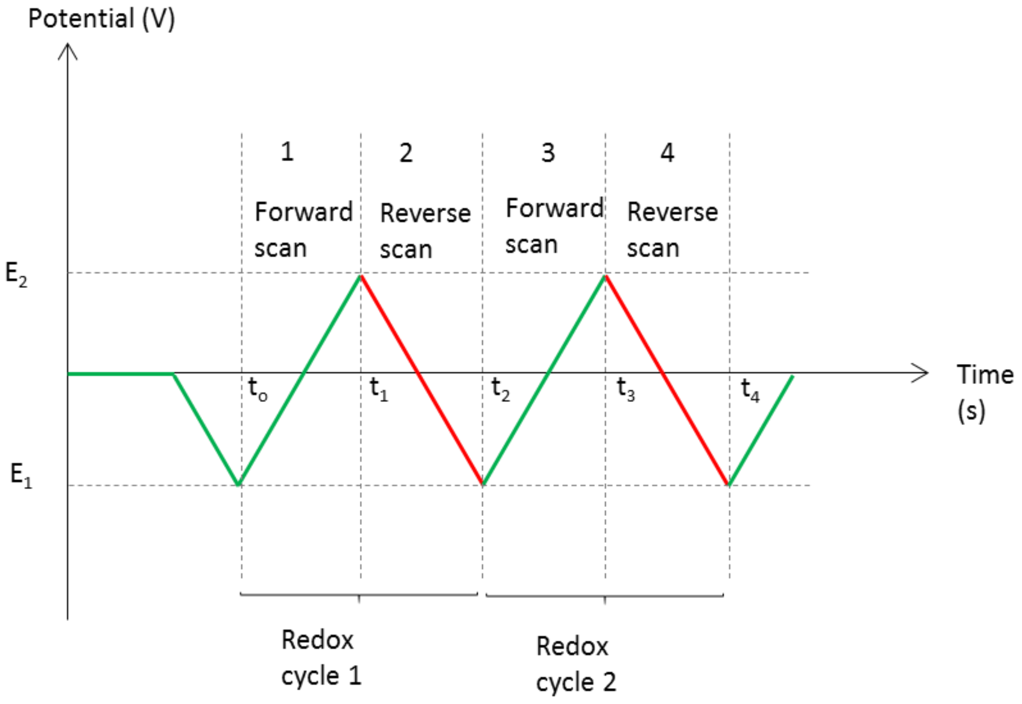

Figure 3.11. The potential signal waveform for cyclic voltammetry for two oxidation-reduction cycles each with a forward scan from the lower vertex (E_1) to the upper vertex (E_2) forward and vice versa for the reverse scans

CV curve is dependent on the geometry of the electrode as this affects the shape of the diffusion layer. Cyclic voltammetry is used in the characterisation of lipid membranes and to study the charge inhibition and capacitive characteristics of lipid membranes on electrode surfaces.

3.4.1.3. Electrochemical Impedance Spectroscopy

Electrochemical Impedance Spectroscopy (EIS) is an indispensable tool in the study of electrode process and interfacial properties of modified electrodes. The basis of EIS is hinged on the concept of resistance in electrical systems as defined by Ohm's law. Impedance can be defined as a complex resistance that can be used to describe the hindrance to current flow under applied voltage in non-ideal resistors, e.g. capacitors and transistors.[74] In EIS, the current response to a small AC potential signal at a range of frequencies, usually within the range of ($0.1 - 10^6$ Hz). Only a small perturbation in potential (1 – 10 mV) is applied so as to achieve a pseudo-linear response to which Ohm's law can be applied.[75] The excitation signal can be expressed as a function of time as

$$E(t) = E_o \sin(\omega t) \qquad \text{Eqn. 3.15}$$

E is the time dependent potential, E_o is the magnitude of the excitation signal, ω is the radial frequency which is equal to 2πf and t is time, the current would be

$$I(t) = I_o \sin(\omega t + \phi) \qquad \text{Eqn 3.16}$$

where ϕ is the phase shift between the potential signal and the response.[75] Applying Ohm's law, the impedance of the system can be calculated as follows

$$Z(t) = \frac{E(t)}{I(t)} = \frac{E_o \sin(\omega t)}{I_o \sin(\omega t+\phi)} = Z_0 \frac{\sin(\omega t)}{\sin(\omega t+\phi)} \qquad \text{Eqn 3.17}$$

therefore the impedance can be expressed as a magnitude (Z_o) and a phase (ϕ) which can be expressed as a complex number using Euler's principle[75]

$$Z(\omega) = Z_o \exp\ (j\phi) = Z_o(\sin\phi + jsin\ \phi) \qquad \text{Eqn 3.18}$$

Expressing impedance as a complex number enables presentation of data as an impedance vector on a Nyquist plot. Impedance data can also be presented in the form of Bode plots which provide information on the specific frequency values at different points or as a Lissajous figure.[76] Impedance analysis for electrochemical systems is carried out by fitting data onto an equivalent electrical circuit, where electrical components such as resistors, capacitors and inductors are utilised to describe the components of the electrochemical cell. Examples of this include electrolyte resistance, which is modelled as a resistor in series, resistance to charge transfer, which is also modelled as a resistor and the electrical double layer which is modelled as a capacitor.[74] In order to account for the non-ideal capacitor behaviour of electrochemical systems, a constant phase element (CPE) is utilised.[75] CPE elements are expressed in terms of capacitance and a coefficient (α= 0.9 to 1.0), where a perfect capacitor is α= 1.0.[77] Important parameters for equivalent circuit model fitting can be obtained from Nyquist and Bode plots Figure 3.12. The solution resistance value (R_S) is the magnitude of real component of impedance at the point where the plot coincides with the Z' axis; this is also the impedance

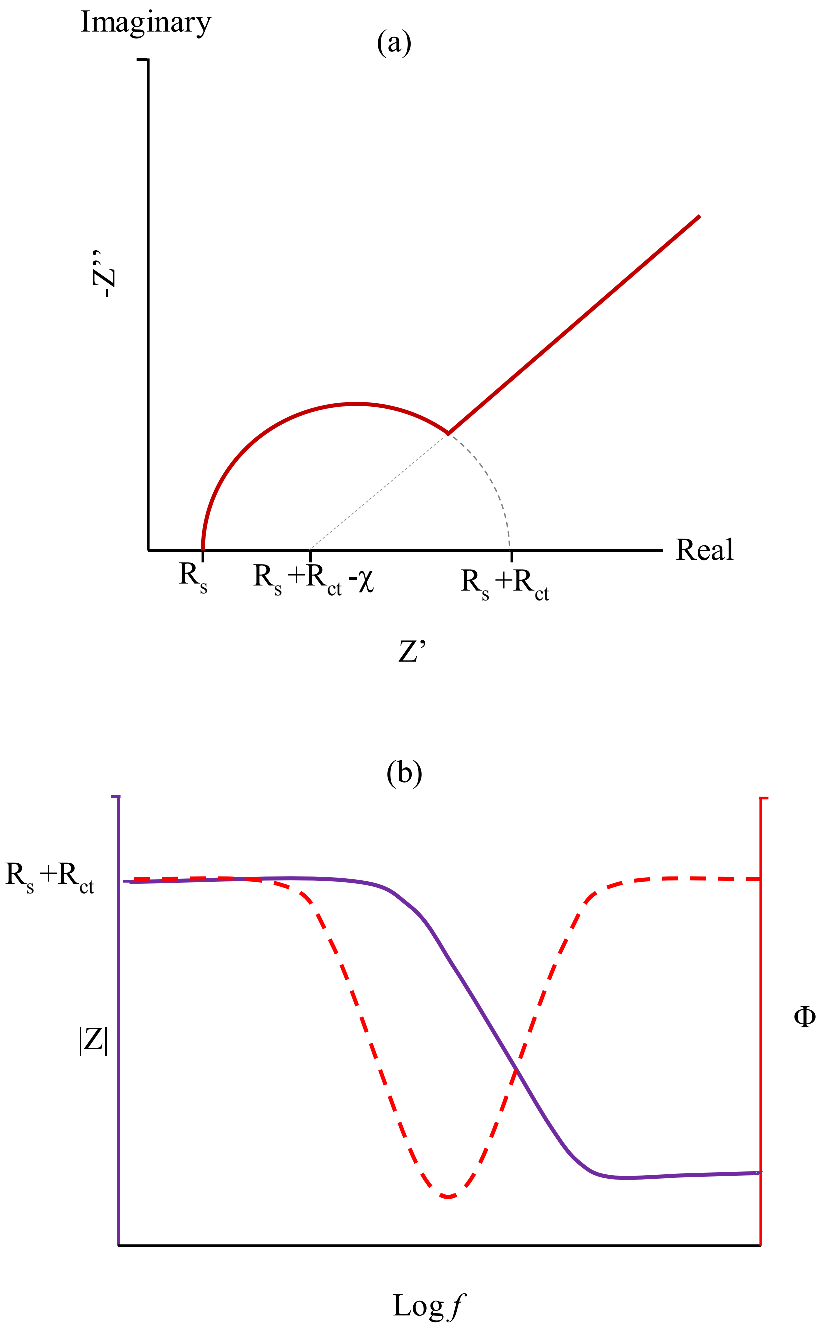

Figure 3.12. Electrochemical impedance spectroscopy data presented in the form of (a) a Nyquist plot and (b) bode plots

value at the highest value of frequency.[66] The diameter of the semi-circle is equivalent to the charge transfer resistance at the interface; this is the difference between the real value at the second intersection for the semi-circle (or an extrapolation of the semi-circle to the real axis) and the R_s value.[66] The semi-circle shape of the Nyquist plot is indicative of a kinetically controlled interfacial processes.[76] The presence of a straight line at an angle of 45° from the axes is indicative of diffusion controlled processes (charge transfer) and can be used to determine the presence of pinholes in immobilised membrane films.[78] The electrical double layer capacitance C_{dl} can be obtained from the point of intersection of an extrapolation of this line to the real axes, which is equal to $R_s + R_{ct} - \chi$, where $\chi = 2\sigma^2 C_{dl}$ and σ is the Warburg coefficient, defined as shown in Eqn 3.19.

$$\sigma = \frac{RT}{n^2F^2A\sqrt{2}}\left(\frac{1}{C_O\sqrt{D_O}} + \frac{1}{C_R\sqrt{D_R}}\right) \qquad \text{Eqn 3.19}$$

where R is the gas constant (J/ K mol), T is temperature (K), n is the number of electrons involved in the reaction (usually 1), F is Faraday's constant, A is the area for of the electrode surface, C_o and D_o are the concentration and diffusion coefficient of the oxidant species respectively and C_R and D_R the concentration and diffusion coefficients of the reductant species respectively.[79]

3.4.1.4. Equipment and Methodology

All electrochemical measurements were taken using the AUT72109 (Metrohm Autolab B.V) potentiostat, coupled with NOVA 1.10 software. The electrochemical cell components were purchased from MicruX Technologies and comprises of a three electrode system fabricated on a glass substrate: Au (working electrode) and Pt (reference and counter electrode) and a drop-cell interface to establish connection between the potentiostat and the three electrodes (Figure 3.13). A borosilicate glass cyclinder with an inner diameter of ˜5 mm and an outer diameter of ˜8 mm was used to contain the electrolyte solution (10 µL). Note: care must be taken to ensure there is no leakage of solution during measurement as this could result in damage of the sensor chip and the drop-cell platform.

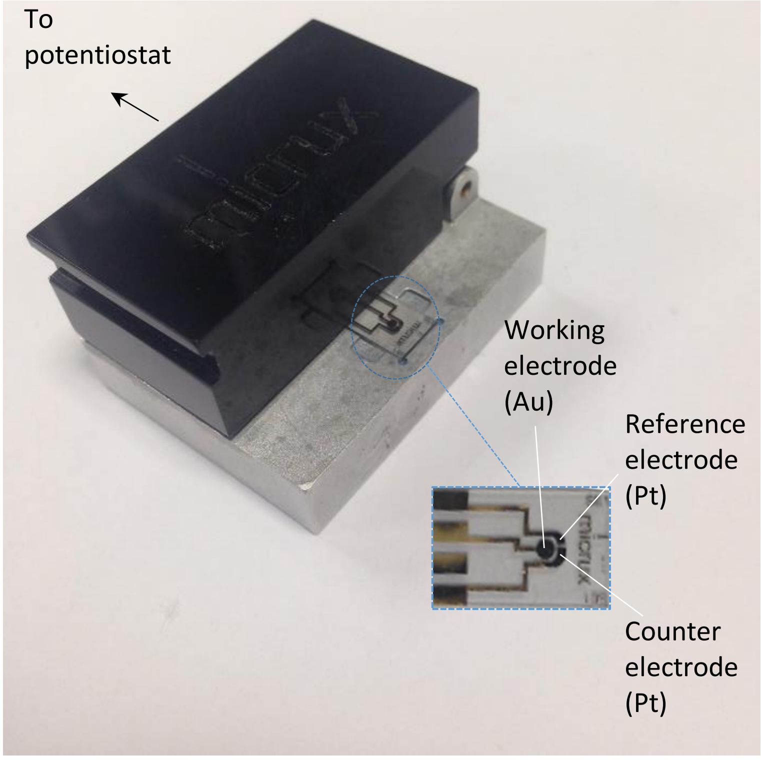

Figure 3.13. A drop-cell connector that serves as an interface of the cell to the potentiostat and a Au/Pt thin film electrode fabricated on a glass substrate (inset, showing the three electrode system

3.4.2. Resonance Enhanced Surface Impedance

Resonance Enhanced Surface Impedance (RESI) is a fairly new and largely unexplored technique that is powerful and could become an indispensable tool in the study of interfacial properties in real time. Similar to EIS, a small perturbation (usually 0.04 V) is applied. Unlike EIS, where impedance values are measured over a range of frequencies, RESI enables the acquisition of impedance data at single frequencies to give time-resolved impedance information. Due to the slow acquisition of EIS data, electrochemical cells investigated using EIS should be in steady state; EIS is not compatible with systems where adsorption and desorption processes take place during the course of measurements.[66] Although single frequency measurements with EIS have been reported, they are usually associated with increased noise and unreliability.[80,81] RESI circumvents the limitations of EIS by operating in resonance mode; the resonance frequency is detected by mapping the resonance peak and translating shifts in the resonance peak position into capacitance.[82] The resonance frequency (f_o) is related to the interfacial capacitance (C) and the external inductance (L) according to the following relationship

$$f_o = \frac{1}{2\pi\sqrt{LC}} \qquad \text{Eqn 3.20}$$

The resonator is comprised of a pair of band shaped microelectrodes on a glass chip in parallel with an external inductor. In addition to the two microelectrodes, the RESI cell set up comprises of an integrated reference and counter electrode (Figure 3.14). An integrated fluidic handling system run by a syringe pump that is refilled from an external container ensures a constant flow of electrolyte solution to the electrodes. The flow rates have a range of 5 µL/min to 200 µL/min. Electrical contact between the electrode and the system is established by insertion of the chip into the docking unit and closing it to form a mechanical seal. This also connects the fluidic channel on the chip to the fluidic system. The integrated injection valve, with a 200 µL injection loop, enables the introduction of test solutions to the microfluidic system. The capacitance measurements are usually taken using a background buffer until a stable reading is achieved; subsequently the test solution is introduced through the injection loop. The z-LAB™ software enables the adjustment of all settings including flow rates, injections, and other operation settings.

The changes in the magnitude of the resonance peak (V_{peak}) provide information on the interfacial resistance and can be used to study the charge transfer processes at the solid-liquid interface. The total current (I) passing through the resonator can be calculated using the expression

$$I = \frac{U_o - V_{peak}}{R} \qquad \text{Eqn 3.21}$$

where U_o is the magnitude of the applied potential and R is an instrument constant.

3.4.2.1. Equipment and Methodology

RESI measurements were acquired using the z-LAB™-210-S2 (Layerlab) instrument. Gold sensor chips were modified with either SAM or BLM membranes as detailed in section 3.2.2. A running buffer of 0.1 M KNO_3 was used at the start of the measurement until the measurements stabilised. The SLN dispersions were centrifuged to remove excess water and redispersed in 0.1 M KNO_3. The Fc-SLN/KNO_3 nano suspension (200 µL) was injected at a flow rate of (5 µL/min) while the capacitance and peak amplitude was monitored continuously.

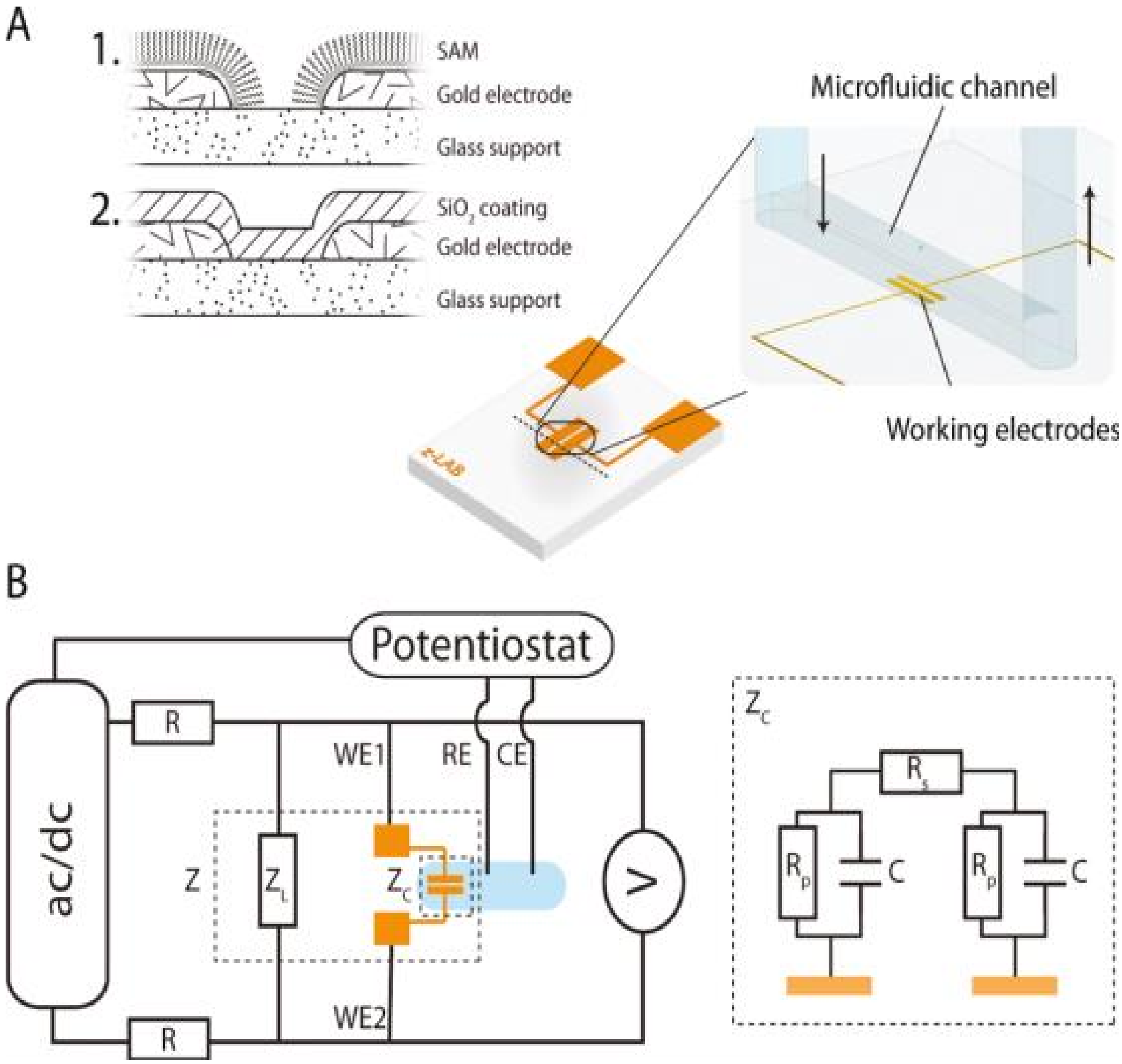

Figure 3.14. Illustrating (a) the setup of the z-LAB ™dual-electrode modified with a SAM or SiO_2 coating and the microfluidic channel system. (b) RESI measurement circuit showing the principal components only. Reprinted from ref. 82 with permission from the American Chemical Society

3.5. References

1 M. Naumowicz and Z. Figaszewski, *Bioelectrochemistry*, 2003, **61**, 21–27.

2 C. Yang, Michigan State University, 2008.

3 R. Campos and R. Kataky, *J. Phys. Chem. B*, 2012, **116**, 3909–3917.

4 H. G. Merkus, *Particle Size Measurements: Fundamentals, Practice, Quality*, Springer Science & Business Media, 2009.

5 S. J. Blott, D. J. Croft, K. Pye, S. E. Saye and H. E. Wilson, *Geol. Soc. London, Spec. Publ.*, 2004, **232**, 63–73.

6 N. Kumar and S. Kumbhat, *Essentials in Nanoscience and Nanotechnology*, John Wiley & Sons, 2016, 2016.

7 Z. Ma, H. G. Merkus, J. G. A. . de Smet, C. Heffels and B. Scarlett, *Powder Technol.*, 2000, **111**, 66–78.

8 D. Lee Black, M. Q. McQuay and M. P. Bonin, *Prog. Energy Combust. Sci.*, 1996, **22**, 267–306.

9 G. Gouesbet, *J. Quant. Spectrosc. Radiat. Transf.*, 2009, **110**, 1223–1238.

10 G. B. J. de Boer, C. de Weerd, D. Thoenes and H. W. J. Goossens, *Part. Charact.*, 1987, **4**, 14–19.

11 W. I. Goldburg, *Am. J. Phys.*, 1999, **67**, 1152.

12 L. Cipelletti and D. A. Weitz, *Rev. Sci. Instrum.*, 1999, **70**, 3214.

13 R. C. Murdock, L. Braydich-Stolle, A. M. Schrand, J. J. Schlager and S. M. Hussain, *Toxicol. Sci.*, 2008, **101**, 239–53.

14 G. Frens, *Nat. Phys. Sci.*, 1973, **241**, 20–22.

15 M. Kaszuba, D. McKnight, M. T. Connah, F. K. McNeil-Watson and U. Nobbmann, *J. Nanoparticle Res.*, 2008, **10**, 823–829.

16 C. Zuo, J. Sun, S. Feng, M. Zhang and Q. Chen, *Opt. Lasers Eng.*, 2016, **80**, 24–31.

17 J. . Bellare, H. . Davis, W. . Miller and L. . Scriven, *J. Colloid Interface Sci.*, 1990, **136**, 305–326.

18 G. Karp, *Cell and Molecular Biology: Concepts and Experiments*, John Wiley & Sons, 6, illustr., 2009.

19 M. Spencer, *Fundamentals of Light Microscopy*, CUP Archive, illustrate., 1982.

20 R. Oldenbourg, *Nature*, 1996, **381**, 811–812.

21 B. G. Vermey, M. G. Chapman, S. Cooke and S. Kilani, *Reprod. Biomed. Online*, 2015, **30**, 67–73.

22 R. Oldenbourg and G. Mei, *J. Microsc.*, 1995, **180**, 140–7.

23 L. Beerden, E. L. M. Flerackers and H. J. Janssen, *Eur. J. Phys.*, 1985, **6**, 139–142.

24 A. Bogner, P. H. Jouneau, G. Thollet, D. Basset and C. Gauthier, *Micron*, 2007, **38**, 390–401.

25 W. Zhou, R. P. Apkarian, Z. L. Wang and D. Joy, in *Scanning Microscopy for Nanotechnology: Techniques and Applications*, eds. W. Zhou and Z. L. Wang, Springer Science & Business Media, illustrate., 2007, p. 15.

26 Z. L. Wang, *J. Phys. Chem. B*, 2000, **104**, 1153–1175.

27 D. C. Joy and A. D. Romig Jr, *Principles of Analytical Electron Microscopy*, Springer Science & Business Media, illustrate., 1986.

28 L. Reimer and P. W. Hawkes, *Scanning Electron Microscopy: Physics of Image Formation and Microanalysis*, Springer, 1998.

29 A. Lubk and F. Röder, *Ultramicroscopy*, 2015, **151**, 136–149.

30 L. Yang, *Materials Characterization: Introduction to Microscopic and Spectroscopic Methods*, John Wiley & Sons, 2009, 2009.

31 J. T. Burke, *J. Chem. Educ.*, 1997, **74**, 1213.

32 B. H. Stuart, *Infrared Spectroscopy: Fundamentals and Applications*, John Wiley & Sons, 2004.

33 B. C. Smith, *Fundamentals of Fourier Transform Infrared Spectroscopy*, CRC Press, illustrate., 1995.

34 US 5438233 A, 1995.

35 J. E. Stewart and J. C. Richmond, *J. Res. Natl. Bur. Stand. (1934).*, 1957, **59**, 405–409.

36 K. Yang and L. Zeng, *Phys. Procedia*, 2012, **33**, 1695–1701.

37 V. C. Farmer, *Philos. Trans. R. Soc. London. Ser. A, Math. Phys. Sci.*, 1982, **305**, 609–619.

38 A. A. Ismail, F. R. van de Voort and J. Sedman, *Tech. Instrum. Anal. Chem.*, 1997, **18**, 93–139.

39 P. R. Griffths, *Science.*, 1983, **222**, 297–302.

40 D. Lin-Vien, N. B. Colthup, W. G. Fateley and J. G. Grasselli, *The Handbook of Infrared and Raman Characteristic Frequencies of Organic Molecules*, Elservier, 1991.

41 B. Van Eerdenbrugh and L. S. Taylor, *Int. J. Pharm.*, 2011, **417**, 3–16.

42 L. Monney, R. Belali, J. Vebrel, C. Dubois and A. Chambaudet, *Polym. Degrad. Stab.*, 1998, **62**, 353–359.

43 P. Wilhelm, *Micron*, 1996, **27**, 341–344.

44 D. D. Laws, H.-M. L. Bitter and A. Jerschow, *Angew. Chemie Int. Ed.*, 2002, **41**, 3096–3129.

45 G. Breit, *Phys. Rev.*, 1930, **35**, 1447–1451.

46 M. C. Gupta, *Atomic And Molecular Spectroscopy*, New Age International, 2007.

47 J. S. Rigden, *Rev. Mod. Phys.*, 1986, **58**, 433–448.

48 D. C. Apperley, R. K. Harris and P. Hodgkinson, *Solid-State NMR: Basic Principles and Practice*, Momentum Press, 2012.

49 R. K. Harris, E. D. Becker, S. M. Cabral De Menezes, P. Granger, R. E. Hoffman and K. W. Zilm, *Solid State Nucl. Magn. Reson.*, 2008, **33**, 41–56.

50 J. D. Peterson, S. Vyazovkin and C. A. Wight, *Macromol. Chem. Phys*, 2001, **202**, 775–784.

51 J. Huang and M. Dali, *J. Pharm. Biomed. Anal.*, 2013, **86**, 92–99.

52 G. W. H. Höhne, K.-H. Breuer and W. Eysel, *Thermochim. Acta*, 1983, **69**, 145–151.

53 S. Tanaka, *Thermochim. Acta*, 1992, **210**, 67–76.

54 P. Gill, T. T. Moghadam and B. Ranjbar, *J. Biomol. Tech.*, 2010, **21**, 167–93.

55 Ü. Gönüllü, M. Üner, G. Yener, E. F. Karaman and Z. Aydoğmuş, *Acta Pharm.*, 2015, **65**, 1–13.

56 L. Montenegro, S. Ottimo, G. Puglisi, F. Castelli and M. G. Sarpietro, *Mol. Pharm.*, 2012, **9**, 2534–2541.

57 A. Guinier, *X-ray Diffraction in Crystals, Imperfect Crystals, and Amorphous Bodies*, Courier Corporation, illustrate., 1994.

58 M. H. J. Koch and J. Bordas, *Nucl. Instruments Methods Phys. Res.*, 1983, **208**, 461–469.

59 V. Jenning, A. F. Thünemann and S. H. Gohla, *Int. J. Pharm.*, 2000, **199**, 167–177.

60 T. Narayanan, O. Diat and P. Bösecke, *Nucl. Instruments Methods Phys. Res. Sect. A Accel. Spectrometers, Detect. Assoc. Equip.*, 2001, **467-468**, 1005–1009.

61 B. Chu and B. S. Hsiao, *Chem. Rev.,* 2001, **101**, 1727–1762.

62 J. M. Mermet, M. Otto, R. Kellner and M. V Cases, *Analytical chemistry: a modern approach to analytical science*, Wiley-VCH, 2 Illustra., 2004.

63 J. M. Parnis and K. B. Oldham, *J. Photochem. Photobiol. A Chem.*, 2013, **267**, 6–10.

64 *Science.*, 1933, **78**, 259.

65 D. R. Crow, *Principles and Applications of Electrochemistry, 4th Edition*, CRC Press, 4th edn., 1994.

66 A. J. Bard and L. R. Faulkner, *Electrochemical Methods: Fundamentals and Applications*, John Wiley & Sons, 2nd edn., 2001.

67 P. M. S. Monk, *Fundamentals of Electro-Analytical Chemistry*, John Wiley & Sons, 2008.

68 F. G. Thomas and G. Henze, *Introduction to Voltammetric Analysis: Theory and Practice*, Csiro Publishing, 2001.

69 G. Inzelt, A. Lewenstam and F. Scholz, in *Handbook of Reference Electrodes*, eds. G. Inzelt, A. Lewenstam and F. Scholz, Springer, Berlin, Heidelberg, 2013, pp. 331–332.

70 Z. Stojek, in *Electroanalytical Methods: Guide to Experiments and Applications*, ed. F. Scholz, Springer, 2013, pp. 301–305.

71 R. G. Compton and C. E. Banks, *Understanding Voltammetry*, Imperial College Press, 2011.

72 Á. Molina, E. Laborda, E. I. Rogers, F. Martínez-Ortiz, C. Serna, J. G. Limon-Petersen, N. V. Rees and R. G. Compton, *J. Electroanal. Chem.*, 2009, **634**, 73–81.

73 F. Marken, A. Neudeck and A. M. Bond, in *Electroanalytical Methods: Guide to Experiments and Applications*, ed. F. Scholz, Springer, 2013, pp. 51–93.

74 L. Callegaro, *Electrical Impedance: Principles, Measurement, and Applications*, CRC Press, 2012.

75 V. F. Lvovich, *Impedance Spectroscopy: Applications to Electrochemical and Dielectric Phenomena*, John Wiley & Sons, 2015.

76 M. E. Orazem and B. Tribollet, *Electrochemical Impedance Spectroscopy*, Wiley, 2011.

77 S. M. Rezaei Niya and M. Hoorfar, *Electrochim. Acta*, 2016, **188**, 98–102.

78 B. E. Conway, in *Impedance Spectroscopy: Theory, Experiment, and Applications*, eds. E. Barsoukov and J. R. Macdonald, John Wiley & Sons, 2nd edn., 2005, p. pp.484.

79 J. R. Scully, D. C. Silverman and M. W. Kendig, *Electrochemical Impedance: Analysis and Interpretation*, ASTM International, 1993.

80 J. Huang, Z. Li and J. Zhang, *J. Power Sources*, 2015, **273**, 1098–1102.

81 B. Ter-Ovanessian, C. Alemany-Dumont and B. Normand, *J. Appl. Electrochem.*, 2014, **44**, 399–410.

82 A. Lundgren, J. Hedlund, O. Andersson, M. Brändén, A. Kunze, H. Elwing and F. Höök, *Anal. Chem.*, 2011, **83**, 7800–7806.

4. pH Controlled Release of Silicones at Ambient Temperatures: Towards 'Green Detergency'

Lipid based carrier vehicles emerged in the late 1950s in the form of nanoemulsions of vegetable oils or triglycerides. They have since received a considerable amount of interest in drug delivery applications and have evolved into different forms or carriers including nanopellets, microspheres and nanospheres. In this article, we investigate the incorporation of different silicone oils into solid lipid microparticles (SLM) in a novel application, household laundry. The silicones investigated are: polydimethylsiloxanes (100,000 and 10,000 cSt, named PDMS100 and PDMS10 respectively), terminal amino silicone (TAS) and a tertiary amino-functionalised silicone (PK10). Two methods of preparation are used in this chapter, solvent emulsification/evaporation using a water insoluble solvent, hexane and solvent evaporation/diffusion using a water soluble solvent, ethanol. Characterisation of these silicone-loaded microparticles is done using various methods including: ^{29}Si NMR, FTIR, DSC, TGA, SAXS, DLS and Optical Microscopy. These methods are employed to probe into the interaction of the silicones with the matrix, structural and morphological information. A comparison is made between the particles prepared from the two methods of preparation and the pH activated release of the silicones from the lipid matrix is shown.

pH controlled release of silicones at ambient temperatures: towards 'green detergency'

4.1 Introduction

The history of fabric softeners can be traced back to the 1900s, where emulsions of vegetable oils (e.g. tallow oil) in soapy water were used to enhance the handle (the perception of softness to touch) of cotton.[1] The introduction of fabric softener formulations on the market was not until the late 1950s in North America and 1960s in Europe and Japan.[2] The transition from tallow-based soaps to synthetic laundry detergents after the Second World War (1940) and the rise in availability of mechanical washing machines and tumble dryers elevated the necessity for fabric softeners.[2–4] Synthetic detergents are effective at lifting soils and preventing redeposition; however, they lack the additional softening effect brought about by soap residues.[2,3] The agitation and abrasion exerted during the mechanical laundry process can distort the fibre structure, compromising the handle.[5] The static charges induced on textile fibres during tumble drying increases the inter-fibre friction, giving fabrics a rough feel.[6] Fabric softeners lubricate textile fibres to minimise both the fibre-fibre and skin-fibre friction to give a perception of softness. The first commercial fabric softeners were cationic surfactants from the family of quaternary ammonium compounds: dihydrogenated tallow dimethyl ammonium chloride (DHTDMAC), ditallowamidoamine quat, and ditallow imidazoline quat (Figure 4.1).[7] DHTDMAC based fabric softeners have a high efficiency of softening and minimisation of static cling. However, DHTDMAC has now been classified as a hazardous material in Europe.[8,9] This decision was based on the poor biodegradability and the aquatic toxicity data from laboratory tests.[10] Ester quats based on triethanolamine (TEA), are a more environmentally friendly alternative; however, their softening ability is inferior.[7,8,11] Another group of fabric softeners, silicone oils are known to impart a superior softness termed 'the silicone softness'.[6]

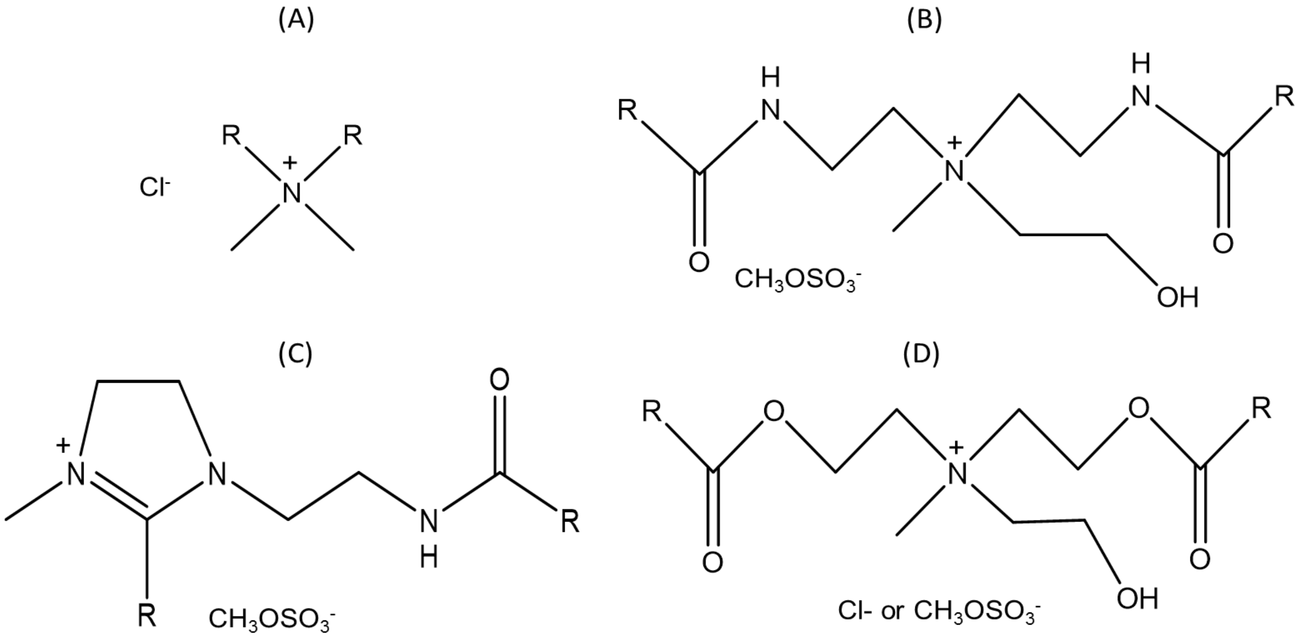

Figure 4.1. Showing the general structures of earlier generations of fabric softeners (a) DHTDMAC (b) Amidoamine quat (c) Imidazoline quat and (d) Ester quat, where R is a C_{11} to C_{17} alkyl group

4.1.1 Silicones

Silicones are inorganic polymers that are based on a Si-O-Si backbone. The most common high molecular weight silicone polymer, polydimethylsiloxane (PDMS), comprises of methyl side chains and terminal groups. The general structure of polydimethylsiloxanes is shown in Figure 4.2. Amino silicones comprise of amine based terminal groups or functional groups. Table 4.1 shows the chemical structure and viscosity of the four different silicones used in this investigation. Amino

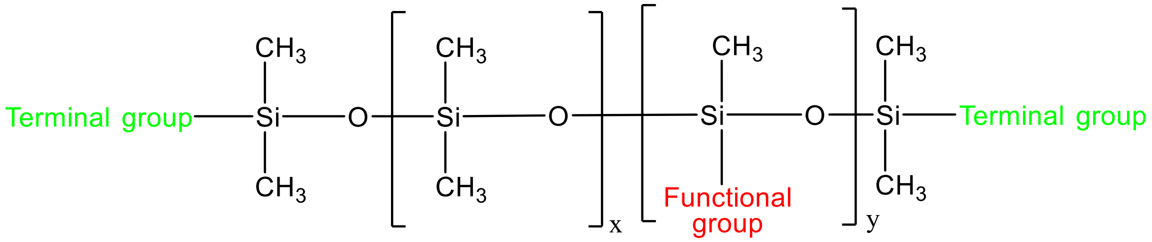

Figure 4.2. The general structure of polydimethylsiloxanes

Silicone	Functional group	Terminal group	Viscosity
PDMS100	—CH_3	—CH_3	100,000 cSt
PDMS10	—CH_3	—CH_3	10,000 cSt
TAS	—CH_3	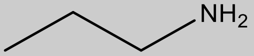	16,000 cSt
PK10	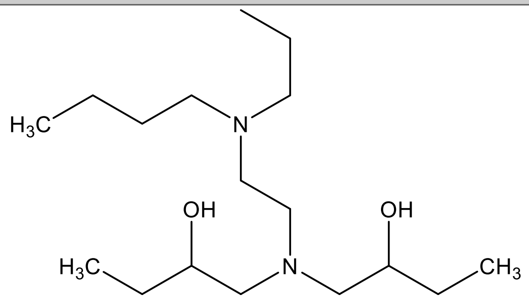	—CH_3	12,000 cSt

Table 4.1. Showing the viscosity and organic composition of the named silicones at the functional and terminal groups highlighted in Figure 4.2

silicones currently dominate the silicone softener market due to their excellent performance as fabric softeners.[12,13] They show higher deposition efficiency and retention owing to ionic interactions with charged fabric surfaces.

Silicones do not pose the same threat to the environment as cationic surfactants. High molecular weight silicones used in fabric softeners (>1000Da) are insoluble in water and have a high binding affinity for organic matter. Due to this, they can be sequestered from municipal water onto sludge during treatment more efficiently (>95% efficiency).[14] Sequestered silicones in the sludge degrade into amorphous silica, carbon dioxide and water via incineration or biodegradation catalysed by clay soils.[15,16] Silicones possess exceptional properties such as: chemical inertness, thermal stability, wettability and biocompatibility, making them ideal candidates in various applications.[17–20] Although silicones are more expensive than traditional cationic softeners, they offer a broad range of benefits in addition to their superior softening ability.[6] Their softening ability is attributed to the high flexibility of the polymer chain.[21]

The flexibility of the silicone polymer chain is caused by the very low rotation barrier about the Si-O-Si chain (0.8 kJ/mol).[22] The comparatively long Si-O and Si-C bonds and the alternating pattern of the Si-O-Si and O-Si-O bond angles minimises steric hindrance between neighboring organic substituents (e.g. methyl groups), rendering a high degree of freedom of rotation about the siloxane backbone.[19,21,23,24] Figure 4.3 shows the values of bond lengths and bond angles on the silicone polymer chain in comparison to the organic chain equivalent.[25] It has been suggested that the large difference in electronegativity between the Si and O atoms (1.9 and 3.4 respectively) also contributes to the silicone flexibility.[26–28] A part-covalent part-ionic bond is formed where the O atoms act as π-donor ligands to the lower energy Si-C σ*orbitals forming a partial and variable double bond.[28] This encourages variations in the Si-O-Si and O-Si-O bond angles, contributing to the flexibility of the chain.[21,25,28,29]

Organosilicons generally show thermal stability for temperatures up to 200-300 °C and retain their flexibility at temperatures down to -100 °C.[19,30] The homolytic bond dissociation energy of the Si-O bond (108 kcal/mol) is relatively higher than the C-C bond (83 kcal/mol) giving silicones superior thermal stability compared to their organic counterparts.[20,25] However, it has been shown that thermal stability is dependent on the specific composition of the silicone polymer.[31] Silicones

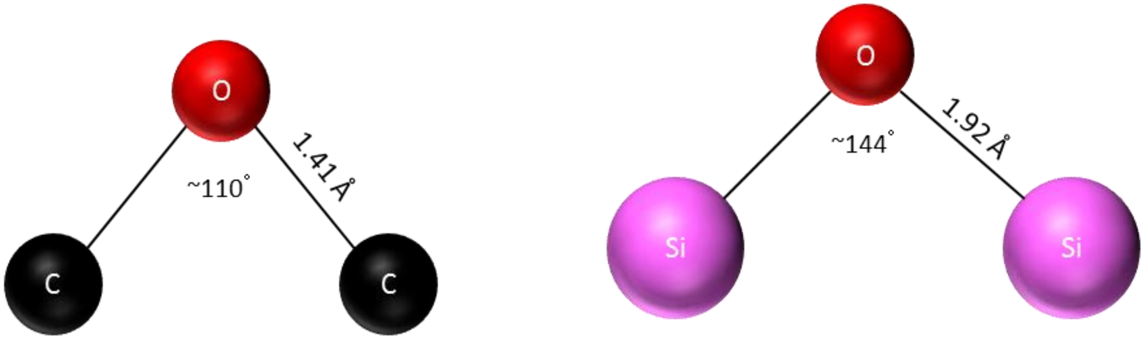

Figure 4.3. An illustration of the difference in bond lengths and angles between Si-O-Si and C-O-C linkages

have good film forming properties and are capable of adsorbing onto organic surfaces due to their low surface tension of wetting (~20 dynes/cm for PDMS).[20,32] The fabric softening phenomena is based on the lubrication of the textile fibres to modify the surface properties and minimise inter-fibre and skin-fibre interaction to give fabric a smooth feel.[33,34] Silicones are ideal candidates for fabric softeners.

Polydimethylsiloxanes (PDMS) are insoluble in water and most hydrocarbons owing to their part-organic part-inorganic nature.[35] Substitution of the methyl side groups with polar groups enhances dispersibility in aqueous media and organic solvents.[36] PDMS interacts with textile fibres almost exclusively by hydrophobic forces, whereas organo-functionalised silicones can also interact by ionic interactions.[33] Silicones in laundry are generally applied in the form of emulsions. Various authors have reportedly researched silicone emulsions of varying size ranges (nano-, micro-, and macro-), charge (ionic- and non-ionic-), emulsifier moieties (organic surfactants, silicone surfactants and biopolymers) and their effect in laundry and haircare applications.[23,37–42] However, the efficiency of deposition associated with silicone fabric softeners from emulsion form in laundry is very low. This is especially a predominant problem in 2-in-1 detergent formulations where the presence of other detergents and actives could affect the stability of the emulsion. A suitable alternative to emulsions is encapsulating the actives in a carrier matrix. A solid carrier matrix reduces the mobility of the actives and hence improves their physical stability in formulation, which is essential for efficient deposition.[43,44] It also prevents chemical interactions between the amino functionalised silicones used as fabric softeners and anionic surfactants used in detergency and introduces the possibility of controlled/triggered release. In addition, solid carrier matrices supersede emulsions because they are applicable in dry laundry applications (powder detergents) in addition to the liquid and gel formulations. This chapter reports an investigation in the use of solid lipid particles as encapsulating matrices in laundry. Solid lipid particles are ideal candidates for this purpose due to their stability, the possibility of controlled/triggered release, the low cost of ingredients and production and biodegradability of the excipients.[45]

4.1.2 Solid Lipid Particles for Silicone Delivery

Miscibility of the active and the lipid melt is essential for the successful loading into SLM.[46] Polydimethylsiloxanes are both lipophobic and hydrophobic which impedes the possibility of incorporation into the lipid matrix. However, this can be circumvented by utilising a solvent-based method of preparation of the SLM.[47] The solvent emulsification/evaporation for preparation of solid lipid nanoparticles was first proposed by Sjostrom and Bergenstahl[48] and has been successfully applied by other researchers.[47,49–51] This method employs a water immiscible solvent to dissolve the lipid and the active; the mixture is subsequently emulsified in aqueous media. A similar method, the solvent emulsification/diffusion method, applies the same procedure as the former but uses a water miscible solvent instead.[52–55] The fate of the solvent after emulsification depends on the type of solvent; water soluble solvents diffuse into the water phase[52–55] and water insoluble solvents are emulsified together with the lipid and active until evaporation, leaving a lipid/active emulsion.[47–51] An illustration of the mechanism involved in the formation of solid lipid matrices from these processes is shown in Figure 4.4.

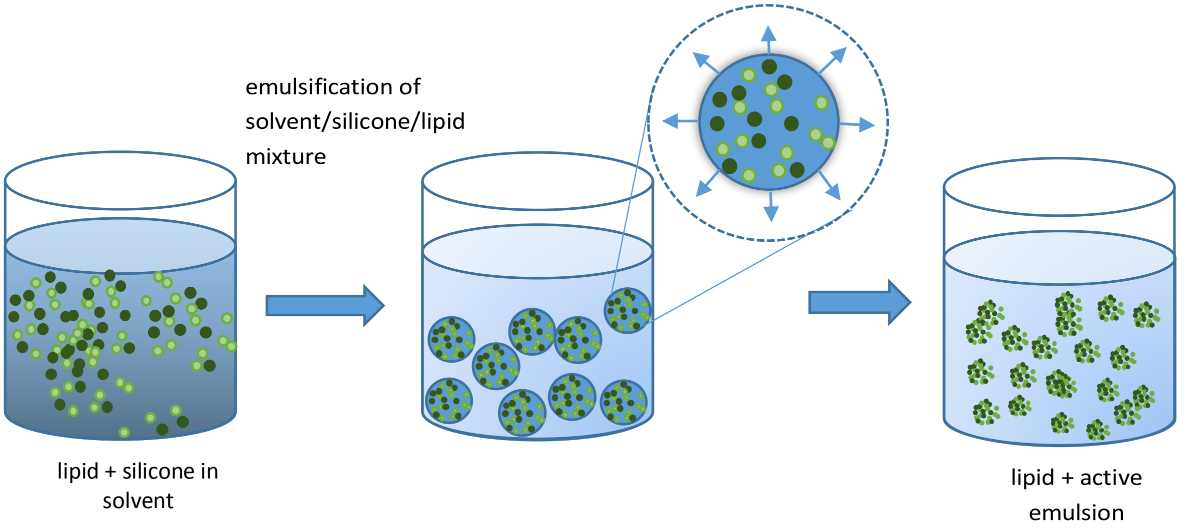

Figure 4.4. Schematic illustration of the mechanism involved in the preparation solid lipid particles via solvent emulsification techniques. The lipid/solvent/silicone mix is emulsified in aqueous solution and the solvent diffuses into the aqueous phase or evaporate from the matrix while maintaining the defined microstructure

4.1.3 Characterisation of Silicones in Solid Lipid Microparticles

4.1.3.1. Loading Capacity and Entrapment Efficiency

Loading capacity (LC) and entrapment efficiency (EE) are critical parameters in assessing the quality and performance of encapsulating matrices.[56–61] The LC gives measure of the total amount of the active compound incorporated into the lipid matrix. EE gives a measure of the amount of drug incorporated as a fraction of the total amount of drug added (see equation below). Knowledge of the amount of the active incorporated into the matrix is essential for computing the LC and EE values.

$$\mathrm{LC}=\frac{\text{mass of silicone in matrix}}{\text{mass of silicone + lipid matrix}}\times 100 \tag{4.1}$$

$$\mathrm{EE}=\frac{\text{mass of silicone in matrix}}{\text{mass of silicone added}}\times 100 \tag{4.2}$$

Analytical methods for the determination of total silicon determination for quantifying organosilicon compounds have are widely reported.[62–66] Chainet et al., completed a comprehensive review of analytical methods for quantifying the Si content from organosilicon compounds at trace levels using atomic spectroscopic methods (AA and ICP), chromatographic and mass spectroscopy based hyphenated methods.[67] Chemical analysis methods such as FTIR and NMR provide more specific detection of organosilicon compounds.[68] FTIR is highly specific to the spectral fingerprints of organic groups attached to the Si atoms and the siloxane backbone. The characteristic bands for organosilicon compounds are shown in Table 4.2. The corresponding height or integrated peak area can be correlated to the silicone concentration relative to the known standard. [66,69,70]

Frequencies (cm^{-1})	Vibrational Mode
1258	Symmetrical methyl deformation in Si-CH_3
1100-1000	Asymmetric stretching in Si-O-Si
800	Methyl rocking vibrations in Si-$(CH_3)_2$

Table 4.2. FTIR bands associated with organosilicon compounds and the responsible modes of vibration [71]

NMR has become an important tool in analysis of organosilicons owing to the abundance of atomic nuclei that resonate in a magnetic field, ^{1}H, ^{13}C, ^{29}Si and ^{15}N (for amino-silicones only). The specificity of ^{29}Si NMR makes it a powerful technique for quantifying silicones in complex samples (composed of more than one organic compound).[72] The relative abundance of the ^{29}Si atom is 4.7% and the NMR response is weak resulting in low sensitivity; hence, ^{29}Si NMR requires longer acquisition times and gives high values of uncertainty in quantitative measurements.[67,69] The typical chemical shifts associated with the silicones in this investigation are shown in Figure

4.5. The D-type unit is abundant in high molecular weight silicone polymers. The M-type, is only available in the non-functionalised PDMS, but terminal groups are undetectable with ^{29}Si NMR for high molecular with polymers.[69] ^{29}Si NMR and FTIR are highly dependent on the chemical composition and molecular weight of the silicone polymer, which vary between the PDMS and the functionalised silicones used in this investigation. Consequently, conclusive comparisons on the exact amount of silicones incorporated in the matrix cannot be made with FTIR and NMR; however, they have been employed as complementary techniques.

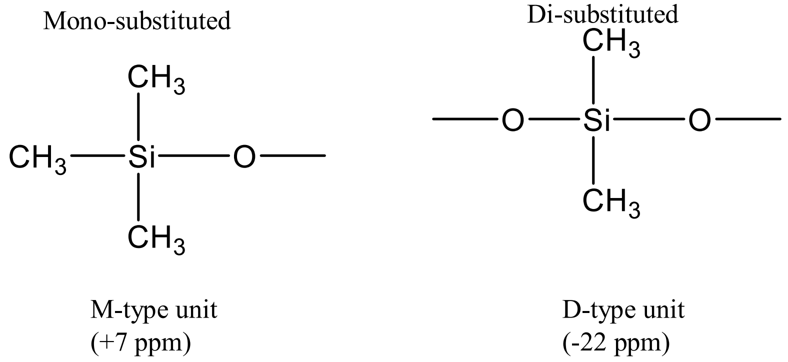

Figure 4.5. Mono- and di-substituted units of polydimethylsiloxanes

Gaul and Angelotti have reported the use of gravimetric methods for quantifying organosilicon compounds after acid dehydration to SiO_2.[73] Kopsch et al., reported the use of Thermal Gravimetric Analysis (TGA) to study the composition of PDMS.[74] TGA measures the weight-loss of substrates as a function of temperature. It can be used to exploit the difference in the onset temperatures for thermochemical events in different materials to determine the composition of composite materials by mass loss at specific temperatures.[75,76] Although silicones of different organic composition vary in thermal stability, they generally have high temperatures for onset of degradation compared to the lauric acid matrix. Moreover, the mass loss of different silicones can be quantified separately and taken into account when quantifying the silicone content of the SLM.

The residual weight at specific temperatures is reported as a percentage of the initial sample weight (lipid + matrix). The loading capacity as calculated from TGA can be expressed as the difference in remnant weight between the silicone-loaded SLM and non-loaded SLM, adjusted for mass loss of the individual silicone oil.

4.1.3.2. pH Triggered Release of Silicones

Most laundry detergents are alkaline, generally in the pH range 9 – 12.[89–91] Alkaline conditions aid the cleaning process by neutralising soils and imparting negative charges to the substrate for enhanced interaction with cleaning agents.[92] pH 10.5 was selected for this study, based on the measured pH values of two commercial detergents. The pH was changed from 5.5 (the measured pH value for an undiluted SLM dispersion) using a $Na_2CO_3/NaHCO_3$ buffer. Optical microscopy was employed for a real time study of the changes in the morphology of the particles upon addition of the buffer to the sample. Laser diffraction was also used to study the changes in the particle size as a result of the pH increase. A concentrated buffer solution was added to the liquid module and the pH was measured to ensure that the desired pH had been reached. Particle size measurements were taken before the addition of the buffer and then once every minute after pH increase.

4.2 Results and Discussion

4.2.1 Particle Size and Morphology

Figure 4.6 shows optical microscopy images of the SLM dispersions prepared using n-hexane. The particles appear to adopt a flake-like shape. There are no distinct differences in the surface morphology between the SLM observed. The non-loaded and the PDMS100-loaded particles show relatively small particles in the range of 50 -70 μm compared to sizes of 100s of μm observed for the PDMS10, TAS and PK10. The differences observed could be due to aggregation of particles or could suggest differences in the interaction between the silicones and the matrix. However, microscopic methods are inherently local and may not give a true representation of the entire

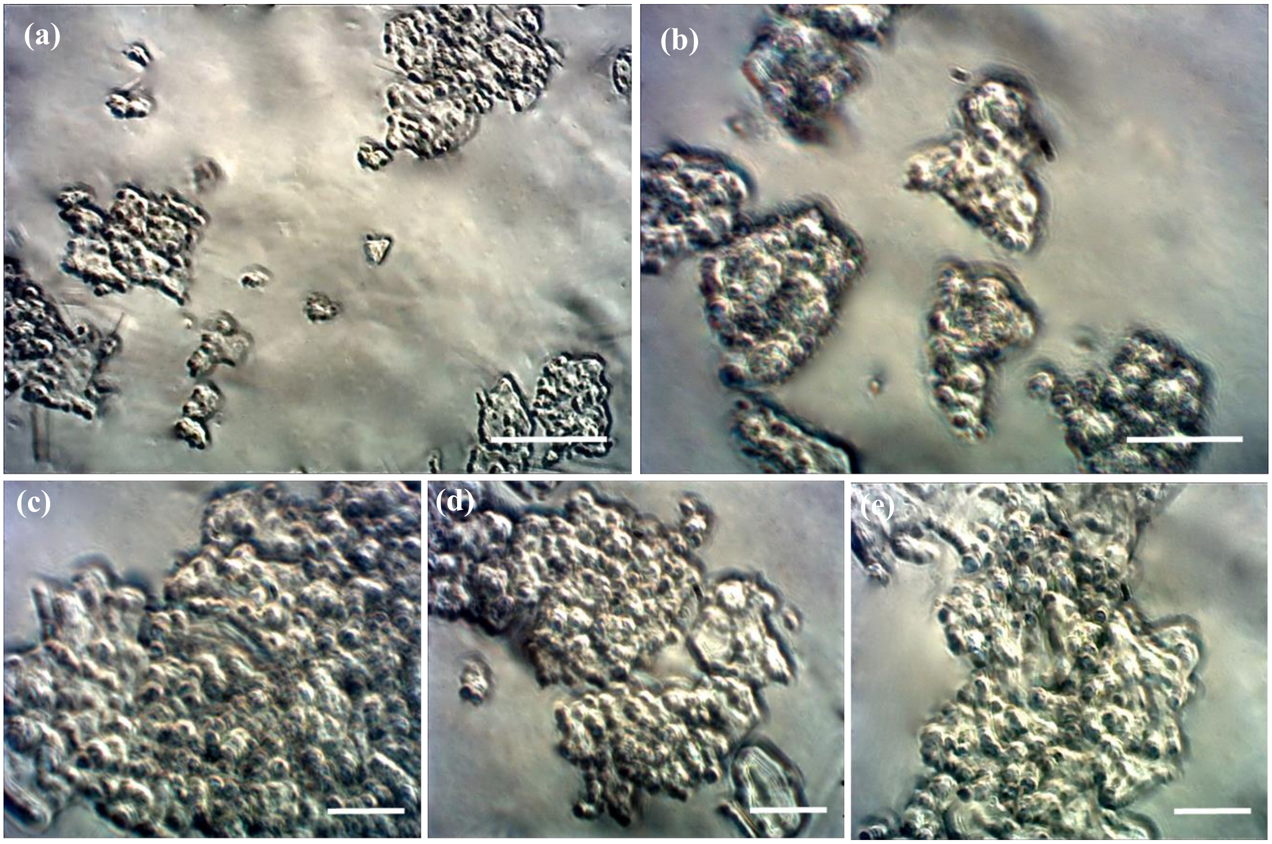

Figure 4.6. Optical microscopy images of SLM dispersions prepared using the solvent emulsification/evaporation method in n-hexane and loaded with (a) no silicone (b) PDMS100 (c) PDMS10 (d) TAS (e) PK10. Scale bar = 50 μm. (Additional images in Appendix 1)

sample. Therefore, laser diffraction was employed for particle size analysis. Table 4.3 shows the particle size measurements obtained by laser diffraction. The tabulated values represent the peak position(s) of the volume weighted particle size distribution (mode). Single particle size distribution peaks were observed for PDMS10- and TAS-loaded SLM at 134 ± 8 and 101 ± 6 µm respectively. Bimodal distribution of sizes were observed for the non-loaded, PDMS100- and PK10-loaded SLM.

The lower peak for the non-loaded and the PDMS-loaded particles (at 63 µm) complements the size range observed by optical microscopy. Additional peaks, not included in the table at sizes above 500 µm for the non-loaded and PK10-loaded particles can be attributed to aggregation of particles or dust. It is unclear why some of the SLM exhibit a multi-modal size distribution (more than once peak in the size distribution curve). However, this behavior is not uncommon in lipid mixtures.[77,78]

Sample	**Peak position (Particle size/µm)**	
Non-loaded	63 ± 4	147 ± 11
PDMS100	63 ± 5	194 ± 12
PDMS10	-	134 ± 17
TAS	-	101 ± 6
PK10	53 ± 4	134 ± 8

Table 4.3. Volume weighted particle size distribution peak position (mode) of silicone-loaded SLM dispersions prepared using the solvent emulsification/evaporation method in n-hexane. See Figure 4.16 for raw data

4.2.2. Chemical Composition and Silicone Loading

4.2.2.1. Fourier Transform Infrared Spectroscopy

Due to the largely ionic character of the Si-O linkage, silicon containing polymers exhibit about five times more intensity of absorption than their carbon based counterparts.[79] This enables the detection of the silicon absorption bands in organic composites even at low levels. The strong characteristic absorption bands expected from organosilicon compounds indicated in Table 4.2 can be observed from the silicone-loaded SLM ATR/FTIR spectra (Figure 4.7), with the exception of the PDMS100-loaded SLM prepared by solvent diffusion evaporation in ethanol (Figure 4.7a). This indicates poor loading for this silicone oil or incompatibility between the silicone and the method of preparation.

The peaks arising from the $Si\text{-}CH_3$ and $(Si\text{-}CH_3)_2$ vibration modes cannot be applied to give quantitative comparisons of loading between the silicones due to their large differences in organic composition and molecular weights. The Si-O-Si intensity bands would be suitable for quantitative comparisons by making chain length based adjustments. However, the characteristic bands for the Si-O-Si linkage at 1100 and 1015 cm^{-1} overlap with other bands arising from the matrix. This makes it difficult to quantify the silicone content using FTIR. However, useful information can still be obtained from the FTIR spectra, such as: confirmation of incorporation of silicones into the matrix and determining the chemical interactions between the lipid and the matrix. The peak positions for the lauric acid remain largely unaffected by the preparation of the SLM. In solid state, lauric acid is thought to exist as dimers with hydrogen bonding between the carboxyl groups.[80] The -OH stretching vibrations in dimeric carboxylic acid units are known to exhibit weak absorption bands in the region 2700 – 2500 cm^{-1}.[71] This band was observed in the spectra for lauric acid bulk and for the SLM, confirming the presence of carboxylic acid dimers in the SLM structure.

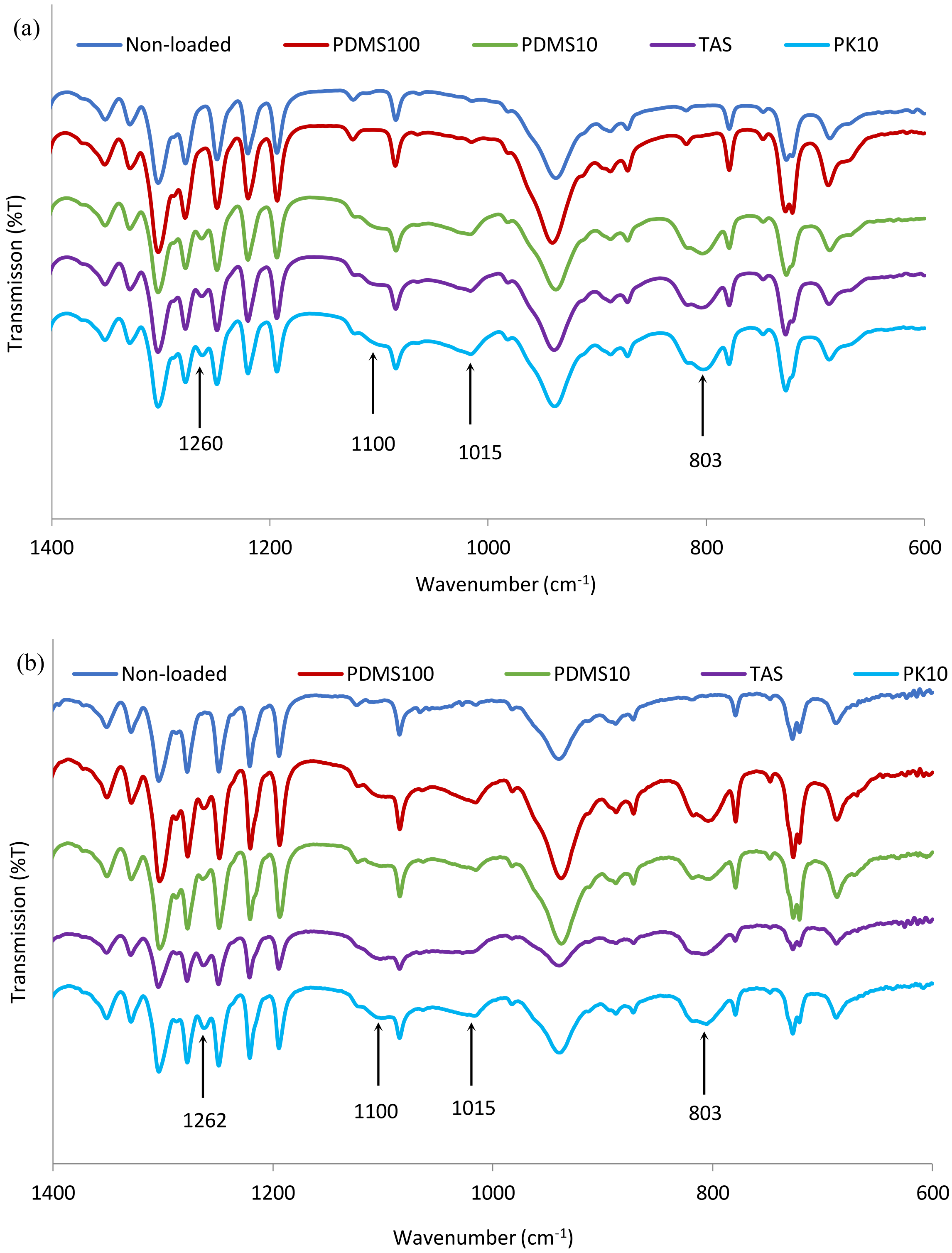

Figure 4.7. ATR/FTIR spectra of non-loaded and silicone-loaded SLM prepared in a) ethanol b) n-hexane

A slight shift in the band frequencies for silicone relative to the pure silicone oil was observed. The peak arising from the Si-CH_3 methyl deformation at 1258 cm^{-1} appears at higher frequencies around 1262 cm^{-1}. The peak at 795 cm^{-1} arising from methyl rocking vibrations has also shifted to higher frequencies of about 803 cm^{-1}. Strong interactions between the silicones and the lipid matrix are more likely to appear at the terminal or functional groups, therefore it is highly unlikely that these peak shifts can be attributed to the formation of bonds. The peak shifts can be attributed to the comparatively low silicone content in SLM compared to the oil and to the variation in relative intensity contributions from lauric acid bands that have closely related frequency bands (1277 and 1249 cm^{-1}). It could also allude to the change in environment surrounding the silicone methyl groups; the presence of the fatty acid molecule around the silicones can restrict the freedom of rotation about the Si-O-Si linkage. The peak arising from the Si-O asymmetric stretching appears largely unaffected by the incorporation into the matrix. The FTIR spectra shows that there are no strong interactions resulting from new bond formation between the lauric acid matrix and the silicone oils.

4.2.2.2. ^{29}Si Solid State NMR

The peak arising from the D-type unit was observed at -22.3 or 22.4 ppm for all the samples except PDMS/SLM prepared in ethanol, which gave no signal at all. Figure 4.8 shows the ^{29}Si spectra obtained for the two PDMS samples prepared by the different methods. No peak was observed for the M-type unit for all the samples (expected around +7ppm), this is expected for high M_w silicones due to the relative abundance of the D-type which would overshadow the response from the terminal units.

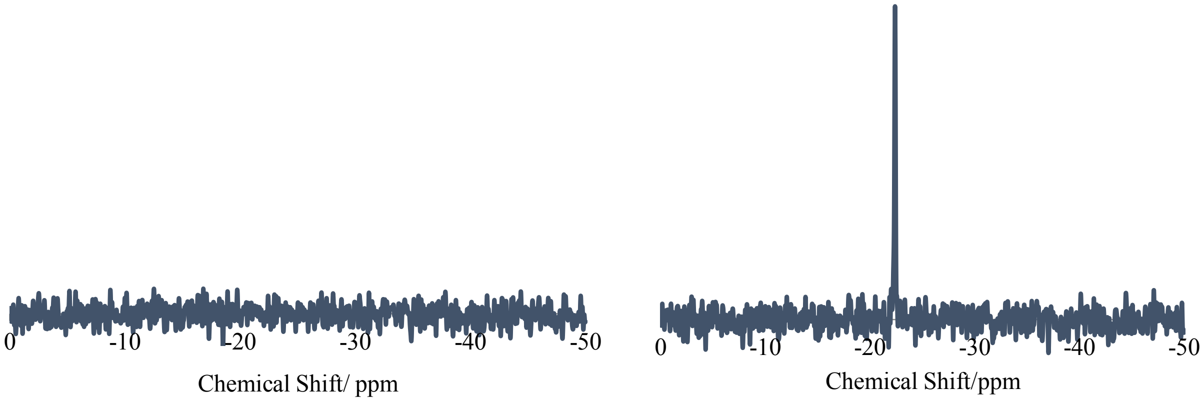

Figure 4.8. ^{29}Si NMR spectra for PDMS100 prepared in a) ethanol and b) n-hexane

Figure 4.9 shows the quantitative estimates of the silicone obtained by integrating the area under the peak. No signal was observed for PDMS100/SLM prepared in using ethanol due to poor loading; this supports the observations from FTIR. PK10 shows a comparatively higher silicone content for both preparation methods. This can be attributed to the comparatively superior miscibility of the PK10 and the lipid. According to Muller et al., miscibility of the active and the matrix is essential for efficient loading onto the SLM matrix.[46] The presence of the amine groups and the high amine number of PK10 increases the polarity of the chain. This enhances miscibility

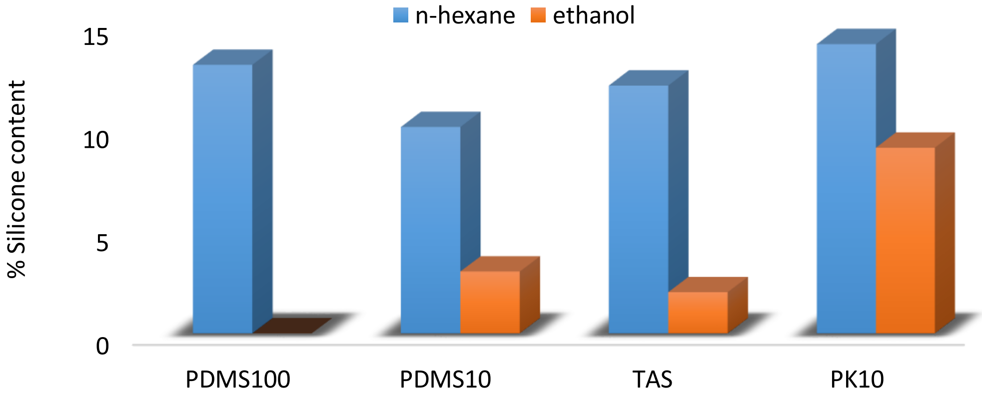

Figure 4.9. Histogram showing the silicone content of the SLM computed from the integrated area under the peak at -22.3 or -22.4 ppm

of the PK10 silicone with the matrix. The graph shows that the SLM prepared in hexane generally show a higher silicone content than those prepared in ethanol. This suggests that n-hexane enhances the miscibility of the lipid and the silicone more effectively than ethanol. According to Lee et al., the compatibility of PDMS to organic solvents is dependent on the cohesive energy density, which is usually expressed in terms of the solubility parameter or the Hildebrand value [$\delta = (U/V)^{1/2}$ ($\mathrm{cal}^{1/2}/\mathrm{cm}^{3/2}$)] where U is the is the molar internal energy (cal/mol) and V is the molar volume (cm^3/mol).[35] Closely matched values of solubility parameter between the polymer and the solvent give the lowest free energy of mixing ΔG_m, which is required for the silicone-solvent miscibility.[35,81] The solubility parameter for PDMS is 7.3 $\mathrm{cal}^{1/2}/\mathrm{cm}^{3/2}$, which is an exact match for hexanes; ethanol has a solubility parameter of 12.7 $\mathrm{cal}^{1/2}/\mathrm{cm}^{3/2}$.[35] Hexane is therefore, a more compatible solvent for the both PDMS and the amino-functionalised silicones which are largely similar composition to the PDMS. This explains the generally higher loading observed for particles prepared in hexane compared to ethanol.

4.2.2.3 Thermal Gravimetric Analysis

TGA was used to study the chemical composition and interactions of the SLM in comparison to the bulk lipid by analyzing the onset temperatures for the chemical events and the amount of residue at specific temperatures. The TGA measurements were carried out under an inert environment to eliminate the possibility of oxidation reactions. This ensures that the main chemical event taking place is thermal decomposition or pyrolysis which leads to the formation of volatile products resulting in mass loss. Figure 4.10 shows the TGA mass loss curves and the first derivative of the mass loss curves as a function of temperature. The onset temperatures (T_{onset}) are shown in table 4.4.

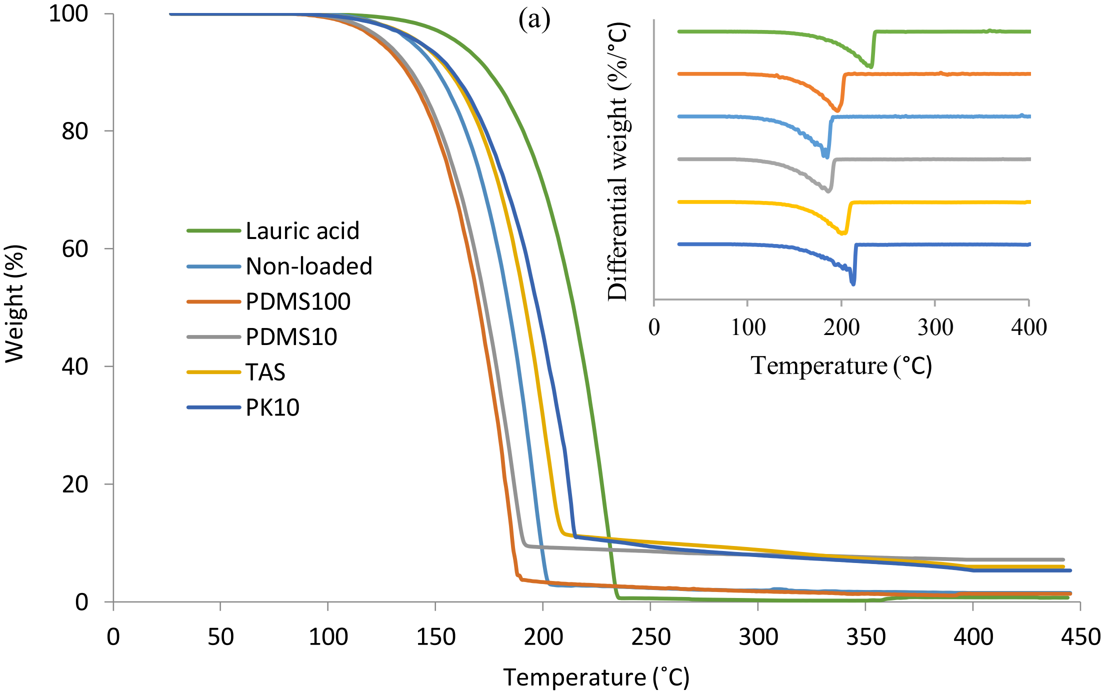

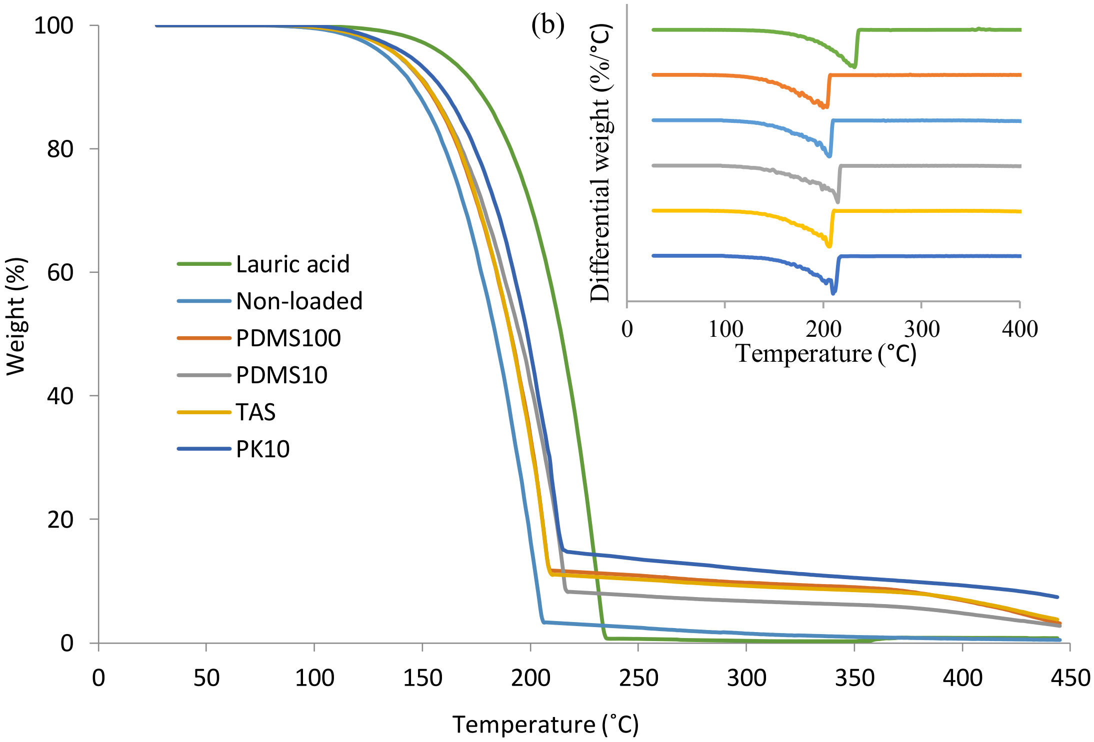

Figure 4.10. TGA curves for SLM prepared in a) ethanol and b) n-hexane insets show the first derivative of the TGA curves

	ethanol	n-hexane
Sample	**T_{onset} (°C)**	**T_{onset} (°C)**
Non-loaded	162 ± 2	161 ± 1
PDMS100	151 ± 1	165 ± 2
PDMS10	158 ± 3	167 ± 2
TAS	176 ± 3	167 ± 3
PK10	172 ± 1	173 ± 2

Table 4.4. Onset temperatures of degradation and temperature of maximum mass loss for SLM systems prepared in ethanol and in n-hexane as obtained from TGA Tonset for the bulk lipid 230 ± 2 °C

The data shows that there are distinct differences in the values of T_{onset} between the bulk lipid and the different SLM. However, the mass loss curve signature is the same for the bulk lipid and for the solid lipid nanoparticles, which alludes to the absence of complex systems formed between the lipid and the silicones excipients.[82] The solid lipid particles exhibit diminished thermal stability compared to the bulk lipid as indicated by the lower T_{onset} (230 ± 2 °C for the bulk lipid). This can be attributed to the presence of surfactants (for non-loaded SLM) which can impair the recrystallisation of the lipid back to its original form and hence compromise the thermal stability. The T_{onset} values for the non-loaded SLM prepared in ethanol and in hexane are very similar, suggesting that the method of preparation does not significantly affect the thermal stability in the absence of silicones. This observation was also made for the PK10-loaded particles. The PDMS-loaded SLM (PDMS100 and PDMS10) prepared in ethanol appear to be less thermally stable than those prepared in hexane. The opposite is true for TAS-loaded particles. This could be ascribed to the polarity of the solvent. Medium to long chain carboxylic acids are known to exist as dimers in non-polar media and monomers in polar solvents and as mixture of dimers and monomers in polar solvents.[83] The presence non-polar PDMS during preparation can inhibit the re-dimerisation of the lipid molecules and hence compromise the stability. It is unclear why TAS-loaded SLM prepared in ethanol has better thermal stability than those prepared in hexane. However, it could be related to the polar nature of the silicone terminal groups and miscibility with ethanol. The general pattern of higher thermal stability for SLM prepared in hexane than those prepared in ethanol can be related to the higher loading capacities of the former (see 4.2.2.2). Silicone oils have much higher thermal stability compared to non-loaded SLM and hence their presence can increase the thermal stability of the composite. Silicones within the particles can also serve as a heat transfer barriers, lowering the thermal conductivity of the particles and increasing the thermal stability.

The TGA curves obtained were also utilized to investigate the quantitative composition of the SLM and calculate the silicone content. Due to the differences in the organic composition of the silicones used in this investigation, it is essential to investigate the thermochemical behavior of the pure silicone oils for a more accurate estimation of the silicone content in the SLM. Figure 4.11 shows the TGA and the first derivative of mass loss curves for the different silicones. The mass loss occurring at temperatures below 100 °C can be attributed to the pyrolysis of the methyl side groups for all silicones and additionally the organo-functional and terminal groups for the amino silicone. The PDMS samples, PDMS100 and PDMS10 exhibit less mass loss compared to the amino-silicones TAS and PK10 which is expected due to the relatively low organic content of PDMS. This also confirms the superior thermal stability of the silicones compared to the lipid,

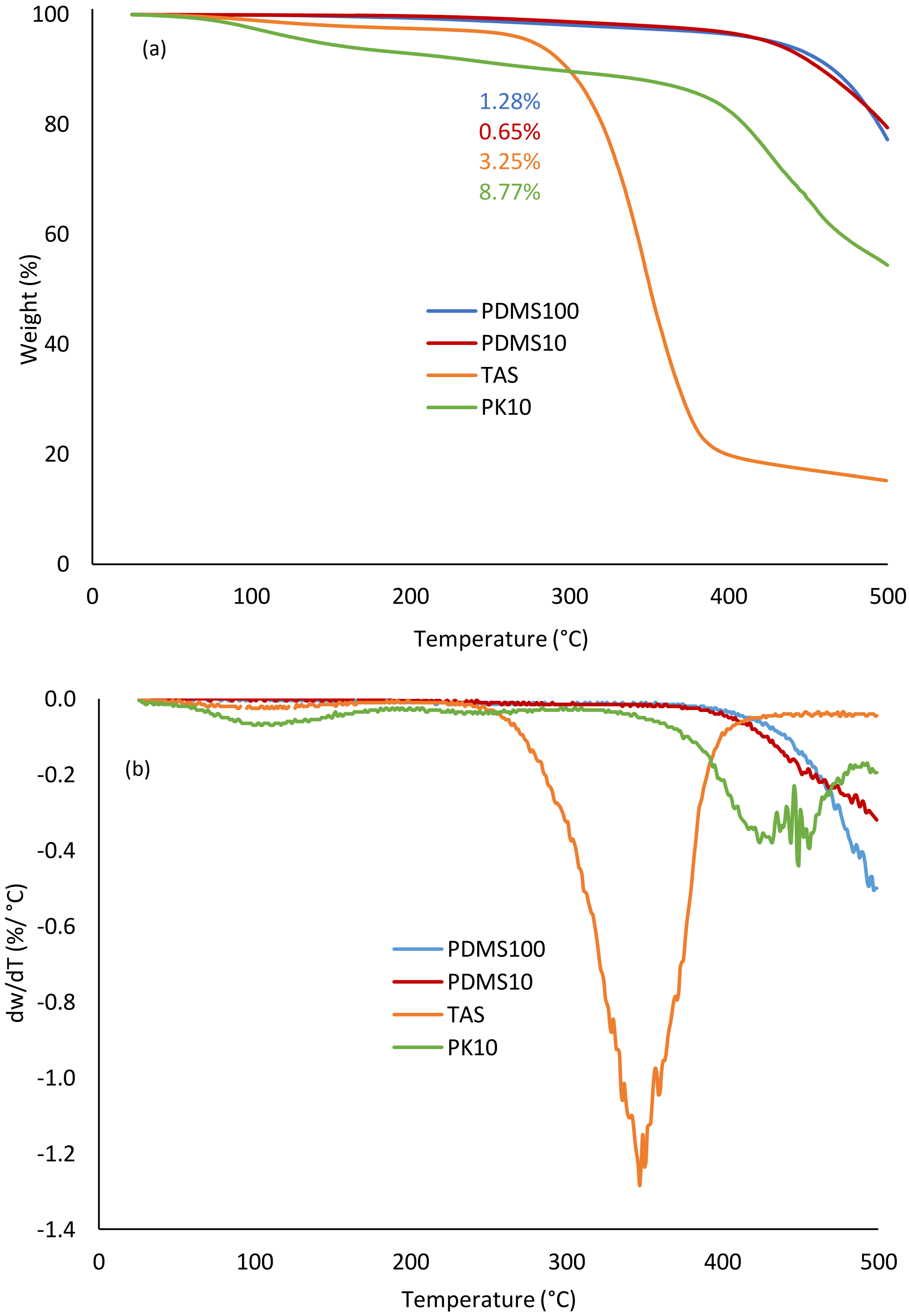

Figure 4.11. Thermogravimetric analysis of the named silicone oils showing (a) TGA curves, showing the values of percentage mass loss at 250 °C and (b) first derivative curves of the TGA curves

which is the basis of this quantitative analysis of the SLM composition. TAS shows the lowest temperature for onset of main chain pyrolysis at 314 ± 2 °C followed by PK10 at 392 ± 10 °C. The PDMS show the onset of main chain pyrolysis at 466 ± 8 °C and 446 ± 6 °C for PDMS100 and PDMS10 respectively. As a result, the quantification of the silicone content in the SLM should be done at temperatures below this and the initial mass loss due to decomposition of the organic groups for each silicone must be taken into account. At 250 °C, lauric acid shows complete mass loss (see figure 4.10) whereas the maximum mass loss obtained for silicones at this temperature was 8.77 % (PK10). The loading capacity/silicone content can approximated to the difference in residual weight between silicone-loaded SLM and non-loaded SLM at 250 °C (2.4%), which takes into account the residual mass of the surfactants.

Figure 4.12 shows the loading capacity values computed from TGA and Table 4.5 shows the entrapment efficiency values. In agreement with the FTIR and ^{29}Si NMR, SLM prepared in ethanol generally show lower silicone content than those prepared in hexane. PK10-loaded SLM show relatively high values for loading capacity and entrapment efficiency when prepared in both

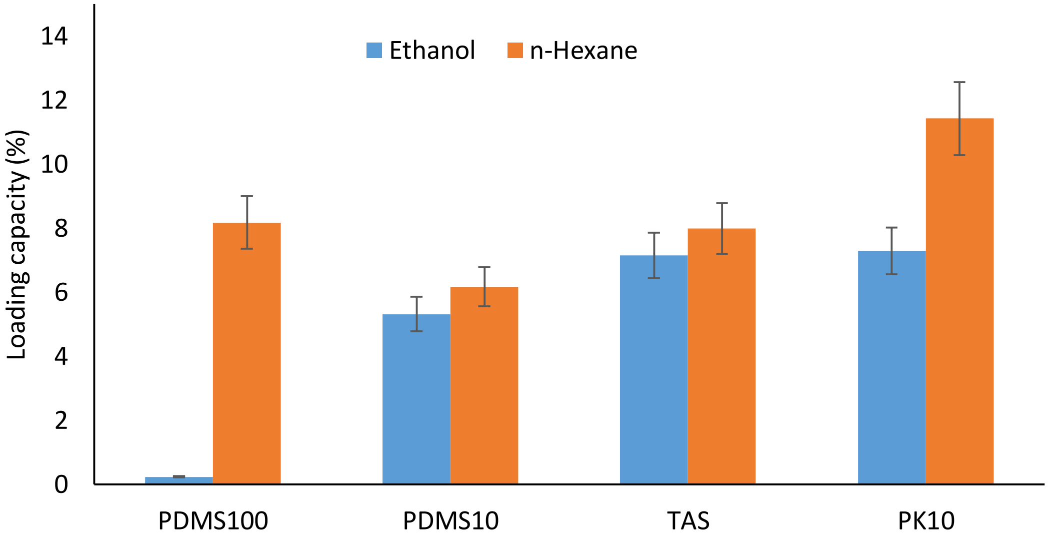

Figure 4.12. Loading capacity values of silicone-loaded SLM as calculated using TGA remnant weight at 250 °C for samples prepare using ethanol or n-hexane

EE%	ethanol	n-hexane
PDMS100	2 ± 1	90 ± 2
PDMS10	69 ± 2	57 ± 2
TAS	86 ± 3	87 ± 3
PK10	92 ± 3	-

Table 4.5: Entrapment efficiency values of silicone-loaded SLM prepared in ethanol and n-hexane obtained from TGA analysis

ethanol and in hexane. It is unclear why the values of loading capacity of the PK10-loaded SLM prepared in n-hexane exceed the anticipated value (9.09%, based on the ratio silicone to lipid used in preparation). For this reason, the entrapment efficiency value for this sample has not been included in Table 4.5 for this reason. This can be attributed to the limitations of TGA as a quantitative tool. It is possible that the PK10 interacts with the surfactants to give stable complexes which increase the residual weight. This can be verified by further study to draw comparisons between the SLM and physical mixtures of the silicones and surfactants. The residual mass of the non-loaded SLM was 2.3 % and 2.4 % for particles prepared in ethanol and n-hexane respectively. This is the remnant mass of the surfactants which is subtracted from the values measured for the silicone-loaded SLM. PDMS100-loaded SLM prepared in ethanol have a significantly low loading capacity compared to those prepared in n-hexane. Again this trend agrees with the observations made from ^{29}Si NMR and is attributed to the miscibility of the solvent with the silicones as well as the lipid matrix. In conclusion, the solvent emulsification/evaporation method using hexane is a more suitable method of preparation of silicone-loaded SLM.

4.2.3 Melting Behavior and Crystallinity

Figure 4.13 shows the endothermic DSC curves for the bulk lipid and the different SLM. The presence of endothermic peaks in all the SLM confirms that the particles are in the solid state. The melting temperatures (T_m) and enthalpy of fusion (ΔH_m) obtained from the DSC curves are shown in Table 4.6. The particles generally show lower melting temperatures compared to the bulk lipid. The melting temperature can be influenced by the colloidal dimensions of the particles.[84] Moreno et al., reported that even n-carboxylic acids transform to the crystalline C-form (monoclinic P21/a = 4) upon heating and recrystallize back to the C-form on cooling.[85] The enthalpy of fusion for the C-form to liquid phase transition reported by this group (36.1 ± 0.8 kJ/mol), is very similar to that observed in this investigation for the bulk liquid, 180 ± 3 J/g (36.1 ± 0.6 kJ/mol) as shown in Table 4.6.

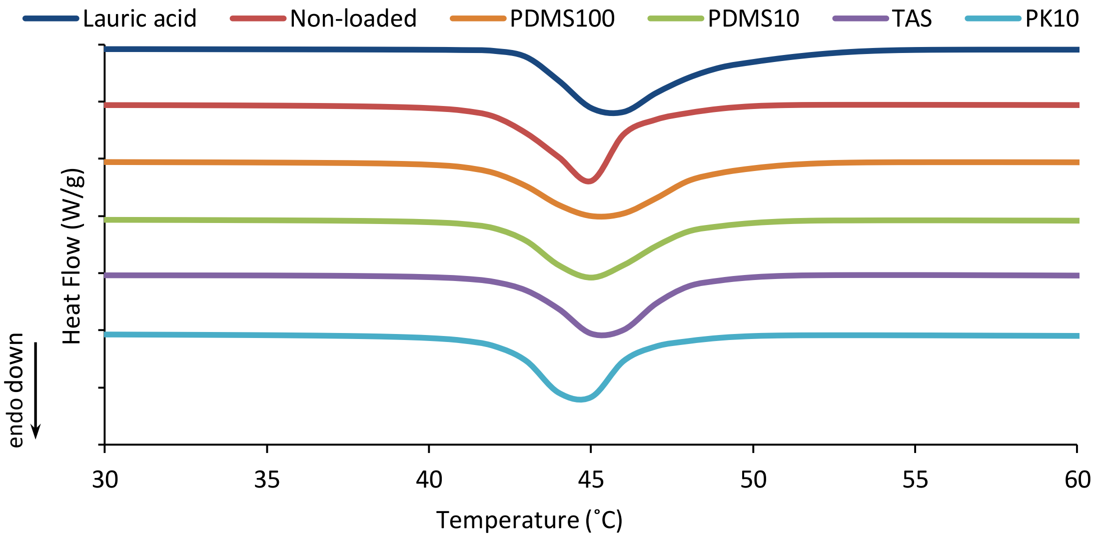

Figure 4.13. DSC curves for bulk lauric acid and SLM prepared using n-hexane, loaded with the named silicones. The samples were heated at a rate of 10 °C/min

Sample	T_m (˚C)	ΔH_m (J/g)
Bulk lauric acid	45.7 ± 0.1	180 ± 3
Non-loaded	45.0 ± 0.3	154 ± 2
PDMS100	45.1 ± 0.4	155 ± 1
PDMS10	44.8 ± 0.5	141 ± 2
TAS	44.9 ± 0.1	130 ± 1
PK10	44.5 ± 0.1	142 ± 5

Table 4.6. Showing melting temperature T_m (˚C) and enthalpy of fusion ΔH_m (J/g) for bulk lauric acid and SLM-loaded with the named silicone

In agreement with Moreno et al, the differences in the enthalpy of fusion are insufficient to warrant a polymorphic transition, which suggests that the lipid in the SLM reverts back to the C-form upon cooling. There are no significant changes in the shape or position of the endotherms observed for the samples, which suggests that there no interactions resulting in complex structures between the lipid and the silicones. The particles are essentially physical mixtures of the silicone and lipid stabilized by surfactants. The reduction in ΔH_m observed for the non-loaded particles can be attributed to the presence of the surfactants and the further reduction for the loaded particles to the presence of silicone oils. The DSC results and analysis confirm that the SLM are indeed solid and that there are no polymorphic transitions and new complex structures formed between the lipid and silicones. This enables the identification of the order of arrangement (incorporation model) of the silicone oils in the lipid matrix. Mullër et al., suggested that SLM can adopt three models of incorporation namely, enriched shell, enriched core and solid solution.[46] Our observations do not support the solid solution model, where the active is molecularly distributed in the lipid matrix and is facilitated by strong interactions between the lipid and the active.[86] This model of incorporation is usually achieved by cold homogenisation which reduces the mobility of the lipid melt and the active and prevents repartitioning into a core-shell arrangement. It is unlikely that the SLM in this investigation adopt this model due to the method of preparation used and insufficient differences observed in the melting behaviour.[87] Therefore, the particles most likely adopt a core-shell model of incorporation. The enriched shell model of incorporation occurs when the active partitions into the aqueous phase during homogenisation or emulsification and re-partitions into lipid during cooling.[86] An increase in the melting temperature of the particles would be expected for this model of incorporation. The silicone shell acts as a thermal shield such that the temperature of the core is slightly lower than that of the outside of the particles; this results in an increase in melting point. In addition, it is unlikely that the silicone partitions into the aqueous phase during emulsification due to the highly hydrophobic nature of silicone oils. Therefore, the most likely model of incorporation of the silicones in the SLM is enriched core model.

4.2.5. Small Angle X-Ray Scattering

SAXS scattering patterns were used to investigate the crystallinity of the lipid matrix and the silicones. The presence of Bragg diffraction peaks for both the bulk lipid and the SLM (Figure 4.14) confirm the crystalline arrangement of the lipid in the SLM. The peak position, the value of the magnitude of scattering vector (q) at maximum peak intensity, is inversely related to the inter-planar spacings of the lipid bilayers, d (001) spacings. Changes in the SAXS peak position can be used to determine the arrangement of the lipid and active inside the SLM. Insertion of silicone oils into the lipid bilayers is characterised by a decrease in the magnitude of scattering vector. The SLM diffraction curves show a shift in the peak position to a higher values of q compared to the bulk lipid (2.31 nm^{-1}). This is due to the difference in the medium used for the measurements; the bulk lipid was measured in powder form and the SLM were measured in dispersion. Water has an electron density of 0.33 e Å^{-3}, which decreases the electron density contrast between the particles and the surrounding environment and shifts the scattering vector to higher magnitudes. The scattering vector is also affected by the electron density contrast between the lauric acid and the silicone oils. The silicones used in this investigation vary in polarity and functionalization and consequently, electron densities. The differences in the composition of the silicones in addition to the differences in the concentration of silicones within the particles (see 4.2.2.2 and 4.2.2.3) results in differences in the electron density contrast with the particle and thus contributes to the variations in the peak position observed for the different SLM (Figure 4.14b - 4.14f). The differences in the particle size between the different SLM (see 4.2.1) also contribute to the shifts in the magnitude of the scattering vector. The differences in the peak position are insufficient to support an argument for significant structural changes, such as insertion of the silicone oils into the lipid bilayer. According to Jenning et al., shifts of small magnitude (<0.1 nm) cannot be attributed to significant

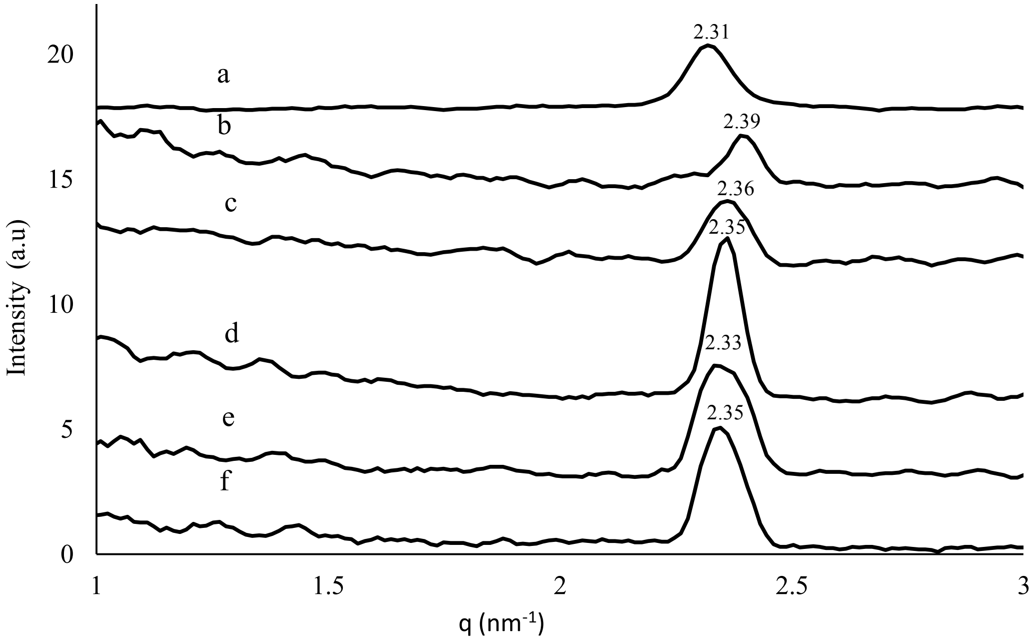

Figure 4.14. SAXS scattering patterns for (a) bulk lauric acid and (b) non- (c) PDMS100- (d) PDMS10- (e) TAS- and (f) PK10-loaded SLM. The intensity is presented as a function of the magnitude of scattering vector (q). A five point moving average has been applied to minimise noise

structural changes to the lipid structure such as those caused by insertion of actives into the lipid layer and strong interactions with the lipid. The absence of strong interactions between the lipid and the silicones also points to the core-shell model of incorporation. The DSC findings suggest that the particles adopt a silicone-enriched core model of incorporation. The drug enriched core model occurs when the active precipitates before the lipid crystallises during cooling, resulting in the repartitioning of the silicone oil within the lipid matrix. This highly likely the case due to the highly hydrophobic and lipophilic nature of silicones. Therefore, from the scattering patterns and melting behavior analysis, it is reasonable to conclude that the particles adopt a silicone enriched core-model.

4.2.6. pH Activated Release

The change in particle size following the pH change was monitored using laser diffraction. The pH was increased from the 5.5 (the measured pH of the dispersion after preparation) to the laundry pH, 10.5. The dissolution of the lipid matrix due to the increased pH results in a decrease in particle size, as observed in Figure 4.15. Lauric acid has a pKa value of ˜4.9. At pH 10.5 lauric acid is deprotonated resulting in the formation of sodium salts in the presence of the $Na_2CO_3/NaHCO_3$ buffer solution. The dissolution of the matrix results in a burst release of silicone droplets into the aqueous solution. The reduced particle size from 134 µm to 58 µm and 110 µm to 63µm for the PDMS10 and TAS-loaded SLM (respectively) confirms the dissolution of the lipid matrix. Similarly, the PK10-loaded SLM distribution with peaks at 48 and 146 µm before the pH change converges to a singular distribution with the mode at 58 µm. The pH-triggered release was also confirmed with optical microscopy (Figure 4.16). The figure shows the morphological changes in

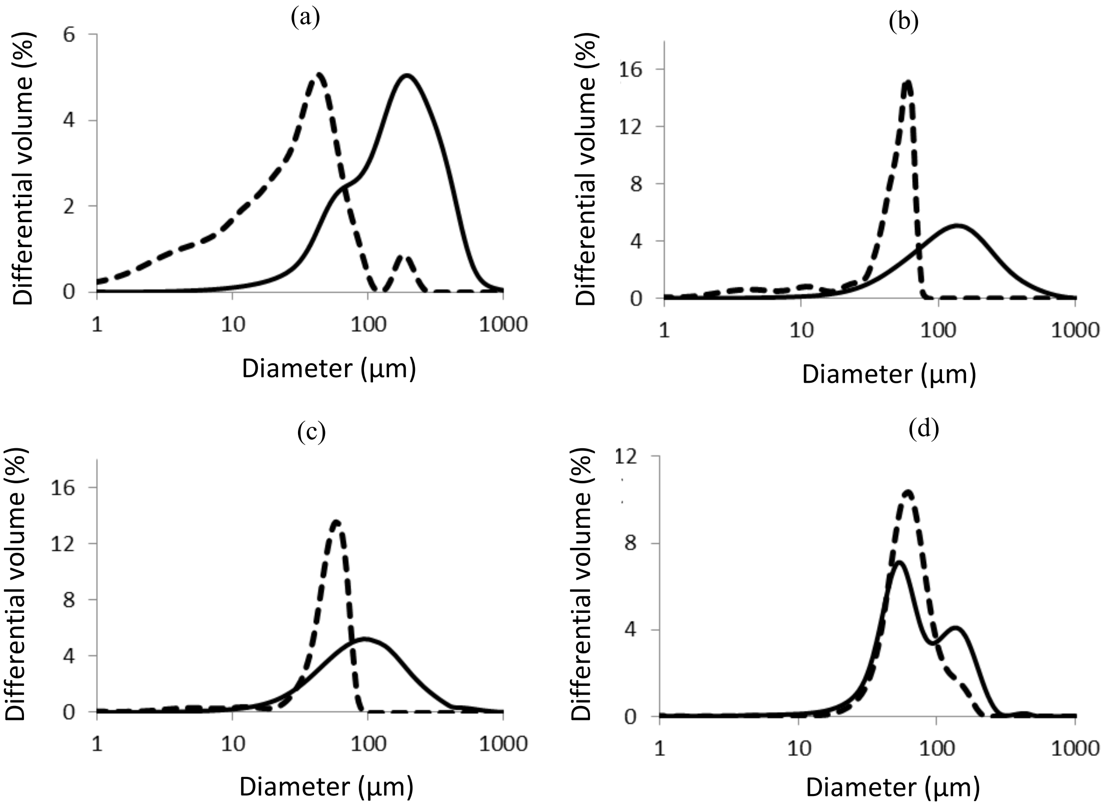

Figure 4.15. Showing the change in particle size after pH change for (a) PDMS100- (b) PDMS10- (c) TAS- (d) PK10-loaded SLM. Solid line = pH 5.0, dashed line = pH 10.5

the TAS-loaded silicone particles after pH is increased to 10.5. The particles are completely dissolved within 40 seconds of the onset of dissolution. See Appendix 2 for more plots showing the evolution of particle size in response to pH change. This burst release behavior is ideal for laundry applications, due to the short timescale of the laundry washing process (20-120 mins). The optical microscopy images also show silicone droplets in the range <1 μm that are not detected by laser diffraction. A slight peak in this range can be observed in Figure 4.15b, but is retarded due to the volume weighting. Volume weighted particle size analysis represents the population of particles based on their volume hence smaller particle sizes are less represented, unless they dominate the population of sizes.[88] The presence of silicone droplets in the micrometer and tens of micrometer size range is of beneficial value in the fabric softening phenomena. The hierarchical

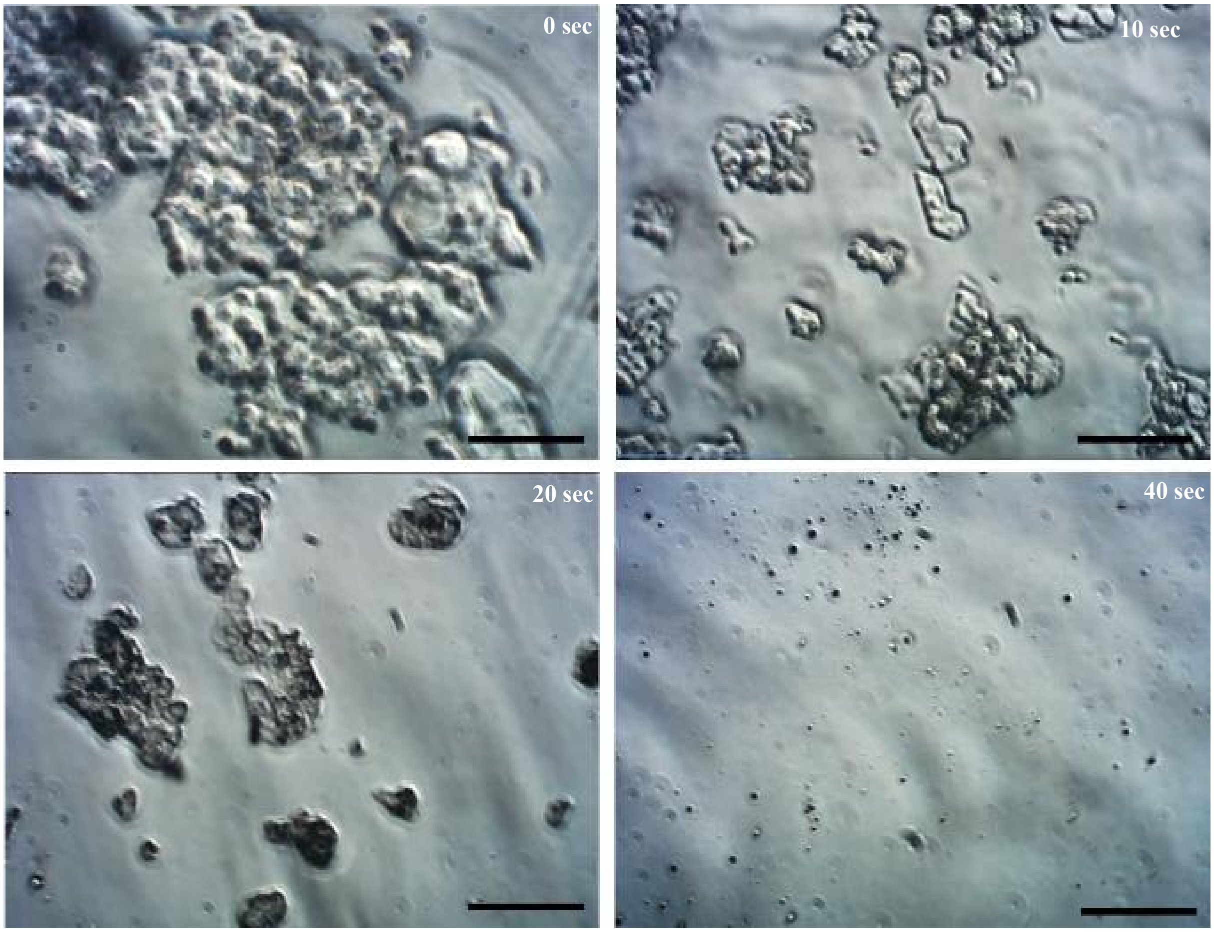

Figure 4.16. Optical microscopy images showing the time dependent changes in morphology of TAS-loaded SLM at pH 10.5 and room temperature change scale bar = 50 µm. Time displayed is the time after onset of matrix degradation.

structure of fabric comprises of micro-fibrils, fibres and yarns. The larger silicone droplets measured by laser diffraction are trapped in the inter-fibre gaps and hence deposit on the yarn surface and lubricate to minimise the dynamic coefficient of friction. This is an important parameter in the perception of softness to skin. The smaller particles (< inter-fibre distances ˜ 20 µm) are able to penetrate the yarn and lubricate the individual fibres which minimises the static coefficient of friction and hence the fibre-fibre interactions. Figure 4.17 shows an illustration of the deposition of silicone droplets of different particle sizes. Lubrication of the individual fibres

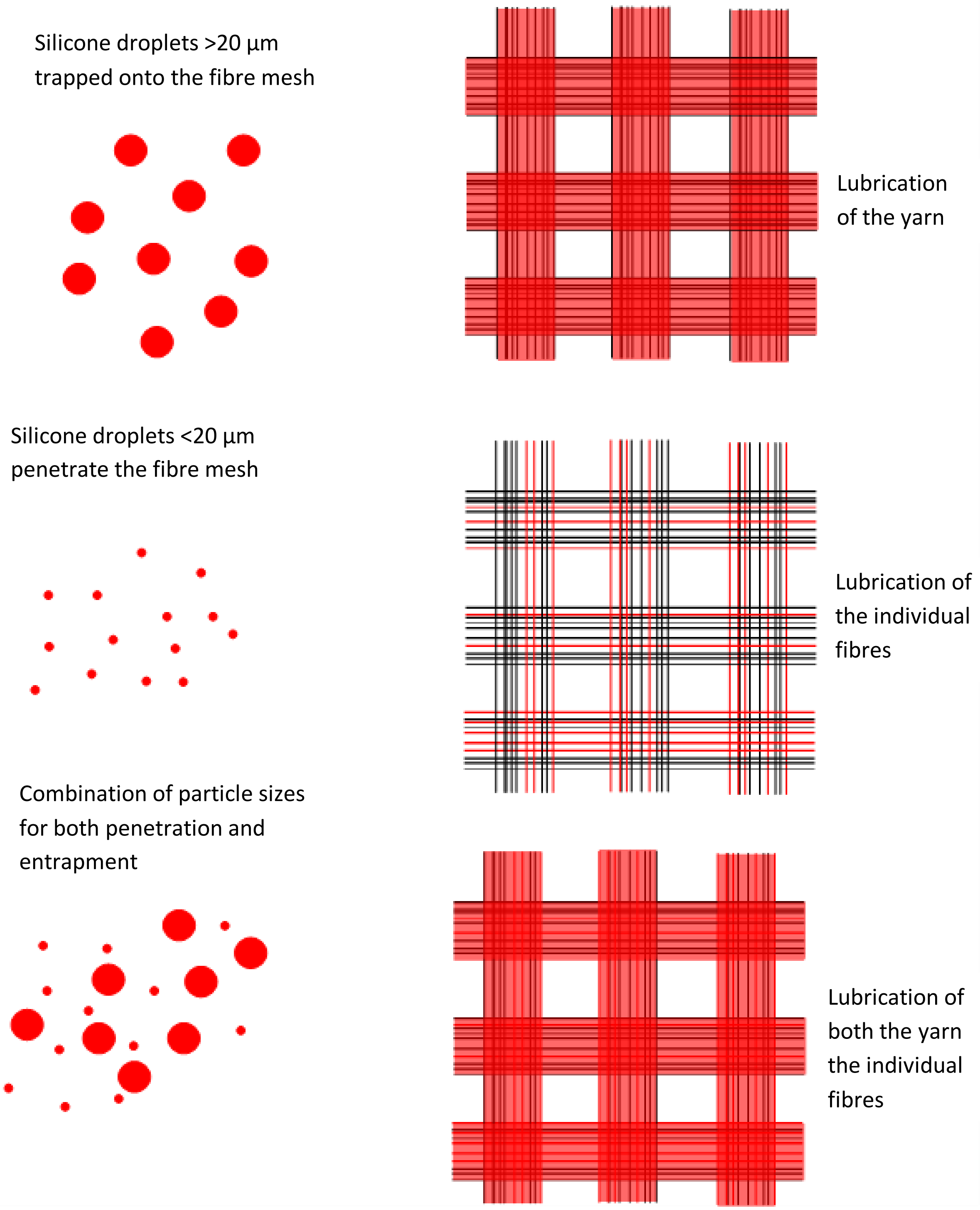

Figure 4.17. Schematic illustration of the size dependent deposition of actives on the yarn and individual fibres

brings additional advantages such as reduction of static cling, ease of ironing and durability of the fibres. See Appendix 3 for experimental data confirming this hypothesis.

4.2.7. SEM Analysis of Deposition onto Fabrics

Cotton and polyester fabrics treated with the silicone-loaded SLM solution where analyzed using SEM (Figure 4.18). The samples treated with SLM in water shows particles (100 -150 μm) trapped onto a fibre yarn. This is in agreement with the particle size analysis carried out using laser diffraction showing particle sizes in the same range. Samples treated with SLM in a pH 10.5 buffer

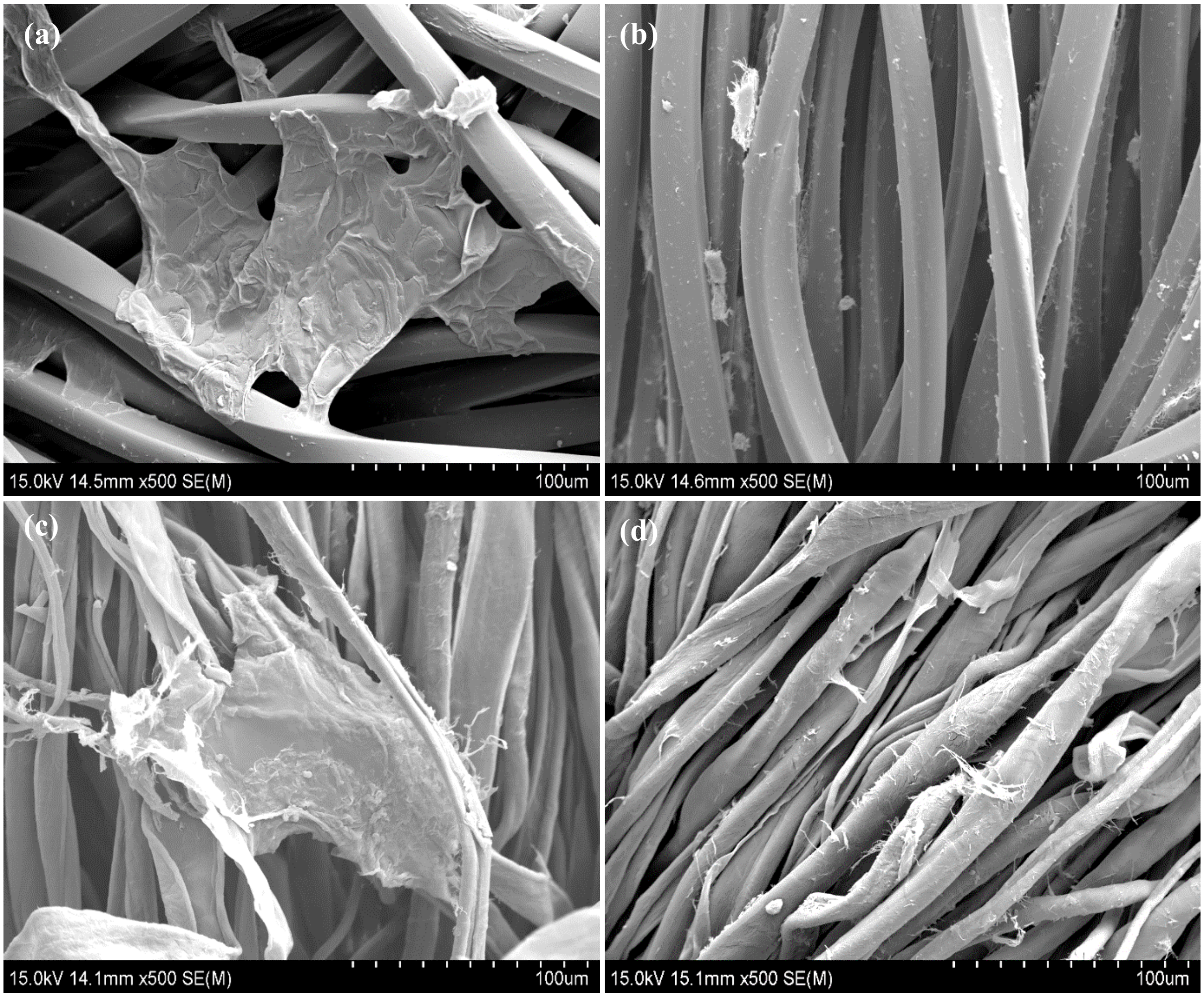

Figure 4.18. SEM images of the fabric samples treated with PDMS100-loaded SLM dispersed in tap water (a) polyester (c) cotton and fabric samples treated with PDMS100-loaded SLM dispersed in a pH 10.5 Na_2CO_3/$NaHCO_3$ buffer solution (b) polyester (d) cotton

solution does not contain these large particles, supporting the dissolution of the matrix observed with laser diffraction and optical microscopy. The released silicone particles deposit onto the yarn surface and form thin films on the fibre surface, which would not be visible via SEM (Figure 4.18b and 4.18d). See Appendix 4 for additional images.

4.3 Conclusions

In conclusion, this thesis has reported the successful preparation of silicone-loaded solid lipid particles, overcoming the immiscibility of the silicones and the lipid matrix by using solvent-based methods of preparation. Loading capacity and entrapment efficiency results have shown that n-hexane is a more suitable solvent for preparation of silicone-loaded SLM compared to ethanol. Thermal and diffraction analysis has shown that the particles adopt a silicone enriched core model of incorporation. The pH triggered release of silicones from the lauric acid matrix was confirmed using laser diffraction, optical microscopy and SEM. This is the first report of the application of solid lipid carrier particles to delivery of silicone oils, which are widely used in fabric care, hair care and cosmetology.

4.4 References

1 F. Case, *inform*, 2006, **17**, 559–561.

2 M. I. Levinson, *J. Surfactants Deterg.*, 1999, **2**, 223–235.

3 H. C. Borghetty and C. A. Bergman, *J. Am. Oil Chem. Soc.*, 1950, **27**, 88–90.

4 R. R. Egan, *J. Am. Oil Chem. Soc.*, 1978, **55**, 118–121.

5 W. R. Goynes and M. L. Rollins, *Text. Res. J.*, 1971, **41**, 226–231.

6 K.-Y. Lai, *Liquid Detergents*, CRC Press, 1996, vol. 19.

7 F. E. Friedli, R. Keys, C. Joe Toney, O. Portwood, D. Whittlinger and M. Doerr, *J. Surfactants Deterg.*, 2001, **4**, 401–405.

8 R. Franklin, M. D. Hoey and J. Zachwieja, in *Oleochemical Manufacture and Applications*, eds. F. D. Gunstone and R. J. Hamilton, CRC Press, 2001, pp. 23–48.

9 C. Overkempe, A. Annerling, C. G. van Ginkel, P. C. Thomas, D. Boltersdorf and J. Speelman, in *Novel Surfactants: Preparation Applications And Biodegradability*, ed. K. Holmberg, CRC Press, 2nd edn., 2003, pp. 347–384.

10 A. Farooq and C. J. Schramm Jr, in *Handbook of Detergents, Part E: Applications*, ed. U. Zoller, CRC Press, 2008, pp. 181–200.

11 R. Lagerman, S. Clancy, D. Tanner, N. Johnston, B. Callian and F. Friedli, *J. Am. Oil Chem. Soc.*, 1994, **71**, 97–100.

12 M. W. Skinner, Caibao Qian, S. Grigoras, D. J. Halloran and B. L. Zimmerman, *Text. Res. J.*, 1999, **69**, 935–943.

13 K. M. Zia, S. Tabassum, S. Barkaat-ul-Hasin, M. Zuber, T. Jamil and M. A. Jamal, *Int. J. Biol. Macromol.*, 2011, **48**, 482–487.

14 C. Stevens, in *Inorganic Polymers*, eds. R. De Jaeger and M. Gleria, Nova Science Publishers, 2007, pp. 97–98.

15 M. D. Berthiaume, in *Principles of Polymer Science and Technology in Cosmetics and Personal Care*, eds. D. E. Goddard and J. V Gruber, CRC Press, 1999, pp. 275–325.

16 S. Xu, R. G. Lehmann, J. R. Miller and G. Chandra, *Environ. Sci. Technol.*, 1998, **32**, 1199–1206.

17 A. R. Colas Curtis, J, *Silicone Biomaterials: History and Chemistry & Medical Applications of silicones* , Elsevier Academic Press, 2004.

18 B. Boutevin, F. Guida-Pietrasanta and A. Ratsimihety, in *Silicon-Containing Polymers*, eds. R. Jones, W. Ando and J. Chojnowski, Springer Netherlands, 2000, pp. 79–112.

19 P. R. Dvornic, in *Silicon-Containing Polymers*, eds. R. Jones, W. Ando and J.

Chojnowski, Springer Netherlands, 2000, pp. 185–212.

20 A. L. Smith, *Introduction to Silicones*, John Wiley & Sons, 1991, vol. 112.

21 P. Habereder and A. Bereck, *Rev. Prog. Color. Relat. Top.*, 2002, **32**, 125–137.

22 R. M. Hill, *Silicone Surfactants*, Taylor & Francis, 1999.

23 A. J. O'Lenick, *J. Surfactants Deterg.*, 2000, **3**, 229–236.

24 M. J. Owen, *Chemtech*, 1981, **11**.

25 D. Graiver and G. Fearon, in *Silicon-Containing Polymers*, eds. R. Jones, W. Ando and J. Chojnowski, Springer Netherlands, 2000, pp. 233–243.

26 J. Emsley, *The Elements*, Clarendon Press, 3rd edn., 1998.

27 J. Kotz, P. Treichel, J. Townsend and D. Treichel, *Chemistry & Chemical Reactivity*, Cengage Learning, 2014.

28 G. Wulfsberg, *Inorganic Chemistry*, University Science Books, 2000.

29 L. Merhari, *Hybrid Nanocomposites for Nanotechnology: Electronic, Optical, Magnetic and Biomedical Applications*, Springer Science & Business Media, 2009.

30 U. Schubert and N. Hüsing, *Synthesis of Inorganic Materials*, Wiley, 2012.

31 Shaow B. Lin, *High-Temperature Properties and Applications of Polymeric Materials*, American Chemical Society, Washington, DC, 1995, vol. 603.

32 C. Jalbert, J. T. Koberstein, I. Yilgor, P. Gallagher and V. Krukonis, *Macromolecules*, 1993, **26**, 3069–3074.

33 M. Zuber, K. M. Zia, S. Tabassum, T. Jamil, S. Barkaat-ul-Hasin and M. K. Khosa, *Int. J. Biol. Macromol.*, 2011, **49**, 1–6.

34 M. Parvinzadeh, *J. Surfactants Deterg.*, 2007, **10**, 219–223.

35 J. N. Lee, C. Park and G. M. Whitesides, *Anal. Chem.*, 2003, **75**, 6544–6554.

36 D. Schaeffer, *Tenside Surf. Det.*, 1990, **27**, 154–158.

37 P. Purohit, P. Somasundaran and R. Kulkarni, *J. Colloid Interface Sci.*, 2006, **298**, 987–990.

38 H. Nazir, P. Lv, L. Wang, G. Lian, S. Zhu and G. Ma, *J. Colloid Interface Sci.*, 2011, **364**, 56–64.

39 M. Parvinzadeh and R. Hajiraissi, in *AIP Conference Proceedings*, AIP, 2007, vol. 929, pp. 216–219.

40 L. Muxin, A. B. Michael, M. Z. Paul and N. R. Amro, in *Colloidal Biomolecules, Biomaterials, and Biomedical Applications*, CRC Press, 2003, pp. 309–328.

41 P. Somasundaran, S. C. Mehta and P. Purohit, *Adv. Colloid Interface Sci.*, 2006, **128–130**, 103–9.

42 A. O'Lenick Jr., *J. Surfactants Deterg.*, 2000, **3**, 387–393.

43 R. Tiwari and P. Tahkistov, in *Nanotechnology Research Methods for Food and Bioproducts*, ed. G. W. Padua Wang, Q., Wiley, 2012, pp. 55–102.

44 H. Jeong. S Park. J, H., Park. K, in *Role of Lipid Excipients in Modifying Oral and Parenteral Drug Delivery: Basic Principles and Biological Examples*, ed. K. M. Wasan, Wiley, 2007, pp. 32–39.

45 W. Mehnert and K. Mäder, *Adv. Drug Deliv. Rev.*, 2001, **47**, 165–196.

46 R. H. Müller, K. Mäder and S. Gohla, *Eur. J. Pharm. Biopharm.*, 2000, **50**, 161–177.

47 M. Nabi-Meibodi, A. Vatanara, A. R. Najafabadi, M. R. Rouini, V. Ramezani, K. Gilani, S. M. H. Etemadzadeh and K. Azadmanesh, *Colloids Surfaces B Biointerfaces*, 2013, **112**, 408–414.

48 B. Sjöström and B. Bergenståhl, *Int. J. Pharm.*, 1992, **88**, 53–62.

49 D. Liu, S. Jiang, H. Shen, S. Qin, J. Liu, Q. Zhang, R. Li and Q. Xu, *J. Nanoparticle Res.*, 2011, **13**, 2375–2386.

50 P. K. Gaur, S. Mishra, M. Bajpai and A. Mishra, *Biomed Res. Int.*, 2014, **2014**, 1–9.

51 Y. Luo, D. Chen, L. Ren, X. Zhao and J. Qin, *J. Control. Release*, 2006, **114**, 53–59.

52 F. Q. Hu, Y. Hong and H. Yuan, *Int. J. Pharm.*, 2004, **273**, 29–35.

53 F.-Q. Hu, S.-P. Jiang, Y.-Z. Du, H. Yuan, Y.-Q. Ye and S. Zeng, *Colloids Surfaces B Biointerfaces*, 2005, **45**, 167–173.

54 M. Trotta, F. Debernardi and O. Caputo, *Int. J. Pharm.*, 2003, **257**, 153–160.

55 M. Trotta, R. Cavalli, M. E. Carlotti, L. Battaglia and F. Debernardi, *Int. J. Pharm.*, 2005, **288**, 281–288.

56 Y. Zhang, C. Wang, Y. Huang, H. Yan and K. Liu, *Eur. Polym. J.*, 2015, **68**, 104–114.

57 S.-S. Hong, S. H. Kim and S.-J. Lim, *Int. J. Pharm.*, 2015, **483**, 142–50.

58 R. Galović Rengel, K. Barišić, Ž. Pavelić, T. Žanić Grubišić, I. Čepelak and J. Filipović-Grčić, *Eur. J. Pharm. Sci.*, 2002, **15**, 441–448.

59 J. Otarola, A. G. Lista, B. Fernández Band and M. Garrido, *J. Pharm. Anal.*, 2015, **5**, 70–73.

60 B. N. Viswanathan, P. A. Thomas, J. K. Pandit, M. G. Kulkarni and R. A. Mashelkar, *J. Control. Release*, 1999, **58**, 9–20.

61 X. Xu, Y. Fu, H. Hu, Y. Duan and Z. Zhang, *J. Pharm. Biomed. Anal.*, 2006, **41**, 266–73.

62 K. J. Slatkavitz, L. D. Hoey, P. C. Uden and R. M. Barnes, *Anal. Chem.*, 1985, **57**, 1846–1853.

63 R. Grümping and A. V. Hirner, *Fresenius. J. Anal. Chem.*, 1999, **363**, 347–352.

64 M. Hornung and V. Krivan, *J. Anal. At. Spectrom.*, 1997, **12**, 1123–1130.

65 V. Blechta, M. Kurfürst, J. Sýkora and J. Schraml, *J. Chromatogr. A*, 2007, **1145**, 175–82.

66 B. A. Cavic-Vlasak, M. Thompson and D. C. Smith, *Analyst*, 1996, **121**, 53R.

67 F. Chainet, C.-P. Lienemann, M. Courtiade, J. Ponthus and O. F. Xavier Donard, *J. Anal. At. Spectrom.*, 2011, **26**, 30–51.

68 R. L. Scholl, G. E. Maciel and W. K. Musker, *J. Am. Chem. Soc.*, 1972, **94**, 6376–6385.

69 M. Andriot, S. H. Chao, A. R. Colas, S. E. Cray, F. deBuyl, J. V DeGroot, A. Dupont, T. Easton, J. L. Garaud and E. Gerlach, 2009, 84.

70 H. M. Klimisch, in *The Analytical Chemistry of Silicones*, 1991, pp. 117–132.

71 L. J. Bellamy, Chapman and Hall, London, 3rd edn., 1975, p. p.374-384.

72 R. B. Taylor, P. B and D. M. Fillmore, in *The Analytical Chemistry of Silicones*, eds. J. D. Winefordner and I. M. Kolthoff, 1991, pp. 347–419.

73 M. D. Gaul and N. C. Angelotto, in *The Analytical Chemistry of Silicones*, eds. J. D. Winfordner and I. Kolthoff, John Wiley & Sons INC., 1991, pp. 175–217.

74 H. Kopsch, *Thermal Methods in Petroleum Analysis*, John Wiley & Sons, 2008.

75 M. A. Osman, M. Ploetze and U. W. Suter, *J. Mater. Chem.*, 2003, **13**, 2359.

76 D. W. Holcomb and R. A. Young, *Calcif. Tissue Int.*, 1980, **31**, 189–201.

77 K. Vezzù, C. Campolmi and A. Bertucco, *Int. J. Chem. Eng.*, 2009, **2009**, 9.

78 J. Li, M. Rodrigues, A. Paiva, H. A. Matos and E. Gomes de Azevedo, *AIChE J.*, 2005, **51**, 2343–2357.

79 N. Wright and M. J. Hunter, *J. Am. Chem. Soc.*, 1947, **69**, 803–809.

80 A. J. Horsewill, A. Heidemann and S. Hayashi, *Z. Phys.*, 1993, **90**, 319–324.

81 W. Zeng, Y. Du, Y. Xue and H. L. Frisch, in *Physical Properties of Polymers Handbook*, ed. J. E. Mark, Springer New York, 2nd edn., 2007, pp. 289–303.

82 V. Tewary and Y. Zhang, *Modeling, Characterization and Production of Nanomaterials: Electronics, Photonics and Energy Applications*, Elsevier Science, 2015.

83 J. Aronhime, S. Sarig and N. Garti, *Food Struct.*, 1990, **9**, 337–352.

84 M. A. Schubert and C. C. Müller-Goymann, *Eur. J. Pharm. Biopharm.*, 2005, **61**, 77–86.

85 E. Moreno, R. Cordobilla, T. Calvet, M. A. Cuevas-Diarte, G. Gbabode, P. Negrier, D.

Mondieig and H. A. J. Oonk, *New J. Chem.*, 2007, **31**, 947–957.

86 M. Uner, *Pharmazie*, 2006, **61**, 375–386.

87 C. Schwarz, W. Mehnert, J. S. Lucks and R. H. Müller, *J. Control. Release*, 1994, **30**, 83–96.

88 N. Stanley-Wood and R. W. Lines, *Particle Size Analysis*, Royal Society of Chemistry, 1992.

5. Solid Lipid Microparticles in Delivery of Hueing Dyes and Dual Active Loading

Laundry actives have the propensity to interact with detergents and other excipients in formulation; consequently, they can be rendered ineffective. Incorporating the actives in a solid matrix can prevent this by isolating the actives from other ingredients. This chapter reports an investigation of the possibility of loading hueing dyes onto a lauric acid matrix. The two dyes used in this investigation are Coomassie Brilliant Blue R and Ethyl Violet. Additionally the possibility of loading two actives (hueing dyes and silicones) to create a dual-active solid lipid microparticle system (SLM) is also reported here. In preliminary studies, the particles were prepared using the solvent emulsification/diffusion method, which gave low values of entrapment efficiency. The double emulsion method of preparation showed a significant increase in entrapment efficiency. The concentration of dye loaded onto the particles was obtained using UV/VIS spectroscopy. Physicochemical characterisation was carried out using laser diffraction, polarised light microscopy, SEM, FTIR, DSC and TGA. Polyester and cotton fabric samples treated with the dye loaded SLM systems at laundry pH (10.5) were studied using confocal microscopy.

5.1 Introduction

Dyes and pigments have been used in textile treatment since prehistoric times and have become detrimental to the modern fabric treatment process.[1–3] Dyes are substances that absorb light at specific wavelengths and consequently control the colour of light transmitted or reflected.[4] The astounding bloom in the dye and pigments industry was fuelled by the emergence of synthetic dyes, which was inspired by the 19th century British chemist, Sir William Henry Perking.[3] He stumbled upon the first known synthetic dye which became widely known as Mauveine, whilst attempting to synthesize an anti-malarial drug.[5,6] This discovery had a severe impact the natural dye industry, which were far more expensive due to the highly inefficient extraction methods and inferior performance in comparison to their counterparts;[7] therefore dyes used in modern industrial processes are predominantly synthetic. Dyes, also referred to as chromogens, comprise of a chromophore group; the chromophore group determines the absorbance and emittance behaviour of the dye.[8] In the textile industry, dyes are classified according to the method of application.[9] The dye application process and choice of dye is dependent the type of fibres and the surface properties of the fibre. Dyes can adsorb to textile fibres by means of strong covalent bonds, as in the case of reactive dyes for cellulosic fibres.[10] They can also interact with textile fibres by means of ionic interactions as in the case or acid dyes, direct dyes and basic dyes.[9] Disperse dyes, used in coloration of synthetic fibres, interact with textile fibres by means of Van Der Waals interactions.[11] The aesthetic appearance and shade of textile fibres tends to depreciate with age, degradation of fibres and repeated laundry cycles. Coloured textiles tend to loose vibrancy and become dull with repeated use and laundering, while white fabrics experience yellowing. [12–14] This can be attributed to the build-up of residual detergents, remnant soils and bleaching agents. Bleaching agents are a common ingredient in detergent formulation; chlorine used in many municipal systems for disinfecting water, has a bleaching effect on fabrics. Aging of the fibres, exposure to sunlight leading to photodegradation and exposure to environmental pollutants can also contribute to the yellowing of white fabrics and dulling of coloured fabrics.[15] Hueing dyes are incorporated into fabric care products to reduce yellowing and boost the appearance dulling colours.[16]

Hueing dyes absorb light at a wavelength that enables neutralisation of yellowing and visually brightens textile fibres to boost the dull appearance of colour and whiteness.[17] White surfaces reflect all incident wavelengths of visible radiation; coloured surfaces absorb some wavelengths and reflect those that are analogous with the perceived colour. Whiteness or vibrancy of colour can thus be described by the reflectance and absorption of visible light. The Kubelka-Munk theory

$$\frac{k}{s} = \frac{(1-R)^2}{2R} \qquad \text{Eqn 5.1}$$

where k is the molar absorption coefficient, s is the scattering coefficient and R is the relative diffuse reflectance of the test material relative to pure white standard (e.g. MgO has been used to describe the optical appearance of natural and synthetic fibres).[18–21] White surfaces have relative diffuse reflectance values close to that of the pure white standard and are characterised by low absorption coefficients and high scattering coefficients. The fabric yellowing phenomena is due to the increase of absorption coefficient in the blue to violet region resulting in a *yellowish* hue (Figure 5.1).[22] Introducing a blue or violet dye on the surface of the fabric can compensate for the absorption to give a visual perception of whiteness.

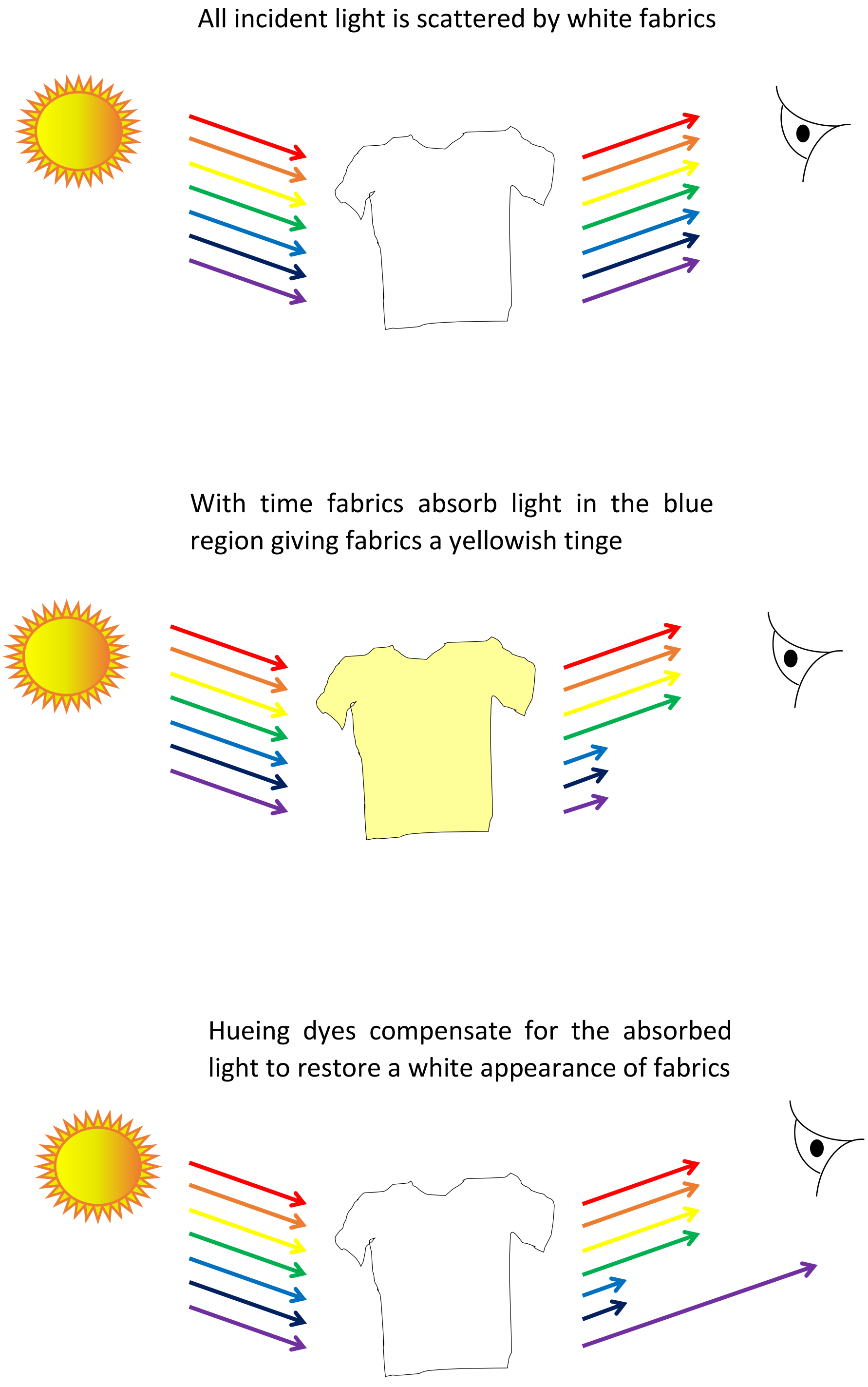

All incident light is scattered by white fabrics

With time fabrics absorb light in the blue region giving fabrics a yellowish tinge

Hueing dyes compensate for the absorbed light to restore a white appearance of fabrics

Figure 5.1. Illustrating the absorption of light in the blue region resulting in yellowing of white fabrics

5.1.1 Hueing dyes in Fabric Care

Several patents have been issued regarding hueing dyes.[13,23–26] Hueing refers to the alteration of shade due to accumulation of colorants; most dyes do not work after a single application but accumulate over time.[13] Hueing agents are compounds belonging to the wider family of dyes, pigments or photobleaches (e.g. copper based phthalocyanines).[27] According to a 1934 magazine article, earlier forms of hueing agents referred to as ‘bluing’ were powder or solution forms of Prussian blue (iron ferrocyanide).[28] A more popular bluing agent, synthetic ultramarine blue also nicknamed Reckitt’s blue after the manufacturing company, Reckitt & Sons, was already on the market by the early twentieth century.[29] Ultramarine blue is a water insoluble pigment incorporated into laundry detergent formulations in powder form or as a dispersion.[30] Hydrophobic hueing agents tend to show patchy deposition on the fabric surface and hence hydrophilic dyes are more preferrable.[31] Examples of suitable hueing dyes include direct azo dyes, dis-azo dyes, acid dyes, basic dyes, other triphenylmethanes and their derivaties and dye polymer conjugates (Figure 5.2).

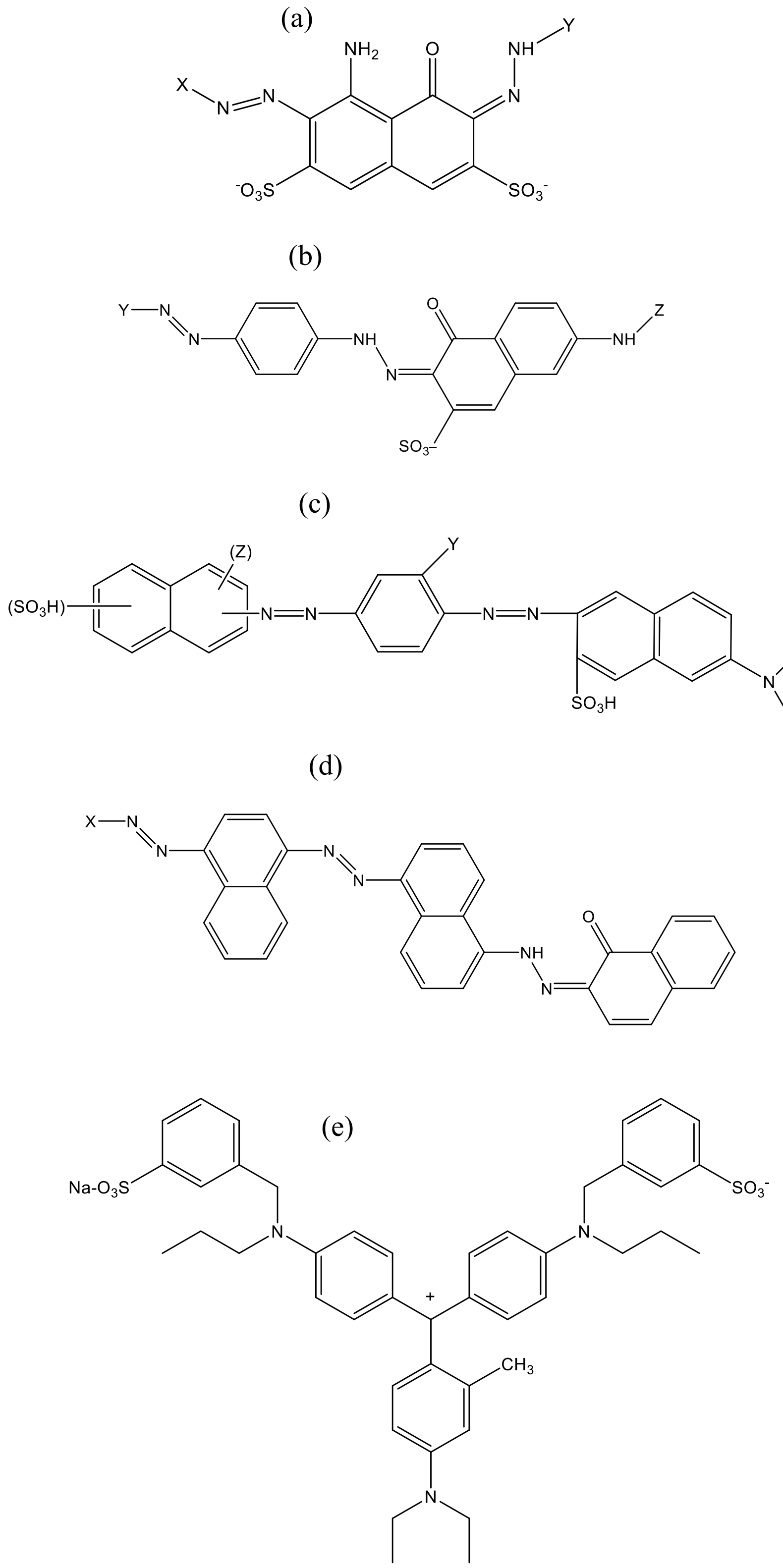

Figure 5.2. Chemical structures of some suitable candidates for hueing agents from the family of (a) blue acid dyes (b) bis-azo direct violet dyes (c) dis-azo dye (d) tris-azo direct blue dye (e) triphenylmethane

5.1.2 SLM for Delivery of Hueing Dyes

Hueing dyes are applied to fabrics in different ways: separately, in detergent formulations (during the wash cycle) or in rinse-added fabric softener formulations (during the rinsing cycle). The emergence of 2-in-1 detergent formulations in the last two decades, has necessitated more research into means of incorporating various actives into one formulation. However, another issue arises concerning the coexistence and maintenance of the effective function of the individual actives. Hueing dyes can interact with anionic detergents and form complexes, which effectively lowers the concentration of the dye available for deposition and detergent available for cleaning and thereby reduces the efficiency of both actives. Recent patents have reported a method of circumventing this by using a unit dose application method.[32–34] Unit dose articles are multi-compartment pouches made from water soluble polymers where incompatible actives are separated by polymer films to ensure stability in formulation. Other particulate polymer based solid matrices for hueing dyes have also been reported.[27] This chapter presents another method of isolating individual or dual actives in a solid lipid matrix. SLM systems are effective at minimising the mobility of actives and could be utilised to minimise bleeding, which is a common problem with dyes in laundry formulations. SLM systems are compatible with both hydrophobic and hydrophilic actives which makes them suitable candidates for encapsulation of various types of hueing agents and other laundry actives. SLM dispersions can be highly applicable in laundry and other household applications as they can be added to detergent formulations that are in liquid or gel form; dehydrated particles can be added to detergents in powder form. Two non-azo dyes, brilliant blue and ethyl violet were used in this investigation. The dye-loaded SLM systems were prepared using a solvent-assisted double emulsion method. The double emulsion method is based on the w/o/w emulsion principle. The w/o/w emulsion is a three phase system where the dye is contained in the inner emulsion (w/o) and is surrounded by a molten lipid phase, which becomes the solid matrix after precipitation. An illustration of the method of preparation and structural arrangement of the double emulsion is shown in Figure 5.3. In addition to the incorporation of dyes using the double emulsion method, this chapter also reports the incorporation two actives onto the same matrix to give a *dual active* system. The concept of incorporation of more than one active into SLN systems has been investigated by Jain et al., who reported the co-encapsulation of albendazole and prednisolone for effective pain management at lower dosage frequencies.[35] In laundry applications, this concept could be instrumental in compact formulations and 2-in-1 detergents. An aminofunctionalized silicone, PK10 was incorporated as the second active; PK10 was added to the oil phase during preparation.

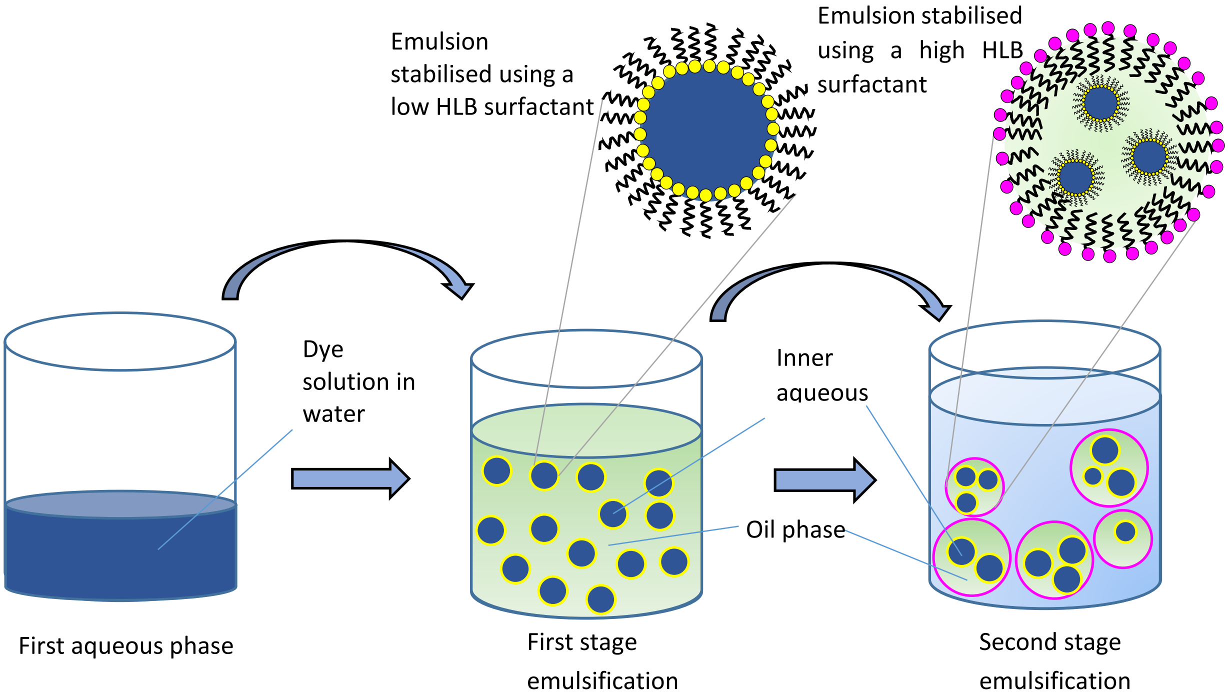

Figure 5.3. Illustrating the two stage emulsification process used to create a w/o/w emulsion. The hydrophilic dye is dissolved in water and emulsified in the oil phase (lauric acid + span 80 with or without silicone)

5.1.3 Brilliant Blue Dye

Brilliant blue dyes, also named Coomassie Brilliant Blue (CBB) after the Ghanaian town, Kumasi, are a group of disulphonated triphenylmethane dyes.[36] Brilliant blue dyes were initially applied in textile applications (e.g. colouring protein fibres such as wool), but they are now widely used in protein chemistry for staining in gel electrophoresis methods and colorimetric determination of protein composition (e.g. in Bradford protein assay).[36–39] Brilliant blue R (referred to as BB for the rest of the chapter) is one of the two main CBB dyes where the suffix denotes the colour of the tint associated with the dye; R denotes a red tint. BB has the propensity to interact with fabrics by electrostatic interactions, van der Waals forces and hydrogen bonding. At neutral to alkaline pH values, the nitrogen atoms (Figure 5.4) in the molecule are deprotonated and can interact with the slightly negatively charged fabric surface through electrostatic interactions. The dyes can also interact with anionic detergents, enzymes and protein based soils preventing the deposition onto fabric surfaces; this can be minimised by encapsulating the dyes in a carrier matrix.

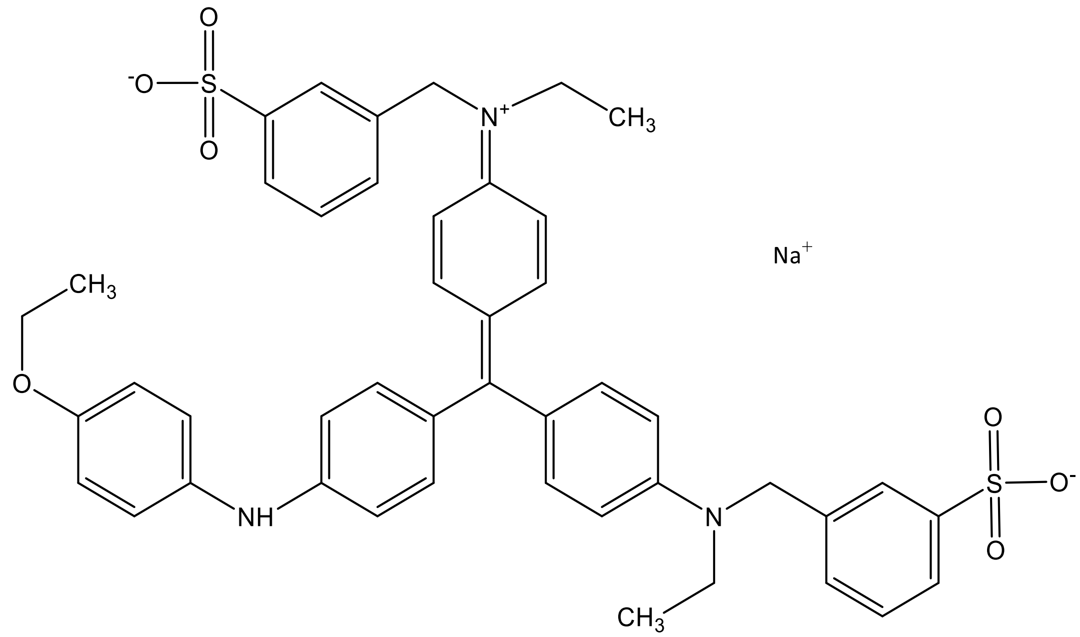

Figure 5.4. The chemical structure of coomassie brilliant blue R dye ($C_{45}H_{44}N_3NaO_7S_2$)

5.1.4 Ethyl Violet Dye

Ethyl violet (EV) dye, also known as basic violet 4, is a cationic triphenylmethane dye (Figure 5.5). EV is a versatile dye that is used in a wide variety of applications. It is used as a stain in biological imaging applications as well as a colorant in textile, paper, food, hair and cosmetic industries. Cationic triphenylmethane dyes interact with fabric surfaces mainly by electrostatic interactions; however, surface energy is thought to play a significant role.[40] Ethyl violet is known to form ion complexes with ionic surfactants, which enables its use in the determination of anionic surfactants.[41] Isolation of EV dyes in laundry applications is essential to prevent these interactions.

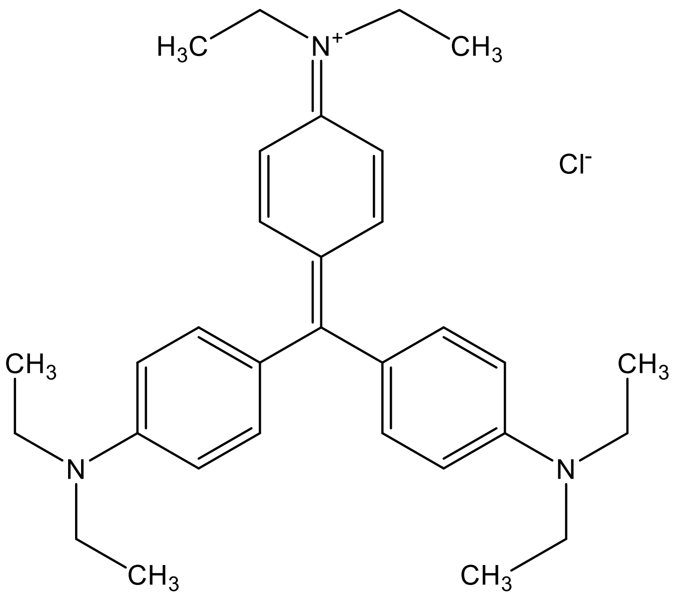

Figure 5.5. The chemical structure of ethyl violet dye, 4-(Bis(4-(diethylamino)phenyl)methylene)-2,5-cyclohexadien-1-ylidene)diethylammonium chloride

5.2. Results and Discussions

5.2.1 Entrapment Efficiency

Calibration curves were constructed for both dyes in water (Figure 5.6) and were used in the calculation of the amount of loaded dye by measuring the concentration of dye in the supernatant (the outer water phase). The maximum intensity peak for the dyes exhibit a linear relationship with concentration as expected. The intensity curves for BB show two peaks with a λ_{max} value of 555 nm for the dominant peak and another at 592 nm. This is similar to the UV/VIS spectra for BB in water media reported by Rayaroth et al., where the λ_{max} value was 554 nm with a similar second peak.[42] The gradient of the calibration plot for the BB dye was $(4.87 \pm 0.02) \times 10^4$ M^{-1} cm^{-1}. Two peaks were observed for the EV dye spectra with λ_{max} at 595 nm and another peak at 553 nm; this matches the λ_{max} value suggested by the supplier. The gradient of the calibration plot for EV was $(1.12 \pm 0.2) \times 10^5$ M^{-1} cm^{-1}.

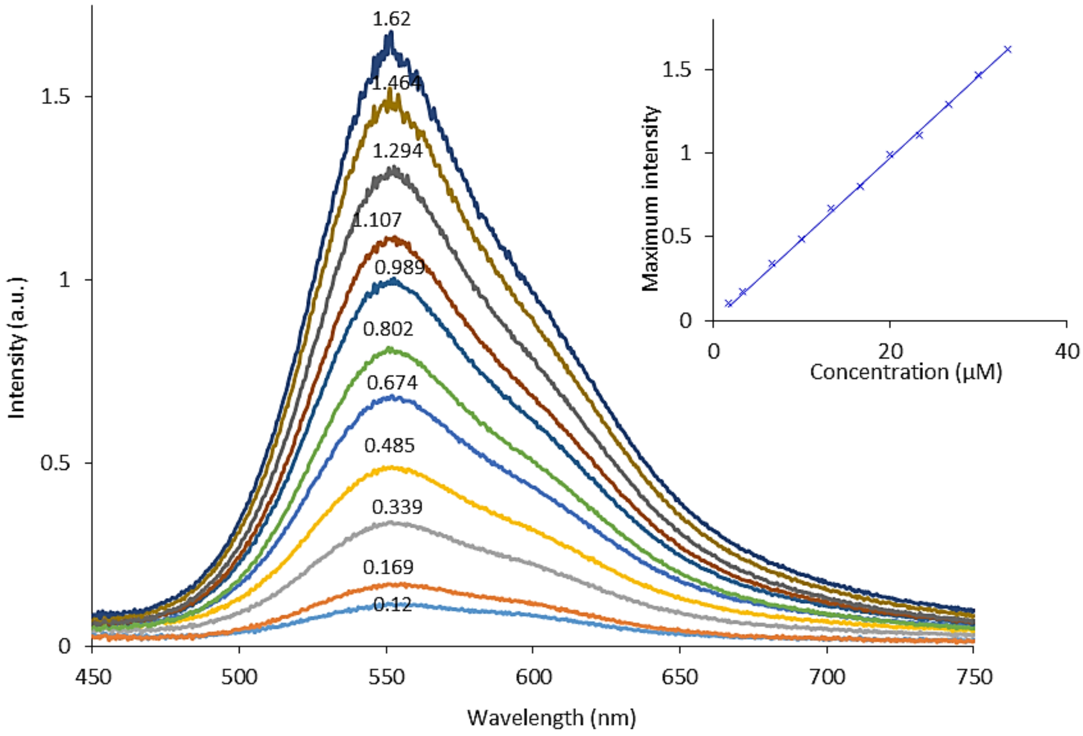

Figure 5.6. UV/VIS spectra for different concentrations of BB in water and the corresponding calibration plots (inset)

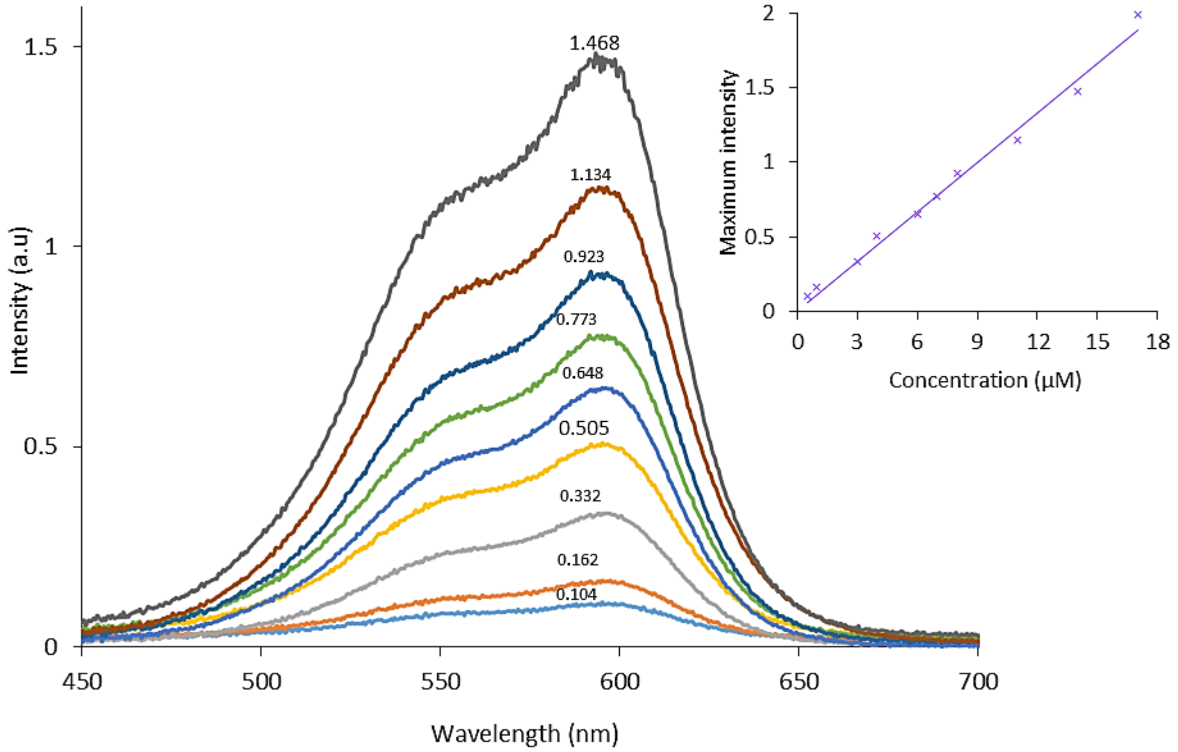

Figure 5.7. UV/VIS spectra for different concentrations of EV in water and the corresponding calibration plots (inset)

A 1 µL aliquot was taken from the continuous phase of the dye-SLM dispersions and diluted in water to give a 2ml sample. The maximum intensity value was used to calculate the concentration of the dye in the sample using the coefficients obtained from the calibration plots and accounting for the dilution. The concentration of the total dye added during preparation was calculated. The entrapment efficiency (EE) was calculated using the expression

$$EE = 100 - \left(\frac{concentration\ of\ dye\ unincorporated\ dye}{Total\ concentration\ of\ added\ dye} x100\right) \qquad \text{Eqn 5.2}$$

EE values for the BB- and EV-loaded single or dual active systems are shown in Table 5.1. A high entrapment value of 88.6 ± 0.1 % for EV-loaded dyes with no silicones and 88.4 ± 0.2 % for the EV-loaded SLM system with silicone. The presence of the silicone in the matrix does not seem to affect the amount of EV dye loaded. Comparatively lower EE values were observed

SLM system	EE (%)
BB-SLM	26.4 ± 5.9
EV-SLM	88.6 ± 0.1
BB-SLM + silicone	10.4 ± 0.6
EV-SLM + silicone	88.4 ± 0.2

Table 5.1. Entrapment efficiency values for SLM systems loaded with BB and EV in a single or dual active system (with or without silicone)

for the BB dye, at 26.4 ± 5.9 % for the single-active system and 10.4 ± 0.6 % for the dual active system, implying poor incorporation of the BB dye into the matrix. The dye leaks into the lipid phase and diffuses through the lipid phase to the continuous phase. The time between emulsification (of the w/o emulsion in the outer aqueous phase) and cooling in an ice-bath could potentially play a significant role in the partitioning of the dye. Therefore, any differences in the preparation of the samples could also potentially affect the entrapment efficiency.

5.2.2 Particle Size and Morphology

The morphology of the dye-loaded SLM systems was studied using optical microscopy methods and electron microscopy. Figure 5.8 shows the bright-field microscopy images of the SLM systems. The BB- and EV-loaded SLM in a single-active system show distinct boundaries between the particles where the particle shapes are inhomogeneous with diameters between 100 μm to 300 μm. There is a distinct colour difference between the liquid background and the particles. The yellow regions represent the solid lipid matrix and the green regions represent the dye that is incorporated into the lipid matrix. For systems where silicone is included in the dye-loaded SLM, larger structures with no distinct boundaries are observed for both dyes in the dual active system. This suggests that the silicone oils alter the physicochemical properties of the SLM. The same images were also taken with a polarized light filter inserted (Figure 5.9). Polarized light microscopy enables visualization of crystalline structures and can be used in combination with light microscopy to confirm the position of the lipid. It can also be used to confirm the recrystallisation of the lipid during precipitation. The images for the SLM systems shown in Figure 5.9 confirm that the lipid has a crystalline arrangement as the regions for the lipid observed by polarization microscopy coincide with those observed by bright field microscopy.

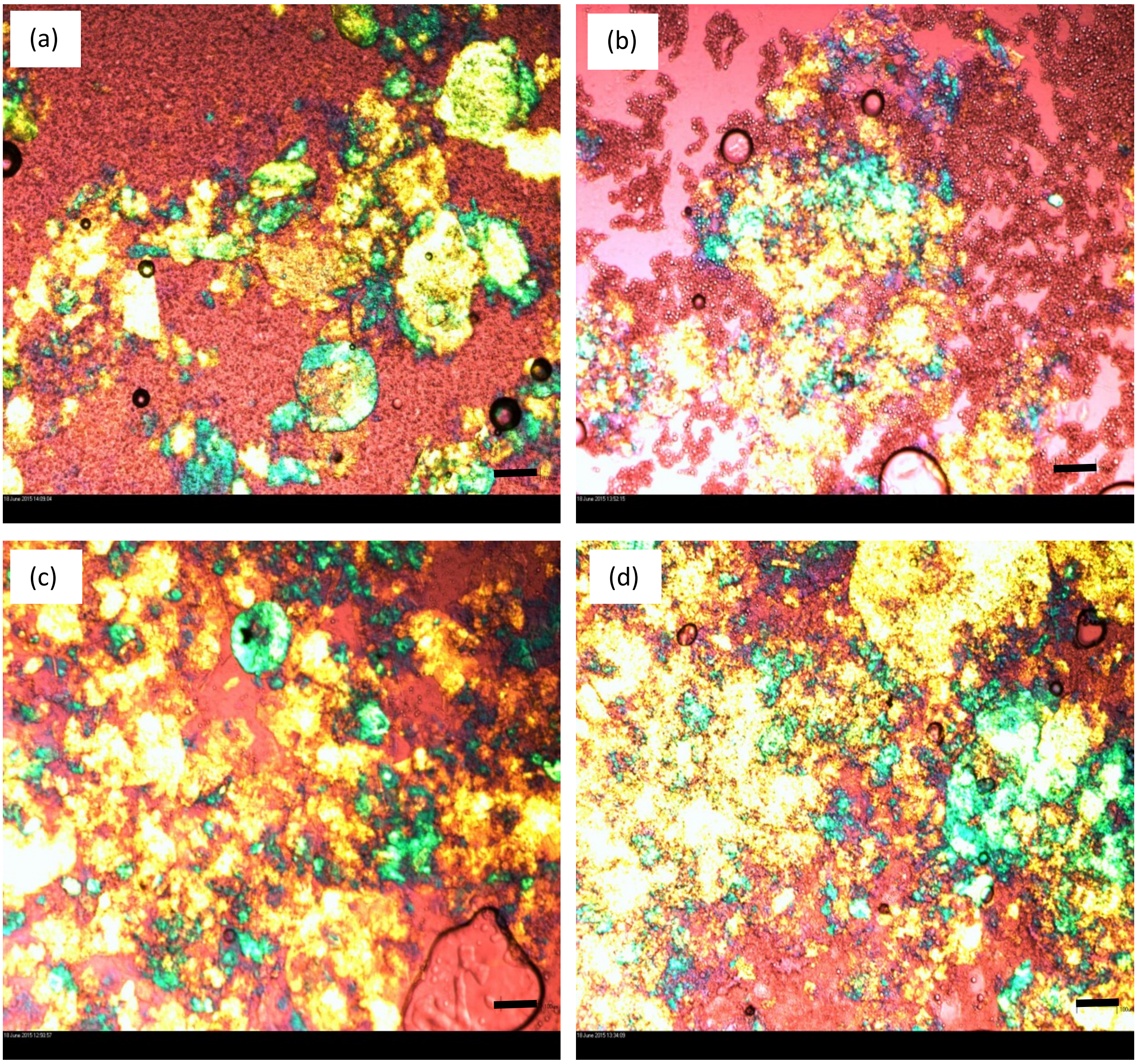

Figure 5.8. Bright field microscopy images of SLM systems loaded with (a) BB dye (b) EV dye (c) BB dye with silicone and (d) EV dye with silicone. Scale bar = 100 µm

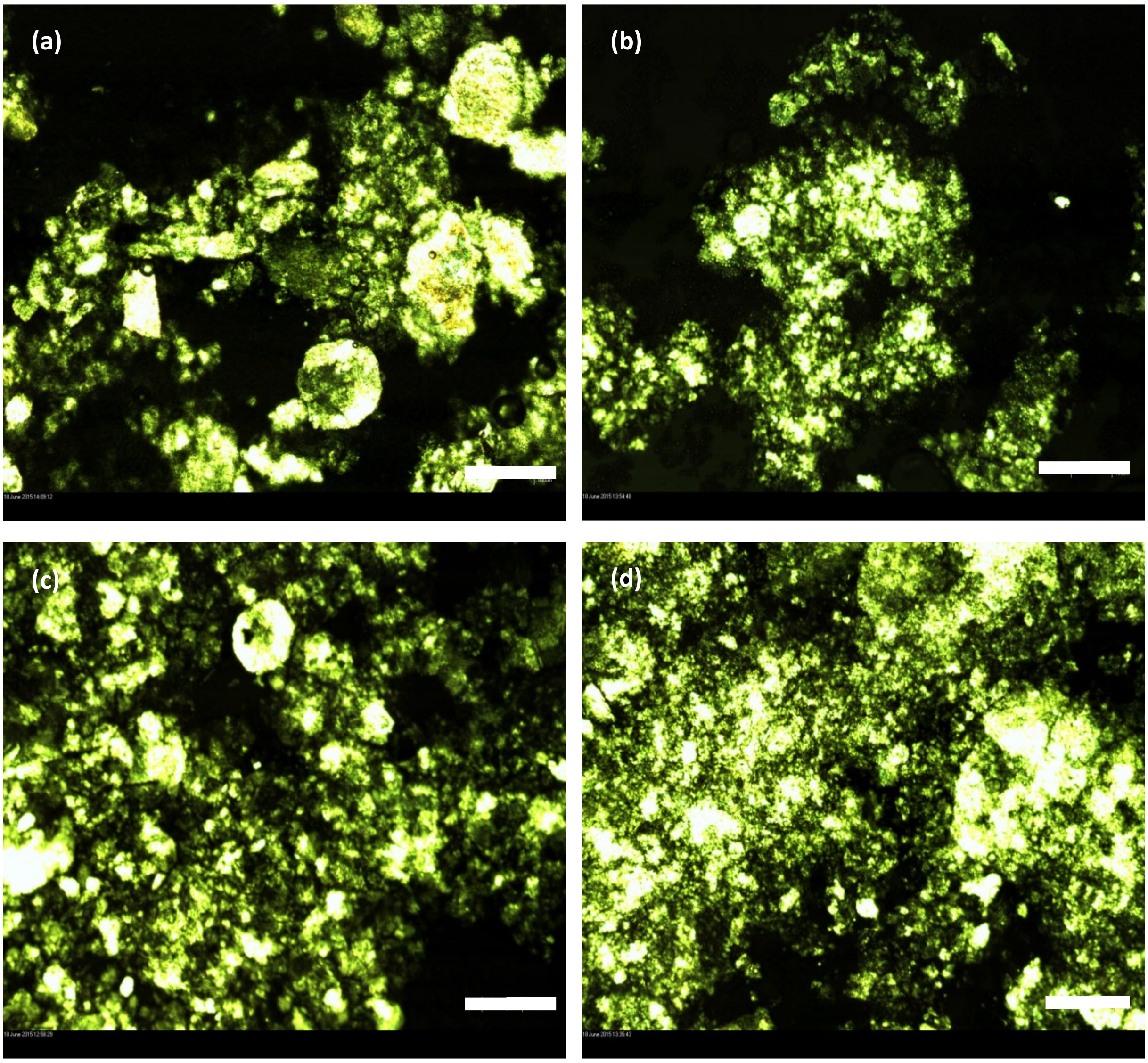

Figure 5.9. Polarized light microscopy images of SLM systems loaded with (a) BB dye (b) EV dye (c) BB dye with silicone and (d) EV dye with silicone. Scale bar = 200 µm

Further morphological characterisation was carried out using SEM (Figure 5.10). Significant differences in the shape, size and surface morphology between the single active and dual active systems were be observed. This complements the optical microscopy findings. The particles with no silicones have distinct boundaries and a rounded shape and a comparatively smooth surface; the inner phase emulsion (water in oil) particles can be observed on the surface of the microparticles as white dots (Figure 5.10ai). The system with silicones is characterised by a rough surface with no observable inner phase emulsion particles on the microparticle surface.

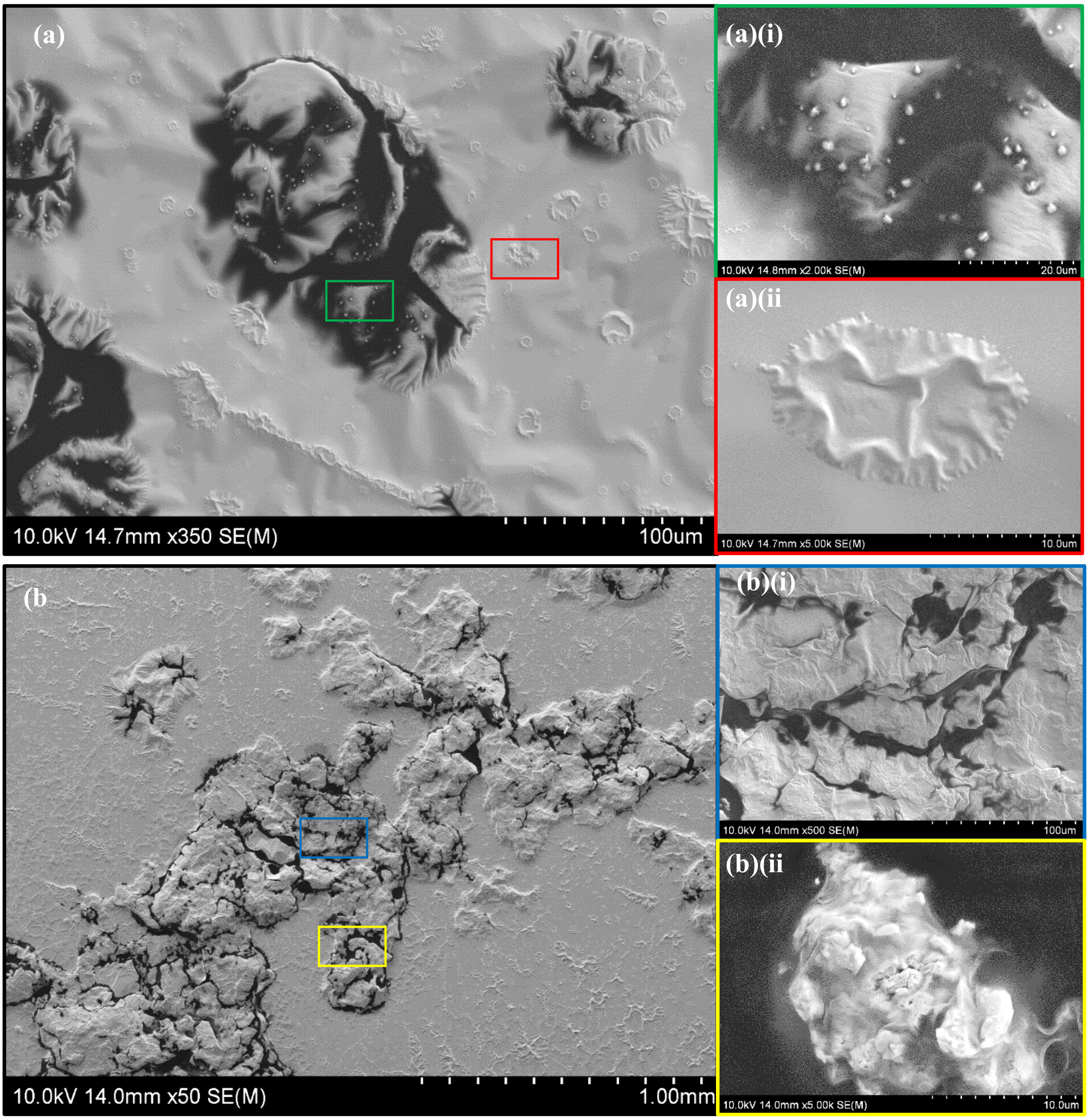

Figure 5.10. SEM images of (a) EV-loaded SLM (b) EV-loaded SLM system with silicone. The inserts show high magnification images of the colour coded highlighted regions

The dark regions within the particles are indicative of highly electron absorbing regions. These regions can be attributed to the dye due to the high charge density of the phenyl ring. The SEM images imply that the dye migrates from the inner phase into the lipid matrix and is randomly distributed across the matrix. This would explain the low EE values obtained for BB dye. The three polar groups on the BB molecule thermodynamically favour partitioning into the aqueous phase, thus reducing the incorporated concentration of dye. It should be noted that microscopy techniques are limited by their inherently local nature and may be affected by sample handling and preparation. However, images were selected to represent the majority of the regions for each sample.

5.2.3. Chemical Analysis

5.2.3.1 Fourier Transform Infrared Spectroscopy (FTIR)

FTIR spectra for both EV and BB dye were acquired to obtain the characteristic bands for both dyes (Figure 5.11). The highlighted peaks reflect the vibrational modes in moieties where interactions with the lipid matrix and other excipients will most likely occur; the peak position and responsible vibrations are shown in table 5.2.

Molecular vibration		BB (cm^{-1})	EV (cm^{-1})
SO_3 stretching	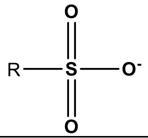	1161	-
N-H stretching	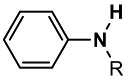	3423	-
C-N stretching	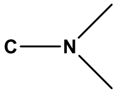	1298, 1339, 1507	1339
C=N stretching	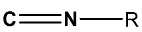	1574	1569
C-O-C symmetric stretching	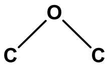	825, 1033	-

Table 5.2. Showing some of the vibration modes and associated wavelengths (cm^{-1}) for brilliant blue R and ethyl violet dye

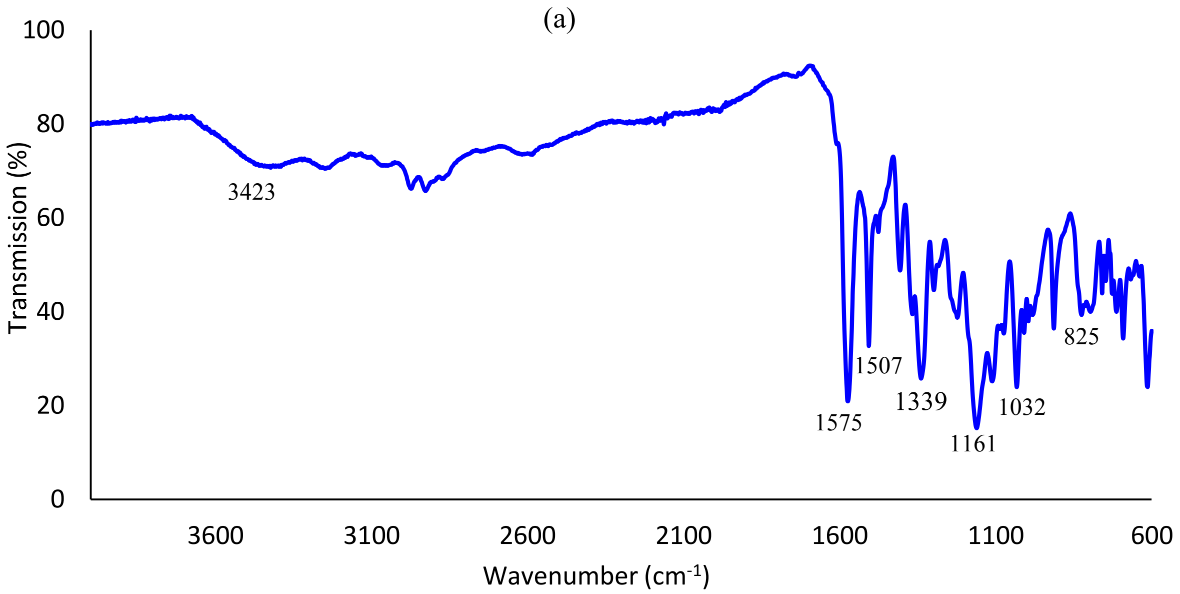

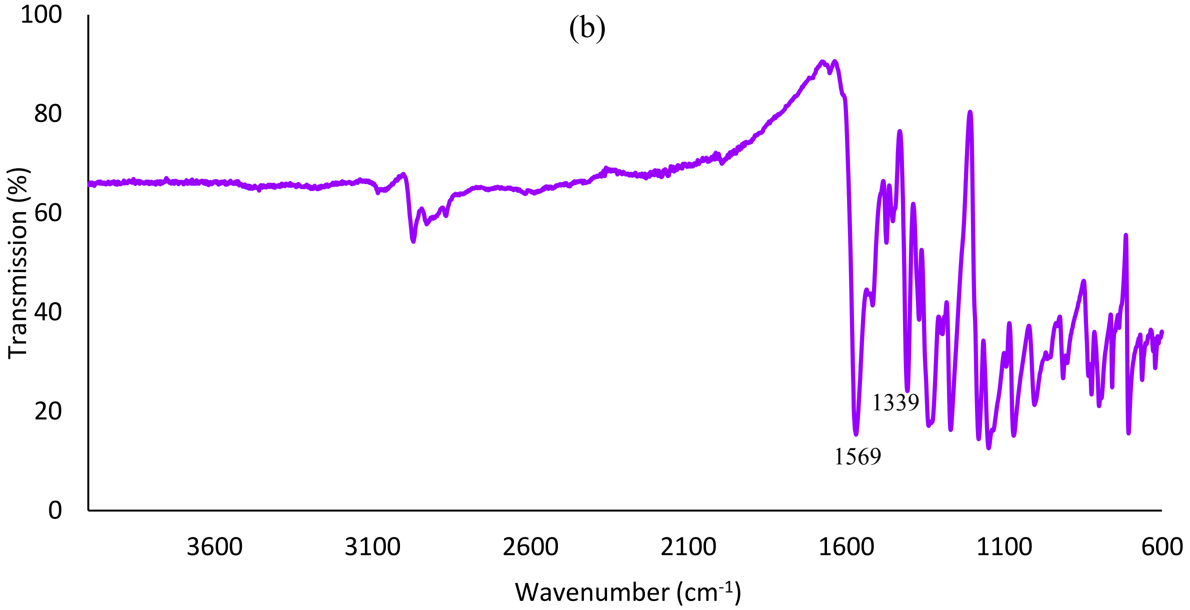

Figure 5.11. ATR/FTIR spectra of (a) brilliant blue R (b) ethyl violet

The FTIR spectra for the dye-loaded SLM systems in comparison to the bulk lipid show a high level of similarity. The Phenyl-N-H stretching vibration peak at 3423 cm^{-1} from the pure BB spectra does not appear on the BB loaded spectra for both the silicone and non-silicone loaded spectra. This could suggest an interaction between the dye and other excipients to give conjugate structures. However, the comparatively low concentration of the dye in comparison to the lipid could also suppress the signal from the dye. In order to minimise the effect of the complex SLM composition, a normalised spectra was obtained by subtracting the non-loaded

SLM spectra from the dye loaded spectra using a vibrational spectroscopy processing software, ProcessIt IR (KnowItAll Informatics System, Bio-Rad). The -C=N stretching vibration peak from the nitrile group observed at 1574 cm^{-1} on the bulk BB spectra does not appear on the normalised BB loaded SLM spectra. A peak shift from 1298 cm^{-1} (bulk BB) to 1274 cm^{-1} (BB/SLM) for the peak attributed to the C-N stretching vibrations on the phenyl-amine linkage. Due to the complex nature of the SLM composition, some peaks coincide making them hard to distinguish and allocate a mode of vibration even after normalisation. The ether linkage (C-O-C) symmetric deformation peak expected at 1033 cm^{-1} coincides with the lauric acid peaks at 1039 cm^{-1} and 1022 cm^{-1} and thus cannot be distinguished. The weak ether linkage expected at 825 cm^{-1} and 1161 cm^{-1} respectively do not appear in the BB-loaded SLM spectra. The differences in the FTIR spectra for the bulk BB and that in the SLM system suggest interactions between the dye and the lipid. BB has the propensity to interact with the lipid through hydrogen bonding, electrostatic interactions and Van der Waals' interactions. The two sulfonic groups have extremely low pKa values and thus are usually deprotonated.[43] At neutral pH values, the nitrogen on the diphenyl amine group carries a positive charge making the overall charge of the dye, -1.[42] Lauric acid has a pKa value of about 4.9 and is deprotonated at neutral pH, giving the molecule an overall charge of -1.[44] The lipid and dye both contain anionic species which can result in repulsive electrostatic interactions. The differences observed in the BB fingerprint in bulk and in the matrix can thus be attributed to the complex nature of the composite and the low concentration of the dye, which can suppress or shift the peak positions of the signal arising from the dye. Similar to the findings from the BB-loaded SLM, the EV-loaded SLM spectra does not show the peak for the C=N stretching vibrations on the nitrile group, which appears at 1569 cm^{-1} for the bulk EV dye. At neutral pH, the nitrogen on the nitrile moiety has a positive charge, giving the molecule an overall charge of +1.[45] It is possible that the EV dye interacts with the lauric acid by attractive electrostatic interactions. This supports the findings from the

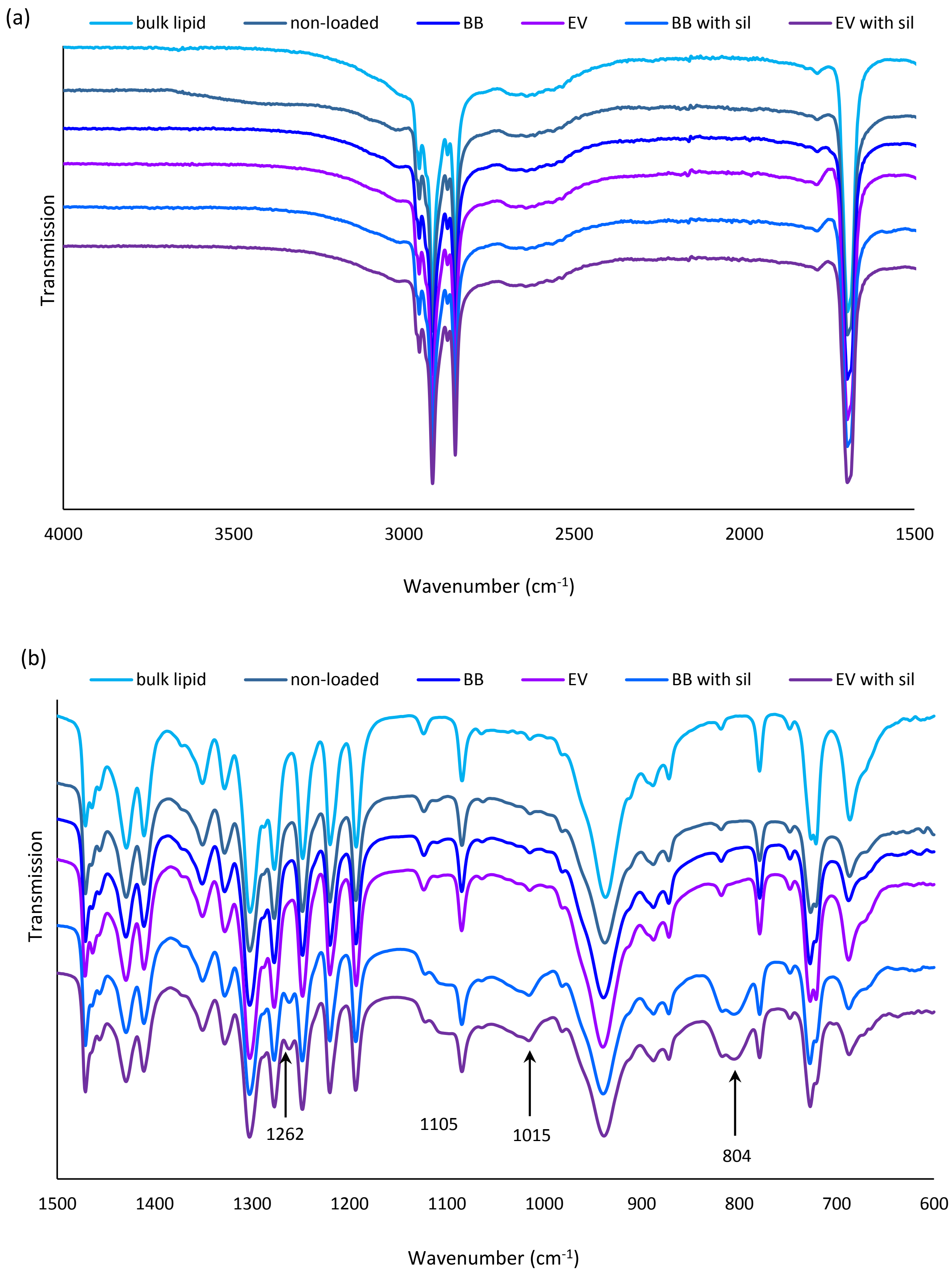

Figure 5.12. ATR/FTIR spectra of bulk lauric acid, non-loaded SLM, EV-loaded SLM, BB-loaded SLM, EV-loaded SLM with silicone and BB-loaded SLM with silicone in the range of (a) 4000 -1500 cm^{-1} (b) 1500 – 600 cm^{-1}

EE measurements that showed significantly higher encapsulation for the EV dye in comparison with the BB dye. The characteristic peaks from the silicone polymer expected at 1260 cm^{-1} (Si-CH_3 symmetric deformation), 1100 cm^{-1} and 1015 cm^{-1} (Si-O-Si asymmetric stretching) and 803 cm^{-1} (Si-$(CH_3)_2$ methyl rocking) all appear on the FTIR spectra both EV-loaded SLM and BB-loaded SLM systems as indicated by the arrows in Figure 5.9b. This confirms the successful incorporation of the silicone in addition to the dye to give a dual active SLM system.

5.2.3.2. Thermogravimetric Analysis (TGA)

The mass loss curves shown in Figure 5.13 show distinct differences in the mass loss behaviour of the dye-loaded SLM systems compared to the bulk lipid; bulk lauric acid exhibits single step degradation whereas the SLM systems decompose in at least two different events. The first degradation step is attributed to the pyrolysis of the lipid matrix; the subsequent events steps allude to the decomposition of the other excipients and possibly dye-lipid complexes. The *single-active* SLM systems exhibit a mass loss of 78 % and 72 % for BB-loaded SLM and

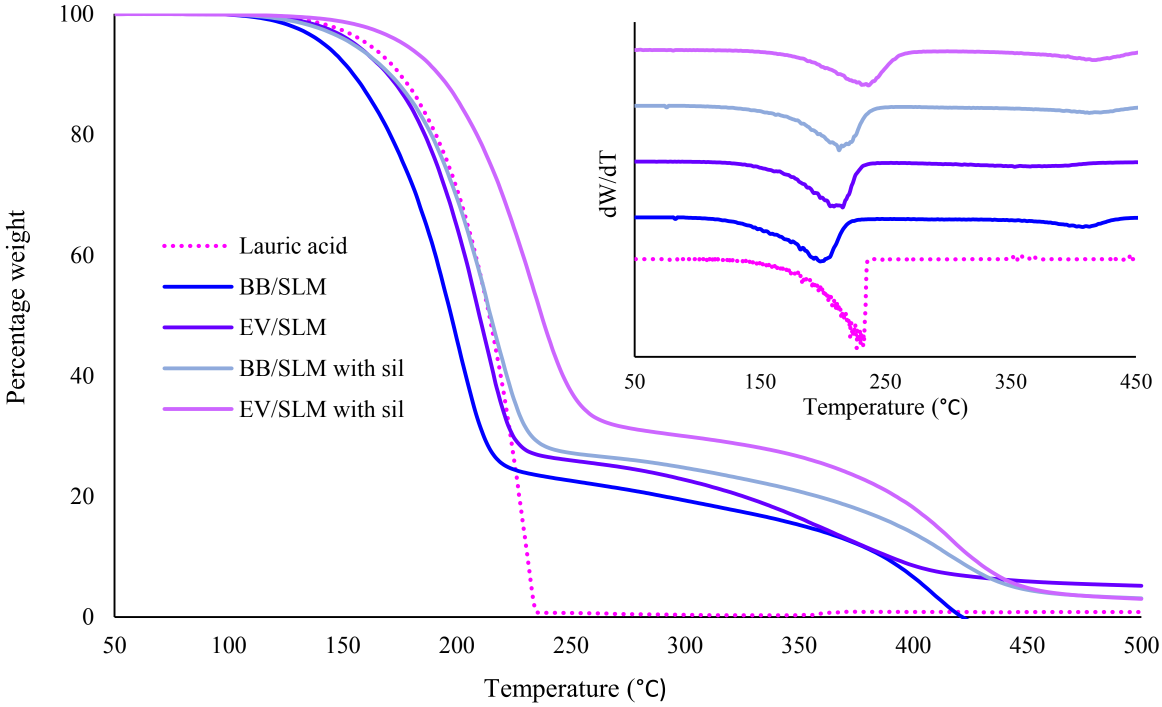

Figure 5.13. TGA mass loss curves for the dye-loaded SLM systems in comparison with the bulk lipid. The insert shows the first derivative of the mass loss curves

EV-loaded SLM respectively in the first step. The onset temperatures (168 °C and 181 °C for BB-loaded SLM and EV-loaded SLM respectively) are lower than that of the bulk lipid (199 °C) pointing to the decreased thermal stability; this can be attributed to the presence of dye and surfactant molecules. The higher thermal stability exhibited by EV-loaded SLM compared to the BB-loaded SLM suggest the formation of more stable dye-lipid complexes, which is possible by electrostatic interactions. The higher thermal stability of the dual active system compared to their single active counterpart can be attributed to the larger particle size as observed by light and electron microscopy results in previous sections. In addition, the presence of silicone reduces the thermal conductivity of the particles, thus increasing thermal stability of the silicone loaded SLM systems.

5.2.4. Melting Behaviour and Crystallinity

The DSC curves in Figure 5.14 show the melting peaks of the lipid matrix in the dye-loaded SLM systems in comparison to the bulk lipid. The presence of the melting peak on the dye-loaded SLM thermograms confirms the solid state of the lipid matrix. A slight reduction in the melting temperature of the lipid matrix is observed at 44.5 °C and 45.6 °C BB-loaded SLM and EV-loaded SLM respectively compared to 45.7 ± 0.1 °C for bulk lauric acid; a further reduction was observed for the dual active system at 44.2 ± 0.3 °C ± and 45.0 ± 0.6 °C for BB-loaded SLM and EV-loaded SLM respectively. This can be attributed to the presence of the other excipients and differences in the particle size of the SLM systems. However, the reduction in the enthalpy of fusion suggests loss of crystallinity as a result of interactions between the lipid and the dye molecules. The enthalpy of fusion for the bulk lauric acid was found to be 36.1 ± 0.6 kJ/mol (180 J/g) which matches that reported for the C-form polymorph of lauric acid (36.6 ± 0.8kJ/mol). The enthalpy of fusion was reduced to 102 ± 5 J/g and 125 ± 3 J/g for BB/SLM and EV/SLM respectively, which is in the same order of magnitude as that of the bulk lipid. Reduction in enthalpy of fusion can be a result of the presence of surfactants

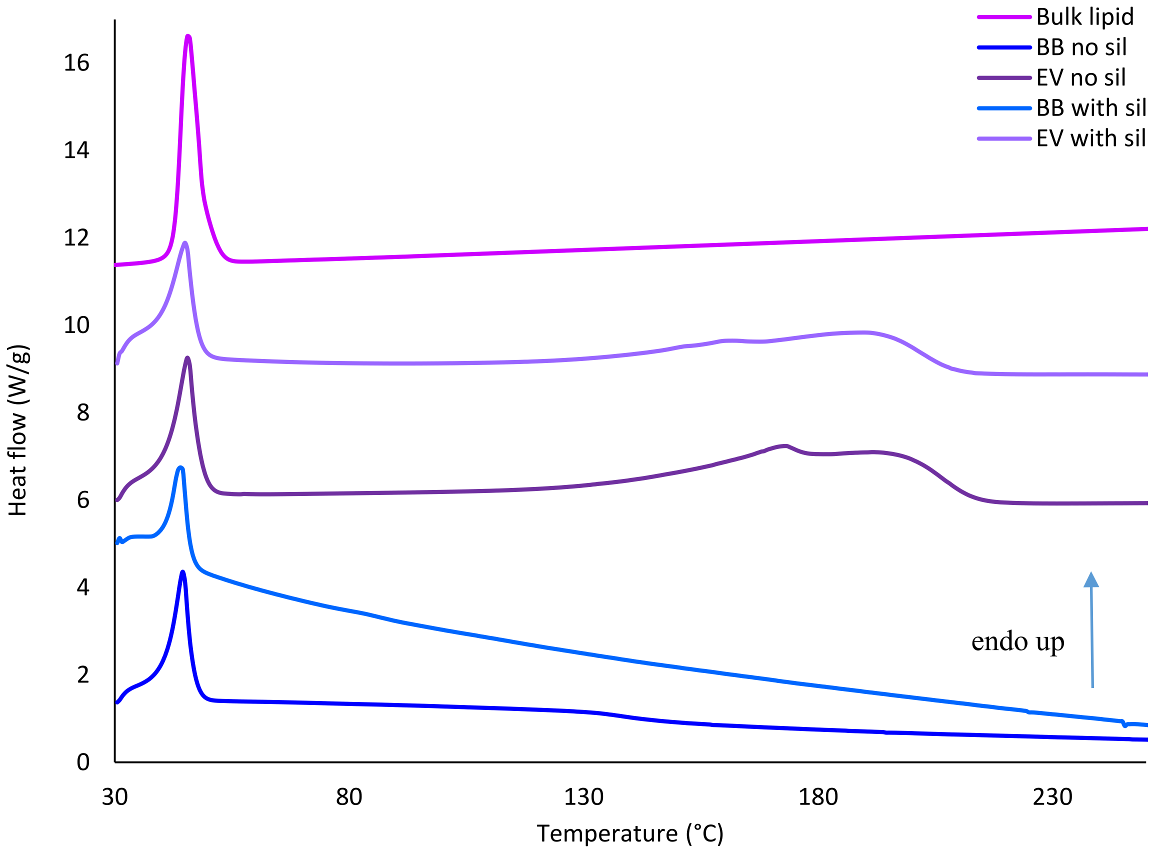

Figure 5.14. DSC thermograms of the BB- and EV-loaded systems in a single active and a dual active system in comparison to the bulk lipid

and dyes, which serve as impurities and hence disrupt the crystalline arrangement of the lipid. This is supported by the further reduction in the enthalpy of fusion observed for the BB-loaded SLM and EV-loaded SLM systems with silicone oil, 60 ± 7 J/g and 90 ± 3 J/g respectively. However, a reduction in enthalpy of fusion observed also suggests interactions between the dye and the lipid matrix.

5.2.5. Dye Release and Deposition on Fabrics

Cotton and polyester fabric samples treated with dye-loaded SLM systems pH 7 and pH 10.5 were analysed using confocal microscopy to confirm the release of the dye and deposition onto fabric surfaces. Cotton has an inherent autofluorescence due to the presence of *Aspergillus flavus* and the presence of other remnant fluorescent cotton plant components such as leaf, stem and seed coat.[46,47] These impurities have absorption maxima at different wavelengths spanning the UV/VIS region from 350 nm to 700 nm.[47] The cotton autofluorescence was utilised to outline the fibre network and to assess the coverage of the fabric surface of the fibres. Figure 5.15 shows images obtained from untreated cotton and polyester fibres, showing the inherent fluorescence properties of the samples used. The maximum fluorescence response from both the cotton and polyester fibres was achieved using a laser beam with a wavelength of 405 nm. Unlike cotton, polyester fibres do not have auto-florescence but a fluorescence response was observed using a laser beam with a wavelength of 405 nm. This response can be attributed to the presence of optical brighteners and other fluorescence materials used in the initial fabric treatment process or in the pre-washing process.

The maximum fluorescence response from both the BB and the EV dye was achieved using a 594 nm laser beam. The images acquired at these wavelengths were overlaid using the LAS software to give a trace of the spatial deposition of the dye onto the fabric surface. For cotton samples treated at pH 7 (Figure 5.16), BB and EV dye shows relatively lower coverage of the fabric surface compared to those treated at pH 10.5. This can be attributed to the slightly

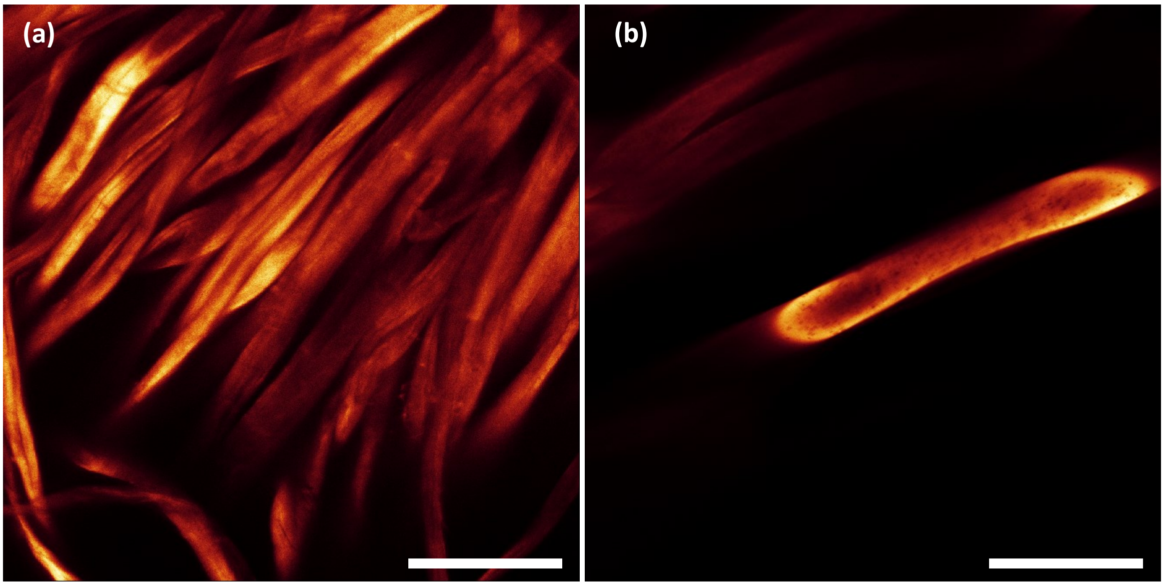

Figure 5.15. Confocal microscopy images of untreated (a) cotton and (b) polyester fibres acquired using a 405 nm wavelength laser. Scale bar = 100 µm

negatively charged surface of cotton at alkaline pH values, resulting in stronger electrostatic interactions between the dye and the fabric surface. There are no significant differences observed between the deposition of BB and that of EV onto the fabric surface from a qualitative point of view. For BB dye treated polyester samples (Figure 5.17), there appears to be no significant difference in the surface deposition between the samples treated at pH 7 and those treated at pH 10.5; only small regions of uncovered surface can be observed. This can be

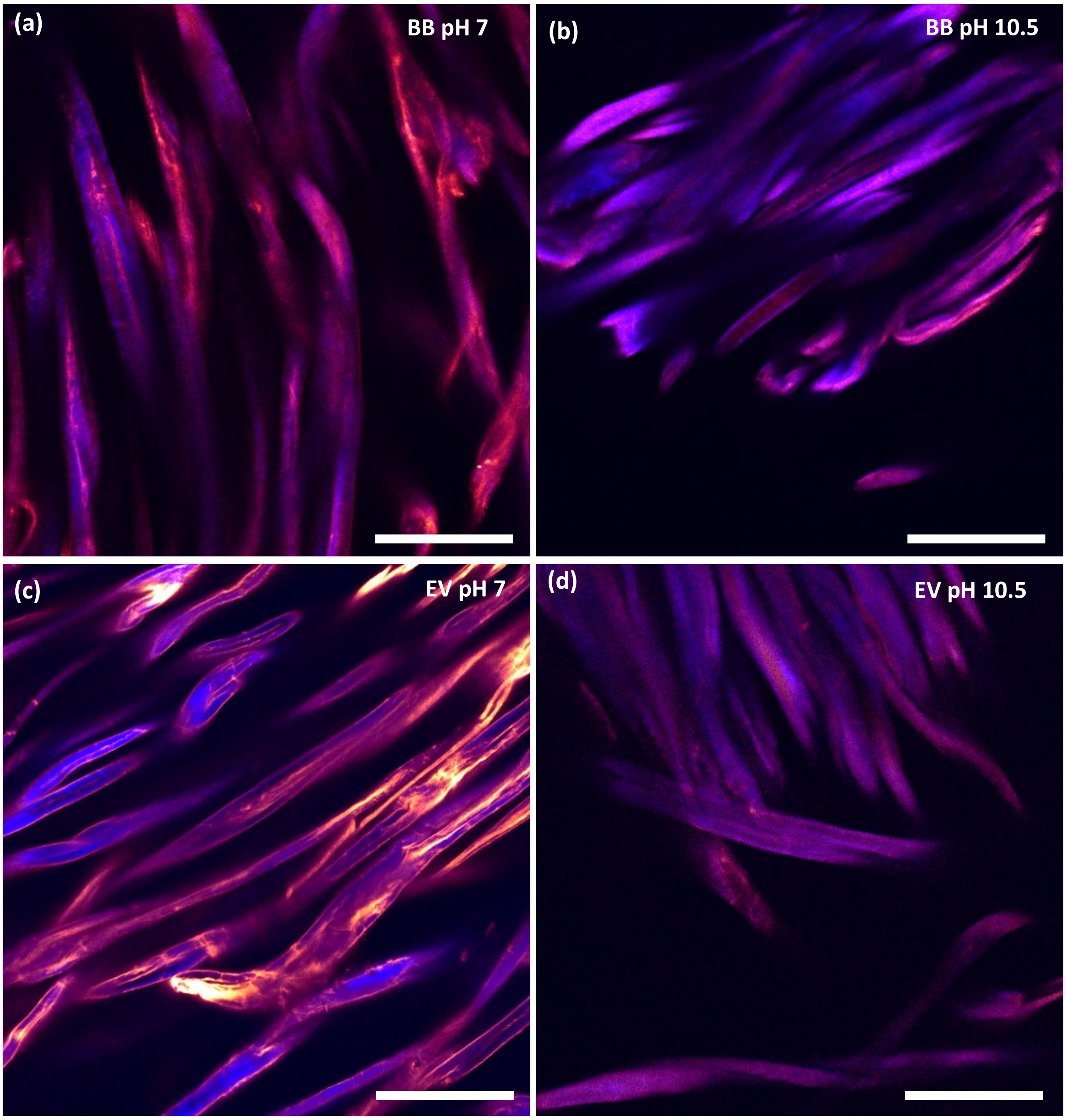

Figure 5.16. Confocal microscopy images of cotton fibres treated with dye-loaded SLM dispersions at room temperature (a) BB dye at pH 7 and (b) BB dye at pH 10.5 (c) EV dye at pH 7 (d) EV dye at pH 10.5. A 594 nm wavelength laser was used for excitation of the dyes. Scale bar = 100 µm

attributed to the low pKa value of the of the terephthalic acid ester groups (3.54 and 4.46).[48] Therefore, at both neutral and alkaline pH values, polyester fibres carry a negative surface charge and thus can interact with the dye by electrostatic interactions. For the EV dye treated polyester samples at pH 7 (Figure 5.17c) regions of non-covered fabric surface can be observed; samples treated at pH 10.5 show better coverage of the surface.

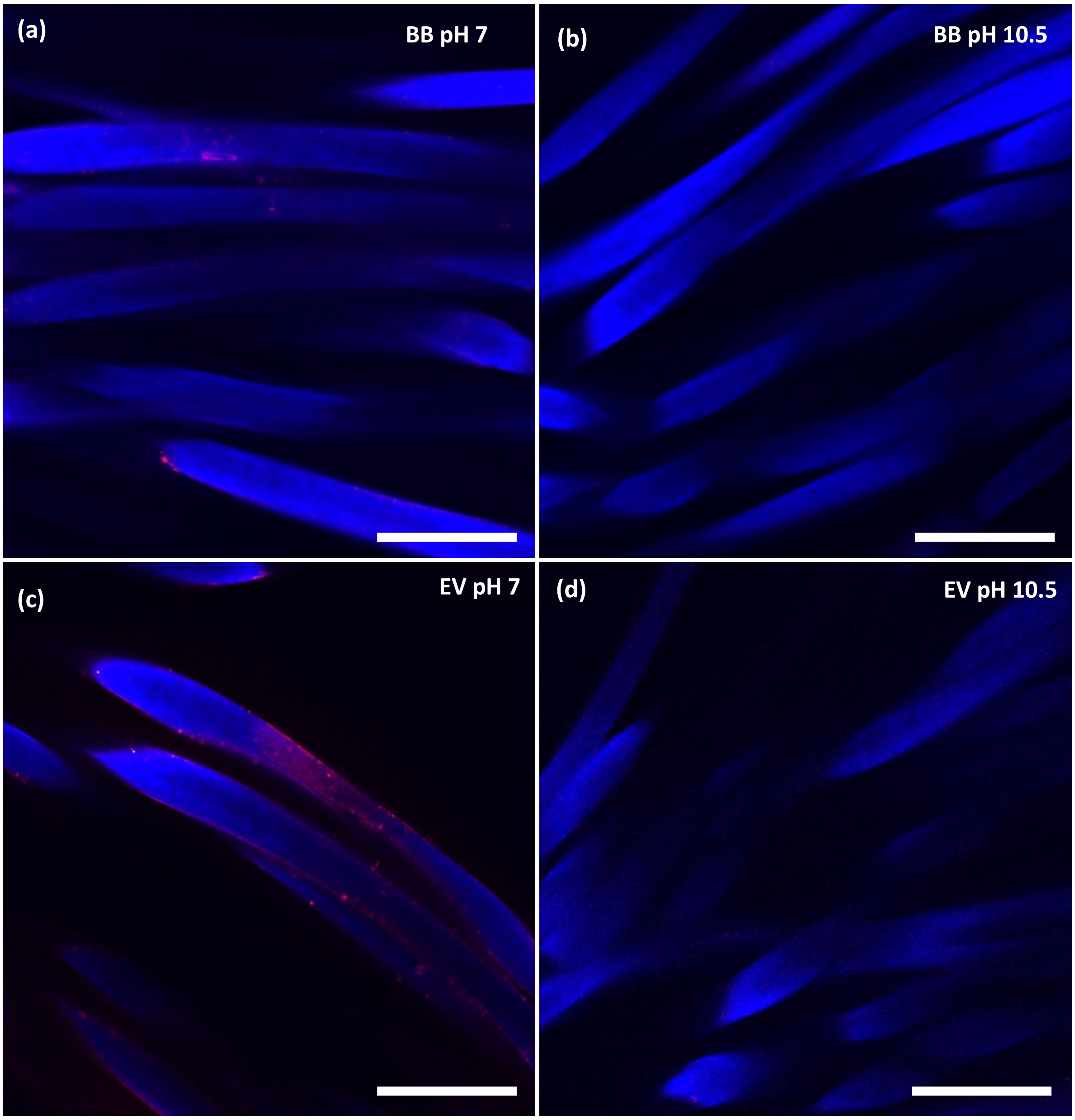

Figure 5.17. Confocal microscopy images of polyester fibres treated with dye-loaded SLM dispersions at room temperature (a) BB dye at pH 7 and (b) BB dye at pH 10.5 (c) EV dye at pH 7 (d) EV dye at pH 10.5. A 594 nm wavelength laser was used for excitation of the dyes. Scale bar = 100 µm

5.3 Conclusions

In conclusion, this chapter has reported the successful incorporation of Coomassie Brilliant Blue R dye and a cationic triphenylmethane dye, ethyl violet into SLM systems. The double emulsion method of preparation was used and gave high values of entrapment efficiencies for the EV loaded systems (88.6 % without silicone and 88.4 % with silicone). The incorporation of two actives into the same matrix, dye and silicone, has also been proved using FTIR to confirm the presence of the silicone oils. The incorporation of silicone does not affect the entrapment efficiency for ethyl violet but a reduction is observed for BB dye with silicone (10 %) compared to the system without silicone (26 %). The incorporation of silicones changes the surface morphology of the particles as observed by light microscopy and SEM. The release of the dye from the matrix was confirmed using confocal microscopy and confirms the distribution of the dye on the fabric surface at pH 10.5 (laundry pH).

5.4. References

1 S. M. Burkinshaw, *Physico-chemical Aspects of Textile Coloration*, John Wiley & Sons, 2016.

2 G. W. Taylor, *Chem. Br.*, **26**, 1155–1158.

3 A. Abel, in *Colour Design*, ed. J. Best, Elsevier, 2012, pp. 433–470.

4 J. W. Lehman, *Multiscale Operational Organic Chemistry: A Problem-solving Approach to the Laboratory Course*, Pearson Prentice Hall, 2009.

5 P. J. Dunn, A. Wells and M. T. Williams, *Green Chemistry in the Pharmaceutical Industry*, Wiley, 2010.

6 V. Galasso, *Chem. Phys. Lett.*, 2008, **457**, 250–253.

7 D. Cristea and G. Vilarem, *Dye. Pigment.*, 2006, **70**, 238–245.

8 J. Fabian, A. Mehlhorn, F. Dietz and N. Tyutyulkov, *Monatshefte für Chemie / Chem. Mon.*, **115**, 21–34.

9 A. R. Horrocks and B. H. Annex, *Handbook of Technical Textiles*, Elsevier Science, 2000.

10 A. Alinsafi, M. Khemis, M. N. Pons, J. P. Leclerc, A. Yaacoubi, A. Benhammou and A. Nejmeddine, *Chem. Eng. Process. Process Intensif.*, 2005, **44**, 461–470.

11 R. Christie, *Colour Chemistry*, Royal Society of Chemistry, 2014.

12 E. Smulders, W. Rähse and G. Jakobi, *Laundry detergents*, Wiley-VCH, 2002.

13 US7205269 B2, 2007.

14 M. E. Orazem and B. Tribollet, *Chemistry, Physics and Application of Surface Active Substances: Application of surface active substances*, Gordon and Breach, 1967.

15 P. A. Duffield and D. M. Lewis, *Rev. Prog. Color. Relat. Top.*, 1985, **15**, 38–51.

16 U. Zoller, *Handbook of Detergents, Part E: Applications*, CRC Press, 2008.

17 G. Broze, *Handbook of Detergents: Properties*, Taylor & Francis, 1999.

18 K. R. Millington, in *The Coloration of Wool and Other Keratin Fibres*, eds. D. M. Lewis and J. A. Rippon, John Wiley & Sons, 2013, pp. 75–101.

19 G. Erkan, K. Şengül and S. Kaya, *J. Saudi Chem. Soc.*, 2014, **18**, 139–148.

20 S. E. Faught, *Abstr. Pap. Am. Chem. Soc.*, 1987, **194**, 89.

21 A. A. Kokhanovsky, *J. Phys. D. Appl. Phys.*, 2007, **40**, 2210.

22 N. Souza, *Fabric Care*, New Age International, 1998.

23 US7235518 B2, 2007.

24 US5130035 A, 1992.

25 US8183197 B2, 2012.

26 US8378083 B2, 2013.

27 WO2010030539 A1, 2010.

28 *Pop. Sci.*, 1934, **125**, 56.

29 E. A. Moffatt, P. J. Sirois and J. Miller, *Stud. Conserv.*, 1997, **42**, 65–73.

30 A. K. R. Choudhury, *Textile Preparation and Dyeing*, Science Publishers, illustrate., 2006.

31 US6645928 B1, 2003.

32 US20150275157 A1, 2015.

33 CA2800008 A1, 2011.

34 Google Patents, EP2982736 A1, 2016.

35 R. Devi, A. Jain, P. Hurkat and S. K. Jain, *Pharm. Res.*, 2015, **32**, 3137–3148.

36 C. R. Merril, M. G. Harasewych and M. G. Harrington, in *Gel Electrophoresis of Proteins*, ed. M. J. Dunn, Elservier, revised., 2014, pp. 323 – 362.

37 T. S. Meyer and B. L. Lamberts, *Biochim. Biophys. Acta*, 1965, **107**, 144 –145.

38 J. Bennett and K. J. Scott, *Anal. Biochem.*, 1971, **43**, 173 – 182.

39 M. M. Bradford, *Anal. Biochem.*, 1976, **72**, 248 –254.

40 L. Pei, J. Wu, Q. Wang and J. Wang, *J Surfact Deterg*, 2016, **19**, 795 – 801.

41 S. Motomizu, S. Fujiwara, A. Fujiwara and K. Toei, *Anal. Chem.*, 1982, **54**, 392 – 397.

42 M. P. Rayaroth, U. K. Aravindb and C. T. Aravindakumara, *Chemosphere*, 2015, **119**, 848–855.

43 US006057160A, 2000.

44 WO2010041134 A1, 2010.

45 F.-D. Mai, W.-L. W. Lee, J.-L. Chang, S.-C. Liu, C.-W. Wu and C.-C. Chen, *J. Hazard. Mater.*, 2010, **177**, 864–875.

46 P. B. Marsh, M. E. Simpson, R. J. Ferretti, G. V. Merola, J. Donoso, G. 0. Craig, M. W. Trucksess and P. S. Work, *J, Agr. Food Chem.*, 1969, **17**, 468–472.

47 G. R. Gamble and J. A. Foulk, *J. Agric. Food Chem.*, 2007, **55**, 4940–4943.

48 T. Okuyama and H. Maskill, *Organic Chemistry: A Mechanistic Approach*, OUP Oxford, illustrate., 2013.

6. ‘Soft’ Electroactive Nanoparticles and their Penetration into Lipid Membranes

This chapter reports for the first time, redox nanoparticles based on the solid lipid nanoparticle (SLN) system and their penetration into solid supported lipid membranes for potential applications ‘intelligent biosensors’, electrochemical assays and other applications. Ferrocene-loaded SLN (Fc-SLN) dispersions based on a lauric acid matrix were prepared using the solvent emulsification evaporation method and characterised electrochemically using DPV; the physicochemical properties of the nanoparticles were characterised using ^{13}*C NMR, FTIR, DLS, TGA and SAXS. Self-assembled monolayers (SAM) were prepared by chemisorption of 1,2-Dipalmitoyl-sn-Glycero-3-Phosphothioethanol (DPPTE) onto a clean gold surface. The BLM was formed by deposition of λ-α-Phosphatidyl-Choline-β-Oleoyl-g-Palmitoyl (POPC) vesicles, driven by hydrophobic interations. Cyclic voltammetry (CV) and electrochemical impedance spectroscopy (EIS) were employed to characterise the membranes and to study penetration of the nanoparticles into the membranes. Resonance enhanced impedance spectroscopy (RESI) is employed to study the real time changes in capacitance of the lipid membranes as a result of adsorption and penetration of the redox nanoparticles into the membranes.*

6.1. Introduction

Redox-active materials such as nanoparticles, ions, molecules, polymers are increasingly gaining attention in many applications including molecular recognition, electron transfer mediation and electrochemical tagging.[1] Redox-active materials include metal complexes (iron and osmium complexes), quinones (hydroquinone, benzoquinone and naphthoquinone), organic dyes (methylene blue) and their polymer derivatives and composites.[2–7] A redox-active moiety that has received a lot of interest as electrochemical tags and electron transfer mediators in biosensing applications is ferrocene and its derivatives.[8–11] This can be attributed to their high redox activity and stability. Ferrocene and ferrocene derivatives have been co-immobilized onto electrode surfaces through polymer networks, self-assembled monolayers and bilayer lipid membranes for electron transfer mediation.[12–15] It is usually the electron transfer agent of choice in hydrophobic solutions; however, recent efforts in dispersing ferrocene in aqueous media have been reported.[16] This chapter reports a new method of dispersing ferrocene and other electroactive substances in aqueous media. The potential applications of this work include, delivery of electrochemical tags in electrochemically multiplexed immunoassays and electrochemical-triggered delivery of actives. This investigation reports the interaction between a novel breed of 'soft' electroactive nanoparticles with self-assembled monolayers and bilayer lipid membranes with a bi-fold objective. Firstly, to assess the viability of the SLN system for transmembrane delivery of electroactive tags and other actives (e.g. pharmaceutical drugs and skincare products) and secondly as a method of embedding electroactive species in pre-formed solid and tethered supported lipid membranes. Solid lipid nanoparticles have many advantages that make them suitable candidates in this application, such as:

- Compatibility with both hydrophobic and hydrophilic actives
- The possibility of co-immobilizing more than one active

- Biocompatibility and biodegradability
- Simple and low cost of production
- Ease of scaling-up production.

6.1.1. Ferrocene

Ferrocene (Fc), bis(η5-cyclopentadienyl)iron, is an organometallic compound comprising of an Fe^{2+} iron between two cyclopentadienyl ($C_5H_5^-$, Cp) groups. Ferrocene was first reported by Pauson and Keally in 1951 and is the first of a group of compounds known as sandwich compounds.[17,18] In 1973, Wilkinson and Fischer were jointly awarded a Nobel Prize in Chemistry for the discovery of the structure of ferrocene (Figure 6.1).[18] Ferrocene exhibits aromatic properties and is highly stable.[19] The cyclopentadienyl anions in Fc each contain six π-electrons which equally participate in the bonding to the Fe^{2+} to form ligands.[20] Ferrocene undergoes a reversible one electron oxidation process to give a cation, ferrocenium ($Fe(C_5H_5)_2^+$,Fc^+). The stability and redox active properties make ferrocene a desirable electrochemical probe in hydrophobic systems.[21] Hydrophilic derivatives of ferrocene such as ferrocene carboxylic acid, acetylferrocene and ferrocenylmethanol are also used as electrochemical tags where hydrophilicity is essential. Immobilisation of ferrocene moieties onto electrode surfaces and nanoparticle surfaces for signal amplification through electron

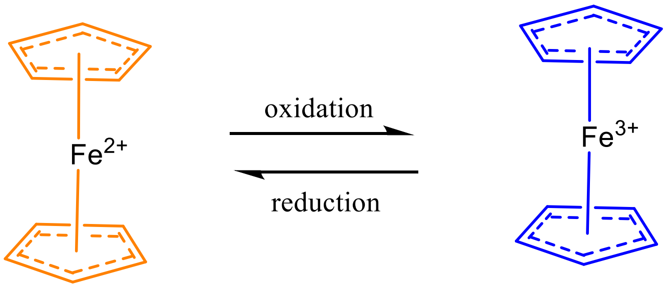

Figure 6.1. One electron oxidation of ferrocene to ferrocenium showing the ferrocene structure as suggested by Wilkinson and Fischer.

transfer mediation is an increasingly growing trend. Mediated electron transfer is facilitated by redox active species confined to the electrode surface or dissolved (or dispersed) in solution. Modification of electrodes with redox species can impart exceptional properties such as selectivity and specificity in sensory and detection applications and capability to facilitate faradaic charge transfer reactions, which is of importance in energy storage applications.[22,23] Redox-functionalised nanoparticles have particularly received a lot of attention in electrode modification systems and electrochemical tagging due to their superior electron transfer properties facilitated by their large surface area and mobility.[24]

6.1.2. Electroactive Nanoparticles

Accounts of the use of nanoparticle systems in electrode modification through direct deposition or by embedding in a matrix such as redox polymers, gel networks, lipid membranes and dendrimers are increasingly surfacing.[25–29] Metallic nanoparticle systems functionalised with redox-active substances such as ferrocenated gold nanoparticles and immobilized on electrode surfaces have been well characterised.[30–33] Similarly, redox-functionalised graphitic based nanoparticles such as carbon nanotubes immobilized on electrode surfaces have also been investigated.[34,35] The main concern limiting the applications of metallic and other 'hard' nanoparticle systems in implantable and wearable biomedical devices would be the in-vivo fate of metallic nanoparticles. Nanoparticles, particularly metallic nanoparticles could potentially have adverse effects on organs, tissue, cells, proteins and other physiological components even though their bulk material is highly inert.[36] 'Soft' nanoparticle systems could potentially circumvent the toxic effects associated with metallic nanoparticles. Soft nanoparticles have become increasingly important to the scientific, biomedical and biopharmaceutical fields. Polymeric nanobeads, gel based nanoparticles and dendrimers have been investigated as alternatives to hard electroactive nanoparticle systems.[1,12] Dendrimers, first discovered by Frank Vögtle in 1978, are synthetic, hyper-branched macromolecular structures with exceptional architectures.[37,38] Dendrimers with redox active sites have shown promising applications in electron transfer applications by mimicking the inaccessible enzyme active site and as electron transfer mediators.[39] Redox active moieties are incorporated to the core or the shell of dendrimers to impart redox activity (Figure 6.2).[28,40]

The Fc-SLN system suggested in this chapter circumvents the complicated synthesis processes associated with other ‘soft’ electroactive systems (e.g. polymeric nanoparticles and dendrimers). The immobilisation of the Fc-SLN onto electrode surfaces can be achieved through lipid membranes. Lipid membranes provide a physiological framework for embedding electrochemical tags, making them more desirable for biosensor applications compared to the polymer matrices used in immobilisation of other soft nanoparticle systems. This chapter investigates the physicochemical and electrochemical properties of Fc-SLN and their penetration into solid supported SAM and BLM lipid membranes.

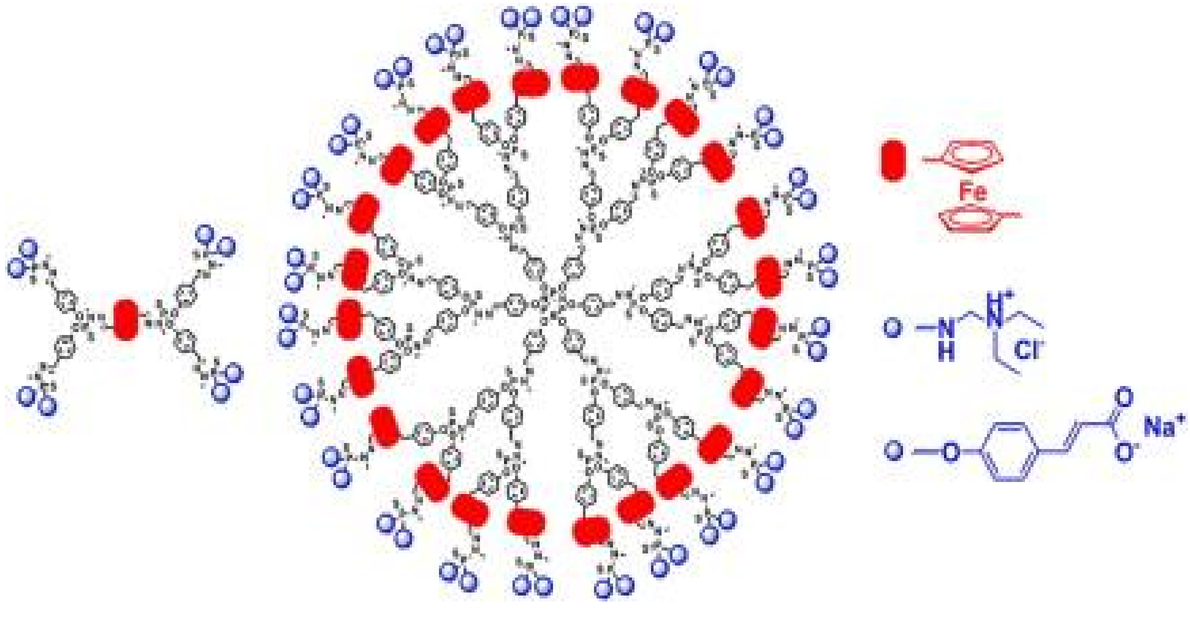

Figure 6.2. The structure of a phosphorous dendrimer incorporating 24 ferrocene moieties. Reprinted from Ref. 16 with permission form Elsevier

6.1.3. Self-Assembled Monolayers

Self-assembled monolayers are a natural framework for incorporation of redox active species and biological substances to give high selectivity and specificity to analytes. Self-assembled monolayers immobilised on electrode surfaces inhibit charge transfer at the surface; incorporation of redox actives into the monolayer enables charge transfer only through the mediators. SAM systems can be assembled at liquid-liquid interfaces or at an aperture. However, solid-supported lipid membranes have received attention due to their stability, comparatively long life time and ease of preparation and characterisation.[41,42] Electroactive SAM systems are usually prepared by the co-immobilisation of redox active molecules and non-functionalised molecules (diluent molecules) (Figure 6.3.). Considerable attention has been given to the development, characterisation and applications of SAM systems prepared by co-immobilisation of ferrocene terminated alkanethiols.[43–46] SAM systems functionalised with other redox species such as naphthoquinone, anthraquinone, and tetrathiafulvalene (TTF) have also been reported. [47–49] The benefits associated with this method of preparing

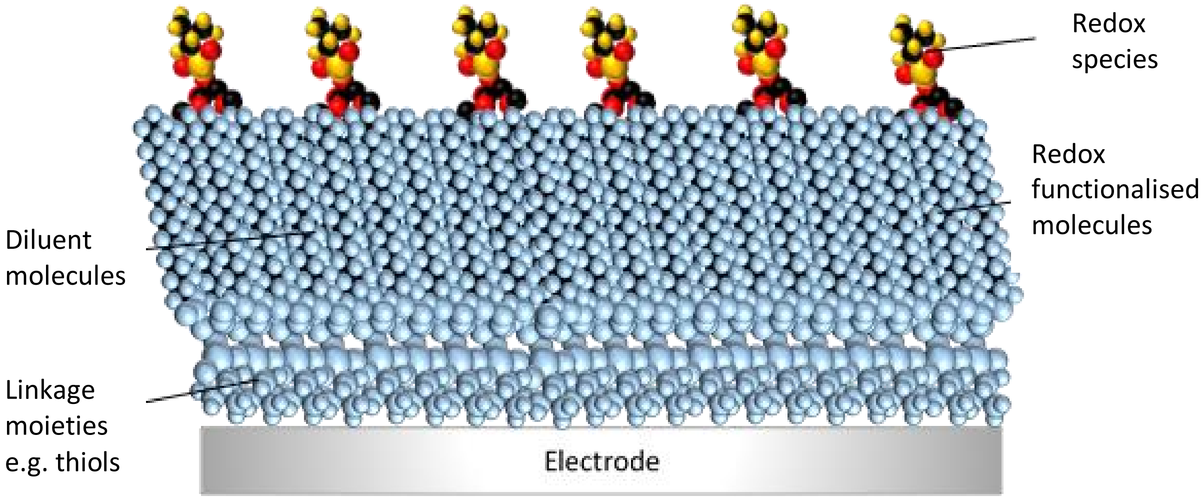

Figure 6.3. An illustration of a redox functionalised self-assembled monolayer formed by co-immobilisation of redox functionalised molecules. The amount of redox groups on the SAM surface is depended on the concentration of redox active molecules in solution during immobilisation

electroactive SAM systems include the tunable characteristics, for instance the redox species are at a fixed and controllable distance from the electrode surface.[50] Other tunable characteristics of redox functionalised SAM systems include the concentration of redox species and compatibility with a range of redox active materials. SAM systems can be immobilised on a variety of surfaces such as silica, quartz, carbon, platinum and gold. Sulfides, disulfides and thiols are particularly useful in modification of gold surfaces through the strong coordination of sulphur donor atoms on onto gold substrates; Van der Waals forces between the methylene groups to facilitate packing, orientation and stability of the monolayer (Figure 6.4).[45,51]

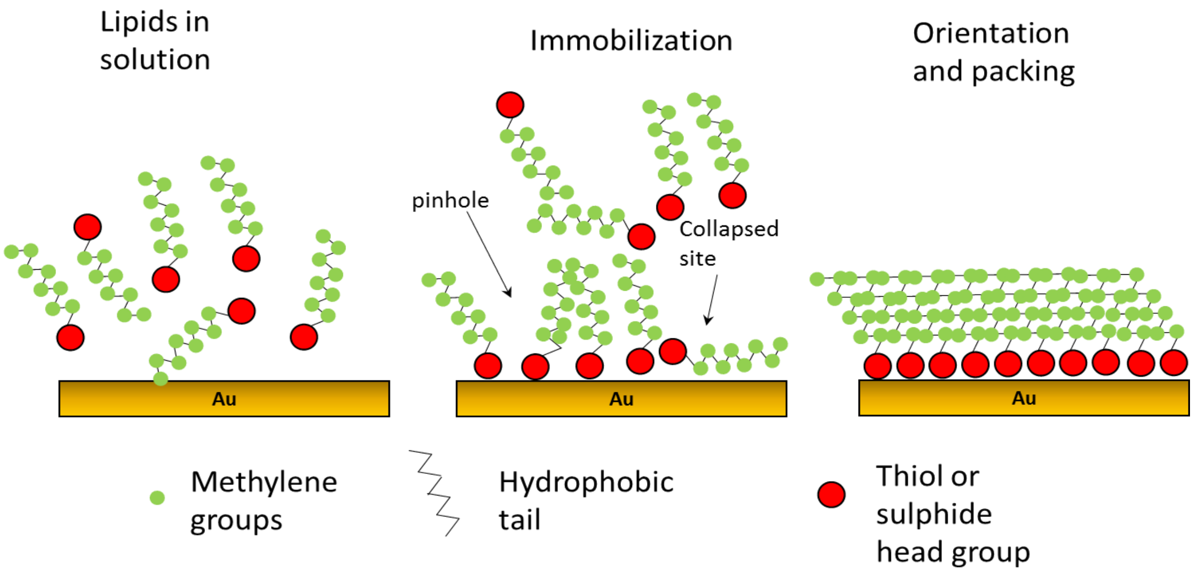

Figure 6.4. Schematic representation of the immobilisation of thiol or sulphide molecules onto gold surfaces through chemisorption and orientation of the monolayer facilitated by Van der Waals interaction between the methylene side groups. Also illustrating some defects that can arise during formation (pinholes and collapsed sites)

SAM systems are a viable, selective and stable method of immobilisation of electron transfer mediators. The technique reported in this chapter suggests a method of embedding redox active substances into already formed and characterised self-assembled monolayers. The mechanism for immobilisation of the redox active species into SAM systems is by hydrophobic interactions.

6.1.4. Bilayer Lipid Membrane

BLM systems have received considerable interest in various applications, including electrochemical biosensors, energy harvesting devices and molecular devices.[52–55] Similar to SAM, BLM systems provide a natural framework for embedding various species to render desirable properties such as redox activity, electrical conductivity, while retaining a biocompatible environment.[55] Redox active substances can be incorporated into bilayer lipid membranes during preparation; Campos and Kataky reported the incorporation of bio-electroactive compounds, ubiquinone-10 and α-tocopherol into a BLM system during adsorption of the upper leaflet (Figure 6.5).[56] Tien et al., reported the successful preparation of redox active BLM systems by incorporating 7,7′,8,8′-tetracyano-p-quinodimethane (TCNQ) or tetrathiafulvalene (TTF) to create electronic conductors capable of redox reactions at membrane solution interfaces.[57] Metallic and semiconductor nanoparticles such as platinum have also been incorporated into s-BLM systems by means of potential cycling.[58–60] It has been suggested that nanoparticles immobilised in solid supported membranes could potentially serve as a nanoelectrode arrays.[60] The main advantages of BLM systems for immobilisation of redox active compounds is similar to that of SAM systems; BLM systems can host different types of mediators to give highly specific and selective electrode systems while maintaining a biocompatible microenvironment.[50,61–64]

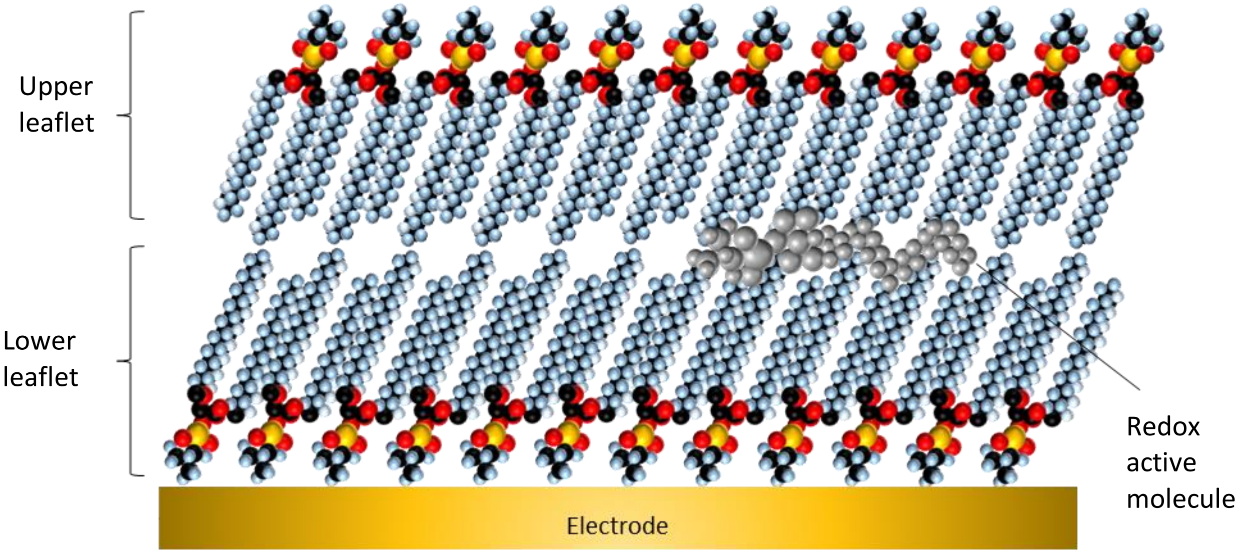

Figure 6.5. Schematic presentation of the structure of a BLM with redox molecules incorporated

6.1.5. Other potential applications of Fc-SLN

Solid lipid nanoparticles, widely used in cosmetic and drug delivery applications could potentially be the next generation redox active system for biosensing applications in enzyme electrode systems. The possibility of co-immobilising (dual active loading) redox active moieties and biological substances and compatibility with a variety of actives make them desirable candidates in electrochemically multiplexed immunoassays. The concept of immunoassays was first described by Berson and Yallow in 1959 and utilises the highly specific nature of interactions between antibodies and antigens for detection of bioanalytes.[65,66] Detection of more than one analyte simultaneously is necessary for monitoring and diagnosis of complex systems such as tumours; simultaneous multi analyte immunoassays (SMIAs) enable detection of multiple analytes in a single run.[67] SLN systems incorporating different redox active probes could potentially become the next generation of generic carrier matrices for electrochemical tags in SMIAs. Redox active SLN systems could also have potential therapeutic applications; redox nanoparticles exhibit antioxidative properties which can be utilised to eliminate overproduced reactive oxygen species, which are associated with many diseases.[68] Redox nanoparticles have been highlighted as an approach to combat neurodegenerative disease.[69,70] Redox active SLN systems have many promising applications in electrochemical sensing, monitoring, preventative and therapeutic treatment.

6.2. Results and discussion

6.2.1. Physicochemical properties of Fc-SLN

6.2.1.1. Loading Capacity and Entrapment Efficiency

The calibration peaks in Figure 6.6 were used to calculate the concentration of ferrocene incorporated into the SLN matrix. The maximum intensity peaks measured for Fc solutions in ethanol with known concentrations and for the dried Fc-SLN sample (0.05g) dissolved in 2ml ethanol were observed at around 444 cm^{-1}, which is expected for ferrocene in ethanol.[71] The maximum peak intensity for the Fc-SLN sample was measured as 0.72 ± 0.02 which corresponds to a concentration of 8.6 ± 0.3 mM. In order the calculate the loading capacity (LC), which is the percentage ratio of the incorporated active to the total amount of the

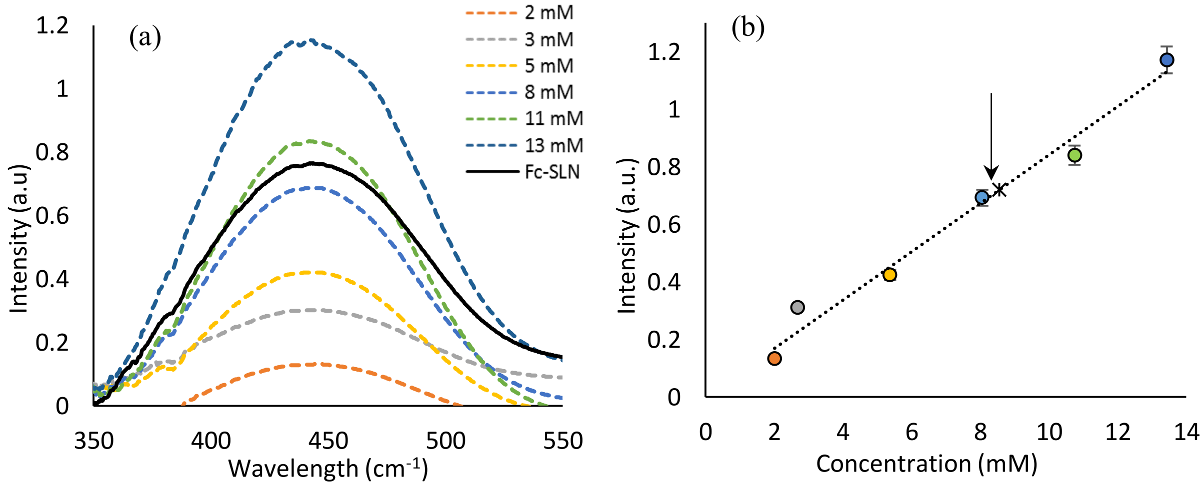

Figure 6.6. Plots showing (a) UV/VIS curves for calibration (dotted lines) and the Fc-SLN sample (solid black line) and (b) peak intensity values (at 444 cm^{-1}) as a function of concentration for calibration curves, showing the calculated concentration of the Fc-SLN sample

composite, the amount of Fc in the measured sample (M) was calculated from the measured concentration to give 0.0032g (= concentration x volume x M_w = 8.6 mM x 2 ml x 186.04 g/mol). The calculated amount of Fc in the sample as a percentage of the amount of the Fc-SLN in the sample, LC becomes 6.37 ± 0.21 % which gives an entrapment efficiency of 70 ± 2 % (based on the anticipated loading capacity of 9.09 %).

6.2.1.2. Particle size and morphology

Dynamic light scattering was used to study the size of the Fc-SLN at stand temperature. Figure 6.7a shows the histogram and cumulative size distribution curve. The average size of the nanoparticles based on volume measurements is 109 ± 17 nm. However, this measurement may not be reliable due to the fluorescent nature of ferrocene which results in the absorption of light by the sample and affects scattering. Cryo-TEM was also used to study the particle shape and size, ImageJ was employed for the particle analysis. Figure 6.7b and 6.7c shows the cryo-TEM image of the Fc-SLN immobilized on a holey carbon grid, and the particle size analysis results. The average particle size obtained using this method was 37± 9 nm, which is much less than that observed from light scattering. It should be noted that cryo-TEM has limitations that must be considered; the low temperatures used during analysis (-50°C) could potentially induce changes to the Fc-SLN morphology. Additionally, as cryo-TEM is a microscopy technique, it can be affected by sample preparation and handling and is inherently local. However, solid lipid nanoparticles prepared using the solvent evaporation methods are usually in the particle size range observed by cryo-TEM.

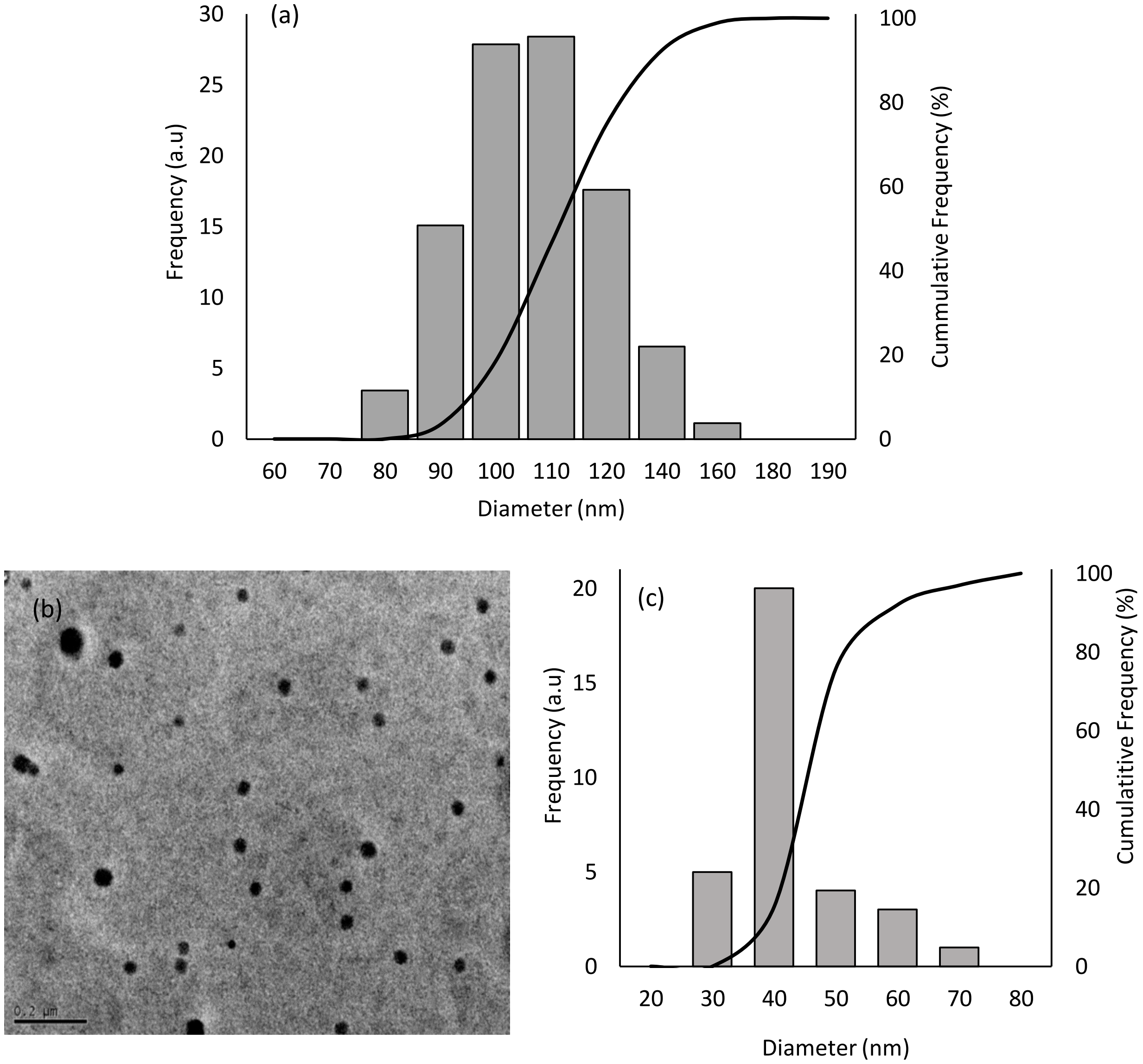

Figure 6.7. (a) Particle size distribution histogram and a cumulative frequency undercurve distribution of Fc-loaded nanoparticles based on percentage volume (raw data in Appendix 5) (b) cryo-TEM micrograph of Fc-SLN on a holey carbon grid, scale bar= 200 nm (c) particle size distribution histogram and a cumulative frequency undercurve distribution

6.2.1.2. Chemical Analysis

It is essential to study the chemical interactions between the lipid matrix and the ferrocene in order to determine the structural and release properties of the SLN system. Different analytical methods (FTIR, ^{13}C, NMR and TGA) were employed in this investigation.

6.2.1.2.1. Fourier Transform Infrared Spectroscopy

FTIR is a powerful, non-destructive technique that utilizes the differences in the absorption and emission properties of different molecular vibrations to identify chemical interactions present. The presence of strong chemical interactions between the lipid and the active can be identified by significant shifts in the spectra for the solid lipid nanoparticles in comparison to that of the ingredients. The characteristic FTIR peak positions together with the peak assignments are shown in Figure 6.8. The strong peak at 1105 cm^{-1} is due to the breathing vibrations of the cyclopentadienyl (Cp) rings, which are attributed to the alternate shrinking and expanding (one shrinks while the other expands) of the rings. The strong peak at 999 cm^{-1} together with the weak peak at 1047 cm^{-1} can be attributed to the in-plane bending vibrations of the C-H bonds on the Cp rings, whereas the peaks at 855 cm^{-1} and 813 cm^{-1} are assigned to the out-of-plane bending vibrations. The FTIR spectra of the Fc-SLN in comparison with the bulk lipid is shown in Figure 6.8.b. The C-H out-of-plane vibration peak has shifted to 817 from 813 cm^{-1}. This slight increase in the wavenumber is most likely due to the coincidence of this peak with the peak at 818 cm^{-1} that arises from the molecular vibrations in the matrix. The characteristic peaks for the Fc-SLN do not exhibit any significant shifts. The rest of the Fc characteristic peaks do not seem to show significant shifts. The peak at 1123 cm^{-1} for the bulk lauric acid due to -CH_3 rocking vibrations coincides with the Cp breathing vibrations resulting in a slight shift to 1120 cm^{-1} and a broader peak in the Fc-SLN spectra. An additional weak peak appears at 1146 cm^{-1}. This peak is absent in the spectra for the bulk Fc and lipid. The peak in itself would be insufficient to suggest any strong interactions between the lipid and the matrix, since there are no significant shifts in the rest of the spectra. This is an expected result as no strong interactions between the lipid and the ferrocene are expected except for hydrophobic interactions.

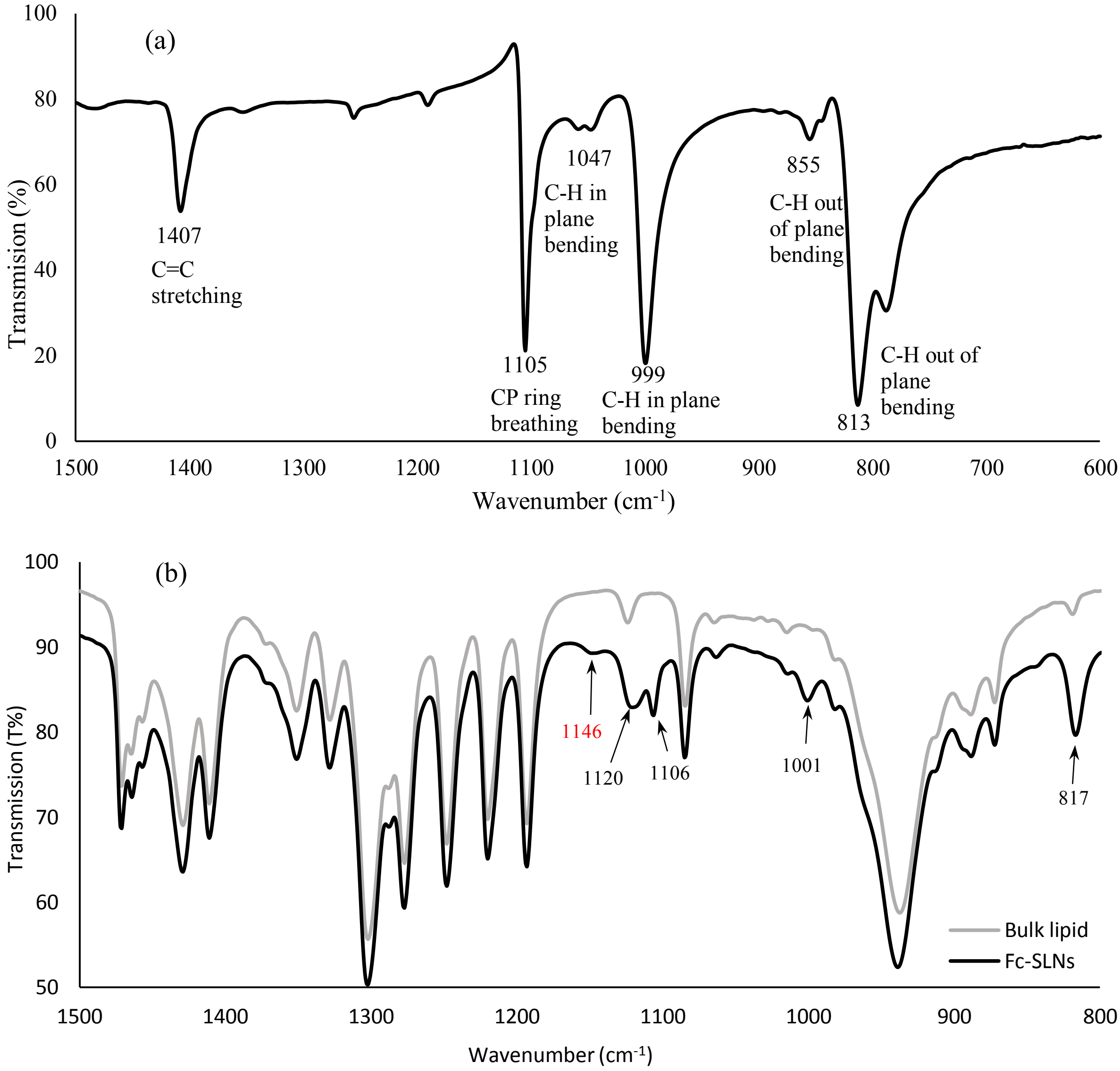

Figure 6.8. The ATR/FTIR spectra of a) ferrocene b) bulk lauric acid (grey) and Fc-SLN (black)

6.2.1.2.2. Nuclear Magnetic Resonance

^{13}C NMR was employed to investigate the interactions between the lipid and the ferrocene. Figure 6.9 shows the spectra obtained for the ferrocene, bulk lipid and the Fc-SLN. The spectra obtained for ferrocene show a single upfield peak at 69.6 ppm. This is expected since the carbon atoms on the Cp rings are all equivalent and hence give rise to a single peak. The lauric acid spectra, (non-loaded SLN) contains non-equivalent carbons and hence has varying chemical shifts for the carbon the peaks at 181.738 ppm in Figure 6.8b and 181.689 ppm in Figure 6.8c represent the carbon on the carboxyl groups. The difference in the chemical shift between the two is not sufficient to suggest a significant change in the environment around this carbon. The ferrocene peak from the bulk ferrocene can be seen at 69.610 ppm in Figure 6.9.a and for the Fc-SLN, it appears at 69.440 ppm (see inset in Figure 6.9c). The difference of 0.17 ppm is not sufficient to warrant any significant changes in the environment around the carbon. The peak at 33.068 ppm is most likely due to the alkyl carbon (-CH_2) and the multiple peaks around it are due to the decoupling of the surrounding protons. Again this remains unaffected by the presence of the ferrocene. In conclusion, the ^{13}C NMR spectra does not support the presence of any strong interactions between the ferrocene and the lauric acid; this is in agreement with the findings from FTIR.

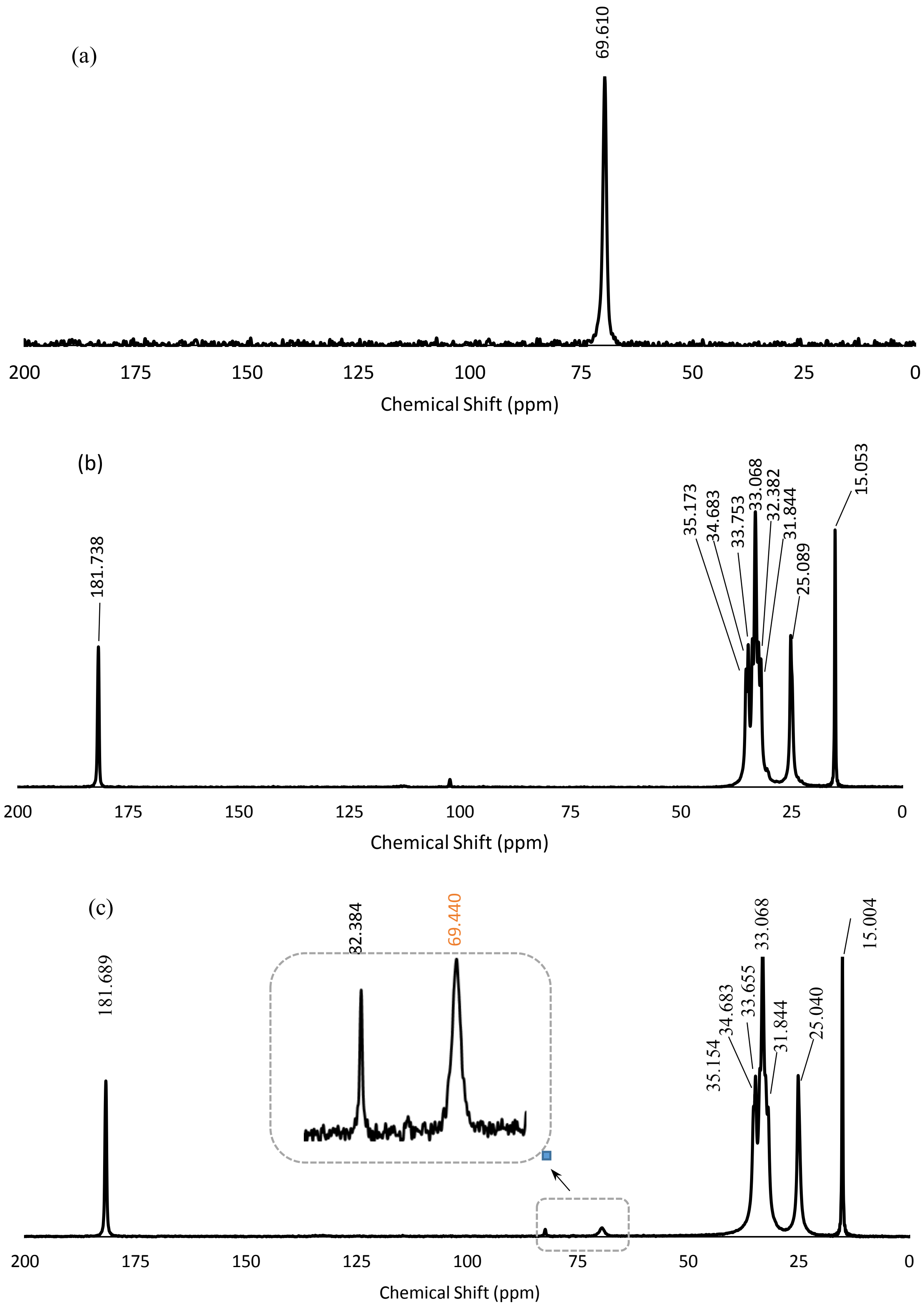

Figure 6.9. ^{13}C NMR spectra of a) bulk ferrocene b) non-loaded SLN and c) Fc-SLN

6.2.1.3. Diffraction patterns

SAXS has often been employed in the characterisation of the structural properties of solid lipid nanoparticles.[72–75] Figure 6.10 shows a SAXS diffraction curve for the ferrocene-loaded nanoparticles in comparison with that of the bulk lipid. The presence of a strong peak for the Fc-SLN dispersion suggest that the lipid maintains crystallinity after preparation. A slight shift in the peak position (about 1nm) in addition to a decrease in the width of the peak was observed. Shifts in the SAXS peak position can result from changes in the long-spacings of the lipid crystalline structure, suggesting insertion of the active the bilayer crystal planes of the fatty acid.[74] However, the small magnitude of the shift is not analogous with such structural change.[74] Moreover, according to Bragg's law, the peak position is inversely proportional to the long spacings. A negative shift in the peak position would be consistent with the widening of the bilayer separation distances due to the insertion of the active, this is not true for the Fc-SLN system. According to Bunjes and Unruh, peak shifts of this magnitude can arise due to a change in the electron density between the nanoparticles and the continuous phase.[75] This is most likely the case for the Fc-SLN dispersion and the bulk lauric

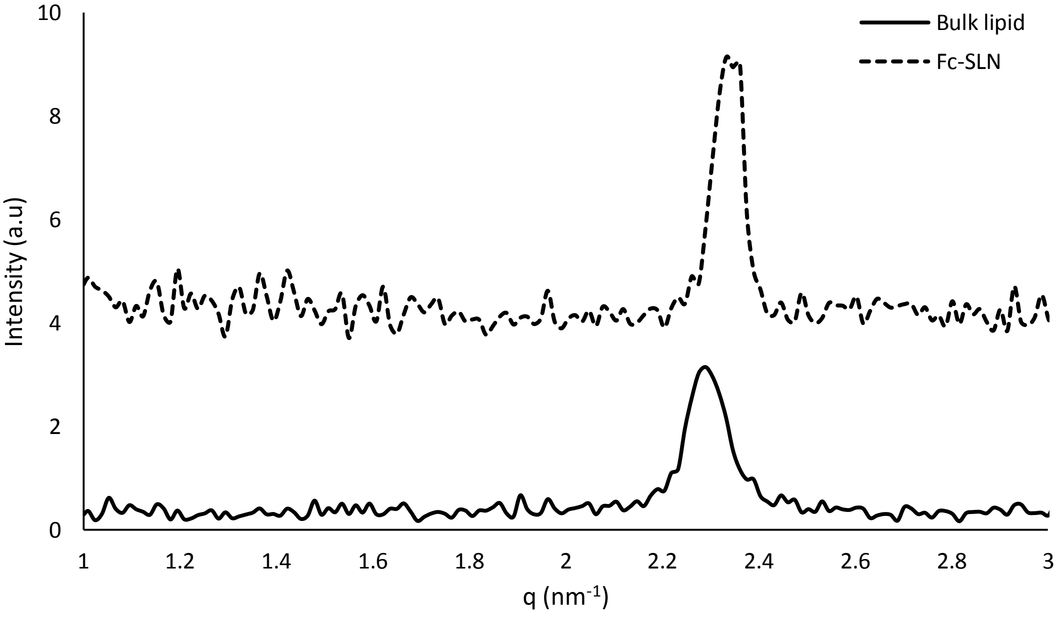

Figure 6.10. SAXS diffraction patterns for non-loaded (solid line) and Fc-loaded (dashed line) SLN dispersions

acid. The sharp peak observed for the Fc-SLN is indicative of a multilayer structure (Figure 6.10).[76]

6.2.1.4. Melting Behaviour

The melting behaviour was studied using differential scanning calorimetry. The melting behaviour of substances can be useful in the investigation of the structural arrangement of the solid lipid nanoparticles in order to understand their stability and release behaviour. Figure 6.11 shows the endothermic DSC curves for the non-loaded SLN and the ferrocene-loaded SLN. The Fc-SLN thermogram shows no significant difference in the energy of fusion compared to that of the non-loaded particles, 155 ± 14 J/g and 154 ± 6 J/g respectively. This shows that the presence of the ferrocene does not affect the crystalline arrangement of the lipid in the nanoparticles, which confirms the findings from SAXS. Therefore, it is unlikely that the ferrocene molecules are incorporated into the interlamellar spaces, minimising the intermolecular interactions between the lipid molecules. It also shows that the Fc-SLN maintain the C-form crystalline arrangement discussed in chapter 4, hence the particles most

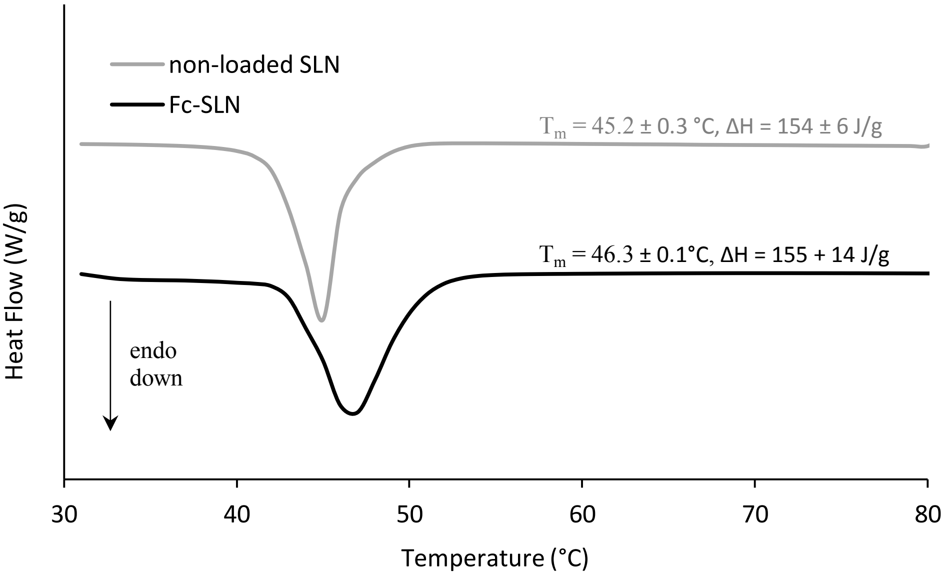

Figure 6.11. Endothermic DSC curves for the non-loaded and Fc-loaded SLN systems

likely adopt a core shell model of incorporation than the solid solution model. The Fc-SLN however, show a slightly higher melting temperature, 46.3 ± 0.1 °C compared to 45.2 ± 0.3 °C for the non-loaded particles. According to Montenegro et al., shifts in melting point can be used to distinguish the structural arrangement of SLN systems;[77] the increase in melting point suggest that the ferrocene is localised in the shell of the particle. Ferrocene has a higher melting point than lauric acid and therefore the ferrocene shell can act as a thermal shield of the Fc-SLN resulting in an increase in melting point. In addition, partitioning of ferrocene into the aqueous phase during emulsification is highly unlikely due to the hydrophobic nature of ferrocene. Therefore, the most likely model of incorporation of the Fc-SLN system is enriched shell-model. Running DSC at different heating rates could provide more information to support this.

6.2.1.2 Electrochemical response of Fc-SLN

6.2.1.2.1. Differential Pulse Voltammetry

In order to measure the electrochemical response of the Fc-SLN was measured using differential pulse voltammetry (DPV). The presence of two peaks in Figure 6.12 is indicative of two electrode processes. The peaks have an intensity ratio of approximately 1:2. The peak at 0.612 V (vs Pt pseudo) is comparable to that reported for ferrocene in aqueous solution, 0.624 V vs SCE.[78] The half peak width of the peak at 0.612 V was found to be 94.7 mV, which is similar to that expected for a one-electron reversible process, at a pulse amplitude of 50 mV at 25 ^{0}C.[21] This confirms that this peak is a result of the one-electron oxidation of Fc. The peak at -0.01 V has a half peak width of 110.9 mV, which is about 15 mV larger than that of expected from a diffusion-controlled event involving one-electron reversible species. The peak is also shifted negative of the second peak. This peak, is likely to be due to the collision of the Fc-SLN, on the electrode surface which gives surface confined electroactive species. Negative shifts in the half-wave potential have been reported previously, with

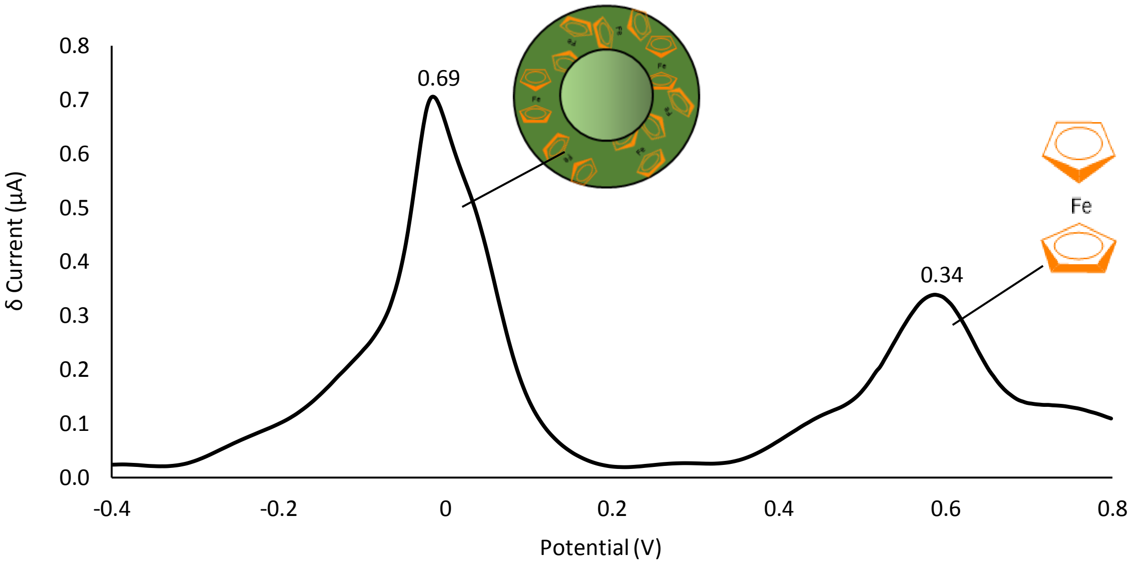

Figure 6.12. Differential pulse voltammogram for the dilute Fc-SLN dispersion on a gold working electrode with a Pt pseudo-reference at a scan rate of 10 mV/s

electrode immobilised dendrimers, suggesting the particles adsorb onto the electrode surface.[79] It can also be attributed to the oxidation of the Fc confined to the Fc-SLN shell, where the shift in the redox potential can be attributed to the shielding effect of the lauric acid. This phenomena has been reported with dendrimer systems.[80,81] The half-wave potential of any redox couple is strongly dependent on the chemical environment of the redox centre.[82] The location of the redox-active species determines the direction of the shift; dendrimer systems with redox species in the core are said to give positive potential shifts and negative shifts result from systems with redox species in the shell.[82] The complex nature of the peak can be attributed to the irregularities between the particles in the system, e.g. differences in the shape, size and concentration of encapsulated ferrocene.

6.2.1.2.2. Electrochemical Impedance Spectroscopy

The combination of voltammetry techniques and electrochemical impedance spectroscopy is powerful in determining the presence of diffusion controlled processes. In Figure 6.13 - 6.16, the Nyquist plots for the Fc-SLN dispersion in a 10 mM KNO_3 background electrolyte on a bare gold electrode and carried out at potentials 0.0V, 0.2V, 0.4V and 0.6V vs platinum pseudo reference are shown. At an applied potential of 0.0V, the system shows the presence of both kinetically controlled processes (indicated by the semi-circle) and diffusion controlled processes (indicated by the line at approximately 45°) shown in Figure 6.13. This can be attributed to the oxidation of the Fc that is incorporated in the Fc-SLN shell. The line at 45° was not observed at an applied potential of 0.2 V and 0.4 V, (Figure 6.14 and 6.15) indicating that only non-faradaic processes occur at the electrode surface. A mixture or both kinetic and diffusion control was observed at an applied potential of 0.6V (Figure 6.16). This is due to the charge transfer between the free ferrocene released from the matrix. The presence of charge transfer indicated by EIS spectra at 0.0 V and 0.6 V supports the DPV findings, showing redox peaks at similar potentials. It is possible that the interfacial processes of the Fc-SLN system with the gold surface adopt the following order: i) adsorption of the Fc-SLN onto the electrode surface ii) oxidation of the Fc in the shell of the Fc-SLN to give Fc^+ which can diffuse into the aquoeus phase iii) Release of Fc into the aqueous solution, triggered by the application of potential iv) oxidation of the released Fc to Fc^+. The direct electron transfer

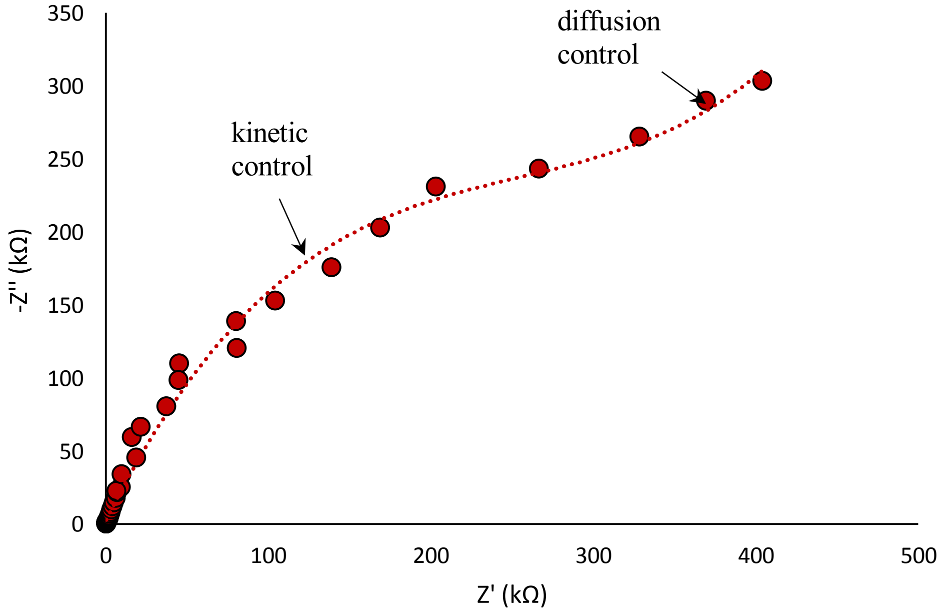

Figure 6.13. Electrochemical Impedance spectroscopy data presented as Nyquist plots for Fc-SLN dispersion on gold in 10 mM KNO_3 background electrolyte measured at a potential 0.0 V vs Pt pseudo reference

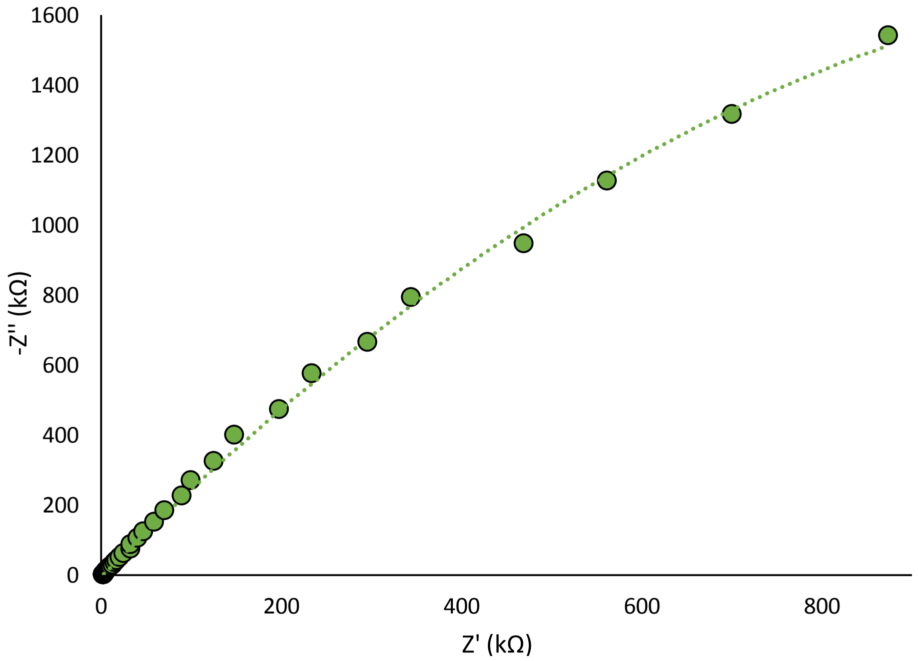

Figure 6.14. Electrochemical impedance spectroscopy data presented as Nyquist plots for Fc-SLN dispersion on gold in 10 mM KNO_3 background electrolyte measured at a potential 0.2 V vs Pt pseudo reference.

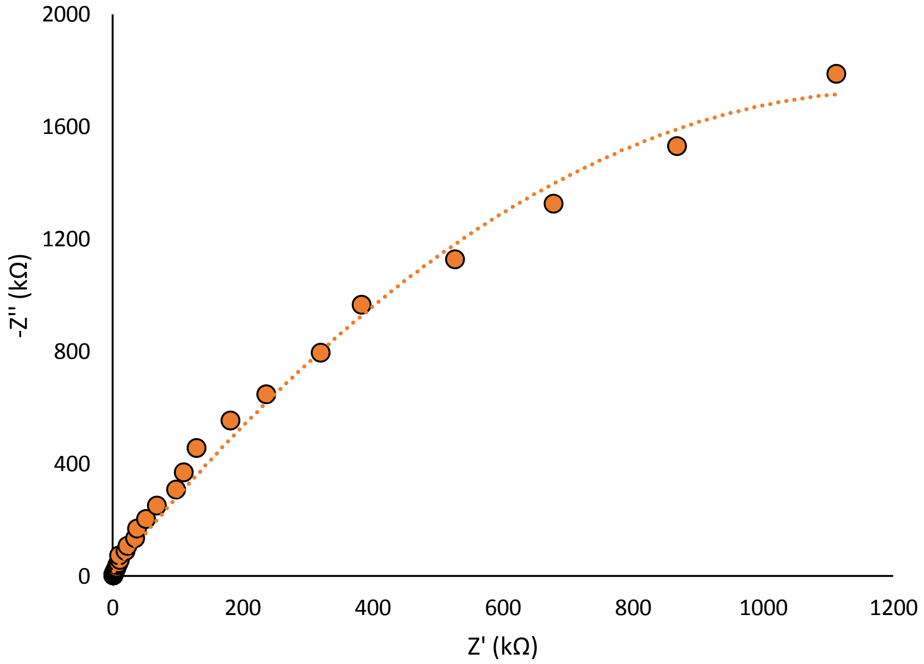

Figure 6.15. Electrochemical impedance spectroscopy data presented as Nyquist plots for Fc-SLN dispersion on gold in 10 mM KNO_3 background electrolyte measured at a potential 0.4 V vs Pt pseudo-reference

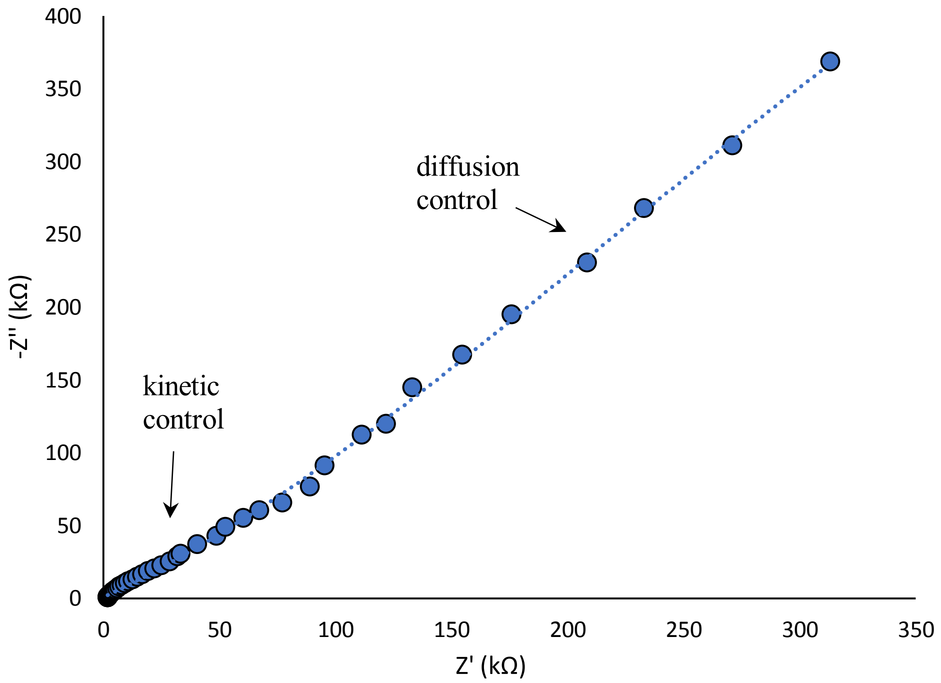

Figure 6.16. Electrochemical impedance spectroscopy data presented as Nyquist plots for Fc-SLN dispersion on gold in 10 mM KNO_3 background electrolyte measured at a potential 0.6 V vs platinum pseudo reference

between electroactive molecules immobilised on an electrode surface with lauric acid has been reported by Kafi et al., who reported charge transfer activity between haemoglobin in a lauric acid film immobilised on a glassy carbon electrode.[83]

6.2.2. Penetration into lipid membranes

In order to study the penetration of the Fc-SLN into lipid membranes, the prepared and characterised lipid membranes were immersed in a solution of Fc-SLN for 60 minutes. EIS and CV measurements were taken before and after immersion.

6.2.2.1. Cyclic Voltammetry

The CV curves for the SAM and the BLM before and after exposure to the Fc-loaded nanoparticle dispersion are shown in Figure 6.16 and 6.17. The increase in the maximum current measured for the SAM film (Figure 6.16) from 0.39 ± 0.03 μA to 12.1 ± 0.1 μA (before and after exposure to Fc-SLN respectively) suggests the penetration of Fc-SLN into the SAM layer. The same trend was observed for the BLM film. The Fc-SLN adsorb onto the surface of the immobilised film and interact with the lipid membrane by hydrophobic interactions and are incorporated into the lipid membrane. The incorporation of ferrocene and other redox active substances into BLM films has been reported to enhance the electrical properties of the lipid film; modification of SAM and BLM systems with mediators imparts electrical conductivity.[15] This explains the increase in current observed for both lipid films after exposure to the Fc-SLN.

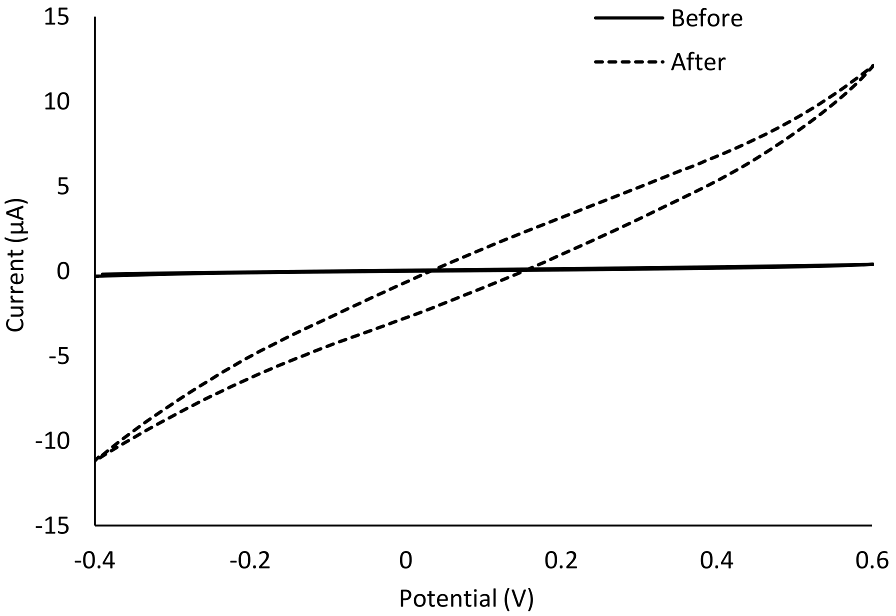

Figure 6.17. Cyclic voltammogram of a SAM modified Au electrode using 0.1M KNO_3 before (solid line) and after (dashed line) exposure to Fc-SLN at a scan rate of 50 mV/s. A Pt pseudo-reference was used

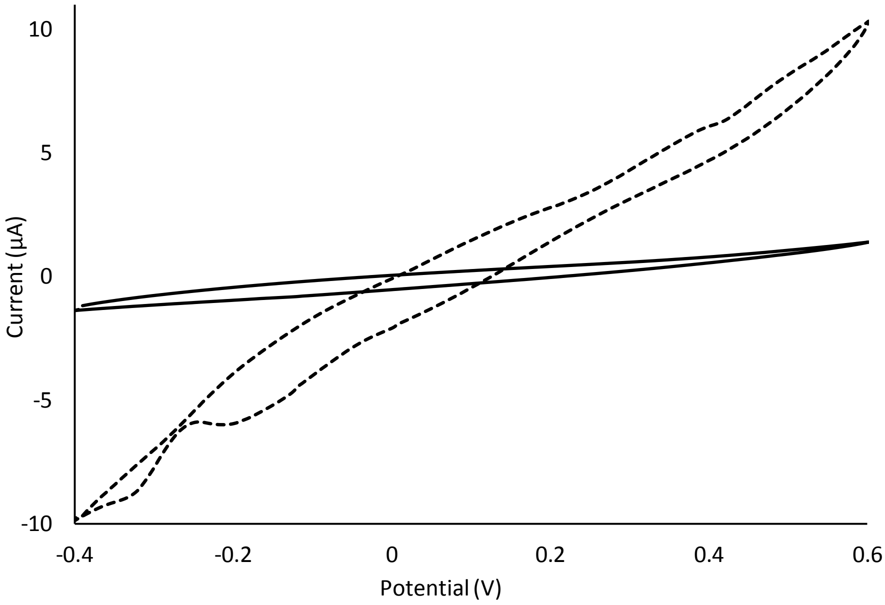

Figure 6.18. Cyclic voltammogram of a BLM modified Au electrode using 0.1M KNO_3 before (solid line) and after (dashed line) exposure to Fc-SLN at a scan rate of 50 mV/s. A Pt pseudo-reference was used

6.2.2.2. Electrochemical Impedance Spectroscopy

The EIS spectra acquired for the SAM and BLM films before and after exposure to the Fc-SLN and their respective equivalent circuit model are shown in Figure 6.19 and 6.20. The Nyquist plot for the SAM film before exposure to Fc-SLN (Figure 6.19a) shows a semi-elliptical shape at high frequency values, followed by a slight deviation from the semi-circular path at low frequencies. This implies poor blocking properties for the SAM film. The system is modelled by a resistor (R1) and constant phase element (CPE1) in series with the solution resistance (R_s) and another constant phase element (CPE2). CPE2 represents the imperfections in the SAM film; these can be attributed to the roughness of the gold electrode surface. The addition of an upper film to form a BLM masks the effect of the imperfections, and hence CPE2 is not required in the equivalent circuit model for the BLM. The resistor, R1 accounts for resistance to charge transfer due to the film blocking properties; the constant phase elements accounts for the imperfect capacitance of the electrical double layer and the film. The Nyquist plot for the SAM after exposure to the Fc-SLN maintains the semi-elliptical shape at high frequencies and another semi-elliptical shape at high frequencies. This system is modelled by a constant phase element in parallel with a resistor with a series connection to another resistor and CPE (Figure 6.19b). A reduction in the order of magnitude of the complex impedance is observed for the SAM film after exposure to the Fc-SLN.

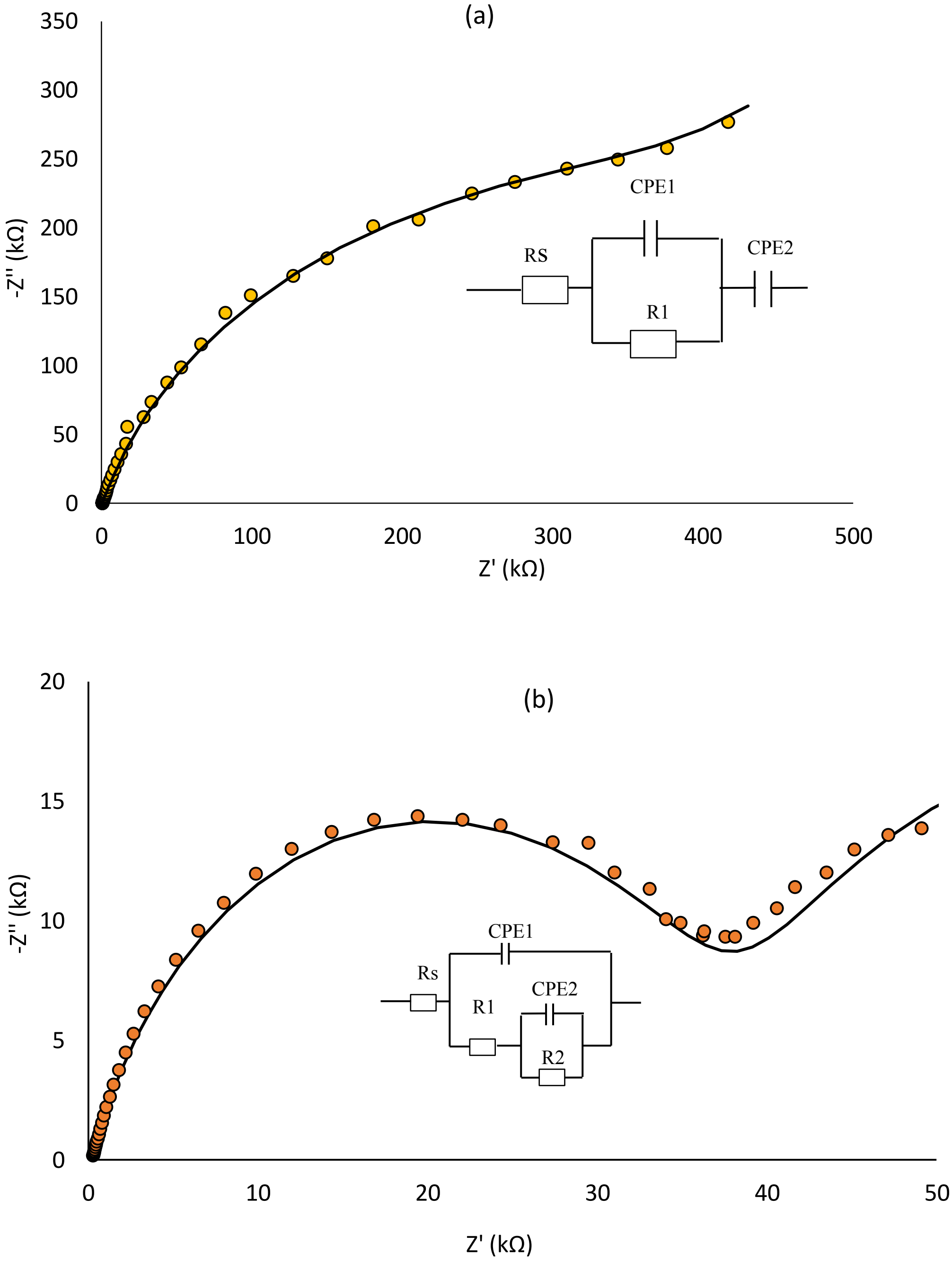

Figure 6.19. Electrochemical impedance spectra in the form of Nyquist plots for SAM modified Au (a) before and (b) after exposure to Fc-SLN. Measured in a 0.1 M solution of KNO_3 at open circuit potential obtained for frequencies in the range from 10^5 to 1 Hz. The solid line shows the model fit for the equivalent circuit shown in inset

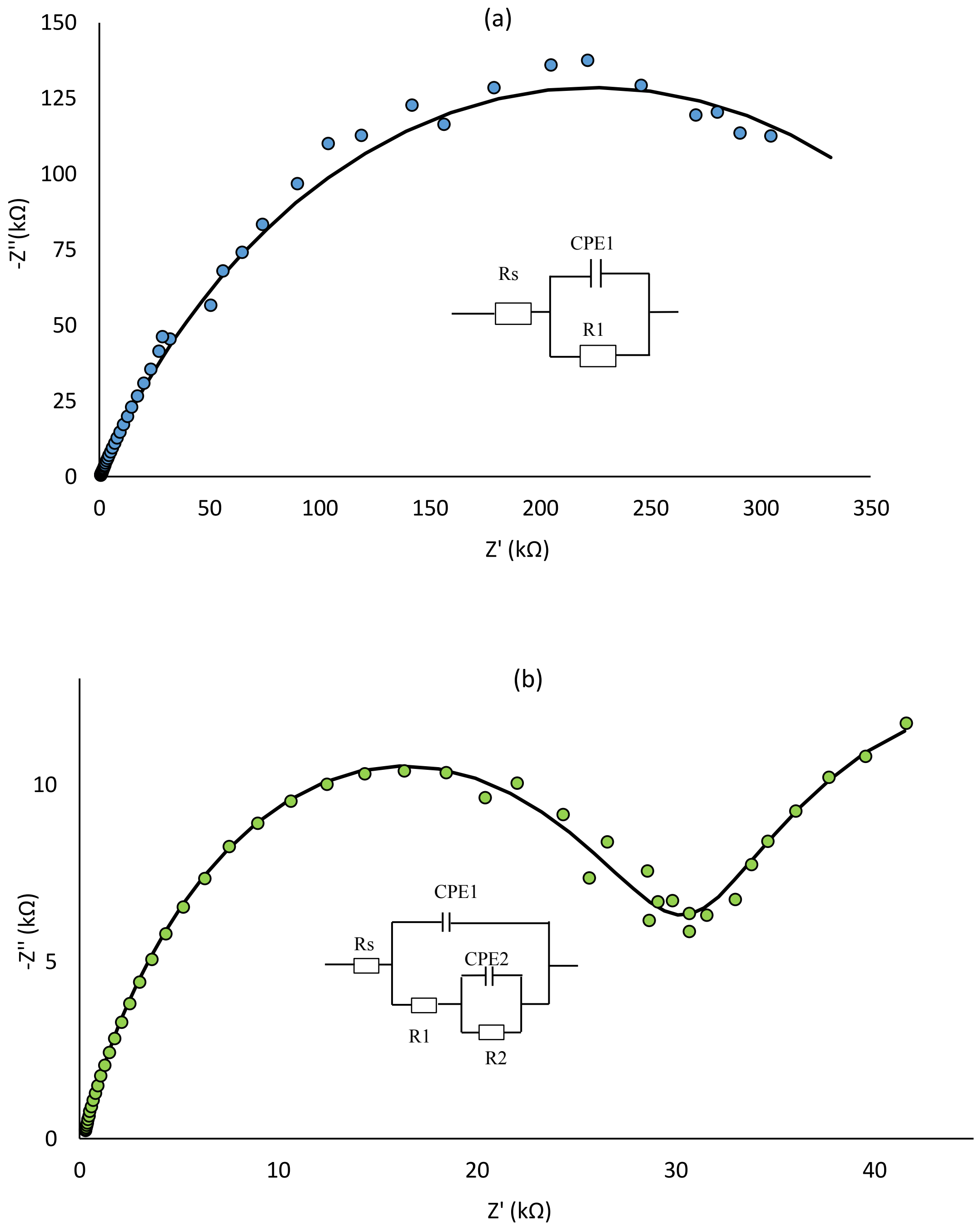

Figure 6.20. Electrochemical impedance spectra in the form of Nyquist plots for BLM modified Au (a) before and (b) after exposure to Fc-SLN. Measured in a 0.1 M solution of KNO_3 at open circuit potential obtained for frequencies in the range from 10^5 to 1 Hz. The solid line shows the model fit for the equivalent circuit shown in inset

The Nyquist plot for the BLM film before exposure to the Fc-SLN shows a semi-elliptical shape throughout the frequency range Figure 6.20a. The equivalent circuit model for this system comprises of a resistor (electrical double layer/BLM film) in parallel with a CPE.

	R1 (kΩ)	CPE1 (μS)	R2 (kΩ)	CPE2 (μS)
SAM before	360.0 ± 34.2	0.18 ± 0.01 (0.858)	-	1.16 ± 0.13 (0.691)
SAM after	39.1 ± 0.01	0.15 ± 0.01 (0.790)	45.8 ± 13.6	8.88 ± 1.92 (0.775)
BLM Before	449.1 ± 0.14	0.30 ± 0.01 (0.662)	-	-
BLM after	31.7 ± 0.10	0.20 ± 0.01 (0.741)	31.0 ± 11.2	11.1 ± 3.2 (0.809)

Table 6.1. The model fit values for the equivalent circuits shown in Figure 6.19 and 6.20

Similar to the SAM film, the BLM film after exposure to the Fc-SLN shows a reduction in the order of magnitude of the complex impedance and an additional semi-elliptical shape appearing at low frequency values. The presence of two semi-elliptical shapes are indicative of two time constants.

The time constant in the high frequency range is due to the SAM impedance and the one in the lower frequency range represents the capacitance and resistance of defects in the lipid membrane.[84] The penetration of Fc-SLN into the lipid film introduces defects in the lipid film, hence the model fitted for both the BLM and SAM after exposure one which is used to model a corrosion of coatings to represent the nanopores where the particles embed into the lipid film.[85] The values corresponding to the equivalent circuits for the BLM and SAM films presented in Figure 6.19 and Figure 6.20 are shown in Table 6.1. The charge transfer resistance (R_{ct}) is equivalent to the total real component of the complex impedance, which is R1 for the SAM and BLM film models before exposure and $R1 + R2^{-1}$ after exposure; $R1 + R2^{-1}$ is approximately equal to R1. A reduction by an order of magnitude is observed for the R_{ct} values for both the SAM and BLM after exposure to the Fc-SLN (360 ± 34 kΩ to 39.1 ± 0.01 kΩ and 449 ± 0.14 kΩ to 31.7 ± 0.1 kΩ) was observed. This supports the increase in the current response observed by cyclic voltammetry, alluding to the enhanced electrical conductivity and sensitivity of the lipid film. The capacitance of the SAM and BLM modified surface can be approximated to the imaginary component of the total impedance of the interface; the constant phase elements are contributors to the imaginary impedance. The impedance of a CPE is expressed as

$$Z_{CPE} = \frac{1}{Y_O(j\omega)^{\alpha}} \qquad \text{Eqn 6.1}$$

Where Y_o is the capacitance, ω is frequency and α is a coefficient that is equal to 1 for an ideal capacitor. The pseudo-capacitance can be calculated by equating the impedance of a CPE to that of a capacitance, i.e. the equivalent value of Y_o for $\alpha = 1$. The pseudo-capacitance can be expressed as

$$C = Q_{CPE}(\omega_{max})^{\alpha - 1} \qquad \text{Eqn 6.2}$$

where Q_{CPE} is the value of the CPE and ω_{max} is the frequency value at maximum imaginary impedance (the maxima of the semi-elliptical curve). The pseudo-capacitance values for the CPEs and the total capacitance values of the system are shown in Table 6.2.

The capacitance C1 can be allocated to the capacitance of the lipid film and C2 to the electrical double layer capacitance.[85] The penetration of Fc-SLN into lipid films results in a reduction of the lipid film capacitance and an increase in the double layer capacitance which results in a reduction of the overall capacitance of the interface. Capacitance is dependent on

	C1 (μF)	C2 (μF)	Total capacitance (μF)
SAM before	0.139 ± 0.008	1.16 ± 0.13	0.124 ± 0.008
SAM after	0.052 ± 0.004	8.88 ± 1.92	0.052 ± 0.004
BLM before	0.185 ± 0.006	-	0.185 ± 0.006
BLM after	0.057 ± 0.003	11.10 ± 3.20	0.056 ± 0.003

Table 6.2. The capacitance calculated from the model fitted CPE parameters shown in Table 6.1 assuming ideal capacitance behaviour. The total capacitance represents the electrical double layer/lipid film capacitance and is calculated by parallel addition of the capacitance. Electrode area = 0.008 cm^2

the surface area and thickness (separation distance between the charges) according to the expression

$$C = \frac{\varepsilon_0 \varepsilon_r A}{d} \qquad \text{Eqn 6.3}$$

In physical terms, the reduction in the lipid membrane capacitance can be attributed to the adsorption of the Fc-SLN onto the lipid membrane surface and penetration of the SLN, which reduces the effective capacitance area. In addition, the permeation of the Fc-SLN enhances the permeability of ions and water molecules to the electrode/film interface, which increases the double layer capacitance. The introduction of charge into the interface also results in the separation of charge such that the system behaves as two capacitors, hence the two time constants observed in Figure 6.19 and 6.20. The contribution of the double layer capacitance to the overall interface capacitance is very small, hence the overall decrease.

6.2.2.3. Real time penetration with RESI

RESI was used to study the penetration of the Fc-SLN into the lipid membranes in real time. RESI is a powerful tool in the analysis of interfacial capacitance, and has high sensitivity. Figure 6.21 and 6.22 show the real time changes in capacitance and peak amplitude as the Fc-SLN dispersion is injected into the system for the SAM and BLM systems, respectively. A decrease in capacitance is noted immediately after injection of the Fc-SLN for both the BLM and SAM films. This can be attributed to the adsorption of the nanoparticles onto the lipid film surface. The occlusive properties of SLN systems can enable film formation which could increase the charge separation distance on the interface. The SAM system shows step-like drops in the capacitance during penetration of the Fc-SLN. This agrees with the observations made by EIS where a decrease in capacitance was noted after exposure of the films to the Fc-SLN. It is possible that each step decrease is due to the penetration of individual Fc-SLN particles. The BLM film also shows a decrease in the capacitance values due to the

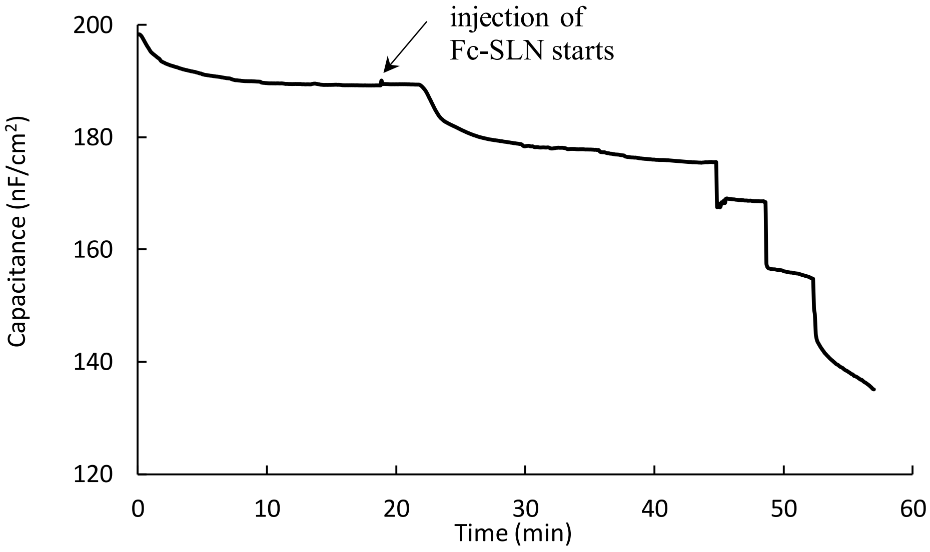

Figure 6.21. Real time interfacial capacitance plot, measured using RESI for a SAM film during injection of Fc-SLN dispersion in a background solution of 0.1 M KNO_3. The arrow indicates the time of injection of the Fc-SLN dispersion

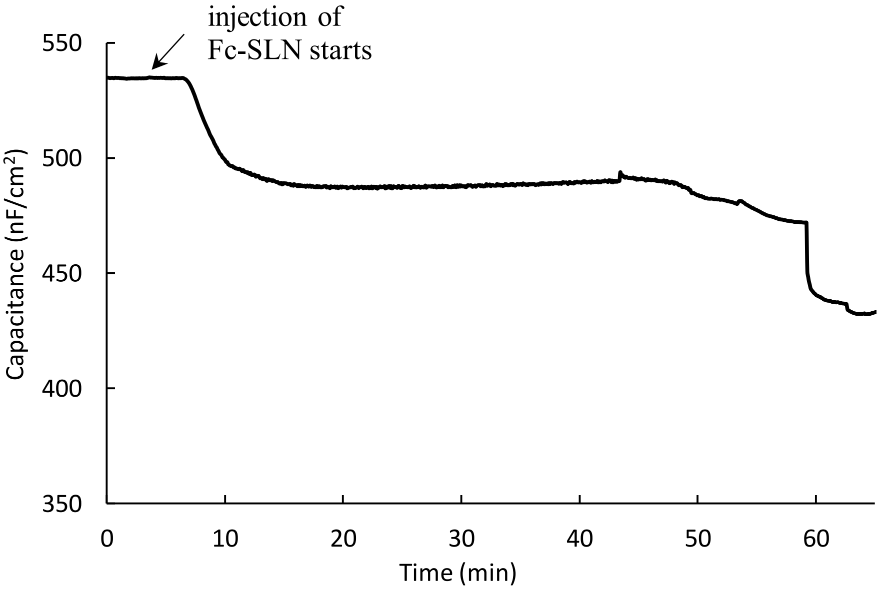

Figure 6.22. Real time interfacial capacitance plot, measured using RESI for a SAM film during injection of Fc-SLN dispersion in a background solution of 0.1 M KNO_3. The arrow indicates the time of injection of the Fc-SLN dispersion

adsorption and the penetration of the nanoparticles into the film; however, the step-changes are less defined than those observed for the SAM system. The penetration of the particles into the SAM is faster than that observed for the BLM. Capacitance changes due to the penetration of the particles can be observed after 14 minutes for the SAM film and after the 38 minutes for the BLM film. This is due to the interaction of the Fc-SLN and the lipid film. The Fc-SLN interact with the film by hydrophobic interactions. The SAM alkyl groups point outwards and so would interact more strongly with the Fc-SLN in comparison with the BLM which has charged moieties pointing outwards (phosphate and choline groups).

6.3 Conclusions

This chapter set out to highlight the incorporation of ferrocene into a lauric acid matrix. The successful incorporation of ferrocene with an entrapment efficiency of 73 ± 2 was reported. Physicochemical characterisation showed that there are no strong interactions present between the Fc and lauric acid matrix and that the system adopts a core shell arrangement, where the Fc is localized in the shell of the nanoparticle. The Fc-SLN showed redox activity when studied in solution by DPV and EIS. The penetration of the Fc-SLN into SAM and BLM films was confirmed by CV, EIS and RESI. The particles adsorb onto the lipid film and are incorporated into the film by hydrophobic interactions. Incorporation of the Fc-SLN into the lipid membrane alters the electrical properties of the lipid membrane. In conclusion, the SLN can be indeed be used to transport electrochemical tags across lipid membranes which is of interest in biosensing applications and they can be used to alter the properties of lipid membranes.

6.4 References

1 S. Takahashi and J. Anzai, *Materials (Basel).*, 2013, **6**, 5742–5762.

2 F. Ricci and G. Palleschi, *Biosens. Bioelectron.*, 2005, **21**, 389–407.

3 S. Reiter, K. Habermüller and W. Schuhmann, *Sensors Actuators B Chem.*, 2001, **79**, 150–156.

4 S. Roldán, M. Granda, R. Menéndez, R. Santamaría and C. Blanco, *J. Phys. Chem. C*, 2011, **115**, 17606–17611.

5 L. A. Shundrin, I. G. Irtegova, N. V Vasilieva and I. A. Khalfina, *Tetrahedron Lett.*, 2016, **57**, 392–395.

6 E. Koutsoumpeli, J. Murray, D. Langford, R. S. Bon and S. Johnson, *Sens. Bio-Sensing Res.*, 2015, **6**, 1–6.

7 H. J. Lorkowski, *Polym. Sci. U.S.S.R.*, 1973, **15**, 358–373.

8 W. A. Amer, L. Wang, A. M. Amin, L. Ma and H. Yu, *J. Inorg. Organomet. Polym. Mater.*, 2010, **20**, 605–615.

9 W. Schuhmann, *Biosens. Bioelectron.*, 1993, **8**, 191–196.

10 W. C. Mak, K. Y. Cheung, D. Trau, A. Warsinke, F. Scheller and R. Renneberg, *Anal. Chem.*, 2005, **77**, 2835–2841.

11 Z. Dai, S. Serban, H. Ju and N. El Murr, *Biosens. Bioelectron.*, 2007, **22**, 1700–1706.

12 J.-Y. Wang, L.-C. Chen and K.-C. Ho, 2013.

13 H. Muguruma, Y. Kase and H. Uehara, *Anal. Chem.*, 2005, **77**, 6557–6562.

14 M. Kasuya and K. Kurihara, *Langmuir*, 2014, **30**, 7093–7097.

15 H. T. Tien and A. Ottova-Leitmannova, *Planar Lipid Bilayers (BLM's) and Their Applications*, Elsevier Science, 2003.

16 E. R. de Jong, E. Manoury, J.-C. Daran, C.-O. Turrin, J. Chiffre, A. Sournia-Saquet, W. Knoll, J.-P. Majoral and A.-M. Caminade, *J. Organomet. Chem.*, 2012, **718**, 22–30.

17 T. J. Kealy and P. L. Pauson, *Nature*, 1951, **168**, 1039–1040.

18 G. B. Kauffman, *J. Chem. Educ.*, 1983, **60**, 185–186.

19 M. Rausch, M. Vogel and H. Rosenberg, *J. Chem. Educ.*, 1957, **34**, 268.

20 H. Werner, *Angew. Chemie Int. Ed.*, 2012, **51**, 6052–6058.

21 A. M. Bond, E. A. McLennan, R. S. Stojanovic and F. G. Thomas, *Anal. Chem.*, 1987, **50**, 2853–2860.

22 M. . E. G. Lyons, *Sensors*, 2003, **3**, 19–42.

23 L. Yu and G. Z. Chen, *J. Power Sources*, 2016.

24 S. Zhang, N. Wang, Y. Niu and C. Sun, *Sensors Actuators B Chem.*, 2005, **109**, 367–374.

25 N. Zhu, J. Ulstrup and Q. Chi, *J. Mater. Chem. B*, 2015, **3**, 8133–8142.

26 S. Manivannan and R. Ramaraj, *Pure Appl. Chem.*, 2011, **83**, 2041 – 2053.

27 X. Pei, Z. Xu, J. Zhang, Z. Liu and J. Tian, *Anal. Methods*, 2013, **5**, 3235.

28 D. Astruc, *Nat. Chem.*, 2012, **4**, 255–267.

29 S. Sun, L. Chen, H. Shi, Y. Li and X. He, *J. Electroanal. Chem.*, 2014, **734**, 18–24.

30 A. Mars, C. Parolo, N. Raouafi, K. Boujlelb and A. Merkoçi, *J. Mater. Chem. B*, 2013, **1**, 2951–2955.

31 D. Li, Y. Zhang, J. Jiang and J. Li, *J. Colloid Interface Sci.*, 2003, **264**, 109–113.

32 T. Takada, T. Tochi, M. Nakamura and K. Yamana, *Preparation of ferrocene-functionalized gold nanoparticles by primer extension reaction on the particle surface*, 2014, vol. 24.

33 A. J. Baca, F. Zhou, J. Wang, J. Hu, J. Li, J. Wang and Z. S. Chikneyan, *Electroanalysis*, 2004, **16**, 73–80.

34 J. Hu, Y. Ji, W. Chen, C. Streb and Y. Song, *Energy Environ. Sci.*, 2016, **9**, 1095–1101.

35 G. Milczarek, *IEEE NANO 2009 : 2009 9th IEEE Conference on Nanotechnology : 26-30 July 2009, Genoa.*, IEEE, 2009.

36 A. M. Schrand, M. F. Rahman, S. M. Hussain, J. J. Schlager, D. A. Smith and A. F. Syed, *Wiley Interdiscip. Rev. Nanomedicine Nanobiotechnology*, 2010, 2, 544–568.

37 E. Abbasi, S. F. Aval, A. Akbarzadeh, M. Milani, H. T. Nasrabadi, S. W. Joo, Y. Hanifehpour, K. Nejati-Koshki and R. Pashaei-Asl, *Nanoscale Res. Lett.*, 2014, **9**, 247.

38 E. Buhleier, W. Wehner and F. Vögtle, *Synthesis (Stuttg).*, 1978, **2**, 155–158.

39 S. Javor, E. Delort, T. Darbre and J. L. Reymond, *J. Am. Chem. Soc.*, 2007, **129**, 13238–13246.

40 C.-Y. Huang and Y. O. Su, *Dalt. Trans.*, 2010, **39**, 8306.

41 H. T. Tien and Z. Salamon, *Bioelectrochemistry Bioenerg.*, 1989, **22**, 211–218.

42 A. L. Plant, *Langmuir*, 1993, **9**, 2764–2767.

43 O. Fontaine, G. Trippé, C. Fave, J.-C. Lacroix and H. N. Randriamahazaka, *J. Electroanal. Chem.*, 2009, **632**, 1–7.

44 A. V. Rudnev, U. Zhumaev, T. Utsunomiya, C. Fan, Y. Yokota, K. Fukui and T. Wandlowski, *Electrochim. Acta*, 2013, **107**, 33–44.

45 C. E. D. Chidsey, C. R. Bertozzi, T. M. Putvinski and A. M. Mujsce, *J. Am. Chem. Soc.*, 1990, **112**, 4301–4306.

46 K. Shimazu, I. Yagi, Y. Sato and K. Uosaki, 2002.

47 A. Hammami, J. Kuliček and N. Raouafi, *Food Chem.*, 2016, **209**, 274–278.

48 N. Darwish, P. K. Eggers, P. Da Silva, Y. Zhang, Y. Tong, S. Ye, J. J. Gooding and M. N. Paddon-Row, *Chemistry*, 2012, **18**, 283–92.

49 S. Campuzano, V. Escamilla-Gómez, M. Á. Herranz, M. Pedrero and J. M. Pingarrón, *Sensors Actuators B Chem.*, 2008, **134**, 974–980.

50 N. K. Chaki and K. Vijayamohanan, *Biosens. Bioelectron.*, 2002, **17**, 1–12.

51 A. Ulman, 1996.

52 M. Zviman and H. T. Tien, *Biosens. Bioelectron.*, 1991, **6**, 37–42.

53 A. Ottova, V. Tvarozek and H. T. Tien, in *Planar Lipid Bilayers (BLM’s) and Their Applications*, eds. H. T. Tien and A. Ottova-Leitmannova, Elsevier Science, 2003, pp. 917 – 963.

54 N. Nagata, Y. Kuramochi and Y. Kobuke, 2008.

55 Z. Salamon, Y. Wang, G. Tollin and H. A. Macleod, *Biochim. Biophys. Acta - Biomembr.*, 1994, **1195**, 267–275.

56 R. Campos and R. Kataky, *J. Phys. Chem. B*, 2012, **116**, 3909–3917.

57 M. Blank, Ed., *Electrical Double Layers in Biology*, Springer US, Boston, MA, 1986.

58 A. Ottova-Leitmannova and H. Ti Tien, *Prog. Surf. Sci.*, 1992, **41**, 337–445.

59 X. K. Zhao, S. Baral and J. H. Fendler, *J. Phys. Chem.*, 1990, **94**, 2043–2052.

60 J.-S. Ye, A. Ottova, H. T. Tien and F.-S. Sheu, *Bioelectrochemistry*, 2003, **59**, 65–72.

61 Y. K. Lee and J.-M. Nam, *Small*, 2012, **8**, 832–7.

62 J. J. Gooding, F. Mearns, W. Yang and J. Liu, *Electroanalysis*, 2003, **15**, 81–96.

63 A. E. Vallejo and C. A. Gervasi, *Bioelectrochemistry*, 2002, **57**, 1–7.

64 T. Wink, S. J. van Zuilen, A. Bult and W. P. van Bennekom, *Analyst*, 1997, **122**, 43–50.

65 A. H. B. Wu, *Clin. Chim. Acta.*, 2006, **369**, 119–24.

66 R. S. Yalow and S. A. Berson, *Nature*, 1959, **184**, 1648–1649.

67 L. Wang, F. Feng and Z. Ma, *Sci. Rep.*, 2015, **5**, 16855.

68 L. B. Vong, M. Kobayashi and Y. Nagasaki, *Mol. Pharm.*, 2016.

69 A. Gupta, S. Das and S. Seal, *Nanomedicine*, 2014, **9**, 2725–2728.

70 S. S. Lee, W. Song, M. Cho, H. L. Puppala, P. Nguyen, H. Zhu, L. Segatori and V. L. Colvin, *ACS Nano*, 2013, **7**, 9693–703.

71 M. A. Vorotyntsev, V. A. Zinovyeva, D. V Konev, M. Picquet, L. Gaillon and C. Rizzi, *J. Phys. Chem. B*, 2009, **113**, 1085–99.

72 D. Hou, C. Xie, X. Yang, H. Xu and Q. Ping, *Yao Xue Xue Bao*, 2007, **42**, 429–33.

73 S. M. Martins, B. Sarmento, C. Nunes, M. Lúcio, S. Reis and D. C. Ferreira, *Eur. J. Pharm. Biopharm.*, 2013, **85**, 488–502.

74 V. Jenning, A. F. Thünemann and S. H. Gohla, *Int. J. Pharm.*, 2000, **199**, 167–177.

75 H. Bunjes and T. Unruh, *Adv. Drug Deliv. Rev.*, 2007, **59**, 379–402.

76 K. A. Riske, L. Q. Amaral and M. T. Lamy-Freund, *Biochim. Biophys. Acta*, 2001, **1511**, 297–308.

77 L. Montenegro, M. G. Sarpietro, S. Ottimo, G. Puglisi and F. Castelli, *Int. J. Pharm.*, 2011, **415**, 301–306.

78 V. V Pavlishchuk and A. W. Addison, *Inorganica Chim. Acta*, 2000, **298**, 97–102.

79 K. H. Boubbou and T. H. Ghaddar, *Langmuir*, 2005, **21**, 8844–8851.

80 A. Lataifeh and H.-B. Kraatz, *J. Inorg. Organomet. Polym. Mater.*, 2010, **20**, 488–502.

81 P. R. Ashton, V. Balzani, M. Clemente-León, B. Colonna, A. Credi, N. Jayaraman, F.

M. Raymo, J. F. Stoddart and M. Venturi, *Chem. - A Eur. J.*, 2002, **8**, 673–684.

82 C.-O. Turrin, J. Chiffre, D. de Montauzon, G. Balavoine, E. Manoury, A.-M. Caminade and J.-P. Majoral, *Organometallics*, 2002, **21**, 1891–1897.

83 A. K. M. Kafi, D.-Y. Lee, S.-H. Park and Y.-S. Kwon, *NanoBiotechnology*, 2006, **2**, 67–70.

84 Ž. Petrovića, M. Metikoš-Hukovićb, S. Omanovicc and M. Leskovacd, *ECS Trans.*, 2010, **28**, 51–63.

85 F. Mansfeld, *J. Appl. Electrochem.*, 1995, **25**, 187–202.

7. Conclusions and Future Work

This thesis set out to investigate new applications of solid lipid matrix systems. Solid lipid nanoparticles and microparticles have found numerous application in pharmaceutical drug delivery, cosmetics and UV protection. This thesis reports for the first time, the application of SLM and SLN systems in laundry delivery and their interactions with lipid membranes.

Chapter 4 highlighted the application of SLM as a carrier vehicle for fabric softeners from the organosilicon family. The microparticles were prepared using solvent assisted microemulsion methods either with a hydrophilic solvent (ethanol) and a hydrophobic solvent (n-hexane). n-hexane enhances the miscibility of the lipid matrix and the silicones (which are largely lipophobic and hydrophobic) and thus the loading capacity. Amino-functionalised silicones have a comparatively high encapsulation efficiency for both methods of preparation. This can be attributed to the higher propensity for interaction between the amino-functional moieties and the lauric acid; however, the experimental methods did not show any evidence to support this hypothesis, except for the higher loading capacities. It is most likely that the silicone SLM adopt a core shell model of incorporation where the silicone is surrounded by the lipid film. The release of the silicone from this matrix under a pH trigger has been shown. The matrix exhibits a burst release mechanism at pH 10.5 (laundry pH), which is ideal for laundry applications due to the short lifetimes of a laundry cycle.

Chapter 5 reported the incorporation of dyes into a lauric acid matrix and in addition, the co-encapsulation of dye and fabric softener into one matrix. The co-encapsulation of actives could potentially be instrumental in compact formulations. Ethyl violet showed higher values of encapsulation which remained unaffected by the addition of silicone in the matrix. However, the presence of the silicone affects the structural and surface properties of the lipid microstructures. Larger aggregated structures were observed in the system dual-active system. Polarized light microscopy showed that the lipid crystallinity in all the systems was maintained; however, DSC showed significant reductions in the enthalpy of fusion, which imply reduction in the lipid crystallinity. Fabric samples treated with the EV dye in a pH 10.5 buffer were compared to those treated in water solution. The dyes both showed enhanced deposition at high pH values (10.5) which is around value of pH produces by laundry formulations. At alkaline values, the dyes have an extra positive charge due to the protonation of the amine groups which enhances the deposition of the actives into the fabrics by electrostatic attraction to the slightly negative fabric surface. Further studies of the surface charge of the fabrics could confirm the observations and conclusions made in this investigation.

For future work, it would be interesting to investigate the encapsulation of other laundry actives such as optical brighteners and other combinations of actives and the interaction of the SLM systems with other passive and active laundry ingredients. Silicones and dyes also play a major role in hair-care applications. This system could be potentially optimized for haircare applications as well.

Chapter 6 reported the investigation of an SLN system as a carrier for a well-known and characterised electrochemical tag, ferrocene. Physicochemical characterisation of the system suggested a core-shell model of incorporation where the ferrocene is localized in the shell of the particles. The particles show an electrochemical response when a potential is applied, demonstrating their viability as electrochemical tags. The particles adsorb onto the lipid membrane and can penetrate a phospholipid monolayer within 14 minutes of exposure and 38 minutes of exposure to a phospholipid BLM.

For future work, this work would most likely incline towards the incorporation of other hydrophilic and hydrophobic redox agents such as TCNQ into the SLN system and also venture towards the encapsulation of hard nanoparticles such as cerium oxide or ferrocenated gold nanoparticles. The co-encapsulation of redox active compounds or the coupling of redox agents with biological systems such as proteins and enzymes could enable the application of this SLN system in various bio-electrochemical where the biodegradability and the biocompatibility of SLN systems would be invaluable. On the whole, SLN and SLM could become indispensable in many applications.

Appendix

Appendix 1

Additional optical microscopy images to supplement data shown in Figure 4.6. Phase contrast microscopy complements the bright field microscopy and shows the morphology of the particles from a different perspective. The images shown here also confirm the particle size range reported for the SLM systems reported in chapter 4.

Appendix 1a. Phase contrast microscopy image of non-silicone loaded SLM at x40 magnification

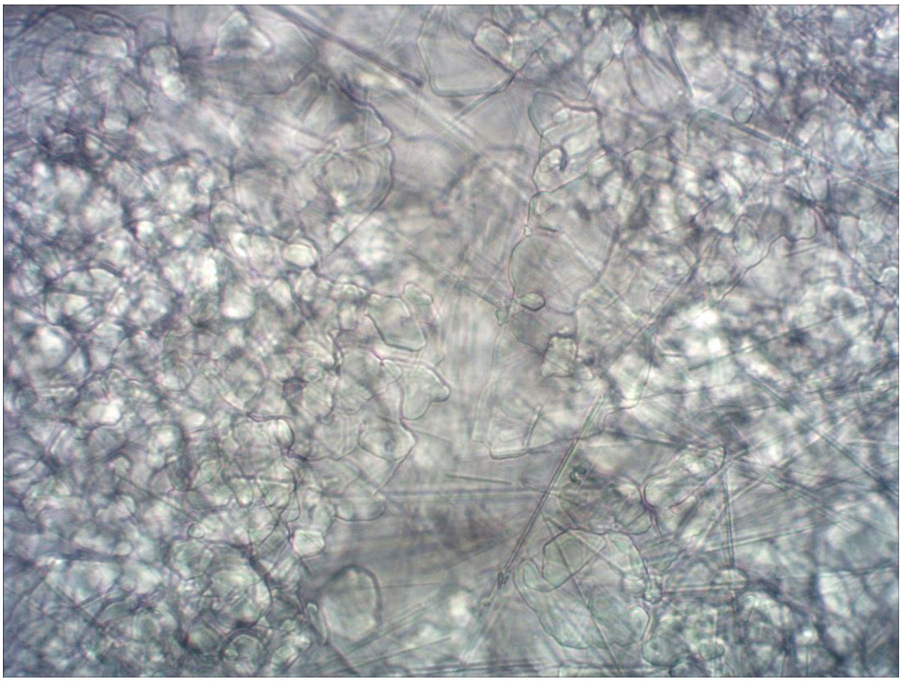

Appendix 1b. Phase contrast microscopy image of PDMS100 loaded SLM at x40 magnification

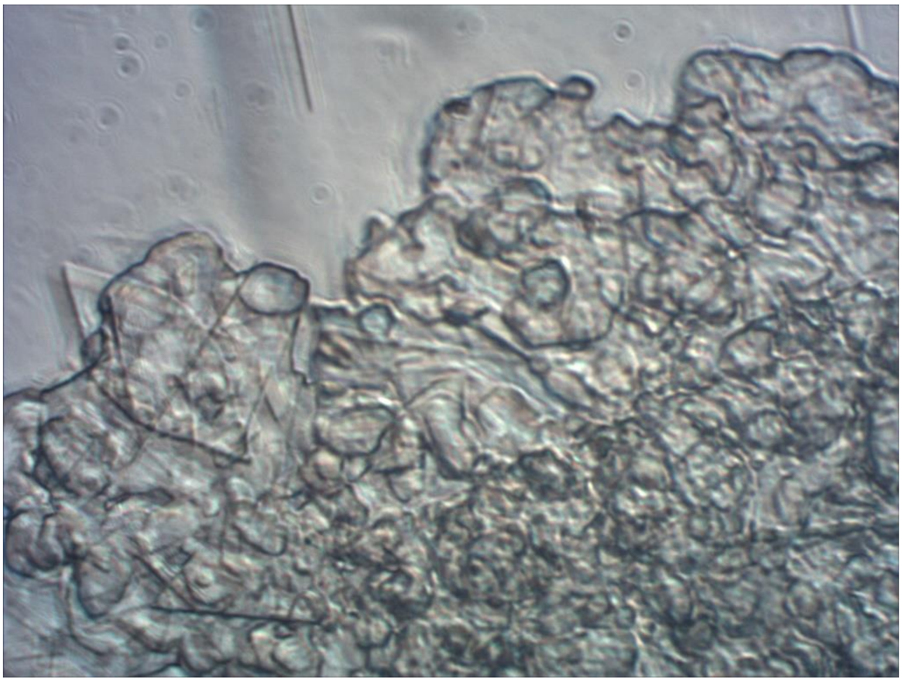

Appendix 1c. Phase contrast microscopy image of PDMS10 loaded SLM at x40 magnification

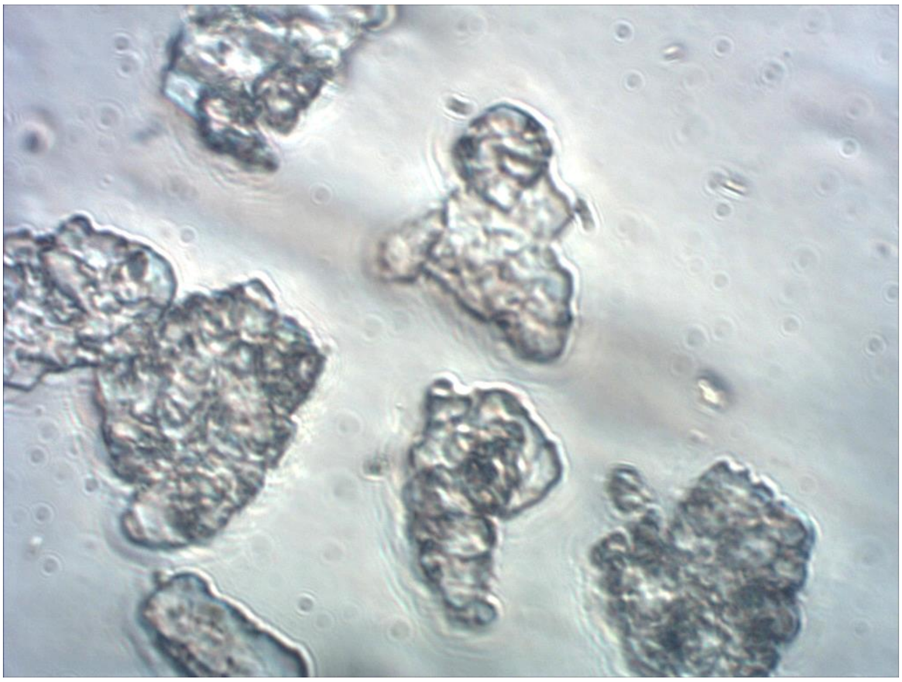

Appendix 1d. Phase contrast microscopy image of TAS loaded SLM at x40 magnification

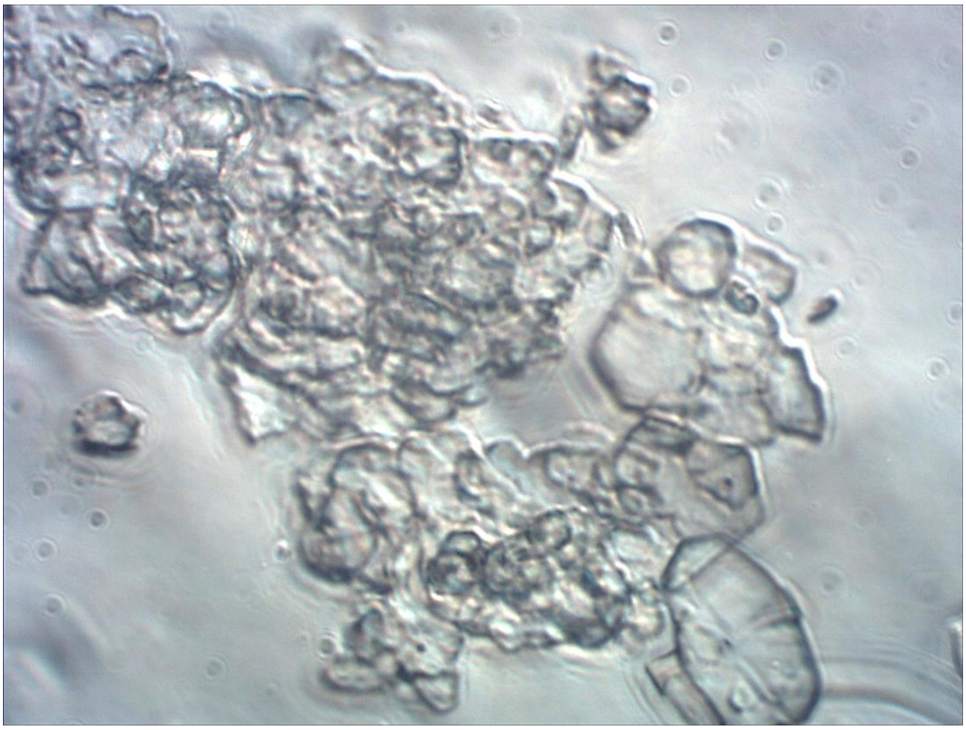

Appendix 1e. Phase contrast microscopy image of PK10 loaded SLM at x40 magnification

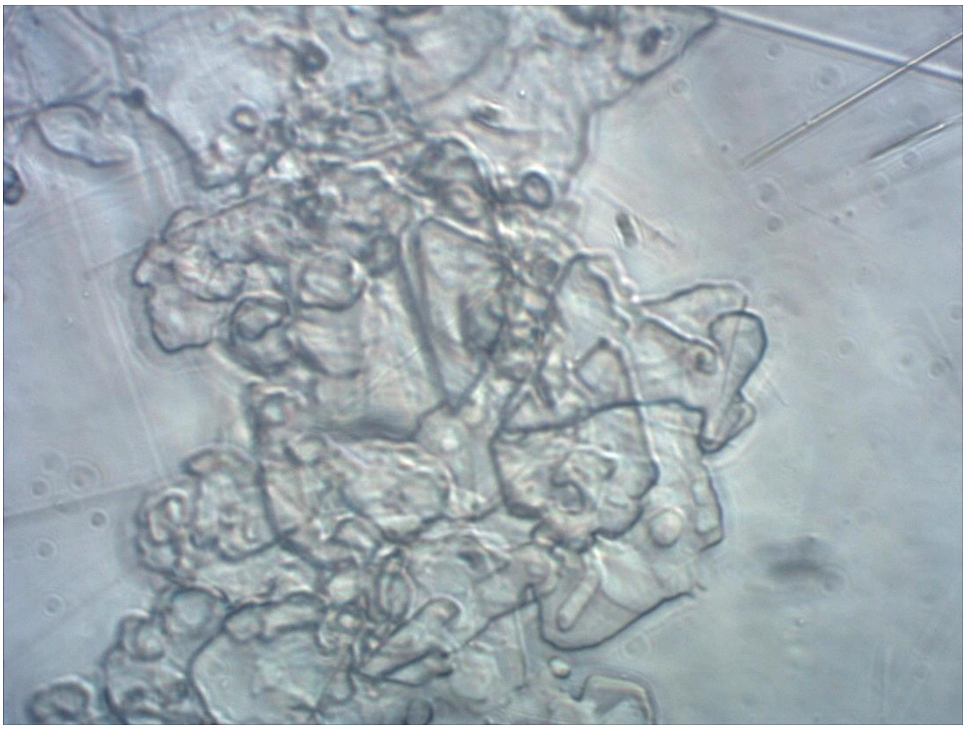

Appendix 2

The evolution of particle size as a response to pH change. Measurements are before addition of buffer to the ALM and every minute thereafter. An immediate shift in the particle size distribution is observed between the data acquired before pH change and that taken a minute after the pH change. The pH was changed from 5.5 to 10.5 using a $Na_2CO_3/NaHCO_3$ buffer. This confirms the short timescale of dissolution of the matrix (burst release) observed with optical microscopy (Figure 4.16). All the samples show a reduction in the particle size in response to the increase in pH; a distinct reduction in the population of particles in the size range of 100s µm (SLM particles) and an increase in the population of particles in the range of 10s µm (released silicone droplets)

Appendix 2a. Particle size distribution of PDMS10 loaded SLM measured before pH change and every minute thereafter.

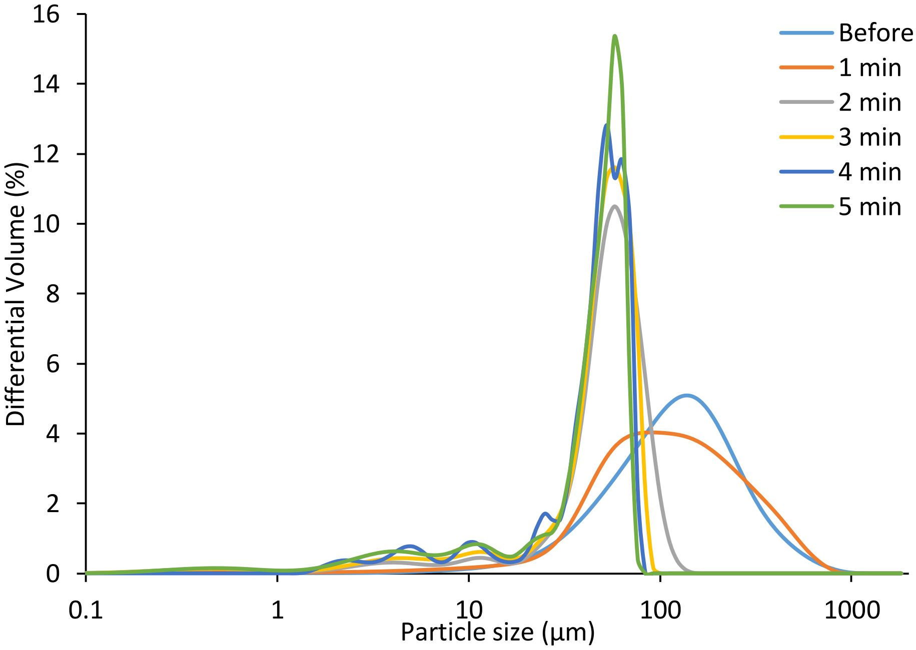

Appendix 2b. Particle size distribution of PDMS100 loaded SLM measured before pH change and every minute thereafter.

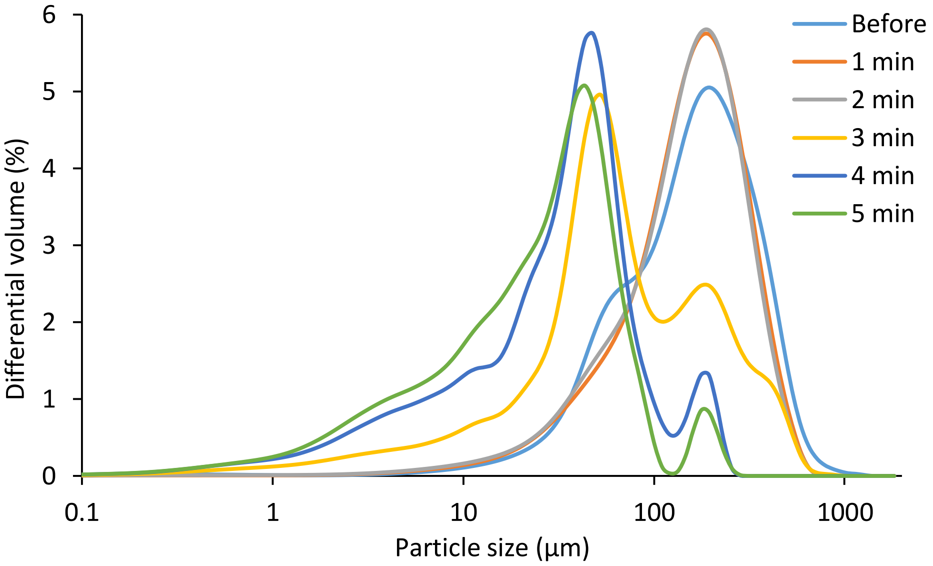

Appendix 2c. Particle size distribution of TAS loaded SLM measured before pH change and every minute thereafter

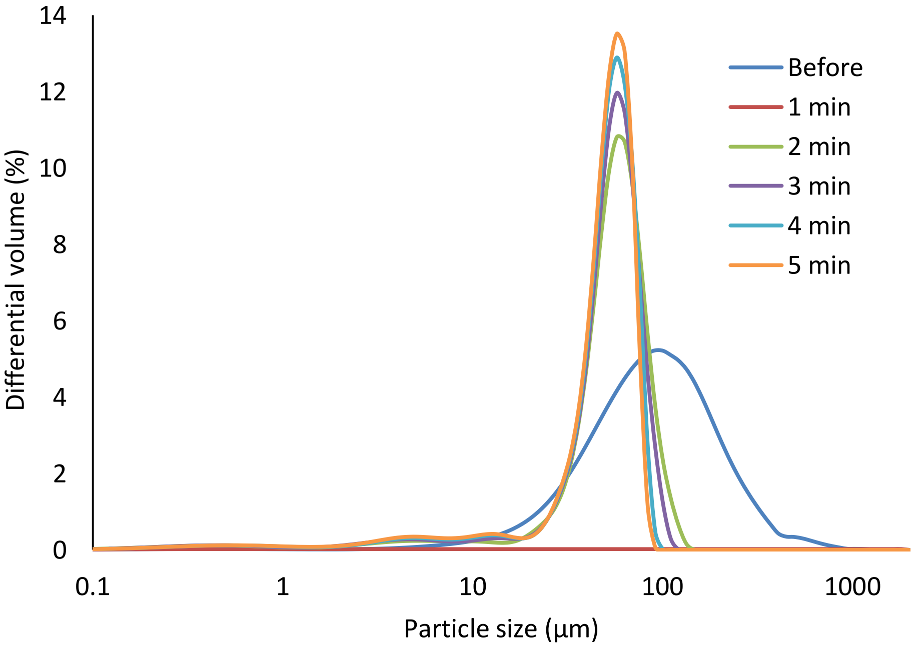

Appendix 2d. Particle size distribution of PK10 loaded SLM measured before pH change and every minute thereafter.

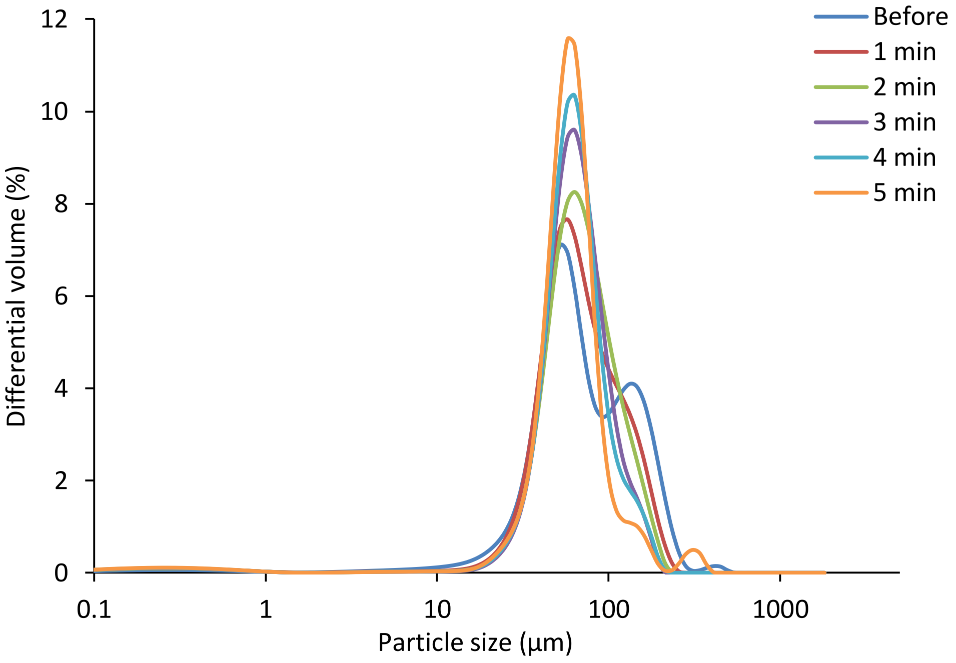

Appendix 3

Relationship between particle size and penetration of silicone into fibres: a micro-XRF study. Micro-XRF images mapping the Si content of the fibres were acquired. This study was carried out as a preliminary investigation to confirm the hypothesis the size dependence of deposition of silicones onto fabrics. PDMS100 and TAS silicone were used in this investigation. Particle sizes ranging from 50 – 1000 nm were achieved by a mixture of n-hexane which is a polydimethylsiloxane compatible solvent and ethanol which is not compatible. Silicone droplets with particle sizes of 5 μm and above were obtained from a gel carrier matrix. Cotton and polyester fabrics were used in this investigation.

Appendix 3a: Porosimetry

Porosimetry analysis showed that both cotton and polyester have more than one distribution of pore sizes, which is expected due to the hierarchical nature of fabrics (see Figure 4.17). Porosity measurements were acquired by mercury intrusion and showed two distinct distributions of pore sizes for cotton and polyester fabrics. The larger pore sizes, 73 μm and 91 μm for cotton and polyester respectively, can be attributed to the inter-yarn gaps. The smaller pore sizes, 9 μm and 24 μm for cotton and polyester respectively, can be attributed to the inter-fibre gaps. Penetration of silicone into the yarn enables deposition onto the individual fibres and hences reduces inter-fibre friction.

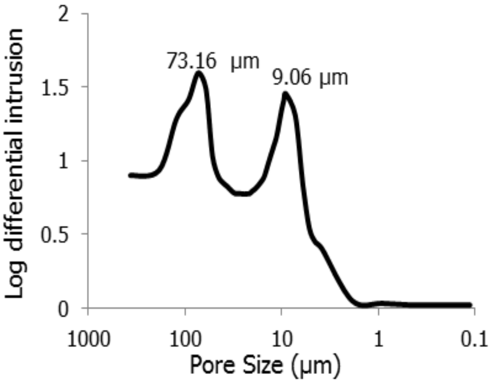
cotton

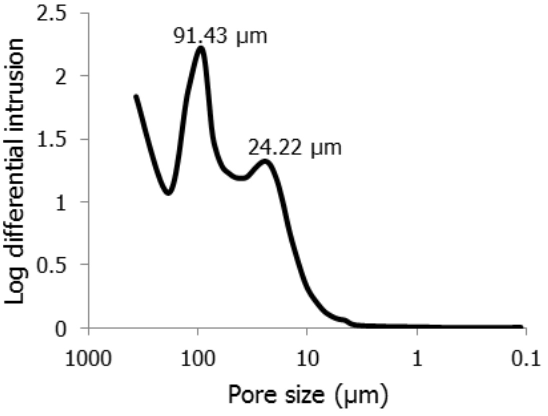
polyester

Appendix 3b: micro-XRF Analysis

Cotton Fibres

Images from the yarn surface were acquired from fibres on the periphery of the sample and those for the yarn bulk were obtained from points within the yarn. Comparisons between the silicon maps obtained on the yarn surface and in the bulk of the yarn generally suggest a higher deposition of silicone on the yarn surface for both actives. The 50 and 500 nm PDMS show the presence of low silicone counts throughout the cellulose fibre for both yarn surface and yarn bulk images suggesting the penetration of the silicone droplets into both the yarn (bundle of fibres) and the individual fibres. The 1000 nm PDMS show brighter spots around the fibres thick silicone films on the surface. Yarn surface maps for 250 nm and 500 nm TAS also show bright spots inside the fibres indicating penetration of silicone particles into the cellulose fibres.

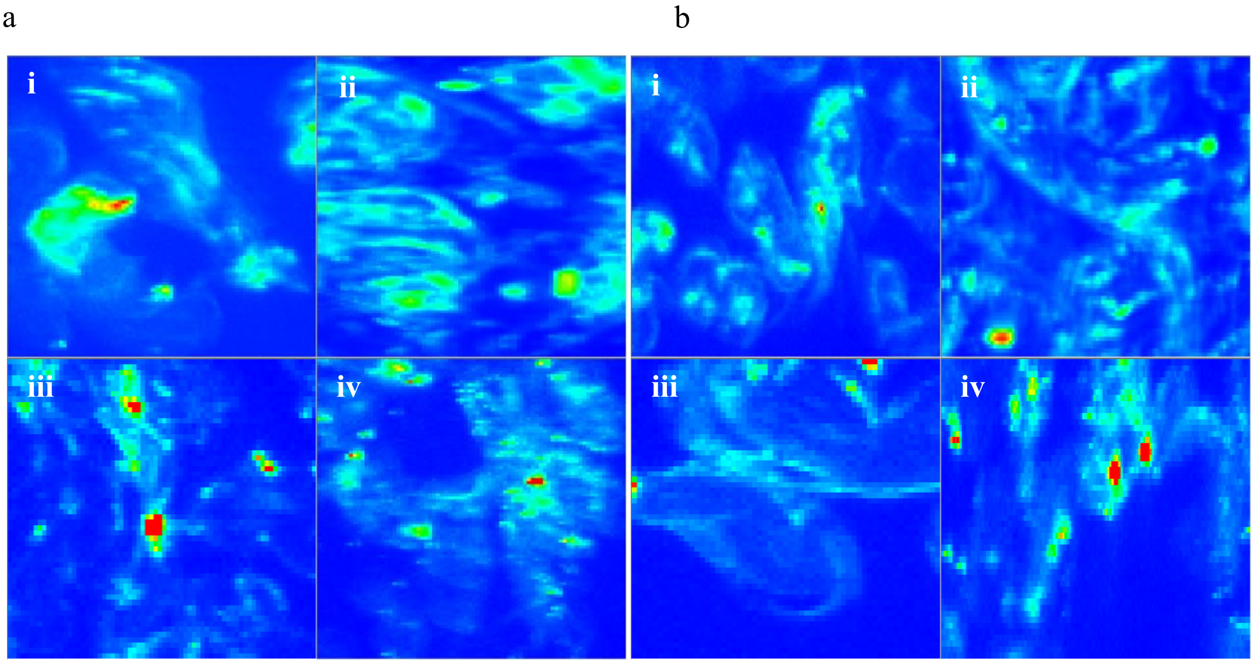

Micro-XRF Si map images of cotton fabrics from a) the yarn surface for i) 50 nm PDMS ii) 500 nm PDMS iii) 1000 nm PDMS and iv) PDMS in gel (about 5000 nm) b) the yarn bulk for) 50 nm PDMS ii) 500 nm PDMS iii) 1000 nm PDMS and iv) PDMS in gel (about 5000 nm)

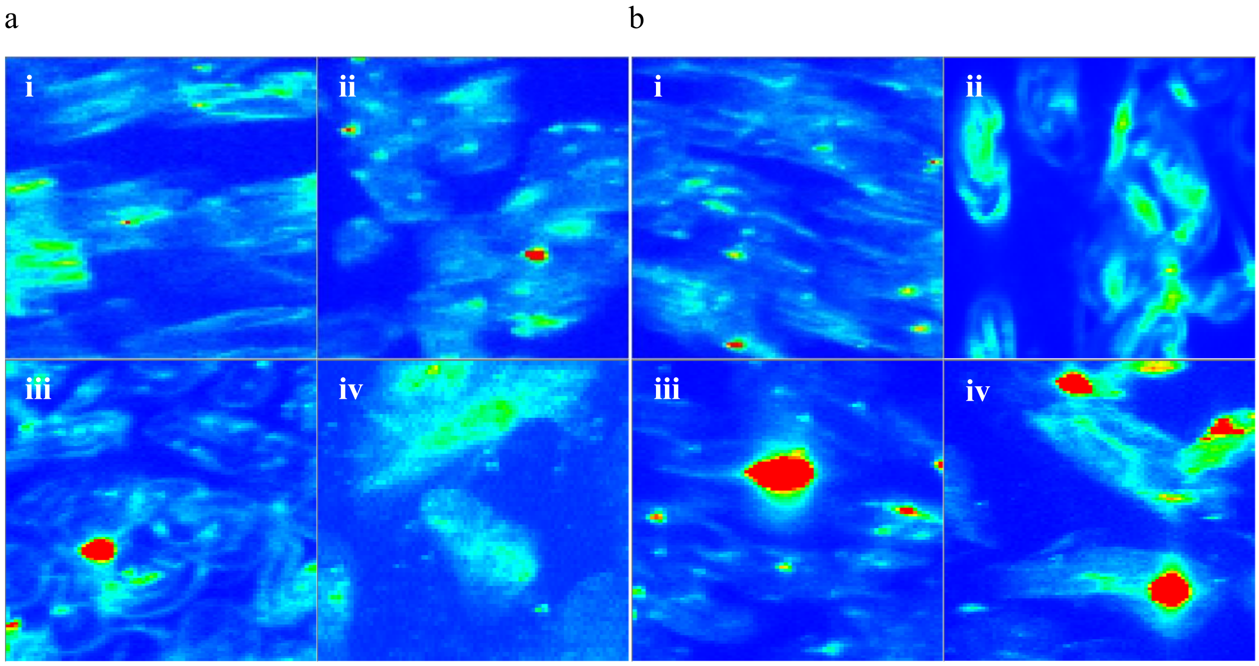

Micro- XRF images of cotton fabrics from a) the yarn surface for i) 50 nm TAS ii) 500 nm TAS iii) 1000 nm TAS and iv) TAS in gel (about 5000 nm) b) the yarn bulk for) 50 nm TAS ii) 500 nm TAS iii) 1000 nm TAS and iv) TAS in gel (about 5000 nm)

Polyester Fibres

Comparisons between the silicon maps obtained on the yarn surface and in the bulk of the yarn generally show little to no difference, suggesting penetration of actives into the bulk of the yarn. This could be explained by the larger pore sizes between the fibres compared to cotton and the well-ordered arrangement of the fibres within the yarn. The actives appear constrained to the surface with no penetration into the individual synthetic fibres. The only exception is the yarn bulk image of 250 nm TAS solution, which shows a droplet in inside an individual fibre figure 10bii. Smaller PDMS droplets, 50 nm (figure 11a and 11c) show higher counts in bulk than on the surface. Again this complements the SEM data suggesting the silicone droplets penetrate the fibre yarn and are not trapped on the fabric surface showing higher deposition in the bulk than on the surface. Larger droplets (500 and 1000 nm) show similar deposition on surface and in yarn for cotton fabrics and higher surface deposition on polyester. On the other hand, TAS (figure 11b and 11d) shows very little difference in the silicon counts between the yarn surface and the yarn bulk for 50 nm and 450 nm solutions.

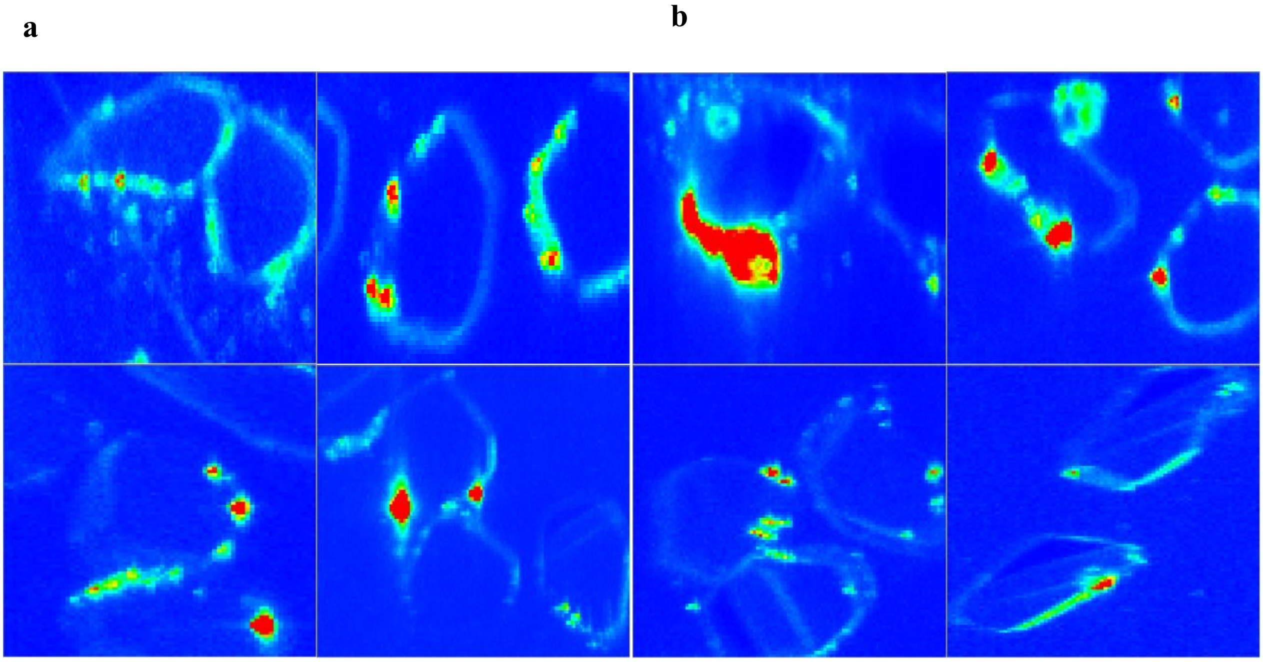

Micro-XRF Si map images of polyester fabrics from a) the yarn surface for i) 50 nm PDMS ii) 500 nm PDMS iii) 1000 nm PDMS and iv) PDMS in gel (about 5000 nm) b) the yarn bulk for) 50 nm PDMS ii) 500 nm PDMS iii) 1000 nm PDMS and iv) PDMS in gel (about 5000 nm)

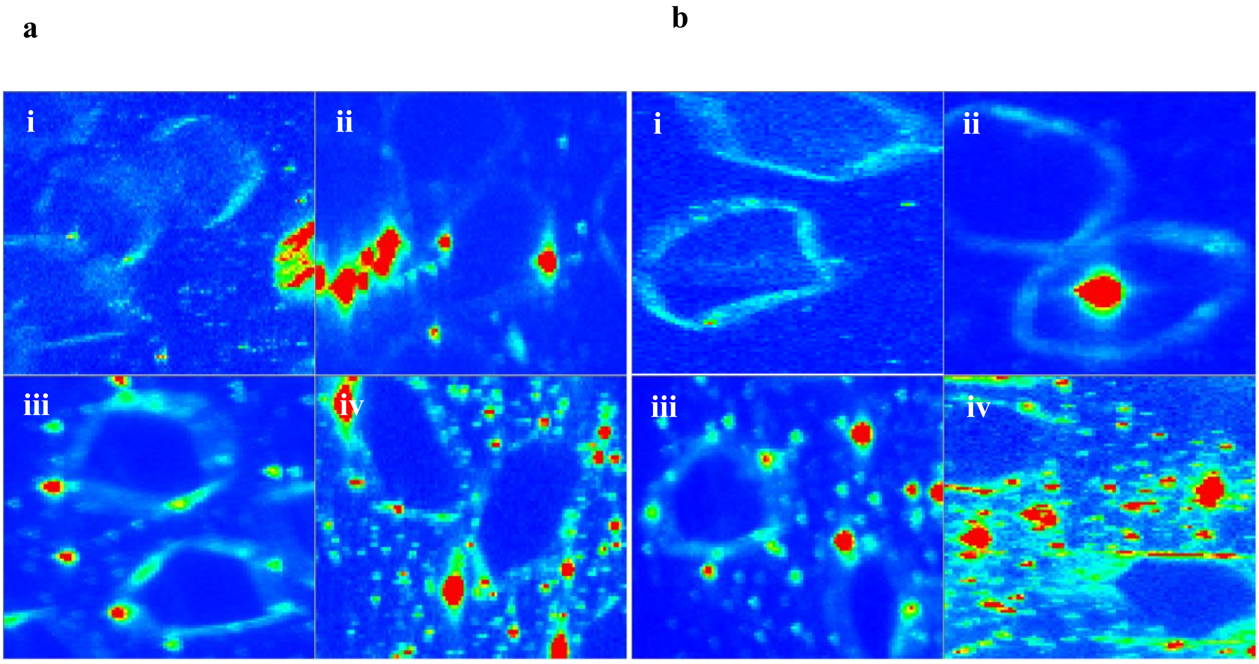

Micro- XRF images of polyester fabrics from a) the yarn surface for i) 50 nm TAS ii) 500 nm TAS iii) 1000 nm TAS and iv) TAS in gel (about 5000 nm) b) the yarn bulk for) 50 nm TAS ii) 500 nm TAS iii) 1000 nm TAS and iv) TAS in gel (about 5000 nm)

Appendix 4

Additional SEM images acquired for cotton and fabric samples treated with silicone loaded SLM to supplement those shown in Figure 4.18.

Appendix 4a. SEM images of cotton and polyester fibres treated with PDMS loaded SLM dispersed in water. SLM particles mostly remain intact and deposit randomly onto both the cotton and polyester fabric surface.

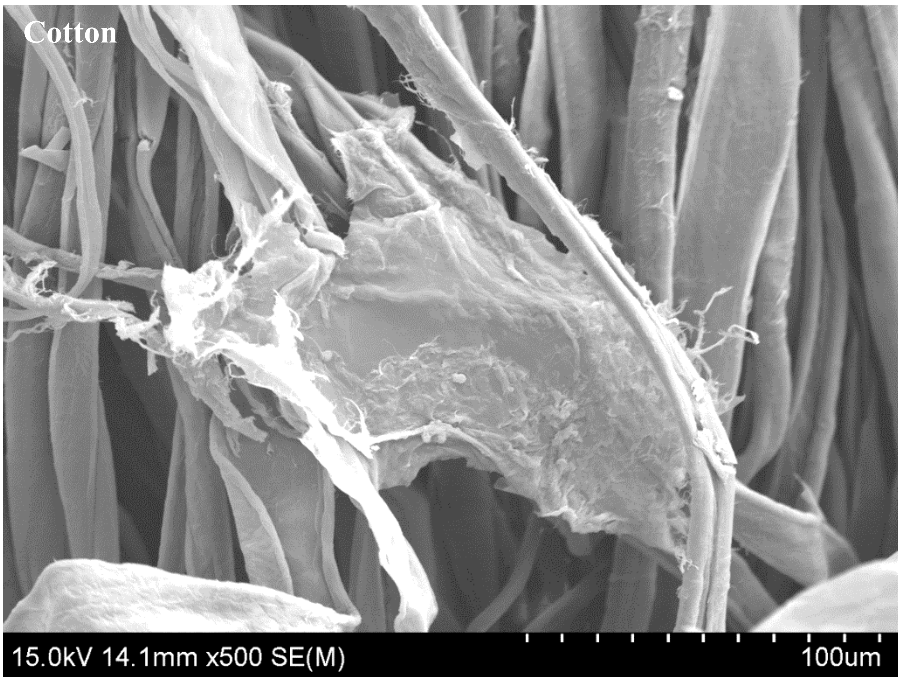

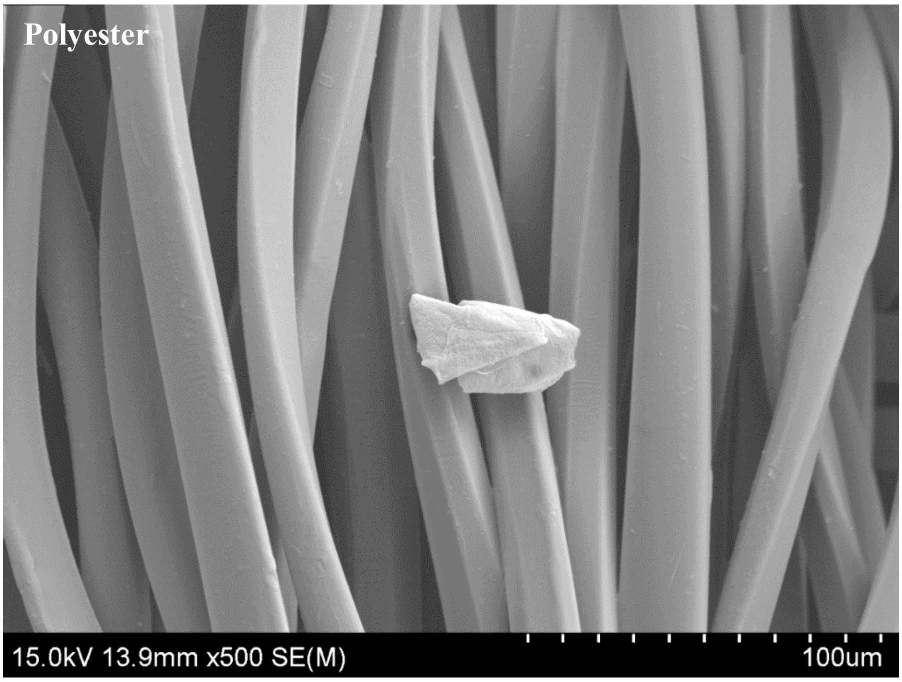

Appendix 4b. SEM images of cotton and polyester fibres treated with PDMS loaded SLM dispersed in a pH 10.5 buffer.The lipid matrix dissociates at alkaline pH values and releases PDMS, which deposits onto the fabric surface

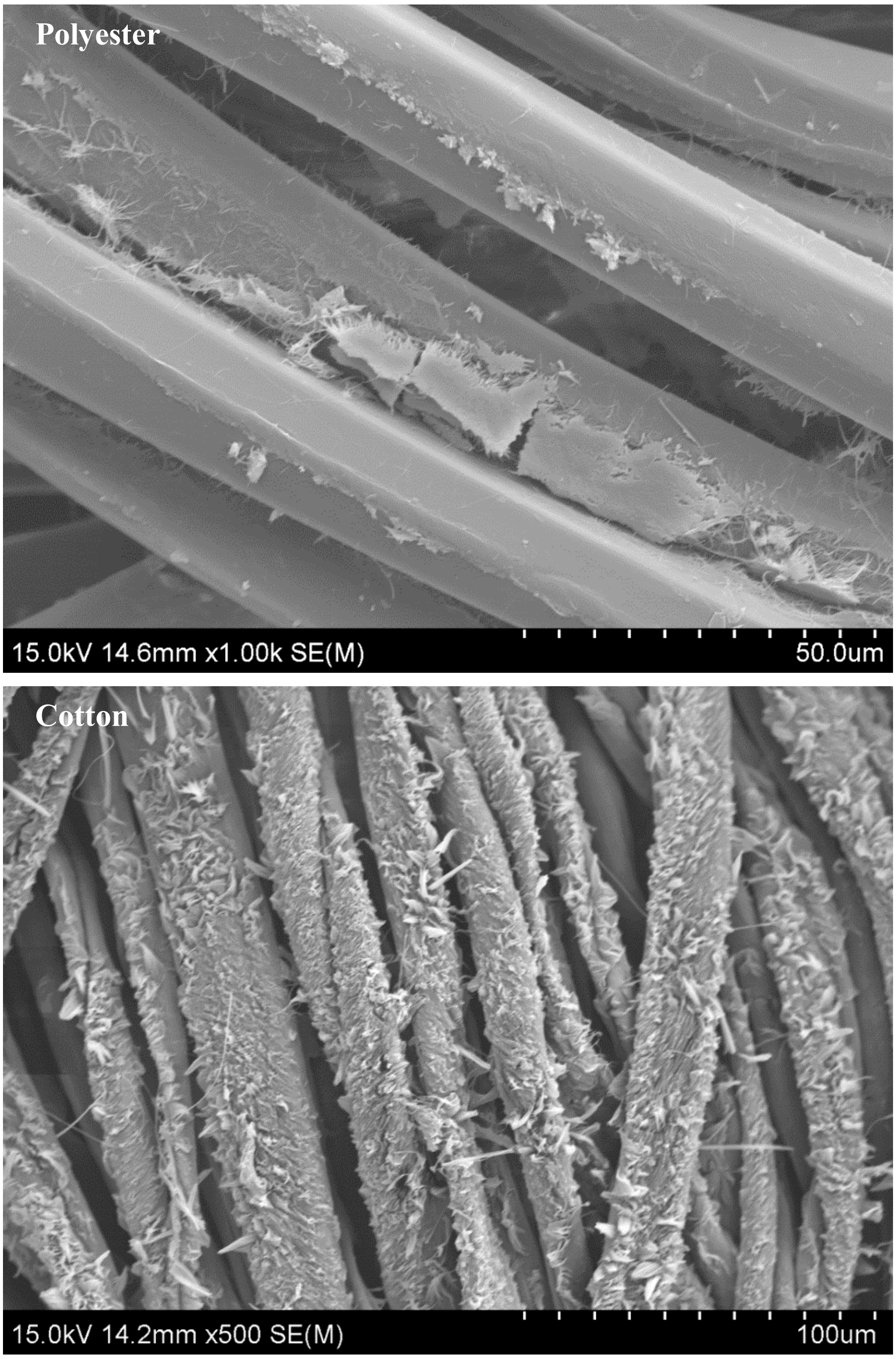

Appendix 4c. SEM images of cotton fibres treated with PK10 loaded SLM dispersed in water. SLM particles mostly remain intact and deposit randomly onto both the cotton and polyester fabric surface.

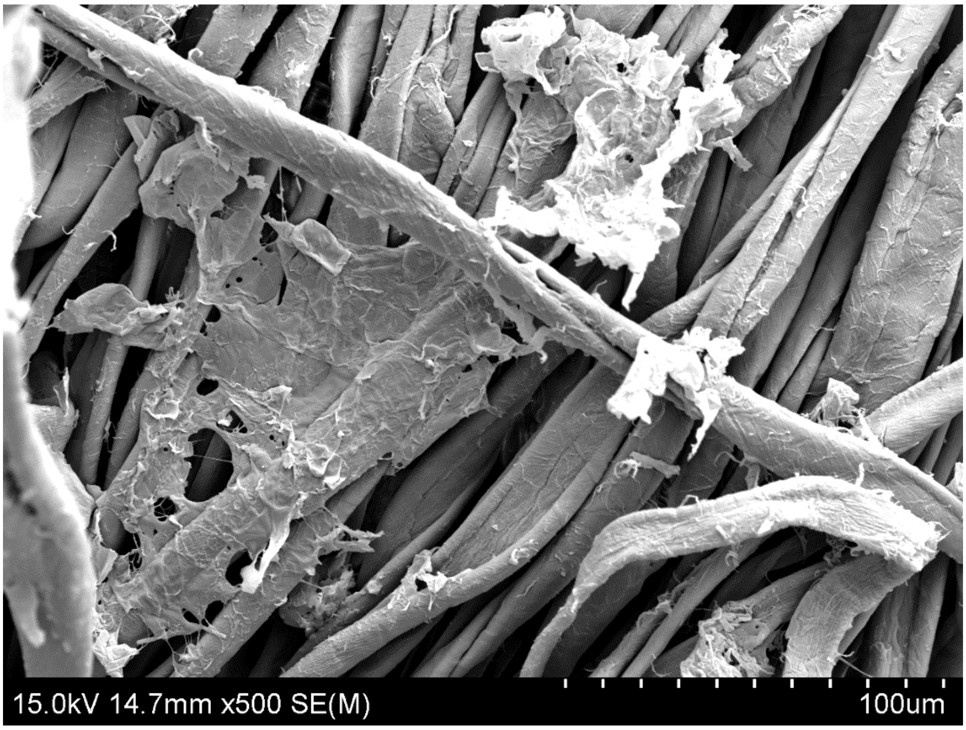

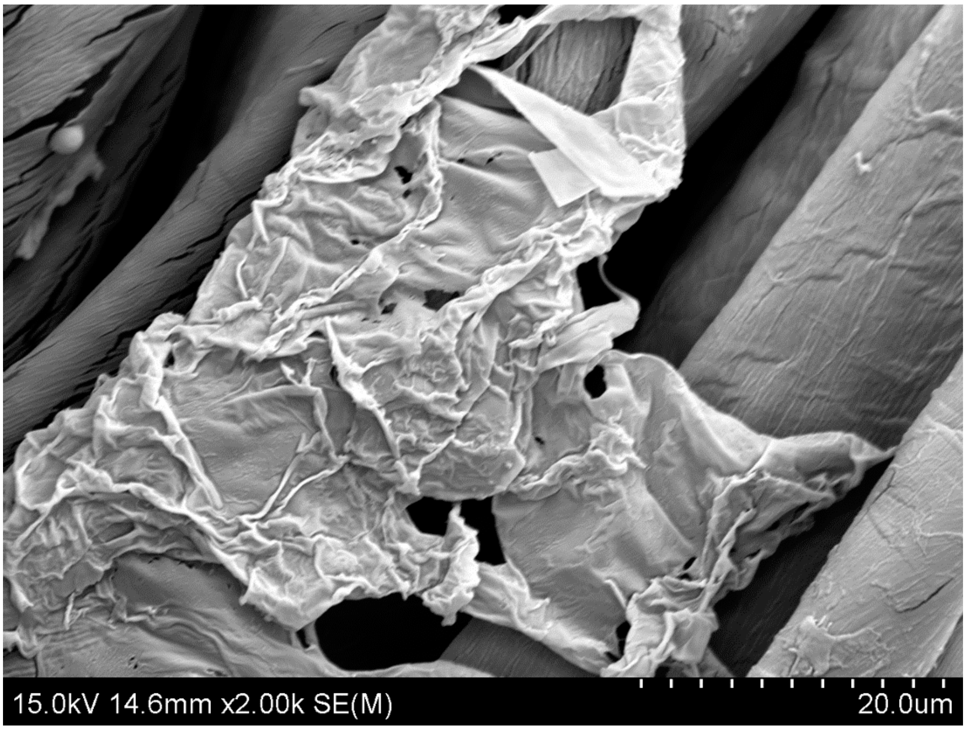

Appendix 4d. SEM images of polyester fibres treated with PK10 loaded SLM dispersed in water. SLM particles mostly remain intact and deposit randomly onto both the cotton and polyester fabric surface.

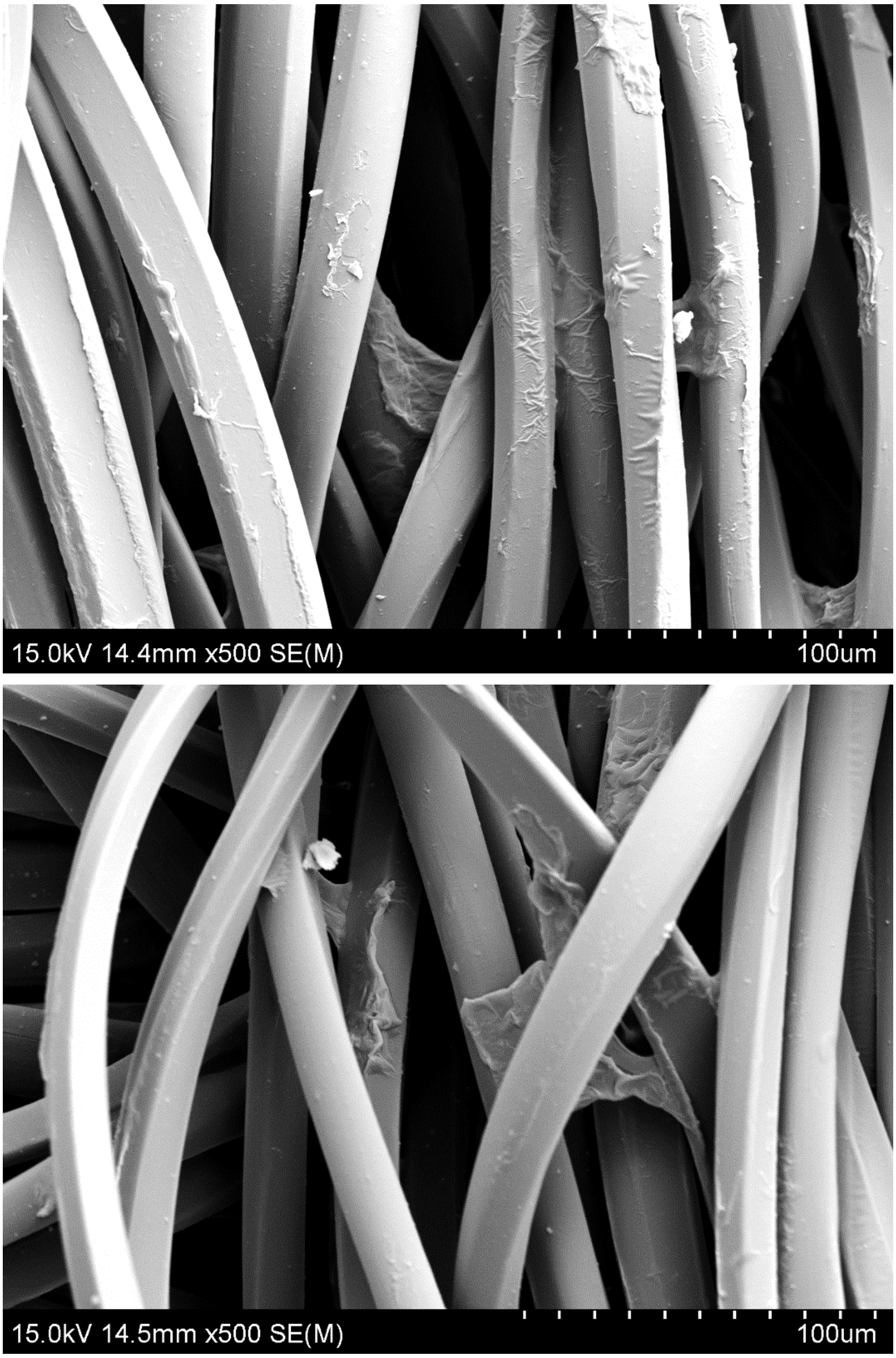

Appendix 4e. SEM images of cotton fibres treated with PK10 loaded SLM dispersed in a pH 10.5 buffer.The lipid matrix dissociates at alkaline pH values and releases PDMS, which deposits onto the fabric surface

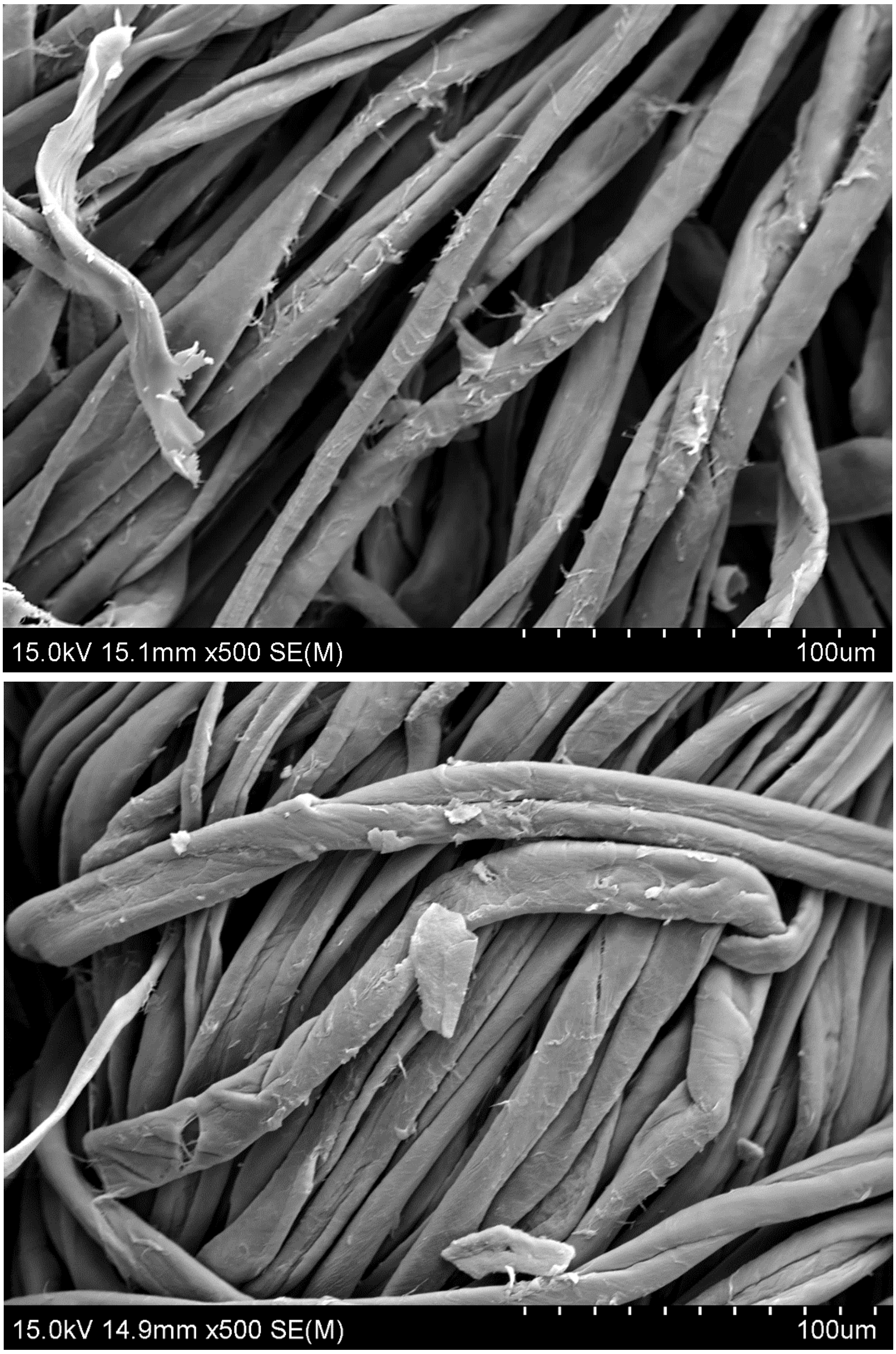

Appendix 4f. SEM images of polyester fibres treated with PK10 loaded SLM dispersed in a pH 10.5 buffer.The lipid matrix dissociates at alkaline pH values and releases PDMS, which deposits onto the fabric surface

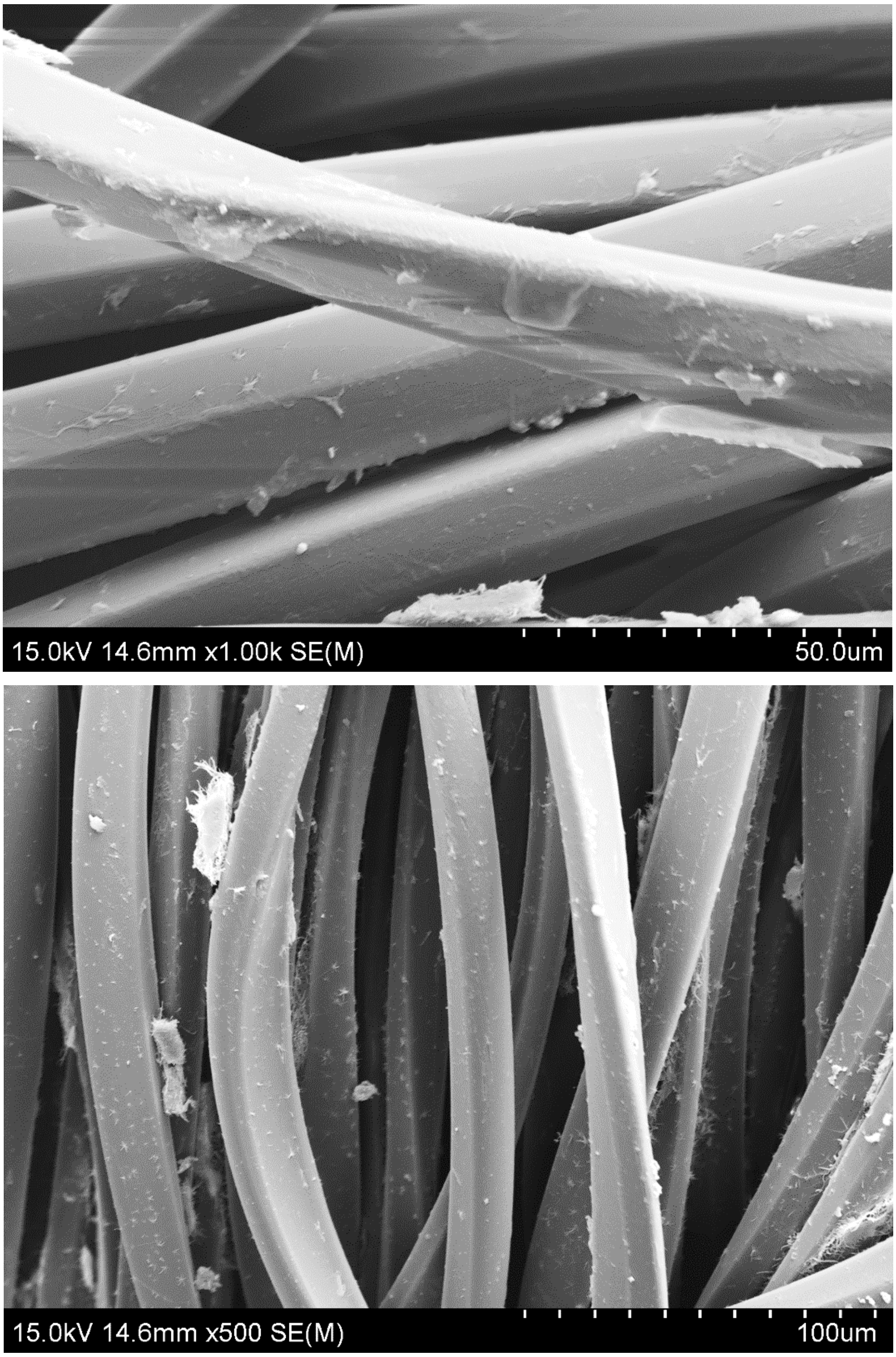

Appendix 5

DLS data showing the full range of the particle size data shown in Figure 6.7a.

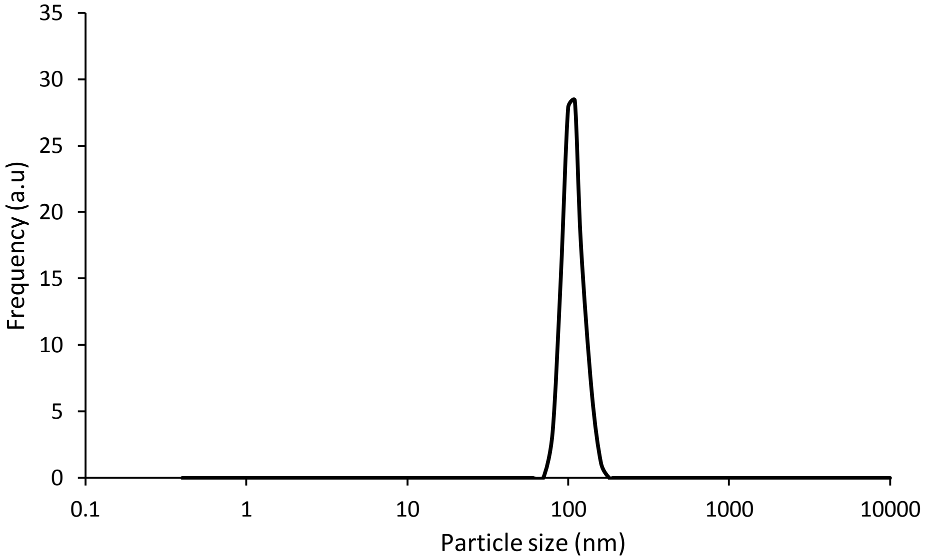

Appendix 6

Additional RESI data to supplement the data shown in Figure 6.21. Interfacial capacitance changes for a bare Au surface, SAM films and BLM films were measured to investigate the response to solid lipid nanoparticle dispersions. The effect of concentration was also investigated by running the experiment with a dilute Fc-SLN dispersion again with a non-loaded SLN dispersion.

Appendix 6a. Fc-SLN dispersion on a bare Au electrode surface. After injection of Fc-SLN into the flow cell, an increase in capacitance is observed. This could be attributed to the introduction of ferrocene and lauric acid in the Fc-SLN which could change the dielectric coefficient of the solution or due to the change in viscosity of the solution. However, the a further increase in capacitance is observed after the solution is changed back to 0.1 M KNO_3 and does not return to the initial capacitance before injection. This suggests that the electrode surface incurs changes after exposure to the Fc-SLN. It should be noted that the difference is very small (1 nF/cm^2) and thus is inconclusive. Extending the measurement period further beyond end of the Fc-SLN injection could help provide more conclusive data.

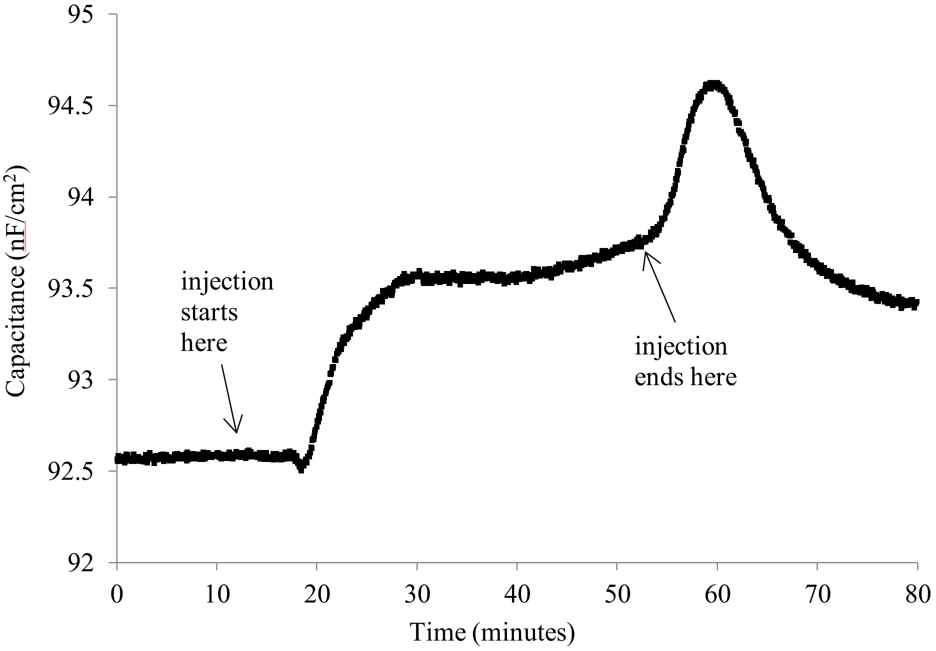

Appendix 6b. Interfacial capacitance changes as a result of exposure to Fc-SLN. The figure here are repeat measurements of the data presented in Figure 6.21. The decrease in capacitance observed is attributed to the adsorption of Fc-SLN onto the SAM film by hydrophobic interactions and further step-like decrease are attributed to the penetration of the Fc-SLN into the SAM film, introducing defects. Figure ii shows a further increase in the capacitance before the end of the injection which could suggest recovery of the SAM film . However, further studies are required to confirm this.

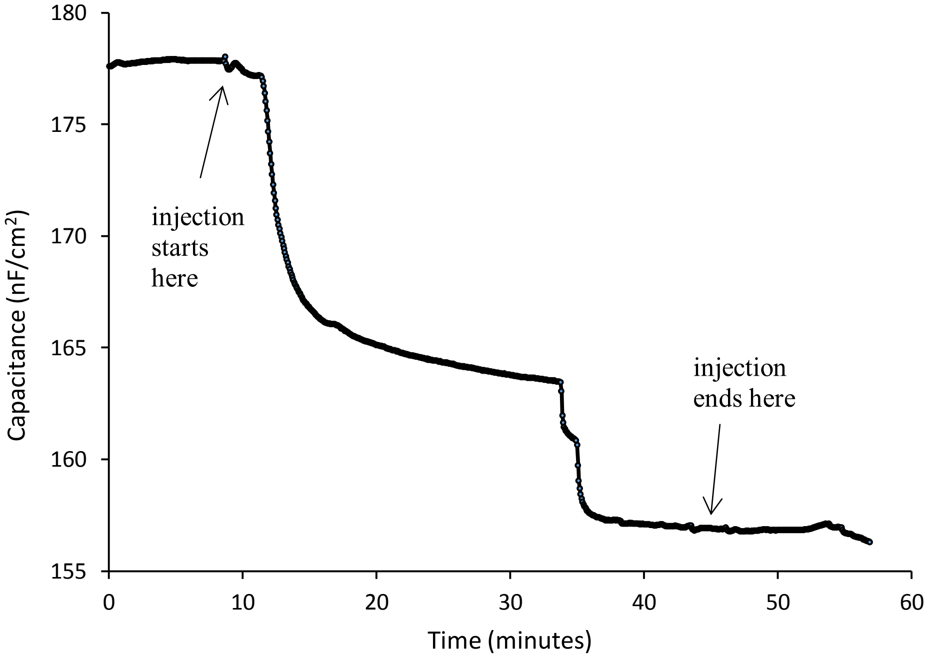

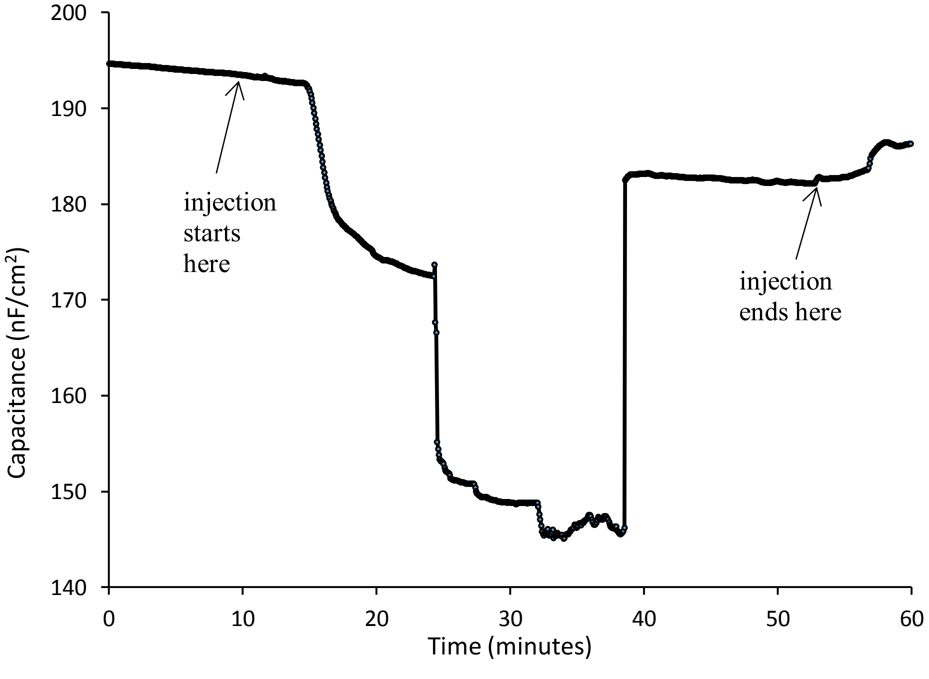

Appendix 6c. Interfacial capacitance changes as a result of exposure to Fc-SLN. The figure here are repeat measurements of the data presented in Figure 6.22. The reduction of in interfacial capacitance observed can be attributed to the deposition of the Fc-SLN onto the BLM surface. The step-like changes observed in Figure 6.22 were not present in the repeat measurements. The data could suggest that the particles deposit onto the BLM surface and are washed off when the solution is changed back to 0.1 M KNO_3, hence the increase in capacitance after injection of Fc-SLN stops.

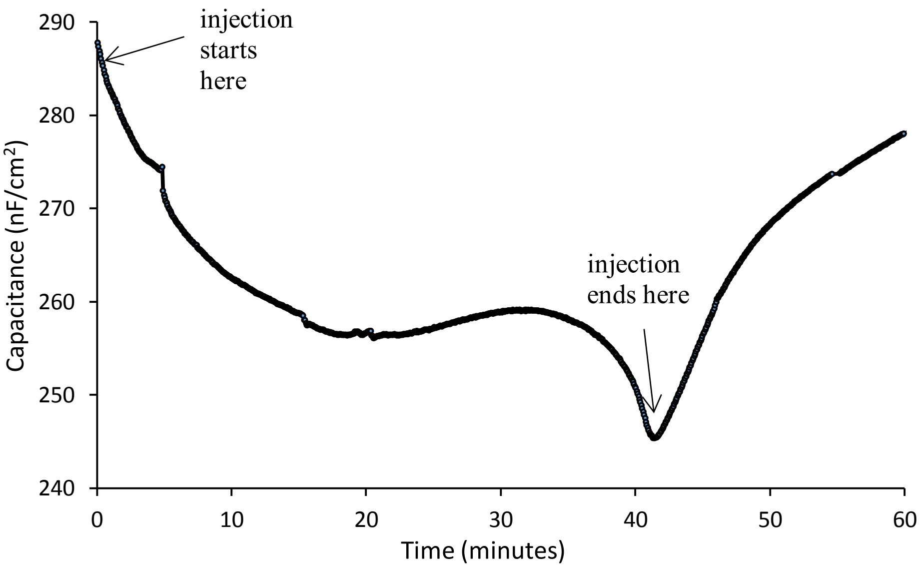

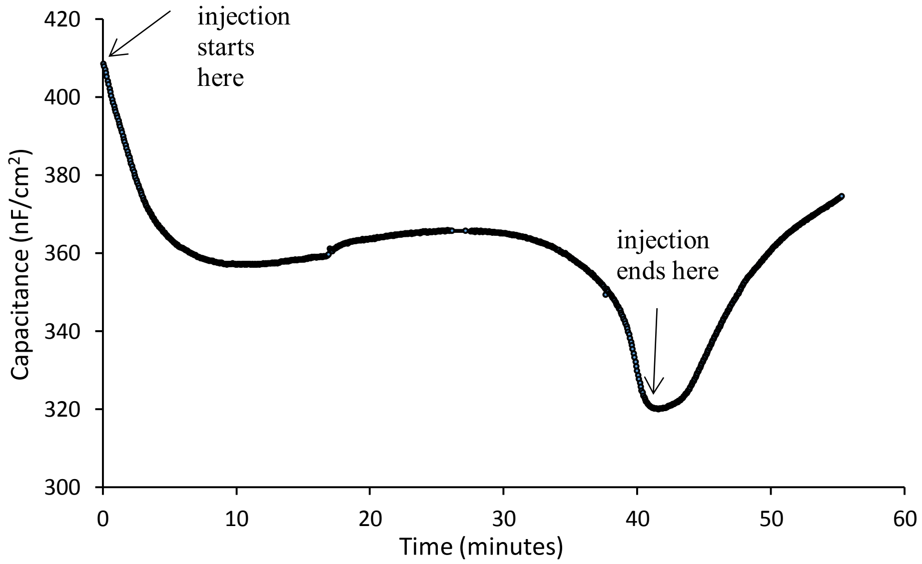

Appendix 6d. Interfacial capacitance changes as a result of exposure to non-loaded SLN. The decrease in capacitance observed is attributed to the adsorption of the non-loaded SLN onto the SAM film by hydrophobic interactions and possibly desorption of the particles when the injection of Fc-SLN stops.

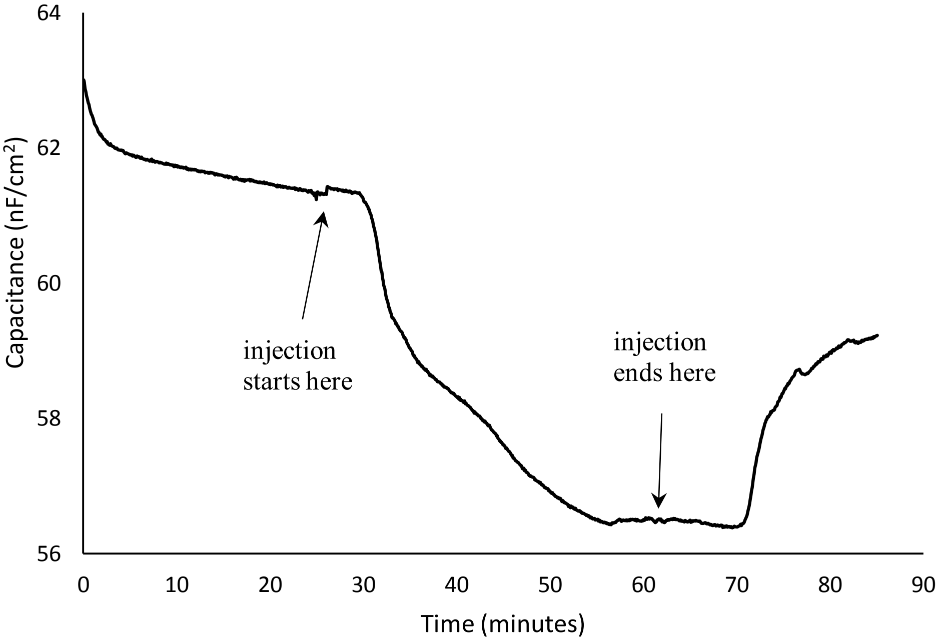

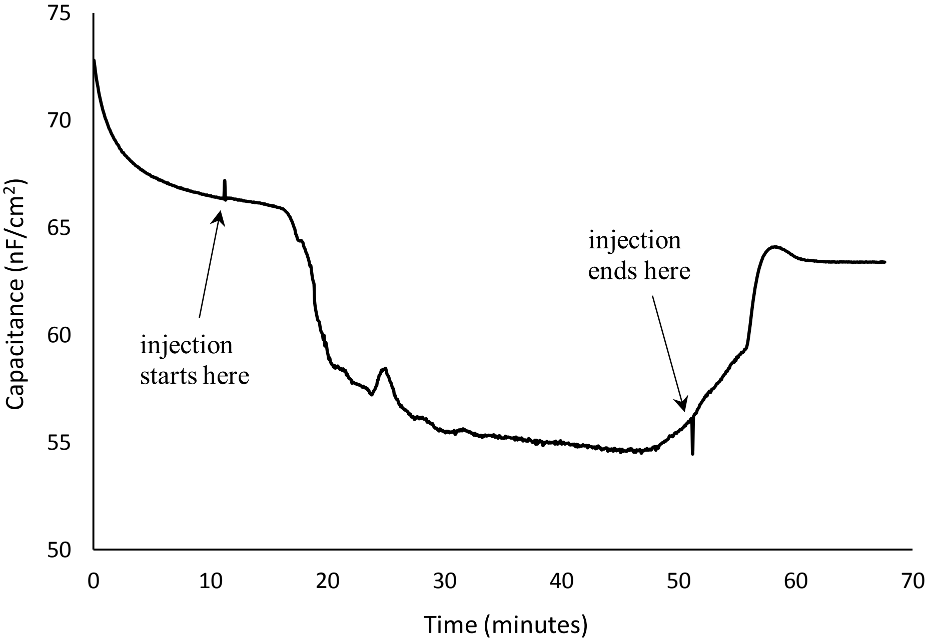

Appendix 6e. Interfacial capacitance changes as a result of exposure to a dilute Fc-SLN. Only a small reduction is observed in capacitance (1.2 nm cm^{-2}) compared to ˜20 nm cm^{-2} observed for SAM samples with a higher concentration of nanoparticles.

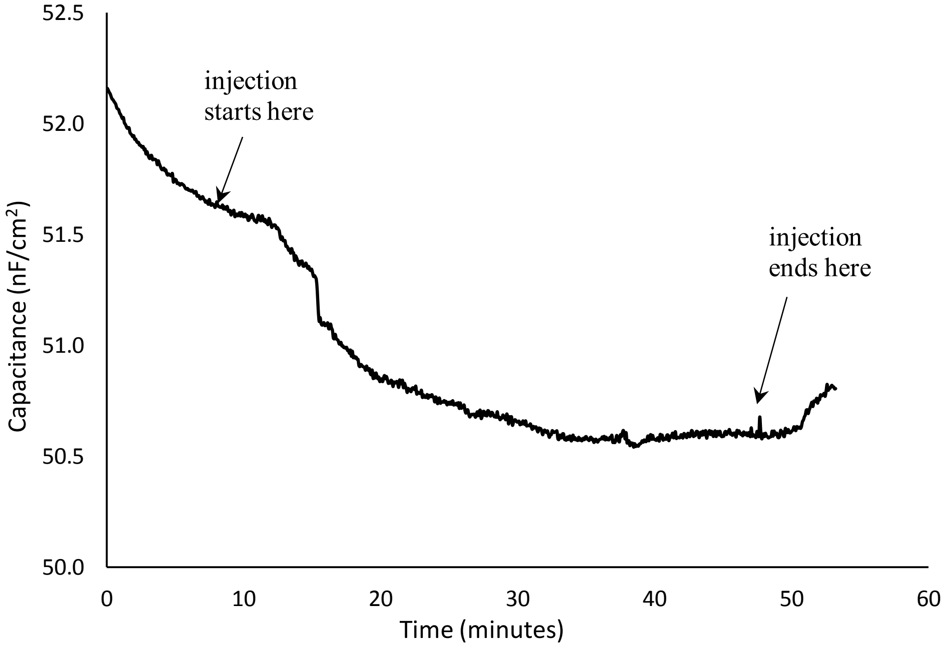

THE END